Paleoproterozoic to Mesoproterozoic evolution of Yukon Territory, Canada

by

Jacob Verbaas

M.Sc., Universiteit Utrecht, 2011
B.Sc., Universiteit Utrecht, 2009

Thesis Submitted in Partial Fulfillment of the
Requirements for the Degree of
Doctor of Philosophy

in the
Department of Earth Sciences
Faculty of Science

SIMON FRASER UNIVERSITY

FALL 2017

Approval

Name:	**Jacob Verbaas**
Degree:	**Doctor of Philosophy**
Title:	***Paleoproterozoic to Mesoproterozoic evolution of Yukon Territory, Canada***
Examining Committee:	**Chair: Dr. Andrew J. Calvert** Professor

Derek J. Thorkelson
Senior Supervisor
Professor

H. Daniel Gibson
Supervisor
Professor

Daniel D. Marshall
Supervisor
Professor

Dejan Milidragovic
Supervisor
Senior Minerals Geologist
BC Geological Survey

Dirk Kirste
Internal Examiner
Associate Professor

Richard E. Ernst
External Examiner
Scientist-In-Residence
Department of Earth Sciences
Carleton University

Date Defended/Approved: November 20, 2017

Abstract

The supercontinent Columbia existed from approximately 1.8 to 1.3 Ga. During this time, complex tectonic interactions occurred between northwestern Laurentia and Australia. This thesis concerns three geologic events on northwestern Laurentia. The first event is the development of a post-collisional sedimentary overlap assemblage at 1.6 Ga herein called the Wernecke-Ogilvie unlithified succession (WOUS). The second event is the formation of the Wernecke Breccia, a set of 1.60 Ga hydrothermal breccia zones. The third is the emplacement of the 1.38 Ga Hart River sills.

The WOUS was a succession of sandstone and mudstone that was deposited after collision between Laurentia and Australia at ~1.6 Ga, and prior to the formation of the Wernecke Breccias at 1.60 Ga. The WOUS is contained as clasts within the Wernecke Breccia. On the basis of detrital zircon U-Pb ages, Lu-Hf model ages and neodymium isotope geochemistry, the WOUS is correlated to sedimentary units within the hydrothermal breccias of the Olympic Dam deposit on the Gawler Craton of Australia.

The Wernecke Breccia occurs as zones that are metres to kilometres in size that are scattered over an area of 300 x 150 km. The breccia zones are post-orogenic and are hosted by the deformed and metamorphosed Wernecke Supergroup. The breccias formed from voluminous hydrothermal surges with a significant gaseous component. These surges vented, and overlying rock units foundered kilometres deep into the breccia zones.

The Hart River sills extend from the eastern Ogilvie Mountains to the Wernecke Mountains. Individual sills are up to 200 km long and 500 m thick. The sills are mafic to intermediate, and tholeiitic. The sills are dated herein at 1382.15 ± 0.39 Ma and 1382.14 ± 0.36 Ma. The magma that formed the sills resulted from ~10% partial melting of spinel bearing mantle similar to a MORB source. Coeval and possibly related magmatism occurred farther south on Laurentia, and to the north on Siberia. These magmatic events occurred on a possible rift axis that extended along the western margin of Laurentia and may signify breakup of the supercontinent Columbia.

Keywords: Proterozoic, Yukon, northwestern Laurentia, Wernecke Breccia, Hart River sills, detrital zircon, paleogeography

To Gurveen, who gave me the determination to finish this manuscript

To Pieter, who left us too soon

To my family, for a lifetime of unwavering love and support

Acknowledgements

I would like to express my gratitude to Derek Thorkelson, my senior supervisor. For enabling me to work on two exciting geological phenomena, the Wernecke Breccia and the Hart River sills. For pushing me to think through all possible avenues and to only deliver work of the highest standard. Lastly, for being patient and taking the time to sit down and discuss complicated matters and making sure that I always understood not only the science, but also the history of it.

My gratitude extends to the other members of my committee, Dan Gibson, Dan Marshall, and Dejan Milidragovic. Thank you for encouragement, discussions, and edits of my work.

The Wernecke Breccia are geologically complicated and trying to understand them was daunting and exciting. My understanding of the breccia zones greatly benefited from discussions with Russ Eley (RTx) and many other geologists in both academia and industry.

J. Payne and an anonymous reviewer provided valuable journal reviews on Chapter 3.

Table of Contents

List of Tables

List of Figures

List of Abbreviations and Acronyms

CA-TIMS	Chemical Abrasion Thermal Ionization Mass Spectrometry
E-MORB	Enriched Mid Oceanic Ridge Basalt
HFSE	High Field Strength Element(s)
HREE	Heavy Rare Earth Element(s)
HRS	Hart River Sills
HRV	Hart River Volcanics
LA-ICPMS	Laser Ablation Inductively Coupled Plasma Mass Spectrometry
LILE	Light Ion Lithophile Element(s)
LREE	Light Rare Earth Element(s)
MC-ICPMS	Multi Collector Inductively Coupled Plasma Mass Spectrometry
MORB	Mid Oceanic Ridge Basalt
N-MORB	Normal Mid Oceanic Ridge Basalt
REE	Rare Earth Element(s)
SFU	Simon Fraser University
SHRIMP	Sensitive High-Resolution Ion Microprobe
SSL	Soft Sediment Lithotype
SWEAT	Southwest US-East Antarctica
WOUS	Wernecke-Ogilvie Unlithified Succession

Chapter 1.

Introduction

1.1. Thesis scope

Yukon Territory is part of the Western Laurentian margin and contains more than 1 billion years of Proterozoic rock record (Young et al., 1979; Delaney, 1981). This record includes thick sedimentary successions punctuated by magmatic, and hydrothermal events (Wheeler, 1954; Green, 1972; Young et al., 1979; Eisbacher, 1981; Delaney 1981; Thompson, 1982, 1995; Abbot, 1997; Thorkelson, 2000). In the past two decades, isotopically determined ages of metamorphic, hydrothermal, and depositional episodes combined with other geological data have allowed for reinterpretation of the paleogeography of Paleoproterozoic to Mesoproterozoic northwestern Laurentia (Thorkelson et al., 2001a, b, 2005; Milidragovic et al., 2011; Furlanetto et al., 2013; 2016; Nielsen et al., 2013; Medig et al., 2014, 2016; Thorkelson and Laughton, 2015). This reinterpretation has revealed that the western Laurentian margin was host to complex continent-continent interactions during the existence of the supercontinent Columbia (also known as Nuna).

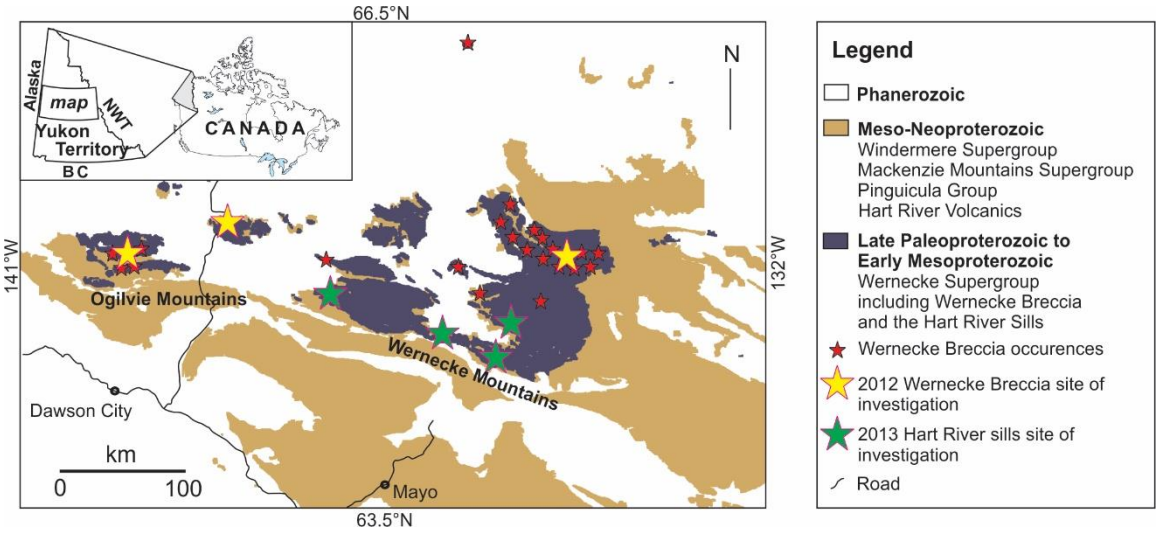

Figure 1.1. Late Paleoproterozoic to Mesoproterozoic inliers of the Yukon Territory and key localities visited in 2012 and 2013.

This thesis concerns the evolution of northwestern Laurentia in the Yukon Territory during an interval that spans the formation of the oldest rock known in Yukon (1.71 Ga) until the emplacement of mafic to intermediate sills during the Mesoproterozoic (1.38 Ga). In particular it focuses on the 1.6 Ga Wernecke Breccia, a hydrothermal breccia system that formed after continental collision of Laurentia and Australia (Thorkelson et al., 2001a; Furlanetto et al., 2013; Nielsen et al., 2013; Thorkelson and Laughton, 2016) and on the Hart River sills, which represent an episode of magmatism at 1.38 Ga (Abbott, 1997; Thorkelson et al., 2005). Over the course of two field seasons in 2012 and 2013 samples were collected and field relations scrutinized at key localities (Figure 1.1). These samples were subsequently used to test existing hypotheses, and advance new ones, regarding the paleogeography of northwestern Laurentia.

1.2. Thesis structure

This thesis contains 4 main chapters (Chapters 2 – 5), an introduction (this chapter) and conclusion (Chapter 6). Chapter 2 contains a description of the field relations and occurrence of sediments with soft sediment textures within the Wernecke Breccia. This chapter was published in the Yukon Exploration and Geology bulletin of the Yukon Geological Survey in 2014 (Verbaas et al., 2014). The publication was co-authored by Derek J. Thorkelson, H. Dan Gibson, Dan D. Marshall, and Dejan Milidragovic. Derek

Thorkelson provided valuable insight in the field and throughout the writing process, and Dan Gibson, Dan Marshall and Dejan Milidragovic provided valuable reviews and input.

Chapter 3 contains detrital zircon and geochemical data of the sediments described in chapter 2. This chapter has accepted in a peer-reviewed journal, and was co-authored by Derek J. Thorkelson, James Crowley, William. J. Davis, David A. Foster, H. Dan Gibson, Dan D. Marshall, and Dejan Milidragovic. Derek Thorkelson provided assistance in the field and throughout the writing process. James Crowley and William J. Davis obtained U-Pb isotopic ages. David A. Foster provided Lu-Hf isotopic data on zircon. H. Dan Gibson, Dan D. Marshall, and Dejan Milidragovic provided help with data interpretation and provided valuable reviews and input. Chapter 4 and 5 are intended for submission.

Chapter 4 contains an evaluation of previously proposed and new models of formation of the Wernecke Breccia. This chapter is intended for publication. H. Dan Gibson, Dan D. Marshall, and Derek J. Thorkelson provided valuable input and reviews.

Chapter 5 contains new U-Pb isotopic ages and a geochemical treatment of the Hart River sills. This chapter is intended for publication. Derek J. Thorkelson and Dejan Milidragovic provided help with the data interpretation and petrology and H. Dan Gibson and Dan D. Marshall provided valuable reviews and input.

1.3. Geologic context

1.3.1. The Wernecke Breccia

The Wernecke Breccia is a set of hydrothermal breccia zones that is exposed over an area of 48 000 km^2 from the Ogilvie Mountains to the Wernecke Mountains and the Southern Richardson Mountains (Thorkelson et al., 2001a; Thorkelson et al., 2005). The Wernecke Breccias were formed at 1598.8 ± 1 Ma as indicated by U-Pb dates on metasomatic titanite (Thorkelson, 2005; Furlanetto et al., 2013). Individual breccia zones are sub-circular to tabular bodies and range in size from several metres to kilometres (Lane et al., 1990; Thorkelson et al., 2001a). Individual clasts range in size from mm-size

to megaclasts that are hundreds of metres in length (Lane, 1990; Nielsen, 2013; Thorkelson and Laughton, 2016). The matrix/clast ratio is highly variable and ranges from 30 – 70%. Alteration in the breccia zones is mainly hematitic and potassic, with local chloritic, sodic and calcic varieties.

The Wernecke Breccias are hosted within the Wernecke Supergroup. The Wernecke Supergroup is a >13 km thick succession of siliciclastic and carbonate rocks that was deposited after 1.66 Ga (Delaney, 1981, 1985; Thorkelson, 2000; Furlanetto et al., 2013; 2016). The Wernecke Supergroup consists of passive margin strata and is underlain by 5-9 km of unexposed stratified rocks and basement (Furlanetto et al., 2013, 2016). The Wernecke Supergroup was deformed and partly subjected to greenschist grade metamorphism during the Racklan Orogeny at ~1.6 Ga (Thorkelson et al., 2005; Furlanetto et al., 2013).

The Wernecke Breccia locally host iron oxide-copper-gold (IOCG) occurrences (Hitzman, 1992; Williams, 2005). They have been interpreted as a non-magmatic end member of IOCG deposits (Hunt et al., 2007). The Wernecke Breccia was correlated to the Olympic Dam IOCG deposit on the Gawler Craton in Australia by Thorkelson et al. (2001a).

Clasts in the Wernecke Breccia are mainly derived from the Wernecke Supergroup. Field relations indicate that most clasts have either moved down through stratigraphy during brecciation, or remained at the same level. Locally abundant igneous clasts also occur, and none of these were derived from the Wernecke Supergroup. These igneous clasts were derived from units previously overlying the Wernecke Supergroup (Nielsen et al., 2013; Furlanetto et al., 2013; Thorkelson and Laughton, 2016).

Igneous clasts in the Wernecke Breccia include the plutonic Bonnet Plume River Intrusions, the Slab volcanics and the Devil volcanics (Thorkelson et al., 2001b; Nielsen et al., 2013). Nielsen et al. (2013) referred to these clasts collectively as the “Wernecke igneous clasts.” The Bonnet Plume River Intrusions are present as small clasts to megaclasts up to 900 x 200 x 30 m and are mafic to intermediate in composition (Thorkelson et al., 2001b; Nielsen et al., 2013). They have been dated via U-Pb on zircon at ca. 1.71 Ga (Thorkelson et al., 2001b) and yield depleted mantle model ages $T_{DM} \approx 2.2$

- 2.1 Ga. The Slab volcanic megaclast is a clast of approximately 200 m in diameter in a Wernecke Breccia zone in the Wernecke Mountains (Thorkelson et al., 2001a; Thorkelson and Laughton, 2016). The Slab volcanic megaclast comprises 34 mafic subaerially deposited flows, with minor sedimentary interbeds (Thorkelson and Laughton, 2016). The Slab volcanics have not been dated. The Devil volcanics are present in the western Ogilvie Mountains and consist of amygdaloidal basalts. Although they have not been dated, they share geochemical characteristics with the Bonnet Plume River Intrusions (Nielsen et al., 2013).

The volcanic and plutonic clasts were sourced from a terrane that was obducted on the Wernecke Supergroup during the ~1.6 Ga Racklan Orogeny (Furlanetto et al., 2013). This obducted terrane is called Bonnetia (Furlanetto et al., 2013). Clasts of Bonnetia foundered into the Wernecke Breccia zones and are currently juxtaposed to the Wernecke Supergroup (Figure 1.2). After the Wernecke Breccia formed, Bonnetia was completely eroded. The only surviving record of Bonnetia are the clasts encased within Wernecke Breccia.

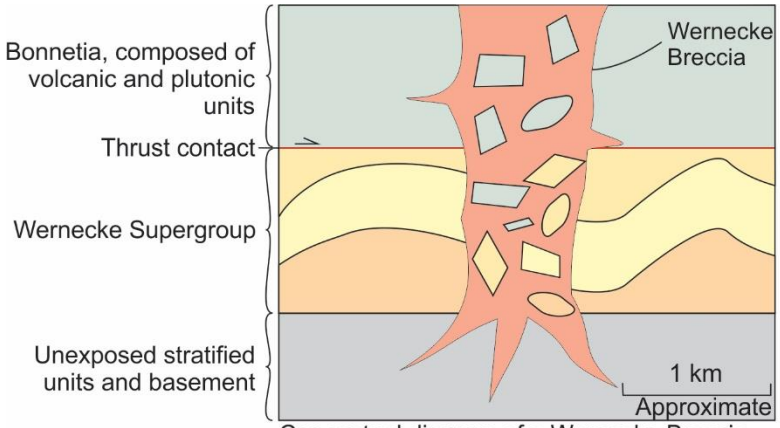

Conceptual diagram of a Wernecke Breccia zone, immediately after formation

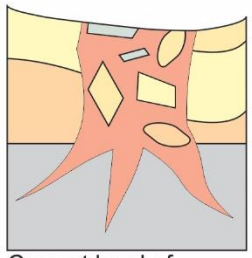

Current level of erosion

Sodically altered Wernecke Breccia. Hammer rests against a clast sourced from the Wernecke Supergroup.

Potassically altered Wernecke Breccia with clasts sourced from the Wernecke Supergroup in metasomatic matrix

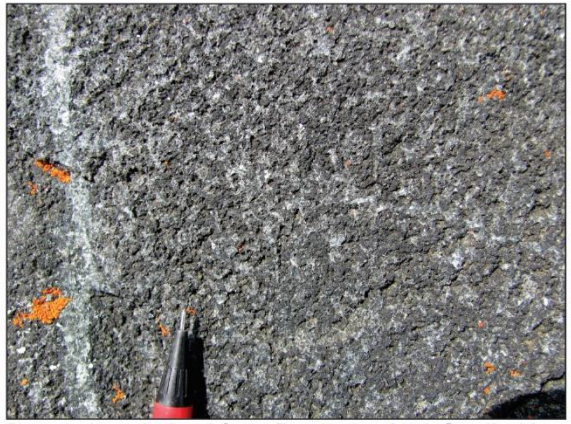

Dated clast derived from Bonnetia: 1.71 Ga dioritic Bonnet Plume River intrusion.

Undated clast derived from Bonnetia: Devil Volcanic clast

Figure 1.2. Detail of a typical Wernecke Breccia zone

1.3.2. The Hart River sills

The Hart River sills are a set of thick mafic to intermediate sills that occur in the Hart River and Wernecke Inliers (Green, 1972; Abbott, 1997). Individual sills can be over 500 m thick and are commonly associated with smaller sills and dykes. The Hart River sills are hosted by the Wernecke Supergroup (Figure 1.3) and are ~1.38 Ga as determined by zircon U-Pb (Abbott, 1997; Thorkelson et al., 2005). Additional dates provided in Chapter 5 of this thesis confirm and refine this age. The extent of the Hart River sills to the west is unknown.

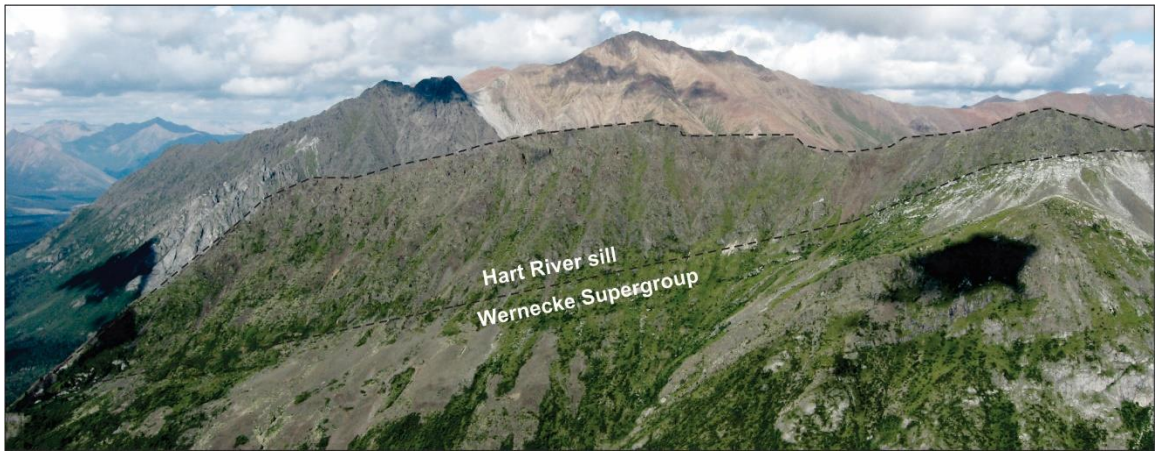

Figure 1.3. A thick (min. 400 m) Hart River sill, hosted within the Wernecke Supergroup

The Hart River sills represent a voluminous injection of mafic magma into the crust during the Mesoproterozoic. Reheating of the crust by the Hart River sills appears to be substantial, as indicated by two 1.38 Ga Lu-Hf garnet dates from the Fairchild Lake Group (Furlanetto et al., 2013) and a 1.38 Ga U-Pb date on metasomatic rutile from a Wernecke Breccia zone (Thorkelson et al., 2001a). The magmatism is also possibly related to the Hart River volcanics, the Hart River deposit (Abbott, 1997) and the Blende deposit (Moroskat, 2009). Although the magmatic event was substantial, the cause of magmatism and ambient tectonic environment have not been studied.

1.3.3. Paleogeography of Paleoproterozoic to Mesoproterozoic northwestern Laurentia

The thrust nappe Bonnetia, which served as a source for igneous clasts in the Wernecke Breccia zones, was depicted as a volcanic arc outboard of Laurentia by Furlanetto et al., (2013). Evolved Sm-Nd model ages of Bonnetia derived rocks were used by Nielsen et al., (2013) to argue that Bonnetia was built on older crust. Thorkelson and Laughton (2016) furthered this idea and proposed that Bonnetia was part of a volcanic arc that flanked Australia, and termed this the Bonnetian Arc (Figure 1.4).

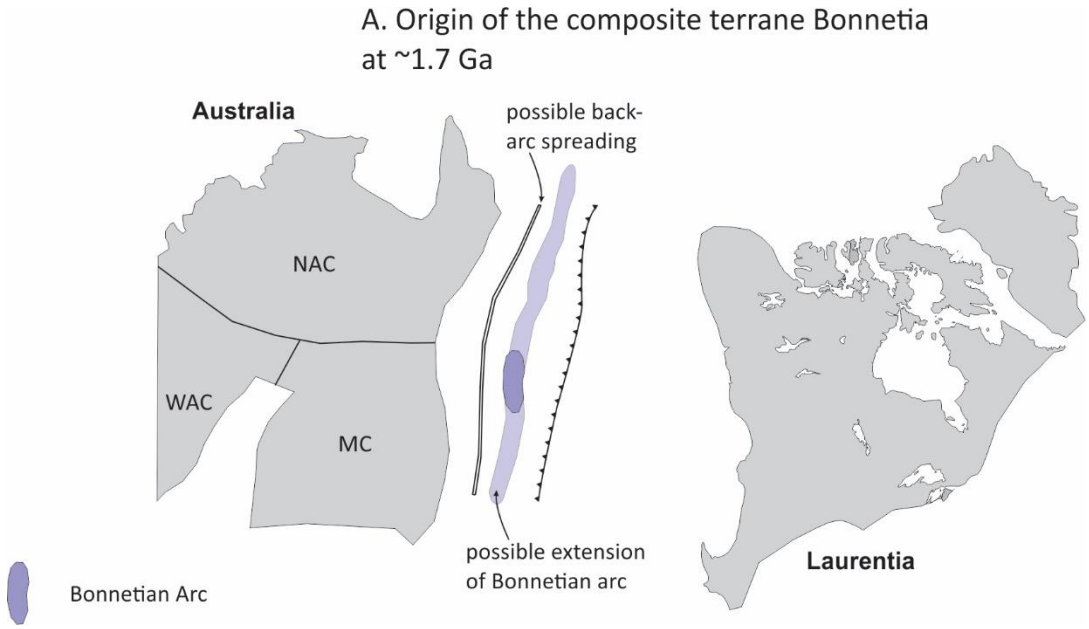

Figure 1.4. Paleogeography at ~1.7 Ga. Abbreviations are MC = Mawson Continent (Gawler Craton and Antarctica after Payne et al., 2009), NAC = Northern Australia Craton and WAC = Western Australia Craton. (Modified from Thorkelson and Laughton, 2016).

A Mesoproterozoic link between Australia and Laurentia has previously been proposed based on detrital zircon provenance studies and other geological data in both the US and Canada (Ross et al., 1992; Goodge et al., 2010; Shufeldt et al., 2010; Doe et al., 2012; Dalziel et al., 2013; Medig et al., 2014; Jones, 2015; Gibson et al., 2017). This link is permissible by paleomagnetic reconstructions from at least 1.77 – 1.50 Ga (Pisarevsky et al., 2014). Data from the Belt Purcell Supergroup indicate that a shift in provenance from Australia derived detritus to Laurentia derived detritus occurred around 1.45 Ga, and interpret this shift to mark separation between Australia and Laurentia.

During the Mesoproterozoic Siberia was located north of Laurentia (Rainbird et al., 1998; Evans et al., 2015; Ernst et al., 2016). Correlations between magmatic episodes are made, amongst others, at 1.75, 1.35, and 0.72 Ga (Ernst et al., 2016). The paleomagnetic record is consistent with this contiguity (Evans et al., 2016). The Hart River sills were emplaced at 1.38 Ga (Abbott, 1997; Thorkelson et al., 2005) and coeval and possibly related magmatic episodes are present in Idaho, US, and on Siberia (Figure 1.5).

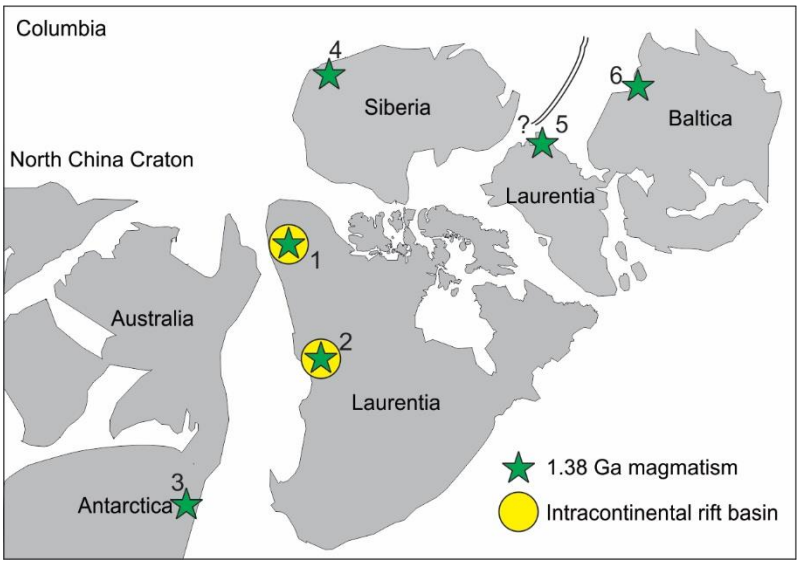

Figure 1.5. Reconstruction of Columbia following Furlanetto et al. (2016). ~1.38 Ga magmatism led to intrusion of the Vestfold Hills Dykes (3, Lanyon et al., 1993), magmatism in the Salmon River arch (2, Doughty and Chamberlain, 1996), the Hart River sills (1, Abbot, 1997; this study), and the Chieress dyke swarm (4, Ernst et al., 2000). Also shown is the rift placed along the margin of Siberia, Baltica, and northeast Laurentia by Puchkov et al. (2013) based on the Mashak event (6, Puchkov et al., 2013) and the Midsommersø dyke swarm (5, Upton et al., 2005). Further shown are roughly coeval intracontinental rift basins on the Laurentian margin: the Belt Purcell Supergroup (2, Ross et al., 1992) and the PR1 basin (1, Medig et al., 2014).

1.4. Thesis objectives

Since the model for the Paleoproterozoic to Mesoproterozoic evolution of the Yukon involving accretion of Bonnetia was published (Furlanetto et al., 2013), significant work has elucidated the affinity of this terrane (Nielsen et al., 2013; Thorkelson and Laughton, 2016). However, an unanswered question remains: “are there other rocks

sourced from Bonnetia within the Wernecke Breccia, and can these be used to constrain the affinity of Bonnetia further?" In order to answer this question, sedimentary rocks unlike those of the Wernecke Supergroup were identified within Wernecke Breccia zones and collected. Field relations are described in chapter 2 and have been published (Verbaas et al., 2014). Whole rock geochemical data and detrital zircon U-Pb and Lu-Hf analyses are described in chapter 3 and have been submitted to a peer reviewed journal, and are used to identify the affinity of Bonnetia.

The Wernecke Breccia has been the target of many exploration programs and academic studies (Thorkelson et al., 2001a; Thorkelson et al., 2005). The Wernecke Breccia is a member of iron oxide-copper-gold deposits (Hitzman et al., 1992; Williams et al., 2005), a mineral deposit type that attracts global exploration interest. The Wernecke Breccia has been described in detail (Lane, 1990; Thorkelson, 2001a), and has been a focal point for paleogeographic reconstructions (Thorkelson et al., 2001a; Furlanetto et al., 2013; Nielsen et al., 2013; Thorkelson and Laughton, 2016). However, it is unknown how exactly the breccias formed. A model of formation may significantly improve our understanding of not only the Wernecke Breccia itself, but also of iron oxide-copper-gold (IOCG) deposits worldwide, and how these deposits can be used for paleogeographic reconstructions. Chapter 4 contains a review of formerly published models, boundary conditions for tenable models, and a new model for the formation of the Wernecke Breccia.

The Hart River sills have been described, dated, and tentatively used in correlations of Laurentia with other continents (Abbott, 1997; Thorkelson et al., 2005; Ernst et al., 2016). However, a rigorous geochemical treatment of the Hart River sills has never been undertaken. The age dating of the Hart River sills was done only on samples of two areas (Abbott, 1997; Thorkelson et al., 2005; Ernst et al., 2008). Chapter 5 contains new high-quality U-Pb dates on zircon, and detailed geochemical whole rock analyses. These analyses are used to identify the ambient tectonic environment of the Hart River sills and place them in global paleogeographic context.

The combined chapters are pivotal in the understanding of the Paleoproterozoic to Mesoproterozoic evolution of Yukon Territory. A heavy emphasis in general is placed on

new and improved paleogeographic interpretations, and the role of Laurentia in Nuna and Columbia. These new interpretations and conclusions are summarized in Chapter 6.

1.5. References

Abbott, G. (1997). Geology of the Upper Hart River Area, Eastern Ogilvie Mountains, Yukon Territory (116A/10, 116A/11). Exploration and Geological Services Division, Yukon, Indian and Northern Affairs Canada, Bulletin 9, 92 p.

Dalziel, I.W.D., 2013, Antarctica and supercontinental evolution: clues and puzzles: Earth and Environmental Science Transactions of the Royal Society of Edinburgh, p. 3–16, doi: 10.1017/S1755691012000096.

Delaney, G.D. (1981). The mid-Proterozoic Wernecke Supegroup, Wernecke Mountains, Yukon Territory. In F.H.A Campbell (Ed.), Proterozoic Basins of Canada pp. 1-24. Geological Survey of Canada, Canadian Government Publishing Centre

Delaney, G.D. (1985). The Middle Proterozoic Wernecke Supergroup, Wernecke Mountains, Yukon Territory. Ph.D. Thesis. University of Western Ontario, 373 p.

Doe, M.F., Jones, J. V., Karlstrom, K.E., Thrane, K., Frei, D., Gehrels, G. & Pecha, M. (2012). Basin formation near the end of the 1.60-1.45 Ga tectonic gap in southern Laurentia: Mesoproterozoic Hess Canyon Group of Arizona and implications for ca. 1.5 Ga supercontinent configurations. Lithosphere. 4. pp. 77–88.

Doughty, P.T. & Chamberlain, K.R. (1996). Salmon River Arch revisited: new evidence for 1370 Ma rifting near the end of deposition in the Middle Proterozoic Belt basin. Canadian Journal of Earth Sciences. 33. pp. 1037–1052.

Eisbacher, G.H. (1981). Sedimentary tectonics and glacial record in the Windermere Supergroup, Mackenzie Mountains, northwestern Canada, Paper 80-27

Ernst, R.E., Buchan, K.L., Hamilton, M.A., Okrugin, A. V & Tomshin, M.D. (2000). Integrated Paleomagnetism and U-Pb Geochronology of Mafic Dikes of the Eastern Anabar Shield Region, Siberia: Implications for Mesoproterozoic Paleolatitude of Siberia and Comparison with Laurentia. The Journal of Geology. 108. pp. 381–401.

Ernst, R.E., Hamilton, M.A., Söderlund, U., Hanes, J.A., Gladkochub, D.P., Okrugin, A. V., Kolotilina, T., Mekhonoshin, A.S., Bleeker, W., LeCheminant, A.N., Buchan, K.L., Chamberlain, K.R. & Didenko, A.N. (2016). Long-lived connection between southern Siberia and northern Laurentia in the Proterozoic. Nature Geoscience. 9, pp. 464-470.

Ernst, R.E., Wingate, M.T.D., Buchan, K.L., and Li, Z.X., (2008), Global record of 1600-700 Ma Large Igneous Provinces (LIPs): Implications for the reconstruction of the proposed Nuna (Columbia) and Rodinia supercontinents: Precambrian Research, v. 160, p. 159–178, doi: 10.1016/j.precamres.2007.04.019.

Evans, D.A.D., Veselovsky, R. V., Petrov, P.Y., Shatsillo, A. V. & Pavlov, V.E. (2016). Paleomagnetism of Mesoproterozoic margins of the Anabar Shield: A hypothesized billion-year partnership of Siberia and northern Laurentia. Precambrian Research. 281. pp. 639–655.

Furlanetto, F., Thorkelson, D.J., Daniel Gibson, H., Marshall, D.D., Rainbird, R.H., Davis, W.J., Crowley, J.L. & Vervoort, J.D. (2013). Late Paleoproterozoic terrane accretion in northwestern Canada and the case for circum-Columbian orogenesis. Precambrian Research. 224. pp. 512–528.

Furlanetto, F., Thorkelson, D.J., Rainbird, R.H., Davis, W.J., Gibson, H.D., Marshall, D.D. (2016), The Paleoproterozoic Wernecke Supergroup of Yukon, Canada: Relationships to orogeny in northwestern Laurentia and basins in North America, East Australia, and China: Gondwana Research, v. 39, p. 14–40, doi: 10.1016/j.gr.2016.06.007.

Gladkochub, D.P., Pisarevsky, S.A., Donskaya, T. V., Ernst, R.E., Wingate, M.T.D., Söderlund, U., Mazukabzov, A.M., Sklyarov, E. V., Hamilton, M.A. & Hanes, J.A. (2010). Proterozoic mafic magmatism in Siberian craton: An overview and implications for paleocontinental reconstruction. Precambrian Research. 183. pp. 660–668.

Gibson, G.M., Hutton, L.J., and Holzschuh, J., 2017, Basin inversion and supercontinent assembly as drivers of sediment-hosted Pb – Zn mineralization in the Mount Isa region, northern Australia: Journal of the Geological Society, v. 174, p. 773–786.

Goodge, J.W., Fanning, C.M., Brecke, D.M., Licht, K.J. & Palmer, E.F. (2010). Continuation of the Laurentian Grenville Province across the Ross Sea Margin of East Antarctica. The Journal of Geology. 118. pp. 601–619.

Green, L.H. (1972). Geology of Nash Creek, Larsen Creek, and Dawson map areas, Yukon Territory. Geological Survey of Canada. Memoir 364. 157 p.

Hitzman, M.W., Oreskes, N. & Einaudi, M.T. (1992). Geological characteristics and tectonic setting of Proterozoic iron oxide (CuUAuREE) deposits. Precambrian Research. 58. pp. 241–287.

Hunt, J.A., Baker, T. & Thorkelson, D.J. (2007). A review of iron oxide copper-gold deposits, with focus on the Wernecke Breccias, Yukon Canada, as an example of a non-magmatic end member and implications for IOCG genesis and classification. Exploration and Mining Geology. 16. pp. 209–232.

Jones, J. V., Daniel, C.G. & Doe, M.F. (2015). Tectonic and sedimentary linkages between the Belt-Purcell basin and southwestern Laurentia during the Mesoproterozoic, ca. 1.60–1.40 Ga. Lithosphere. 7. 465–472.

Lane, R.A. (1990). Geologic setting and petrology of the Proterozoic Ogilvie Mountain breccias of the Coal Creek Inlier, Southern Ogilvie Mountains, Yukon Territory. The University of British Columbia. 223 p.

Medig, K.P.R., Thorkelson, D.J., Davis, W.J., Rainbird, R.H., Gibson, H.D., Turner, E.C. & Marshall, D.D. (2014). Pinning northeastern Australia to northwestern Laurentia in the Mesoproterozoic. Precambrian Research. 249. pp. 88–99.

Medig, K.P.R., Turner, E.C., Thorkelson, D.J. & Rainbird, R.H. (2016). Rifting of Columbia to form a deep-water siliciclastic to carbonate succession: The Mesoproterozoic Pinguicula Group of northern Yukon, Canada. Precambrian Research. 278. pp. 179–206.

Moroskat, M.J.A. (2013). On the genesis of the Blende Zn-Pb-Ag deposit, Wernecke Mountains, Yukon: Structural and geochemical evidence. University of Alberta, M.Sc. thesis. 103 p.

Nielsen, A.B., Thorkelson, D.J., Gibson, H.D. & Marshall, D.D. (2013). The Wernecke igneous clasts in Yukon, Canada: Fragments of the Paleoproterozoic volcanic arc terrane Bonnetia. Precambrian Research. 238. pp. 78–92

Pisarevsky, S.A., Elming, S.-Å., Pesonen, L.J. & Li, Z.X. (2014). Mesoproterozoic paleogeography: Supercontinent and beyond. Precambrian Research. 244. pp. 207–225.

Rainbird, R.H., Stern, R.A., Khudoley, A.K., Kropachev, A.P., Heaman, L.M. & Sukhorukov, V.I. (1998). U-Pb geochronology of Riphean sandstone and gabbro from southeast Siberia and its bearing on the Laurentia-Siberia connection. Earth and Planetary Science Letters. 164. pp. 409–420.

Ross, G.M., Parrish, R.R. & Winston, D. (1992). Provenance and UPb geochronology of the Mesoproterozoic Belt Supergroup (northwestern United States): implications for age of deposition and pre-Panthalassa plate reconstructions. Earth and Planetary Science Letters. 113 (1-2). pp. 57–76.

Shufeldt, O.P., Karlstrom, K.E., Gehrels, G.E. & Howard, K.E. (2010). Archean detrital zircons in the Proterozoic Vishnu Schist of the Grand Canyon, Arizona: Implications for crustal architecture and Nuna supercontinent reconstructions. Geology. 38. pp. 1099–1102.

Thompson, R.I., and Roots, C.F. (1982). Ogilvie Mountains project, Yukon: a new mapping program, part A. *In* current research, part A. Geological Survey of Canada, Paper 82-1A, pp. 403-411.

Thompson, R.I., (1995). Geological compilation (1:250 000) of Dawson map area (northeast of Tintina Trench). Geological Survey of Canada, Open File 3223.

Thorkelson, D.J. (2000). Geology and mineral occurrences of the Slats Creek, Fairchild Lake and ``Dolores Creek'' areas, Wernecke Mountains (106D/16, 106C/13, 106C/14), Yukon Territory. Exploration and Geological Services Division, Yukon, Indian and Northern Affairs Canada, Bulletin 10, 73 p.

Thorkelson, D.J., Abbott, J.G., Mortensen, J.K., Creaser, R.A., Villeneuve, M.E., Mcnicoll, V.J. & Layer, P.W. (2005). Early and Middle Proterozoic evolution of Yukon, Canada. Canadian Journal of Earth Sciences. 42. pp. 1045–1071.

Thorkelson, D.J. & Laughton, J.R. (2016). Paleoproterozoic closure of an Australia-Laurentia seaway revealed by megaclasts of an obducted volcanic arc in Yukon, Canada. Gondwana Research. 33. pp. 115 – 133.

Thorkelson, D.J., Mortensen, J.K., Davidson, G.J., Creaser, R.A., Perez, W.A. & Abbott, J.G. (2001a). Early Mesoproterozoic intrusive breccias in Yukon, Canada: The role of hydrothermal systems in reconstructions of North America and Australia. Precambrian Research. 111. pp. 31–55.

Thorkelson, D.J., Mortensen, J.K., Creaser, R.A., Davidson, G.J. & Abbott, G.J. (2001b). Early Proterozoic magmatism in Yukon, Canada: constraints on the evolution of northwestern Laurentia. Canadian Journal of Earth Sciences. 38. pp. 1479–1494.

Upton, B.G.J., Rämö, O.T., Heaman, L.M., Blichert-Toft, J., Kalsbeek, F., Barry, T.L. & Jepsen, H.F. (2005). The Mesoproterozoic Zig-Zag Dal basalts and associated intrusions of eastern North Greenland: Mantle plume-lithosphere interaction. Contributions to Mineralogy and Petrology. 149. pp. 40–56.

Wheeler, J.O. (1954). A geological reconnaissance of the northern Selwyn Mountains region, Yukon and Northwest Territories. Geological Survey of Canada, Paper 53-7

Williams, P.A.J.W. (2005). Iron Oxide Copper-Gold Deposits: Geology, Space-Time Distribution, and Possible Modes of Origin. Economic Geology. 100. pp. 371–405.

Young, G.M., Jefferson, C.W., Long, D.G.F., Delaney, G.D., and Yeo, G.M. (1979). Middle and Late Proterozoic evolution of the Canadian Cordillera and Shield. Geology. 7 pp. 125-128.

Chapter 2.

Field relations and lithologies of fallback sediments within Wernecke Breccia

This chapter derives with minor modification from: Verbaas, J., Thorkelson, D.J., Gibson, H.D., Marshall, D.D., and Milidragovic, D., 2015, Soft sediment textures in clasts in Wernecke Breccia: Reconstruction of an eroded late Paleoproterozoic succession in northern Yukon, in MacFarlane, M.G., Nordling, M.G., and Sacks, P.J. eds., Yukon Exploration and Geology 2014, Yukon Geological Survey, p. 145–156.

2.1. Abstract

The 1.60 Ga hydrothermal Wernecke Breccias are hosted within metasedimentary rocks of the Wernecke Supergroup and exposed in the Wernecke, Ogilvie and southern Richardson Mountains of northern Yukon. Breccia clasts with soft sediment deformation textures were previously identified and interpreted as fragments of the Wernecke Supergroup that were torn off and carried upward during mud volcanism. This model was subsequently discounted because field relations and geochronology indicated that the Wernecke Supergroup was lithified and metamorphosed prior to brecciation. Our recent work confirms the presence of soft sediment within zones of Wernecke Breccia and demonstrates the need for an unlithified sediment source. Two types of soft sediment materials have been identified: red mudstone to sandstone, and green mudstone. These unlithified sediments were likely derived from late Paleoproterozoic water-saturated sediments. During breccia formation, the surface was breached and fragments of the unlithified sediments foundered into the breccia zones, mixing with clasts of lithified country rock. The sediments descended to depths of at least 4 km where they were lithified and encased by hydrothermal cement. Subsequent erosion removed the source beds and exposed the breccia zones.

2.2. Introduction

Wernecke Breccia is a collective term for a set of hydrothermal breccia zones that are distributed over more than 48 000 km^2 in the Wernecke, Ogilvie, and southern Richardson mountains in northern Yukon (Figure 2.1; Thorkelson et al., 2001a). Individual breccia zones range in size from several metres to several kilometres across. They are hydrothermal in origin and were dated at 1598.8 ± 1 Ma by U-Pb metasomatic titanite (Furlanetto et al., 2013). Iron oxide copper gold (IOCG) occurrences in and near the breccia zones have attracted significant exploration interest (Hunt et al., 2011).

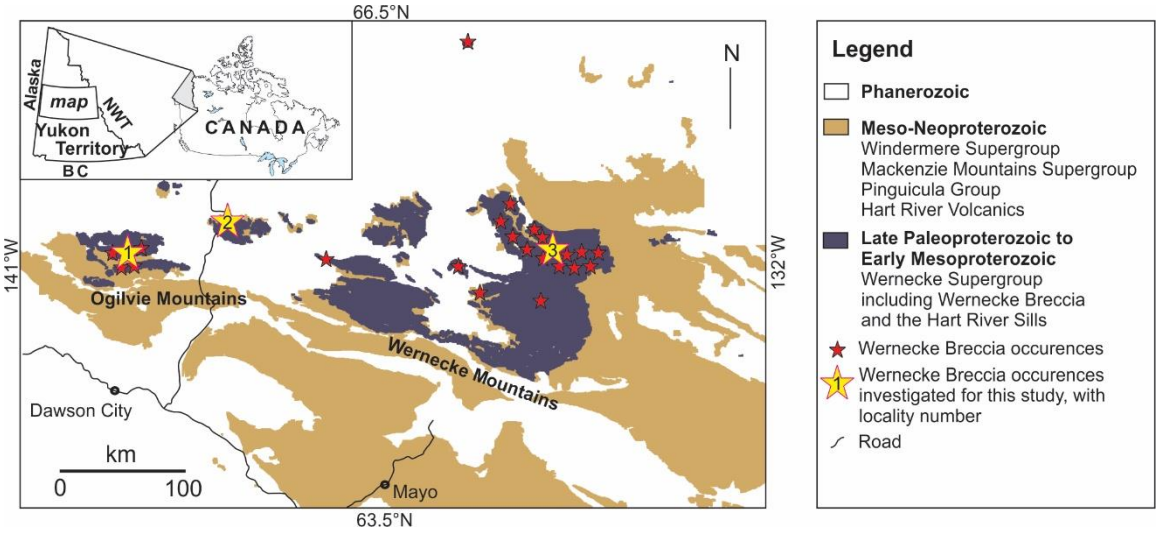

Figure 2.1. Wernecke Breccia occurrences in the Wernecke and Ogilvie Mountains, Yukon Territory, Canada. (UTM locations 1: 578059E, 7182329N, 2: 636061E, 721754N, NAD83. Location 3 pertains to stored drill core of uncertain origin near the SLAB mineral occurrence).

The Wernecke Breccia is hosted by the Wernecke Supergroup, a >13 km thick succession of clastic and carbonate rocks deposited on the western margin of ancestral North America (Delaney, 1981, 1985; Thorkelson, 2000; Furlanetto et al., 2016). The Wernecke Supergroup was deformed and metamorphosed to greenschist facies during the ca. 1.6 Ga Racklan Orogeny prior to the hydrothermal brecciation. Strata of the Fifteenmile Group and the Pinguicula Group (Thompson et al., 1992; Medig et al., 2010, 2016) unconformably overlie the Wernecke Supergroup and Wernecke Breccia. The Wernecke Supergroup is presumed to have been deposited on either crystalline basement

or an intervening sedimentary succession (Thorkelson et al., 2005). Detrital zircon analysis constrains the Wernecke Supergroup to ≤ 1.66 Ga (Furlanetto et al., 2013).

The majority of clasts in Wernecke Breccia consist of siltstone, shale, sandstone, carbonate and minor phyllite and fine-grained schist that were sourced from the Wernecke Supergroup (Thorkelson et al., 2001a). Previously, Lane (1990) showed that a small proportion of the clasts displayed soft sediment textures indicating they were incorporated into Wernecke Breccia prior to lithification. He also suggested that these clasts were derived from the Wernecke Supergroup. However, this interpretation is incompatible with the current understanding that the Wernecke Supergroup was entirely lithified and metamorphosed before breccia formation (Mercier, 1989; Thorkelson, 2001a). In this paper, we address the issue of soft sediment textures in clasts of the Wernecke Breccia. We provide the reader with textural and lithological descriptions and explore the implications of the soft sediment clasts within the Wernecke Breccia zones.

2.3. Terrane accretion prior to brecciation

2.3.1. Wernecke Igneous clasts and their source

Locally abundant igneous clasts occur within the breccia zones. The Wernecke Supergroup does not contain any igneous rocks and these clasts were therefore derived from a different source. Three main types of igneous clasts have been identified: 1) the Bonnet Plume River intrusions (Thorkelson et al., 2001b; Nielsen et al., 2013), 2) the Slab volcanics (Thorkelson and Wallace, 1998; Thorkelson and Laughton, 2016, and 3) the Devil volcanics (Nielsen et al., 2013). The igneous clasts were collectively termed the Wernecke Igneous Clasts by Nielsen et al., (2013). The largest known igneous clast is a block of diorite 900 metres long, 300 metres wide and a minimum of 30 metres thick (Thorkelson, 2000; Nielsen et al. 2013). Clasts of the Slab volcanics are known in at least three localities in the Wernecke Mountains, with the largest clast consisting of a 160 m-thick succession of 31 mafic lava flows intercalated with minor volcanic breccia and sandstone (Thorkelson and Laughton, 2016; Figure 2.2). Sedimentary megaclasts from the Wernecke Supergroup are also locally present and range up to hundreds of metres across (Hunt et al., 2002).

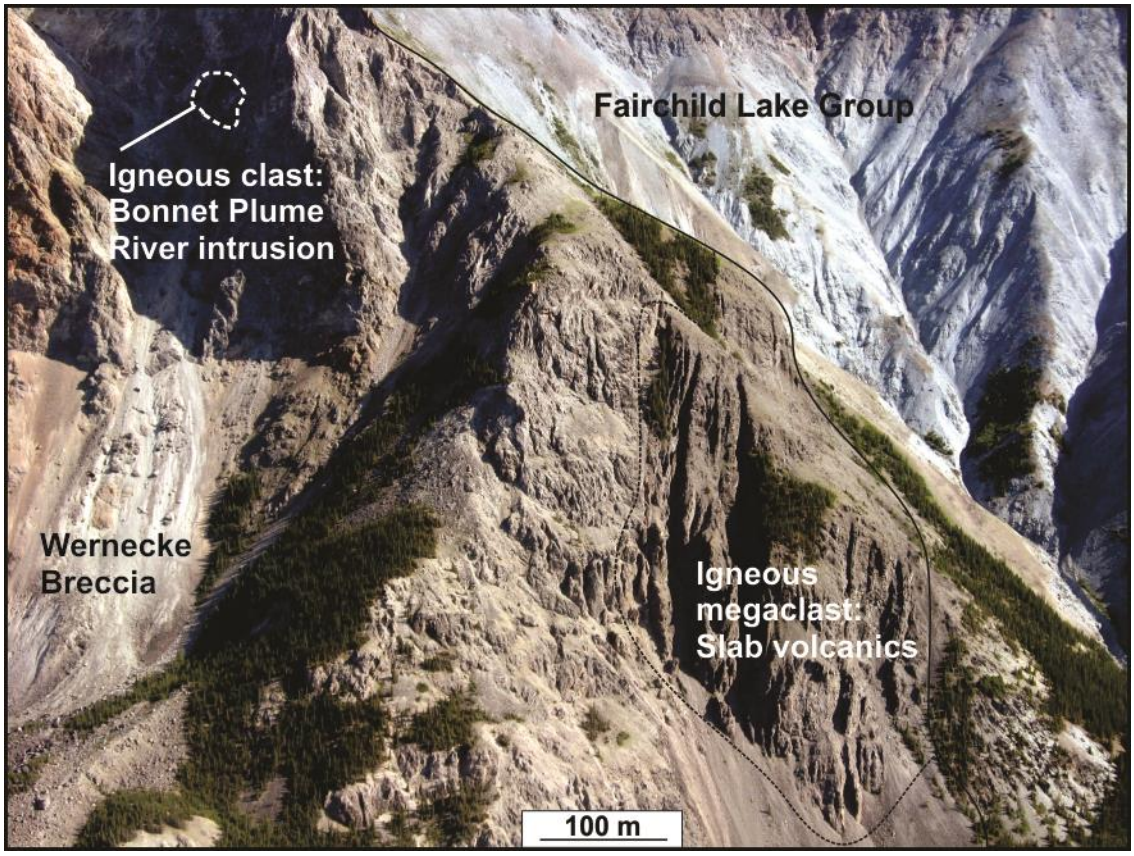

Figure 2.2. Igneous megaclasts in the Wernecke Breccia zone at Slab Mountain as described by Hunt et al. (2002), and Laughton et al., (2005).

The Bonnet Plume River intrusions have been dated at 1.71 Ga by U-Pb zircon (Thorkelson et al., 2001b). As demonstrated by Furlanetto et al. (2016), the age of the Wernecke Supergroup is <1.66 Ga, which is at least 50 m.y. younger than the dated igneous clasts (Thorkelson et al., 2005; Nielsen et al., 2013). Furlanetto et al. (2013) postulated that the source of the igneous clasts was an obducted terrane, which they named Bonnetia. Clasts of Bonnetia foundered into the breccia zones during brecciation and became juxtaposed with the underlying Wernecke Supergroup. Bonnetia was completely eroded after the brecciation, and igneous clasts that are now exposed within zones of Wernecke Breccia are the only record of its existence (Furlanetto et al., 2013; Nielsen et al., 2013, Thorkelson and Laughton, 2016).

2.4. Lithologies of soft sediment clasts

Sedimentary lithologies with soft sediment textures occur in three areas in the Ogilvie Mountains. The first area is near the headwaters of the Fifteenmile River (labeled: “1” in Figure 2.1). This area is rugged and mountainous, and best accessed by helicopter. The second is located near the Dempster highway on both sides of the Blackstone River (labeled: “2” in Figure 2.1). The exposures and related coarse rip-rap (roadside talus) on the west side of the river are adjacent to the highway. The exposures to the east of the Blackstone River occur in the bed of “Spectacular creek” (Yukon MINFILE 116G 082) and are accessible by a combination of light watercraft and foot traverse. The third area is the area surrounding the Slab Prospect (labeled “3” in Figure 2.1; Thorkelson, 2000; Hunt et al., 2002) This area can be accessed by helicopter, or by fixed wing aircraft via the ‘copper point’ airstrip immediately west of Slab Mountain, or via the Bonnet Plume River.

2.4.1. Red to white sandstone to mudstone

The term red soft sediment clasts is herein collectively applied to red to pink sedimentary lithologies in Wernecke Breccia that commonly exhibit soft sediment deformation. Red soft sediment clasts include red mudstone, red sandstone and pink sandstone and occur as two textural end-members and intermediate varieties. One textural end-member consists of interbedded red mudstone and fine-grained pink sandstone (Figure 2.3A). Stratification thickness ranges from 2 mm to 10 cm. Cross stratification is locally present. The other textural end-member is a clast-supported granule and pebble-sized conglomerate also composed of red mudstone to sandstone (Figure 2.3B). Some fragments within the second end-member are rounded but many have irregular outlines that fit tightly together in jigsaw-like patterns without intervening matrix (Figure 2.3C-F).

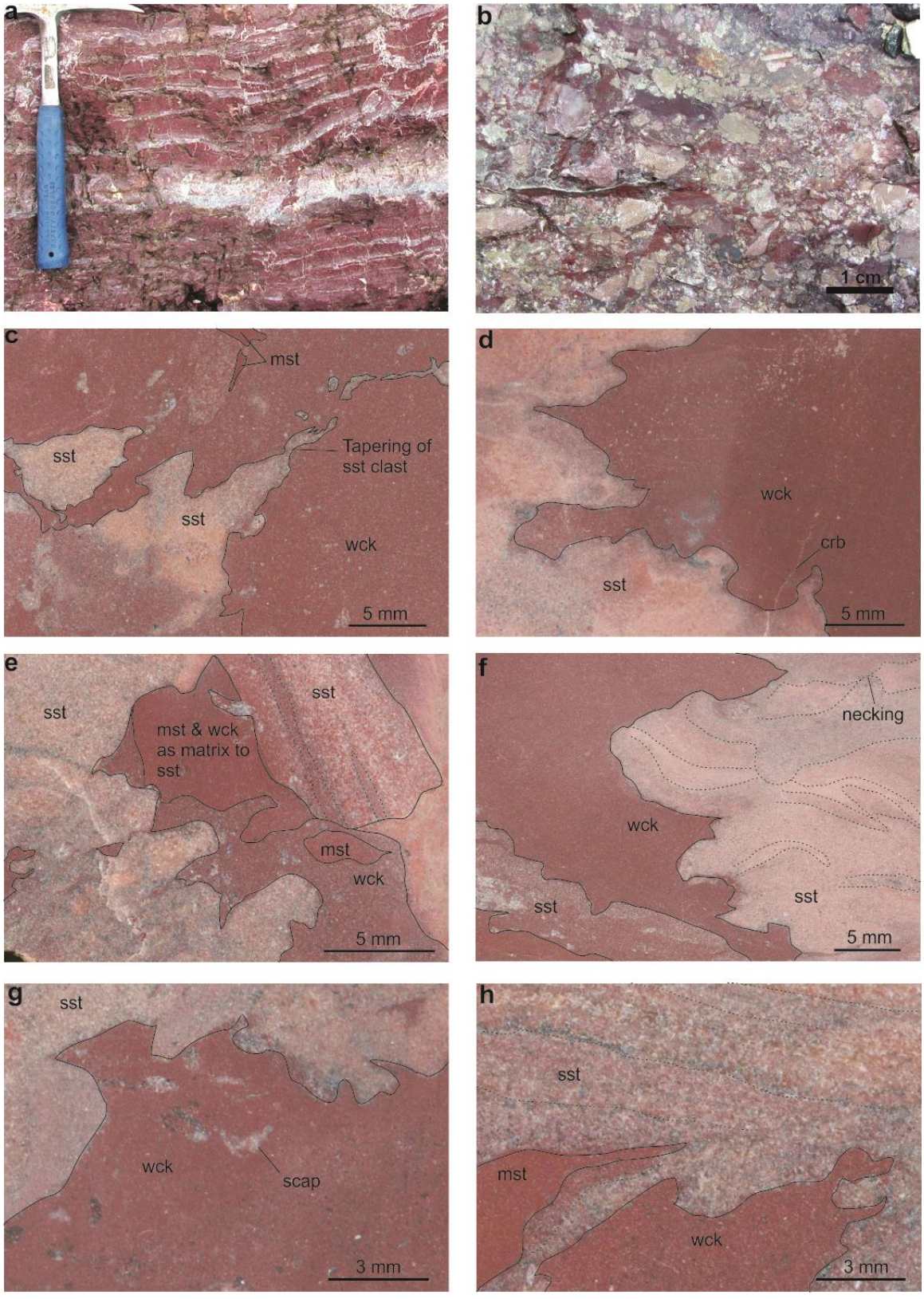
a
b
1 cm
c
mst
sst
Tapering of
sst clast
sst
wck
5 mm
d
wck
crb
sst
5 mm
e
sst
sst
mst & wck
as matrix to
sst
mst
wck
5 mm
f
necking
wck
sst
sst
5 mm
g
sst
wck
scap
3 mm
h
sst
mst
wck
3 mm

Figure 2.3. Red sandstone to mudstone end members and field relations. a) End-member 1: well-bedded red mudstone and pink sandstone lacking soft sediment deformation textures. b) End-member 2: breccia consisting of tightly packed clasts of sandstone to mudstone with soft sediment deformation textures (textures are clear in Fig 4c-h). c) Breccia showing a sandstone clast tapering out, a wacke matrix and two distinct mudstone clasts. d) An irregular sandstone clast and wacke. Note also the secondary carbonate veinlet. e) Irregular sandstone clasts with mudstone and wacke as matrix. f) Sandstone clasts with wacke as matrix. Note the contorted layering and necking of layers within the sandstone clast. g) Irregular sandstone clast and wacke. Note secondary scapolite. h) highly irregular boundaries of mudstone, wacke and sandstone. Note the lack of any metasomatic Wernecke Breccia cement and matrix in between mudstone, sandstone and wacke in c-h.

The red soft sediment clast-supported conglomerate consists of ovoid to irregularly shaped fragments. There is no Wernecke Breccia matrix present among the clasts. Some clasts of sandstone taper into folded streaks surrounded by an irregular patchwork of mudstone and wacke clasts (Figure 2.3C). Many clasts show distorted internal layering (Figure 2.3F). The conglomerate is interpreted to have formed from a red sandstone to mudstone succession that was disaggregated into soft and ductile clasts and reconstituted into a tightly packed assemblage. None of these textures are prevalent in the Wernecke Supergroup, or in the Wernecke Supergroup clasts that are present in Wernecke Breccia.

The contacts between the red soft sediment clasts and typical Wernecke Breccia are gradational. The gradation is characterized by a mixture of red soft sediment clasts and other breccia clast types including orange, black and grey weathering mudstone, dolomitic sandstone and minor phyllite that appear to have been derived from the Wernecke Supergroup host-rock (Figure 2.4A, B). Other notable clasts within this gradational contact include fine-grained to aphanitic green mafic igneous rocks of the Devil volcanics (Nielsen et al. 2013; Figure 2.4C). Red soft sediment clasts have angular to subangular edges and irregular shapes both where they are incorporated in a tightly packed conglomerate and where they are surrounded by Wernecke Breccia hydrothermal matrix (Figure 2.4D). Red soft sediment clasts wrap around clasts of previously lithified igneous rock and Wernecke Supergroup. These relations indicate that red soft sediment clasts were unlithified and ductile when they were incorporated into Wernecke Breccia.

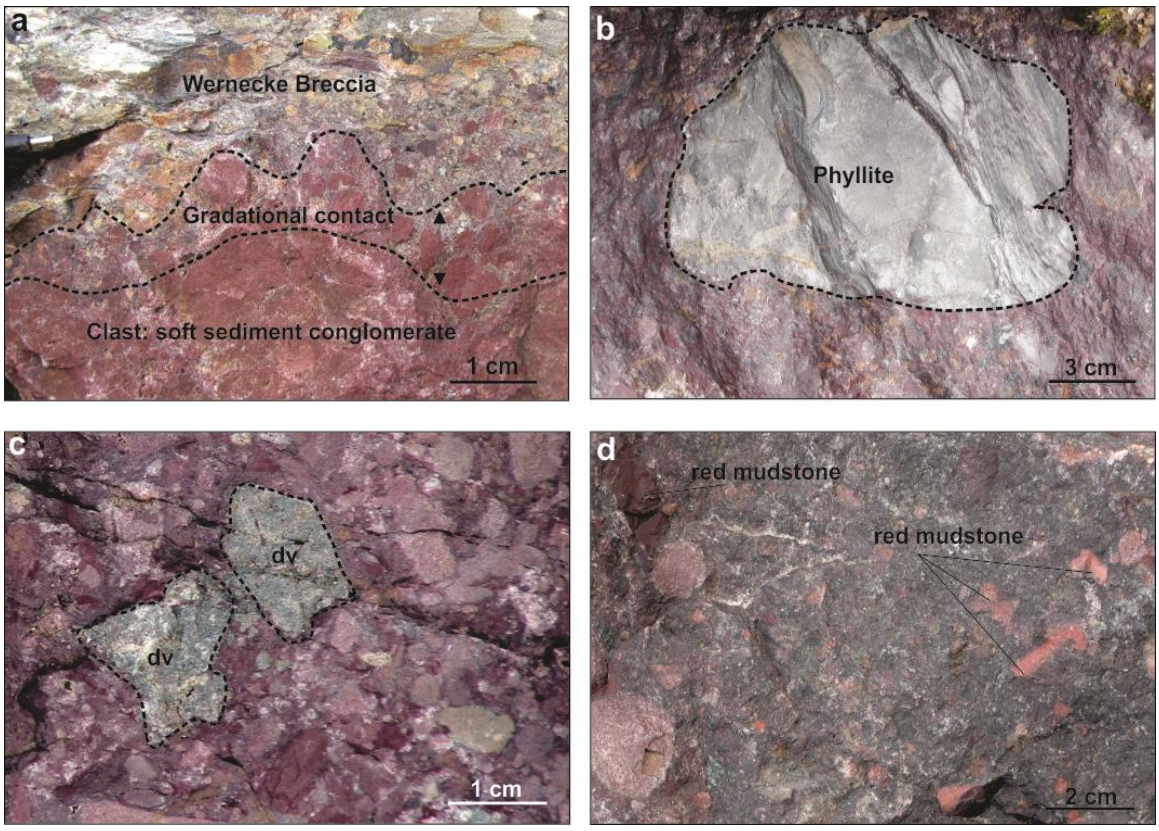

Figure 2.4. Gradational boundary of the soft sediment conglomerate. b) Wernecke Supergroup phyllite in gradational boundary of the red SSL. Note there is no Wernecke Breccia metasomatic matrix present in between clasts, the red SSL serves as matrix. c) Devil volcanic clasts (dv) and Wernecke Supergroup clasts embedded within the gradational boundary of the red SSL. The matrix transitions from red mudstone and sandstone into metasomatic Wernecke Breccia matrix; both igneous clasts and clasts of Wernecke Supergroup may be present within the gradation. d) Wernecke Breccia with red mudstone and pink sandstone clast.

Thin section petrography reveals that the red mudstone is poorly sorted and immature. The red mudstone consists of a submicroscopic assemblage, opaque minerals and minor sand grains (Figure 2.5A). Some of the opaque grains are fine-grained hematite that formed metasomatically during breccia formation; others may be detrital. Metasomatic carbonate minerals and scapolite occur as veins and disseminated grains. Clasts of the mudstone have curved edges and internally deformed layering (Figure 2.5B). The sandstone component is poorly sorted and contains rounded to subrounded grains of quartz and minor carbonate. Laminations within the sandstone are commonly contorted and attenuated. The red soft sediment clasts are not strongly compacted or

metamorphosed, in contrast to the highly compacted and variably metamorphosed Wernecke Supergroup (Furlanetto et al., 2013; 2016).

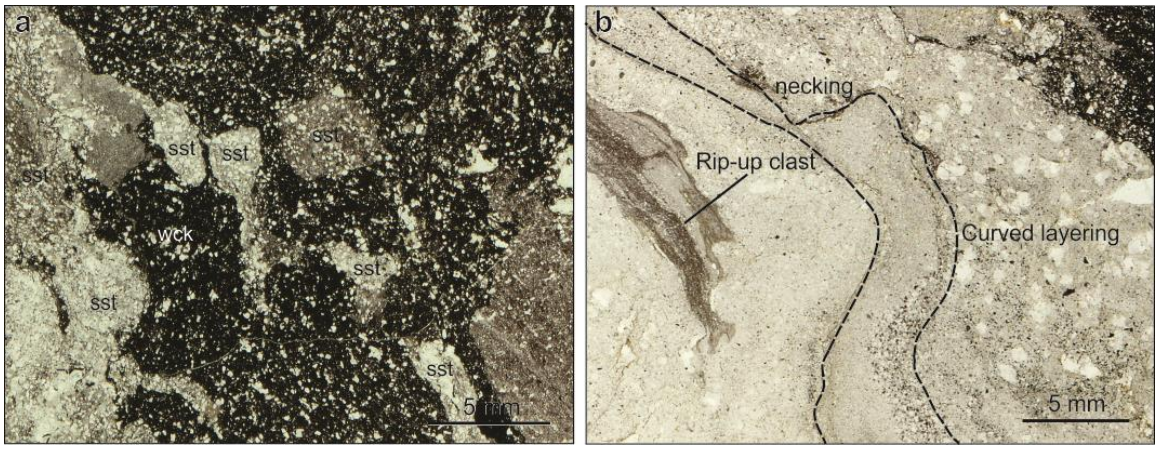

Figure 2.5. Microstructures of the red sandstone to mudstone soft sediment conglomerate. a) Wacke serves as a matrix to sandstone clasts without intervening Wernecke Breccia metasomatic matrix. b) Soft sediment textures in the red sandstone to mudstone.

The presence of soft sediment textures in the red to pink sandstone to mudstone, and its gradational boundary with typical Wernecke Breccia, indicate that this lithology was only partially consolidated at the time of breccia formation. After its incorporation into the breccia and mixing with other lithologies, the red to pink sandstone to mudstone became lithified.

2.4.2. Green mudstone

The second lithology that displays soft sediment textures is a light green mudstone. The mudstone occurs interstitially between Wernecke Breccia clasts as curviplanar coatings, streaks and bands up to 5 cm thick (Figure 2.6A, B). Where it is thick, the mudstone serves as matrix to Wernecke Breccia clasts, such that smaller (cm-scale) clasts of Wernecke Breccia are completely encapsulated within the mudstone. The encapsulated fragments include both Wernecke Supergroup clasts (Figure 2.6A) and red mudstone clasts (Figure 2.6B). We did not identify individual clasts of the green mudstone.

The green mudstone is immature and consists of a submicroscopic assemblage and very fine-grained quartz, muscovite and flakes of metasomatic hematite associated

with Wernecke Breccia formation. Lamination within the green mudstone is curviplanar, mantling the boundaries of adjacent sandstone clasts (Figure 2.6C). Some of the laminated texture may reflect original sedimentary layering, and some may have been generated during flow within the breccia zone. Locally dark green chlorite-hematite coatings rim the margins of the green mudstone (Figure 2.6D).

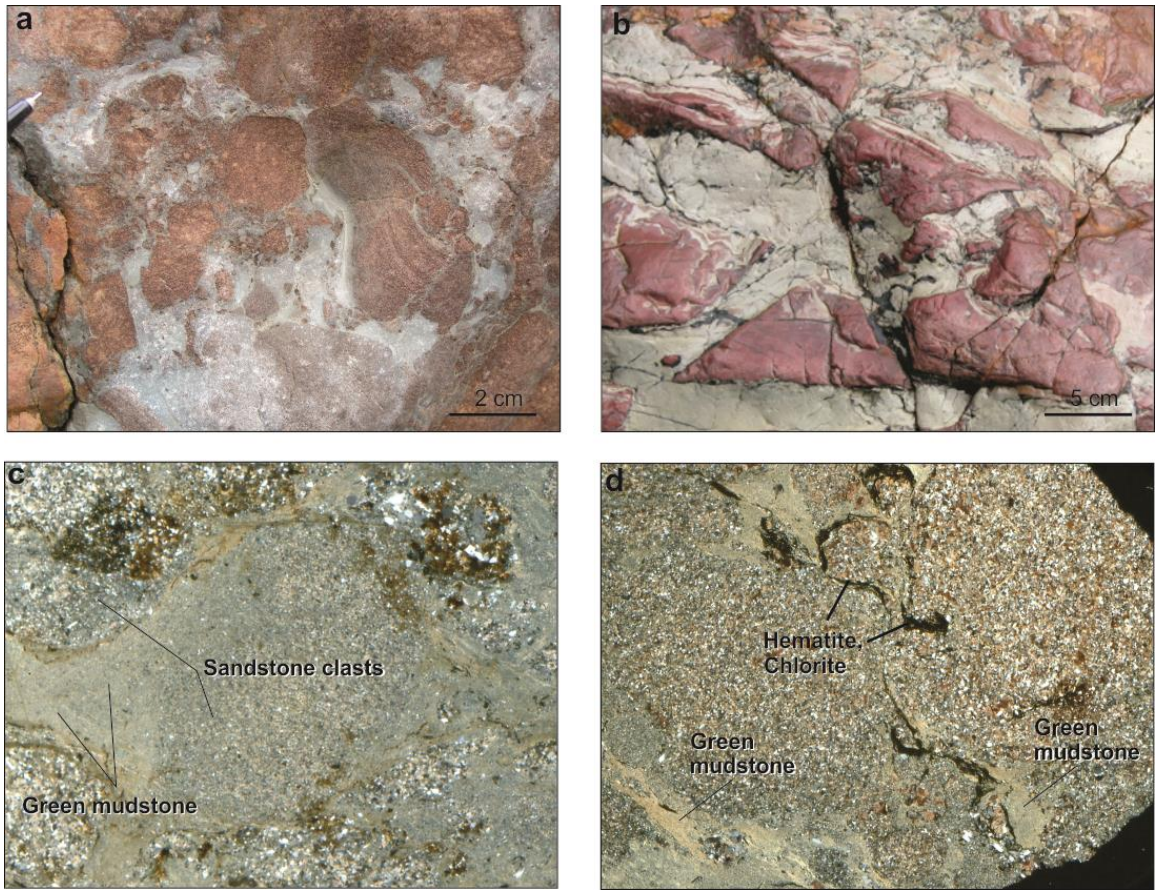

Figure 2.6. Meso-scale (a, b) and micro-scale (c, d) structures and field relations of the green mudstone. a) Green mudstone encapsulating clasts of Wernecke Supergroup. b) Green mudstone encapsulating clasts of red mudstone. c) Sandstone clast rimmed by green mudstone; image in crossed polars. d) Green mudstone is locally associated with hematite and chlorite; image in crossed polars.

The irregular shapes and matrix-forming nature of the green mudstone and its relation to the Wernecke Supergroup clasts suggest that this material was entirely unconsolidated and flowed through the breccia zone as liquid mud at the time of Wernecke Breccia formation. After the mud came to rest, it became lithified within the interstices among breccia clasts and was affected by hydrothermal alteration.

2.4.3. Field relations of soft sediment clasts and green mudstone with Wernecke Breccia

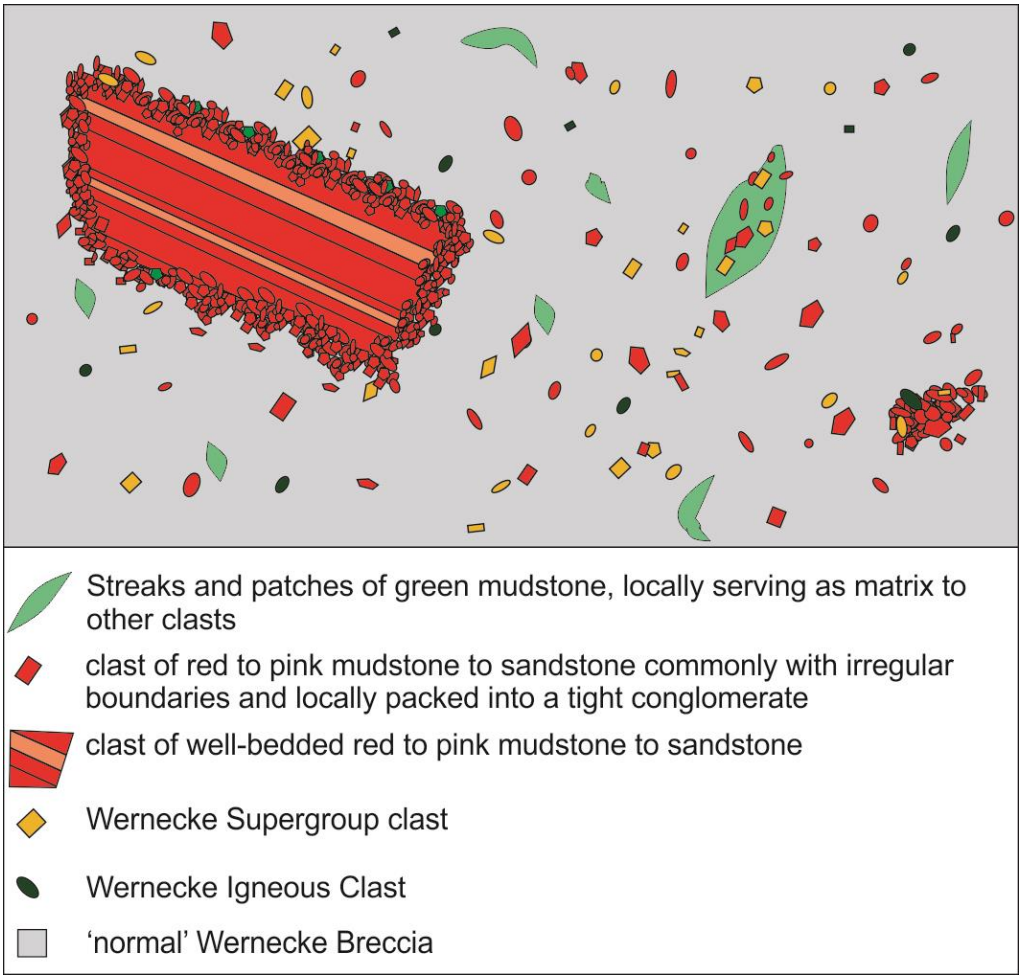

Figure 2.7. Conceptual diagram of the soft sediments within Wernecke breccia

Figure 2.7 is an idealized diagram that shows how the different end-members and intermediate varieties of the soft sediment clasts occur within Wernecke Breccia. Large clasts of interbedded sandstone to mudstone are surrounded by a carapace of smaller clasts, forming a tightly packed conglomerate. The gradational boundary around the soft sediment conglomerate is a mixture of soft sediment fragments and other clasts of Wernecke Breccia. Irregular patches and streaks of green mudstone occur both spatially associated with red soft sediment clasts and isolated. Surrounding this mixture is typical Wernecke Breccia with few, if any, fragments of red soft sediment clasts.

2.5. Discussion

2.5.1. Significance of soft sediment textures

The incorporation of soft sediment into zones of Wernecke Breccia poses a complex geological problem. Hunt et al., (2011) addressed the depth at which mineralization in Wernecke Breccia took place. Using a combination of new fluid inclusion data and Delaney's (1981) estimates for stratigraphic thickness, Hunt et al. (2011) proposed that the hydrothermal activity within various zones of Wernecke Breccia occurred at pressures of 0.4 – 2.4 kbar, corresponding to depths of 1.2 – 7.2 km. However, stratigraphic thickness cannot be used as an estimate of depth because the Wernecke Supergroup was deformed and overthrust by Bonnetia prior to the formation of the Wernecke Breccia (Thorkelson et al., 2001a; Furlanetto et al., 2013). Two other estimates of depth derived from data in Hunt et al. (2011) are also considered. One estimate, based on the fluid inclusion studies alone, ranges from 5.7 – 11.3 km. The other estimate equates equilibration temperatures from stable isotopes to depth based on an assumed geothermal gradient. At equilibration temperatures of (250-295˚C) and a geothermal gradient of 25-30˚C/km, calculated depths range from 7-9 km. These estimates are for different breccia zones in the Wernecke Mountains whereas breccias in our study are located in the Ogilvie Mountains and have not been thoroughly evaluated for pressures and temperatures. However, the metasomatic mineral assemblage of the Wernecke breccias in the Ogilvie Mountains includes chlorite, mica and feldspar and lacks clay or other low metamorphic-grade minerals. Hence the Wernecke Breccia zones that host the soft sediment materials were likely positioned at several kilometres depth.

The only plausible source of the unconsolidated green mudstone is a water-saturated sedimentary deposit on the surface of the Earth. The source of the red soft sediments is likely to have been a partially lithified sedimentary succession that had been buried to shallow depths. Mixing of the Wernecke Supergroup and Bonnetia clasts with the non-lithified materials must have occurred rapidly, allowing sediment from the surface and near-surface environments to mix and come to rest at depths of several km beneath the surface. The structure of the Proterozoic crust prior to brecciation is depicted in Figure 2.8 based on the foregoing descriptions of the sedimentary rocks. If water were present

above the green mudstone, in the form of a lake or sea, it probably would have flowed down into the breccia zones along with the unlithified sediments. Phreatic activity may have accompanied breaching of the surface by the Wernecke Breccia.

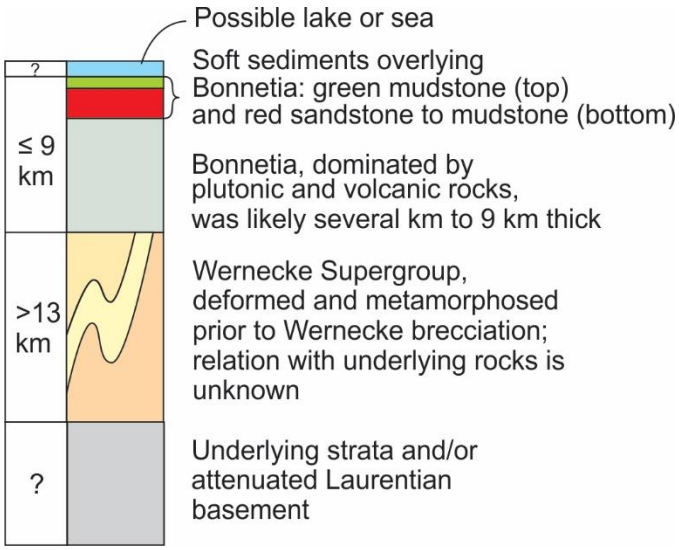

Figure 2.8. Crustal column prior to the formation of the Wernecke Breccias

Considerable downward transport of the igneous clasts derived from Bonnetia to within zones of Wernecke Breccia is required (Furlanetto et al., 2013). Nielsen et al. (2013) estimated the most likely transport distance of the igneous clasts to be 1-2 km. That estimate was based on the perceived need to minimize the transport distance by deriving the clasts from a short distance above the surface of obduction, and by regarding the current mountain peaks to lie a nominal distance of 1 km below the obduction surface (Nielsen et al., 2013). The existence of lithologies with soft sediment textures within the Wernecke Breccia that were sourced from the surface corroborates the interpretation of overall downward transport of clasts. A surface origin would require that the unconsolidated sediments descended through the entire Bonnetia nappe, which locally may have been up to 9 km thick (Nielsen et al., 2013). These considerations are consistent with foundering of the unlithified sediments for several km (possibly >9 km) into the Earth's crust. The depth of clast foundering will be elaborated upon in chapter 4.

2.5.2. Breaching of the surface and incorporation of fallback sediments

The foregoing model accords with a depiction of hydrothermal breccia formation offered by Laznicka and Edwards (1979), utilized by Hitzman et al. (1992) and developed by Thorkelson et al. (2001a), Furlanetto et al. (2013), Nielsen et al. (2013) and Thorkelson and Laughton (2016). In particular, the model involves the ascent of hydrothermal solutions from depth, fragmentation of country rock, breaching of the surface, development of open space by some combination of dilation and expulsion of rock at the surface, and descent of clasts for thousands of metres (Figure 2.9). The recognition of surface-derived unconsolidated material within Wernecke Breccia underscores the need for breaching of the surface. Hence, the soft sediment clasts can be considered fallback sediments, similar to those described within other breccia systems that breach the surface of the Earth such as in kimberlite pipes and impact craters. The Earth's surface in this region was ruptured by numerous large hydrothermal vents, some or all of which may have been under water. The vents are envisaged as large openings that existed long enough for wall-rock and water-saturated surface materials to collapse, founder, mix with hydrothermal solutions and settle to depths of several km.

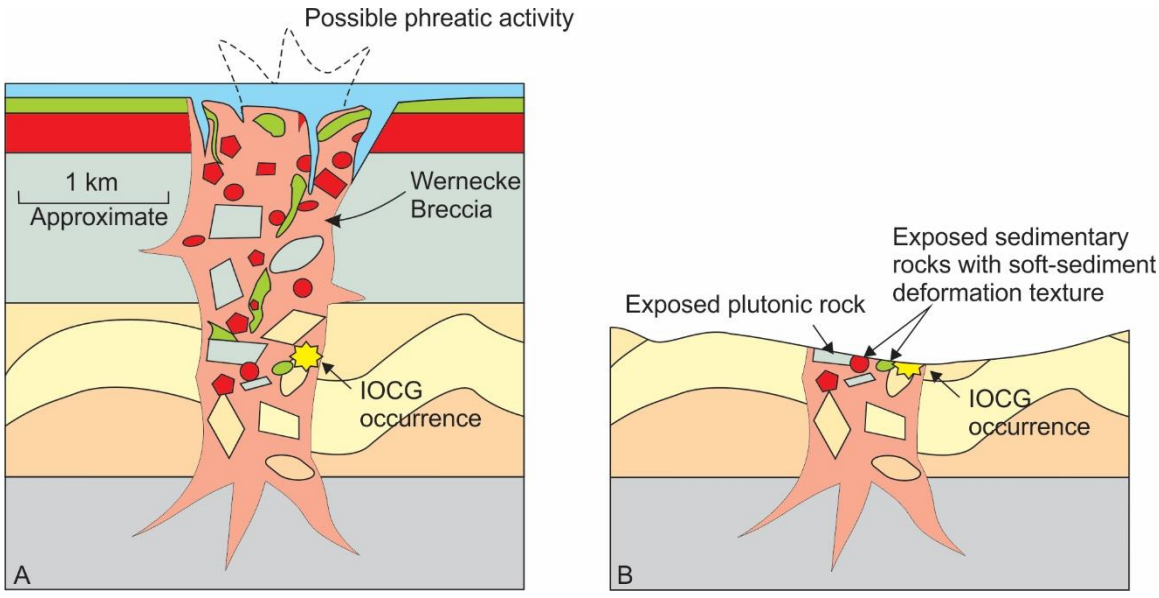

Figure 2.9. **A. Crustal column during and immediately after brecciation. B. Current crustal column. The nature of the continuation of the breccia zones in the basement is unknown.**

2.6. Conclusions

Clasts in Wernecke Breccia showing soft sediment deformation were noted by Lane (1990). Our investigation corroborates Lane's findings and has led to the identification of two sedimentary lithologies with soft sediment textures. One is red mudstone to pink sandstone and the other is green mudstone. The soft sediment textures indicate derivation from at or near the Earth's surface. The red lithology appears to have been consolidated but unlithified whereas the green lithology appears to have been unconsolidated. The unlithified sediments flowed downward into zones of Wernecke Breccia in response to breaching of the surface. The soft sediments are estimated to have descended to depths of at least several km.

We regard the most likely source for the soft sediments to have been a weakly to non-lithified succession that was deposited on top of the obducted terrane Bonnetia shortly before the formation of Wernecke Breccia. The soft sediments mixed with other clasts, came to rest at depth and became lithified and can be considered as fallback sediments. The terrane and its overlying succession were entirely eroded in the Mesoproterozoic (Furlanetto et al., 2013).

2.7. Acknowledgements

Funding was provided by NSERC grants to DJT. The Yukon Geological Survey provided logistical support in 2012. Jim Mortensen provided input on an earlier draft. Grant Abbott and Patrick Sack provided input that led to significant improvements.

2.8. References

Delaney, G.D. (1981). The mid-Proterozoic Wernecke Supegroup, Wernecke Mountains, Yukon Territory. In F.H.A Campbell (Ed.), Proterozoic Basins of Canada pp. 1-24. Geological Survey of Canada, Canadian Government Publishing Centre

Delaney, G.D. (1985). The Middle Proterozoic Wernecke Supergroup, Wernecke Mountains, Yukon Territory. Ph.D. Thesis. University of Western Ontario, 373 p.

Furlanetto, F., Thorkelson, D.J., Rainbird, R.H., Davis, W.J., Gibson, H.D. & Marshall, D.D. (2016). The Paleoproterozoic Wernecke Supergroup of Yukon, Canada: Relationships to orogeny in northwestern Laurentia and basins in North America, East Australia, and China. Gondwana Research. 39. pp. 14–40.

Furlanetto, F., Thorkelson, D.J., Gibson, H.D., Marshall, D.D., Rainbird, R.H., Davis, W.J., Crowley, J.L. & Vervoort, J.D. (2013). Late Paleoproterozoic terrane accretion in northwestern Canada and the case for circum-Columbian orogenesis. Precambrian Research. 224. pp. 512–528.

Hunt, J.A., Baker, T., Cleverley, J., Davidson, G.J., Fallick, A.E. & Thorkelson, D.J. (2011). Fluid inclusion and stable isotope constraints on the origin of Wernecke Breccia and associated iron oxide – copper – gold mineralization, Yukon. Canadian Journal of Earth Sciences. 48 (10). pp. 1425–1445.

Hunt, J.A., Laughton, J.R., Brideau, M., Thorkelson, D.J., Brookes, M.L. & Baker, T. (2002). New mapping around the Slab iron oxide-copper-gold occurrence, Wernecke Mountains Yukon. pp. 125–138.

Lane, R.A. (1990). Geologic setting and petrology of the Proterozoic Ogilvie Mountain breccias of the Coal Creek Inlier, Southern Ogilvie Mountains, Yukon Territory. The University of British Columbia.

Laznicka, P. & Edwards, R.J. (1979). Dolores Creek, Yukon – A disseminated copper mineralization in sodic metasomatites. Economic Geology. 74. pp. 1352–1370.

Medig, K.P.R., Turner, E.C., Thorkelson, D.J. & Rainbird, R.H. (2016). Rifting of Columbia to form a deep-water siliciclastic to carbonate succession: The Mesoproterozoic Pinguicula Group of northern Yukon, Canada. Precambrian Research. 278. pp. 179–206.

Medig, K.P.R., Thorkelson, D.J. & Dunlop, R.L. (2010). The Proterozoic Pinguicula Group: stratigraphy, contact relationships, and possible correlations. Yukon Exploration and Geology. pp. 265–278.

Mercier, E. (1989). tectoniques d'origine compressive dans le Proterozoique du nord de la Cordillere Canadienne (montagnes Ogilvie, Yukon). Canadian Journal of Earth Science. 26. pp. 199–205.

Nielsen, A.B., Thorkelson, D.J., Gibson, H.D. & Marshall, D.D. (2013). The Wernecke igneous clasts in Yukon, Canada: Fragments of the Paleoproterozoic volcanic arc terrane Bonnetia. Precambrian Research. 238. pp. 78–92.

Thompson, R.I., Roots, C.F. & Mustard, P.S. Geology of Dawson map area (116B, C) (northeast of Tintina Trench). Geological Survey of Canada, Open File 2849.

Thorkelson, D.J. (2000). Geology and mineral occurrences of the Slats Creek, Fairchild Lake and “Dolores” Creek areas, Wernecke Mountains (106D/16, 106C/13, 106C/14), Yukon Territory. 73 p.

Thorkelson, D.J., Abbott, J.G., Mortensen, J.K., Creaser, R.A., Villeneuve, M.E., Mcnicoll, V.J. & Layer, P.W. (2005). Early and Middle Proterozoic evolution of Yukon, Canada. Canadian Journal of Earth Sciences. 42. pp. 1045–1071.

Thorkelson, D.J. & Laughton, J.R. (2016). Paleoproterozoic closure of an Australia-Laurentia seaway revealed by megaclasts of an obducted volcanic arc in Yukon, Canada. Gondwana Research. 33 (May 2016). pp. 115 – 133.

Thorkelson, D.J., Mortensen, J.K., Creaser, R.A., Davidson, G.J. & Abbott, G.J. (2001). Early Proterozoic magmatism in Yukon, Canada: constraints on the evolution of northwestern Laurentia. Canadian Journal of Earth Sciences. 38 (10). pp. 1479–1494.

Thorkelson, D.J., Mortensen, J.K., Davidson, G.J., Creaser, R.A., Perez, W.A. & Abbott, J.G. (2001). Early Mesoproterozoic intrusive breccias in Yukon, Canada: The role of hydrothermal systems in reconstructions of North America and Australia. Precambrian Research. 111 (1-4). pp. 31–55.

Yukon Minfile 2014 – A database of mineral occurrences. Yukon Geological Survey, <http://www.geology.gov.yk.ca/databases_gis.html>

Chapter 3.

A sedimentary overlap assemblage links Australia to northwestern Laurentia at 1.6 Ga

This chapter derives, with minor modification, from: Verbaas, J., Thorkelson, D.J., Crowley, J.L., Davis, W.J., Foster, D.A., Gibson, H.D., Marshall, D.D., and Milidragovic, D., 2017, A sedimentary overlap assemblage links Australia to northwestern Laurentia at 1.6 Ga: Precambrian Research, v. In press.

3.1. Abstract

The Columbia (Nuna) supercontinent existed from approximately 1.9 Ga to 1.3 Ga. Laurentia was part of Columbia, and the western edge of Laurentia (current coordinates) was likely proximal to a large landmass during parts of this interval. Here, we present detrital zircon ages of a Paleoproterozoic sedimentary succession in northern Yukon, Canada, that bear on the evolution of Columbia. The sedimentary succession is preserved as clasts within 1.60 Ga hydrothermal megabreccias. Analyses of detrital zircon reveal abundant 1.78 – 1.68 Ga zircon with evolved Hf isotope values ($-16.1 < \varepsilon Hf(t) < +1.4$). Sm-Nd isotope analysis on clasts yields εNdi from -5.3 to -5.5 and model ages from 2.4 to 2.2 Ga. The detrital zircon age distribution is strikingly similar to those from sedimentary megaclasts in the ca. 1.59 Ga Olympic Dam Breccia Complex on the Gawler Craton of Australia. The whole rock Sm-Nd ratios are consistent with derivation from the Gawler Craton. We propose that the sedimentary material contained in both breccia complexes was derived from an overlap assemblage deposited on Australia and Laurentia at ca. 1.6 Ga. This model supports a previous hypothesis that the Gawler Craton was connected to northwestern Laurentia at ca. 1.6 Ga, and that these regions shared a single hydrothermal province that is recognized in northwestern Laurentia as the Wernecke Breccia and in the Gawler Craton as the Olympic Dam Breccia Complex and associated IOCG deposits. The sedimentary overlap succession was deposited after collision between Australia and Laurentia. Australia was subsequently translated southward along the Laurentian margin,

placing the Gawler Craton next to southwestern Laurentia and the Mt. Isa Inlier adjacent to northwestern Laurentia by 1.5 G.

3.2. Introduction

The provenance of sedimentary rocks is a cornerstone of continental reconstructions and orogenic analysis. Sedimentary provenance reflects the transport of sediment from highlands to basins and serves to constrain the timing and nature of geological processes such as uplift, subsidence and magmatism. In turn, these constraints may be used to develop models of tectonic activity including convergence, collision, rifting and continental separation. In Precambrian rocks, studies of sedimentary provenance are particularly valuable because the fossil record is of limited use and the record of seafloor growth is unavailable. Studies of Precambrian sedimentary successions typically involve detrital mineral geochronology and isotope geochemistry, and whole-rock trace element and isotope geochemistry to constrain depositional ages, source-region identities and sedimentary transport paths.

The Precambrian history of western Laurentia (ancestral North America) and the paleogeographical configuration of Columbia (also termed Nuna) have been investigated with studies of sedimentary provenance (Ross et al., 1992; Medig et al., 2014), igneous provinces (Ernst et al., 2008, 2013), orogenic belts (Betts and Giles, 2006; Betts et al., 2008), hydrothermal fields (Thorkelson et al., 2001a), and geophysical investigations of paleomagnetism and deep crustal structure (Cook et al., 1998; Zhang et al., 2012; Pisarevsky et al., 2014). In a pivotal study, Ross et al. (1992) identified a population of detrital zircon in the Mesoproterozoic Belt-Purcell basin that was likely sourced from Australia. The ages of these exotic zircon grains lie within an interval of sparse magmatism in Laurentia called the North American magmatic gap (NAMG, ca. 1.6-1.5 Ga). The NAMG contrasts with the magmatic record of Australia and Antarctica, where magmatism was abundant during this interval and throughout much of the Paleo- to Mesoproterozoic (Ross et al., 1992; Page and Sun, 1988; Peucat et al., 2002; Ross and Villeneuve, 2003; Link et al., 2007; Goodge et al., 2008; Betts et al., 2009; Goodge and Fanning, 2010, 2016). Following Ross et al. (1992), additional studies on the Belt-Purcell succession and other basins scattered from the southwestern United States to northwestern Canada have

revealed the presence of zircon with NAMG ages, supporting a model of eastward transport of Australian sediment (current geographical coordinates) to Proterozoic basins on Laurentia (Ross et al., 1992; Blewett et al., 1998; Fanning et al., 2009; Shufeldt et al., 2010; Doe et al., 2012; Medig et al., 2014). These provenance studies coupled with other evidence consistently point to Australia and Antarctica as the most likely landmasses to have been in contact with western Laurentia in the Meso- to Neoproterozoic, and perhaps the Paleoproterozoic. However, the details of how the continents came together, interacted and then separated remain uncertain. In addition, the possible involvement of other continents and volcanic arcs has not been fully addressed. These uncertainties reflect the complexity of the Precambrian geological record of western Laurentia, which involves several cycles of sedimentation interwoven with deformation, metamorphism, magmatism and hydrothermal brecciation (Thorkelson et al., 2005).

This study focuses on late Paleoproterozoic to early Mesoproterozoic rocks in Yukon Territory of northwestern Canada. Previous studies in this region have defined linkages with Australia, and clarified how and when the interactions occurred (Thorkelson et al., 2001a; Furlanetto et al., 2013; Nielsen et al., 2013; Thorkelson and Laughton, 2016). NAMG-aged zircon in one of the Yukon successions was also used to define a provenance linkage with the Mount Isa inlier of northwestern Australia (Medig et al., 2014). In a recent model, northwestern Laurentia was shown to undergo rifting and passive margin development in the late Paleoproterozoic, followed by ocean closure, obduction of an exotic terrane named Bonnetia, and collision with Australia (Furlanetto et al., 2013; Nielsen et al., 2013; Thorkelson and Laughton, 2016).

We provide results of detrital zircon geochronology and sedimentary geology of a newly recognized sedimentary succession in northern Yukon. The succession was removed by erosion in the Mesoproterozoic, except for clasts preserved in zones of hydrothermal breccia. Using these remnant clasts, we examine the ages, Hf-isotopic compositions and grain morphologies of the zircon, along with petrography, geochemistry and Nd isotope geochemistry on whole rocks. The findings are combined with regional field relations to identify the source of the sediment and the nature of the basin. The information is used to clarify the sedimentary and tectonic history of western Laurentia

from ca. 1.7-1.6 Ga and refine models of how Laurentia, Bonnetia and Australia interacted in Proterozoic time.

3.3. A former unlithified sedimentary succession in Wernecke Breccia

Most of the breccia clasts were sourced from the metasedimentary Wernecke Supergroup and others from igneous rocks. The presence of anomalous sedimentary clasts and interstitial mudrock that display soft sediment textures indicate the former presence of an unlithified sedimentary succession (Figure 3.1, Verbaas et al., 2014). This unlithified succession and its bearing on Precambrian paleogeography are the main topics of this paper. The hydrothermal breccia zones which enclose the former soft-sediment material are collectively called the Wernecke Breccia (Thorkelson et al., 2001a). Clasts with soft-sediment textures within the breccias were first described by Lane (1990), although their origin and significance were not yet understood. The soft-sediment clasts are composed of sandstone and mudstone that exhibit ductile and fluidal features such as convolute bedding, rip-up textures and mantling of lithified clasts (Verbaas et al., 2014). The soft-sediment clasts occur within breccia zones that span more than 200 km in the Ogilvie Mountains, and extend to at least one breccia zone in the Wernecke Mountains, and hence the sedimentary succession must have occupied an area of at least 50 X 250 km (Figure 3.1). This sedimentary succession was previously unrecognized and will be referred to as the Wernecke-Ogilvie unlithified succession (WOUS).

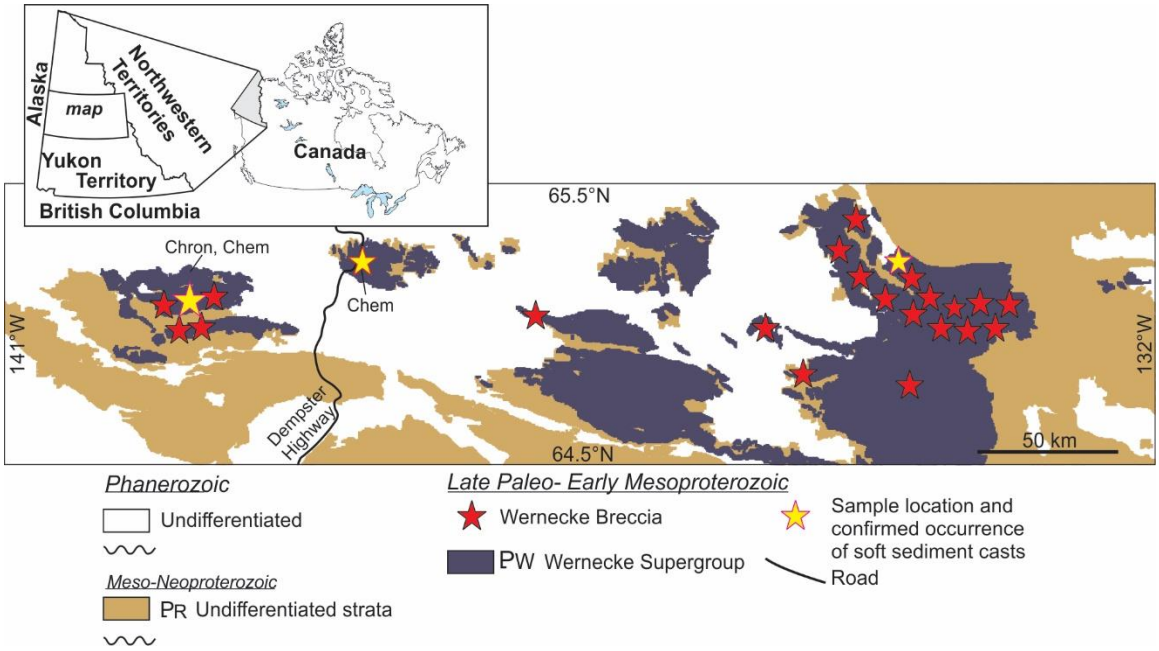

Figure 3.1. Geology of Paleoproterozoic to Mesoproterozoic inliers in Yukon Territory and occurrences of the Wernecke Breccia and soft sediment clasts within them. Chron: geochronology Chem: Whole rock geochemical analyses.

The Wernecke Breccia is hosted by a thick Paleoproterozoic succession called the Wernecke Supergroup, and is unconformably overlain by Mesoproterozoic sedimentary strata (Thompson et al., 1992; Thorkelson, 2000). The Wernecke Supergroup is a 14 km-thick succession of siliciclastic and carbonate metasedimentary rocks (Delaney, 1981; Thorkelson, 2000) that was deposited on a passive margin after 1.66 Ga and prior to 1.60 Ga, at the end of the Paleoproterozoic (Furlanetto et al., 2013). The youngest detrital zircon grains that occur in both the oldest and youngest unit of the Wernecke Supergroup are 1.66 Ga (Furlanetto et al., 2013), which is interpreted as the maximum age of deposition. The base of the Wernecke Supergroup is unexposed. Between 5 and 9 km of strata underlie the Wernecke Supergroup and overlie crystalline basement of Laurentia (Hall and Cook, 1998; Crawford et al., 2010; Thorkelson and Laughton, 2016; Furlanetto et al., 2016).

3.3.1. Soft sediment clasts and fluidal mudstone

Clasts of the soft-sediment material sourced from the WOUS occur as two general lithotypes: 1) red mudstone and pink sandstone, and 2) curviplanar streaks and interstitial patches of green mudstone (Verbaas et al., 2014; Chapter 2). The majority of our data comes from the clasts of red mudstone and pink sandstone, although both lithotypes will be used in the reconstruction of the WOUS.

The clasts of pink to red mudstone and sandstone occur in two forms. In the first form, primary layering is preserved as millimeter- to centimeter-size laminations and cm-size cross-stratification (Figure 3.2A). In the second form, primary layering is not discernable and instead the clasts consist of tightly packed, millimetre- to centimetre-size fragments of mudstone and sandstone (Figure 3.2B). These fragments have ragged to curviplanar boundaries, contorted internal laminations, and are firmly packed together with little or no interstitial matrix. They resemble a collection of tightly packed rip-up clasts (Figure 3.2C). As such, we refer to this form of clast as soft-sediment clast-supported conglomerate. Taken together, both forms of clasts represent a succession of interlayered mud and sand.

The green mudstone occurs as patches, streaks and ribbons and lacks sedimentary structure or layering. The mudstone appears to have behaved fluidly in the Wernecke Breccia zones and locally serves as a matrix to other clasts (Figure 3.2D).

The green mudstone and soft-sediment conglomerate differ from the majority of clasts in Wernecke Breccia which were lithified and variably metamorphosed prior to brecciation. Locally, previously lithified clasts are encapsulated within both soft-sediment lithotypes. This relationship shows that Wernecke Breccia, at the time of formation, was a mixture of both lithified and non-lithified material and requires that both solid rock and unlithified sediment simultaneously contributed to the clast population (Verbaas et al., 2014; Chapter 2). Figure 3.3 conceptually shows how the different soft sediment materials occur within Wernecke Breccia.

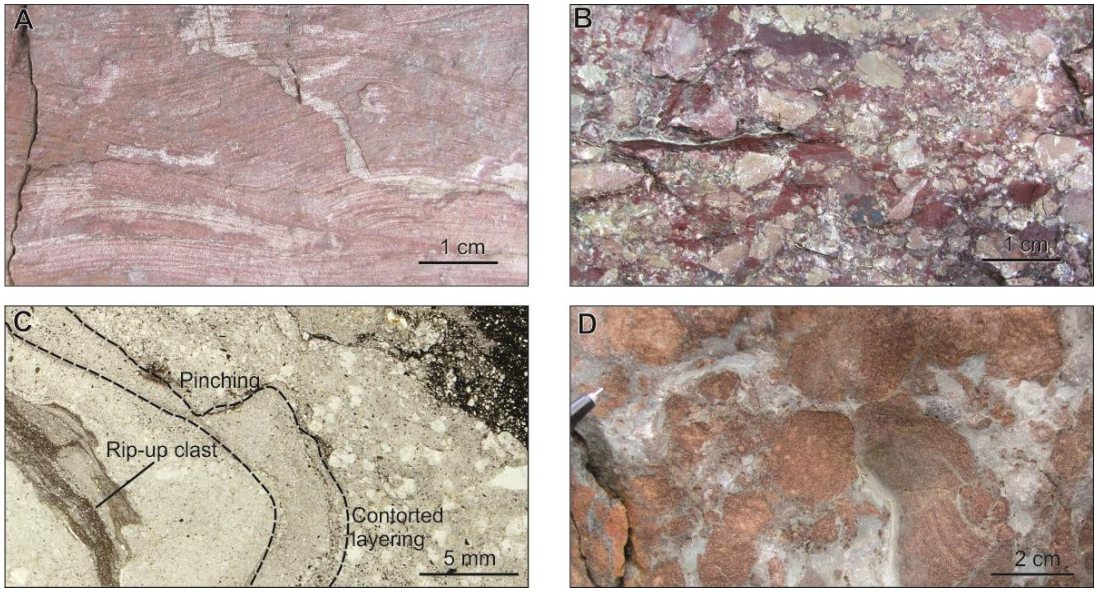

Figure 3.2. **Soft sediment clasts and fluidal mudstone. A. Cross stratified laminated white to red sandstone to mudstone. B. Tightly packed soft sediment conglomerate of red to pink mudstone and sandstone. C. Microstructures of tightly packed soft sediment conglomerate. D. Green mudstone as matrix to Wernecke Supergroup clasts.**

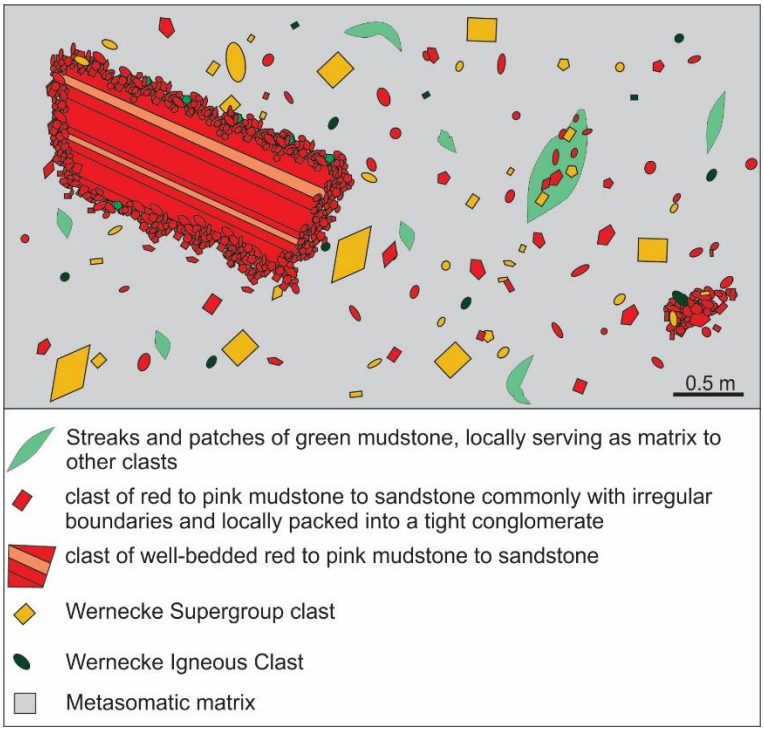

Figure 3.3. **Conceptual diagram of the soft sediments within Wernecke breccia.**

3.3.2. The hydrothermal Wernecke breccia

The Wernecke Breccia comprises metre- to kilometre-size hydrothermal cross-cutting breccia zones that are scattered throughout a vast region in Yukon. They occur between latitudes 64˚N and 66.5˚N from near the Alaska border in the west, to near the Northwest Territories border in the east (Figure 3.4). The breccias have been dated at 1598.8 ± 1.0 Ma by U-Pb on metasomatic titanite (Furlanetto et al., 2013). Brecciation followed the Racklan orogeny, an interval of polyphase deformation and metamorphism between ca. 1.65 and 1.60 Ga (Furlanetto et al., 2013). The hydrothermal activity led to local iron oxide-copper-gold mineralisation (Hunt et al., 2005, 2007). Veins in the soft-sediment clasts are dominated by hematite, carbonate and quartz.

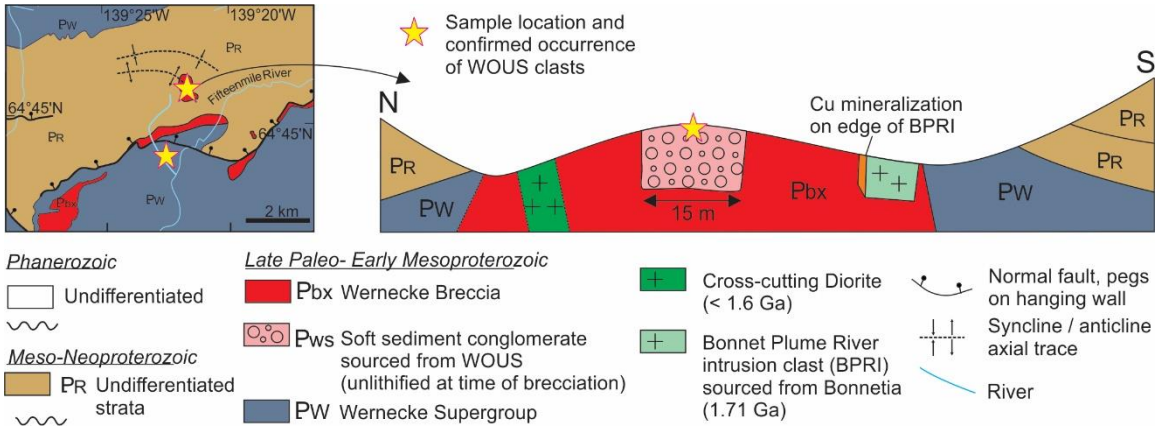

Figure 3.4. Sample locations in the Ogilvie Mountains, and field relations of sample JV1214 (UTM: 578059E, 7182329N, NAD83). Other sample locations are reported in Table 3.5.

3.3.3. Stratigraphic and structural substrate to the unlithified sediments

Most of the clasts within Wernecke Breccia were sourced from the direct country rock, but the igneous clasts cannot be correlated to either the Wernecke Supergroup, or any other known rock units on northwestern Laurentia. Instead, the igneous clasts have been interpreted as fragments of an obducted terrane named Bonnetia that was thrust onto the margin of Laurentia in the final stage of Racklan orogeny (Furlanetto et al., 2013, Nielsen et al., 2013). The orogeny produced craton-verging folds and upper greenschist facies metamorphism in the Wernecke Supergroup (Thorkelson, 2000; Thorkelson et al., 2005). The deformation affected much of northwestern Laurentia, and is partly correlative

with the Forward Orogeny to the east (Cook and MacLean, 1995; Furlanetto et al., 2016). Peak metamorphism was dated at ca. 1.6 Ga using Lu-Hf on garnet and is characterized by biotite-garnet thermometry at approximately 500°C (Furlanetto et al., 2013). Hydrothermal activity within the breccia zones produced veining and alteration of both clasts and country rock (Thorkelson et al., 2001a; Nielsen et al., 2013). Plutonic and volcanic clasts of Bonnetia foundered into zones of Wernecke Breccia during intense hydrothermal activity (Furlanetto et al., 2013, Nielsen et al., 2013). Many of the clasts came to rest deep in the breccia zones, flanked by metasedimentary rocks of the Wernecke Supergroup. Bonnetia and the overlying unlithified sediments were subsequently eroded, exposing the Wernecke Supergroup and zones of Wernecke Breccia.

Bonnetia was regarded by Thorkelson and Laughton (2016) as an obducted sliver of a volcanic arc that was built on the eastern edge of Australia. Rocks of Bonnetia include the Bonnet Plume River intrusions, the Devil volcanic clasts and the Slab volcanic megaclast (Thorkelson et al., 2001b; Nielsen et al., 2013; Thorkelson and Laughton, 2016). The geochemical signature of both plutonic and volcanic rocks sourced from Bonnetia are consistent with an origin from a volcano-plutonic arc that was possibly modified by a plume, rift, or slab window (Nielsen et al., 2013). On the basis of Nd isotopes, the igneous clasts have depleted mantle model ages from 2.4 – 2.2 Ga (Nielsen et al., 2013). These model ages are substantially older than the corresponding crystallization ages of ca. 1.71 Ga (Thorkelson et al., 2001b), and imply that Bonnetia may have been built upon older crust.

Given these constraints, the source for the WOUS is regarded as a succession deposited after the Racklan Orogeny and before Wernecke Breccia formation, on Bonnetia. The WOUS was unlithified at the time of Wernecke Breccia formation (Verbaas et al., 2014). In turn, Bonnetia would have overlain the deformed and metamorphosed Wernecke Supergroup along an obduction surface. The entire allochthon would have been separated from cratonal rocks of Laurentia by a contractional decollement (Figure 3.5; Furlanetto et al., 2013), which is consistent with a general model of western Laurentian structure based on geophysical data (MacLean and Cook, 2004; Cook et al., 2005). Within

this framework, we examine the provenance of the WOUS and apply our findings to outstanding questions of tectonic evolution and regional paleogeography.

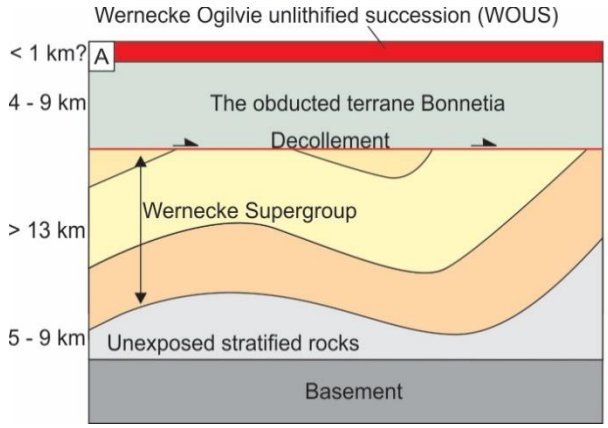

Figure 3.5. Crustal column immediately preceding the time of brecciation (modified from Thorkelson and Laughton, 2016). Thicknesses of units after Delaney et al., 1981; Thorkelson, 2000; Nielsen et al., 2013; Furlanetto et al., 2016.

3.4. Provenance of the unlithified succession from geochronology and geochemistry

3.4.1. Analytical methods

Samples for geochronology and geochemistry were taken from locations in the Ogilvie Mountains. Sample JV1214 was taken from a 15 m-wide clast of soft-sediment conglomerate. The conglomerate is tightly packed with clasts of pink to red mudstone with irregular boundaries. Sample JV1214 is pervasively hematite-altered, crosscut by minor veinlets of carbonate and hematite, and contains millimetre sized blebs of scapolite. The sample was taken from a regolith that formed prior to deposition of overlying sediments. Detrital zircon was separated at Simon Fraser University using standard crushing and milling techniques, followed by magnetic susceptibility and density separation, and hand picking. All zircon was picked from the mineral separate in order to avoid bias related to grain size, morphology or colour.

The zircon was analyzed at Boise State University by laser ablation inductively coupled plasma mass spectrometry (LA-ICPMS) using a quadrupole ICPMS laser ablation

system after imaging by cathode luminescence (CL) on a scanning electron microscope. The zircon was ablated with a 25 µm wide laser spot using fluence and pulse rates of 5 J/cm2 and 10 Hz, respectively, during a 45 second analysis (15 sec gas blank, 30 sec ablation) that excavated a pit ca. 25 µm deep. For U-Pb and $^{207}Pb/^{206}Pb$ dates, instrumental fractionation of the background-subtracted ratios was corrected and dates were calibrated with respect to interspersed measurements of the Plešovice zircon standard (Sláma et al., 2008). A zircon secondary reference material was treated as an unknown to assess accuracy, interspersed as groups of two analyses for every 20 unknown analyses. Full LA-ICPMS methods are presented in appendix A.

A second zircon set from the same sample was analysed in the J.C. Roddick Ion Microprobe laboratory located at the Geological Survey of Canada (GSC) in Ottawa. Grains were mounted in epoxy and imaged by both CL and back scattered electron (BSE) imaging techniques. The zircon grains were analysed in two sessions with the Sensitive High-Resolution Ion Microprobe II (SHRIMP-II) following analytical procedures of Stern et al., (1997). Zircons 719-1.1 – 719-53.1 were analysed with a Kohler beam aperture of 100 µm resulting in a 17 x 23 µm spot size. Zircons 721-1.1 – 721-127.1 were analysed using a Kohler beam aperture of 120 µm resulting in a 13.5 x 19 µm spot size. Target areas were selected for their absence of cracks and secondary alteration. Pb/U calibration was done with Sri Lankan zircon standard z6266 (also known as BR266) with an age of 559.0 ± 0.2 Ma (Stern and Amelin, 2003). An internal zircon standard z1242, with an age of 2679.7 ± 0.3 Ma was used to monitor accuracy of the measured $^{207}Pb/^{206}Pb$ ratio. Ages from both sets of zircons were analyzed using Isoplot 2.0 (Ludwig, 2009).

The zircon analysed via SHRIMP-II that yielded ages of < 5 % discordance were further analysed at the University of Florida for Hf isotopes via LA-ICPMS using a New Wave 213 nm laser. The ablated material was analyzed using a Nu Plasma multi-collector plasma source mass spectrometer (MC-ICP-MS) following methods described in Mueller et al. (2008). Lu/Hf calibration was done using Sri Lankan zircon standard z6266 (Woodhead et al., 2004). Depleted mantle values are based on a linear model ($\varepsilon Hf = 0$ at 4.56 Ga and 16 at 0 Ga; Mueller et al., 2008). Of the 49 grains, 29 were successfully analysed and yielded viable crustal residence ages. Other grains were either too small to be analysed by LA-ICPMS, or were dislodged from the epoxy puck during transport. Lu-

Hf chondritic values are from Söderlund et al. (2004), and the Lu decay constant is taken from Bouvier et al., (2008).

Whole rock major, minor and trace elements were analyzed at Activation Laboratories, Ontario, Canada. Samples were fused in a lithium metaborate/tetraborate bead to ensure full digestion and subsequently dissolved in weak nitric acid. Samples were subsequently analyzed using a combination of inductively coupled plasma mass spectrometry (ICP-MS), inductively coupled plasma optical emission spectra (ICP-OES) and instrumental neutron activation analyses (INAA).

Whole-rock Sm–Nd isotopic data were determined at the University of Florida using isotope dilution and ICP-MS methods after Heatherington and Mueller (1991). The uncertainty of Nd measurements is less than 0.00002 (2 σ), based on reproducibility of the La Jolla Nd standard (Heatherington and Mueller, 1991). The current CHUR value for $^{143}Nd/^{144}Nd$ was taken from White (2009). Sm-Nd model ages (T_{DM}) were calculated following methods in DePaolo (1981).

3.5. Analytical results

3.5.1. Zircon Morphology

Detrital zircon grains separated from sample JV1214 are rounded to sub-angular and range in size from 30 to 120 µm. The majority of grains range in size from 50 – 80 µm and are sub-angular. The zircon grains contain variable amounts of primary fractures (e.g., not due to separation and mounting), secondary radial fractures, and inclusions. Most zircon grains exhibit well-defined oscillatory growth zoning. Minor embayments are locally present. Zircon overgrowths are common and display a sieve texture (Figure 3.6). Out of approximately 150 analyses, 75 yielded ages with a discordance ≤5 %; analyses with a discordance >5 % were not included in further data treatment and interpretation.

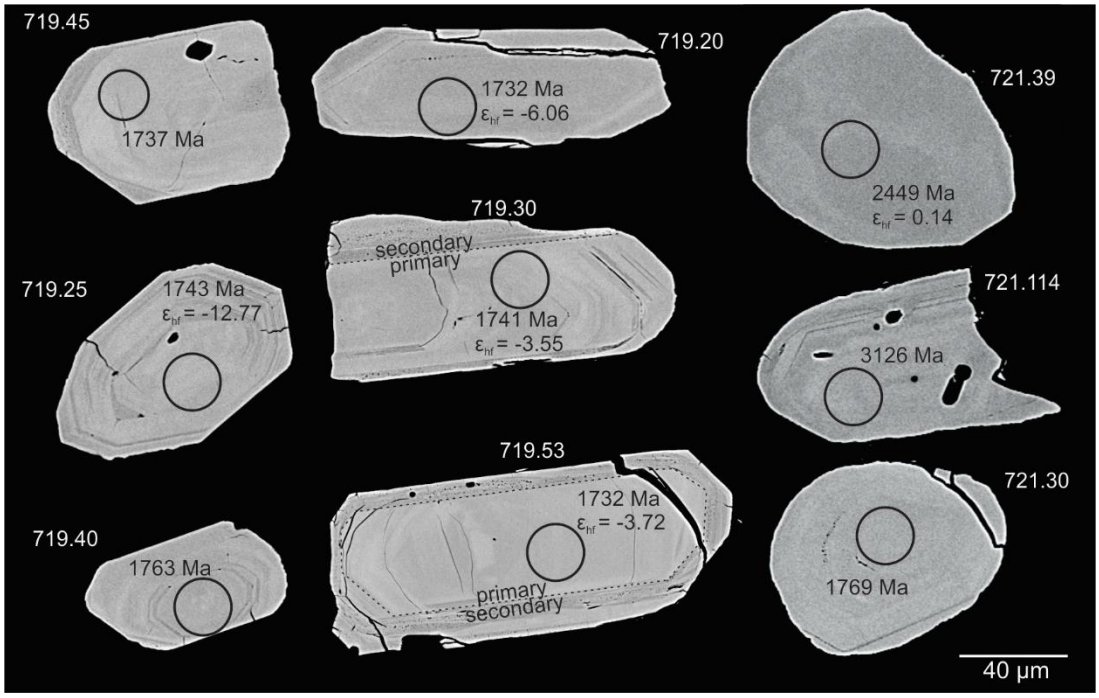

Figure 3.6. Backscattered electron images showing angular to rounded zircon separated from sample JV1214. The majority of the zircon grains are sub-angular.

3.5.2. Zircon U-Pb age determinations and zircon chemistry

Of 75 analyses with discordance <5%, 26 were obtained via LA-ICPMS (Figure 3.7, **Error! Reference source not found.**), and have a mean 2σ uncertainty of 62 Ma (uncertainties on individual dates include a standard calibration uncertainty of 0.66% (2σ)). A probability plot of LA-ICPMS dates define a bimodal distribution, with 13 out of 26 grains in the age range 1.78 – 1.68 Ga. Eight grains are slightly older, and range from 1.86 – 1.78 Ga. Three grains are 2.53 – 2.52 Ga and the remaining two grains have ages of 2.43 and 2.36 Ga. The remaining 49 analyses were obtained by SHRIMP II (Figure 3.7, Table 3.2) and have an average 2σ value of 19.5 Ma. Out of 49 obtained ages with discordance <5%, 33 ages fall within the age range 1.78 – 1.68 Ga. Five zircon ages are 2.1 Ga – 1.85 Ga, 3 grains are 2.51 – 2.45 Ga and single ages are 2.72 Ga and 3.13 Ga. The most notable feature of the combined data set is a prominent peak at 1.74 Ga. Of the total dataset, over 40% of the combined ages range from 1.78 – 1.68 Ga. Several zircon grains are as young as ca. 1.64 Ga. Smaller clusters of ages range from 2.53 – 2.43 Ga and 2.1 – 1.78 Ga. Two older zircon are 3.08 and 2.72 Ga.

Zircon mineral chemistry was used as an indicator of source rock composition following Belousova et al. (2002). Two discrimination diagrams that are described in Belousova et al. (2002), yielded different results in 40% of all cases, with the most common error between larvikite (a variety of syenite) and granitoid (21/63 zircon). Hence, syenite and granitoid are combined and reported as 'felsic'. Mafic to intermediate rocks are grouped and reported as 'mafic - intermediate'. Zircon that yielded $^{207}Pb^*/^{206}Pb^*$ ages with discordances >10% were used to identify the relative error between the two classifications but are not used for further constraining the source. Zircon chemistry and source rock interpretation is reported in Table 3.3. Zircon chemistry and Figure 3.8.

Protolith inferred from zircon trace element chemistry (following Belousova et al., 2002).

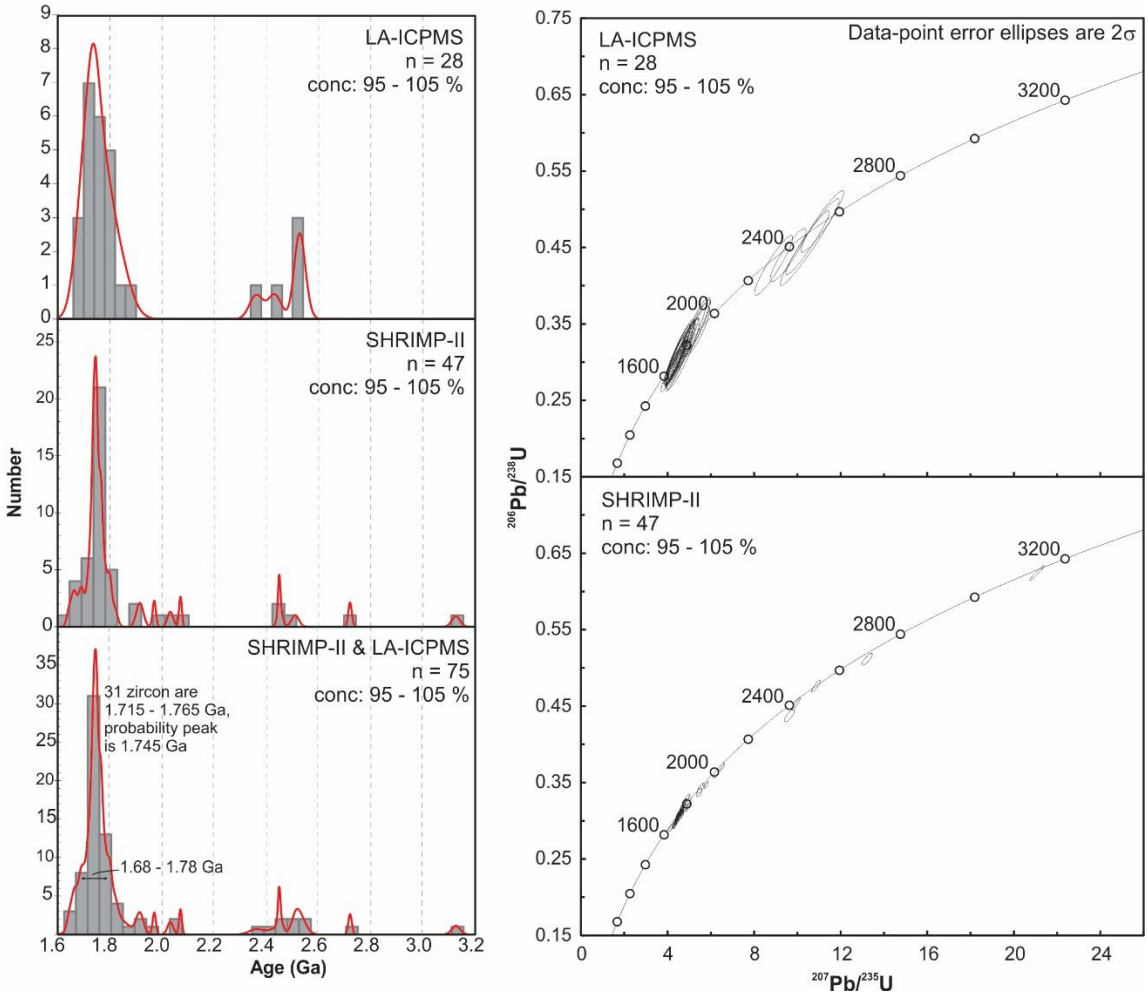

Figure 3.7. Probability and concordia plots of zircon ages obtained via LA-ICPMS and SHRIMP-II. n = sample size and conc. = concordance.

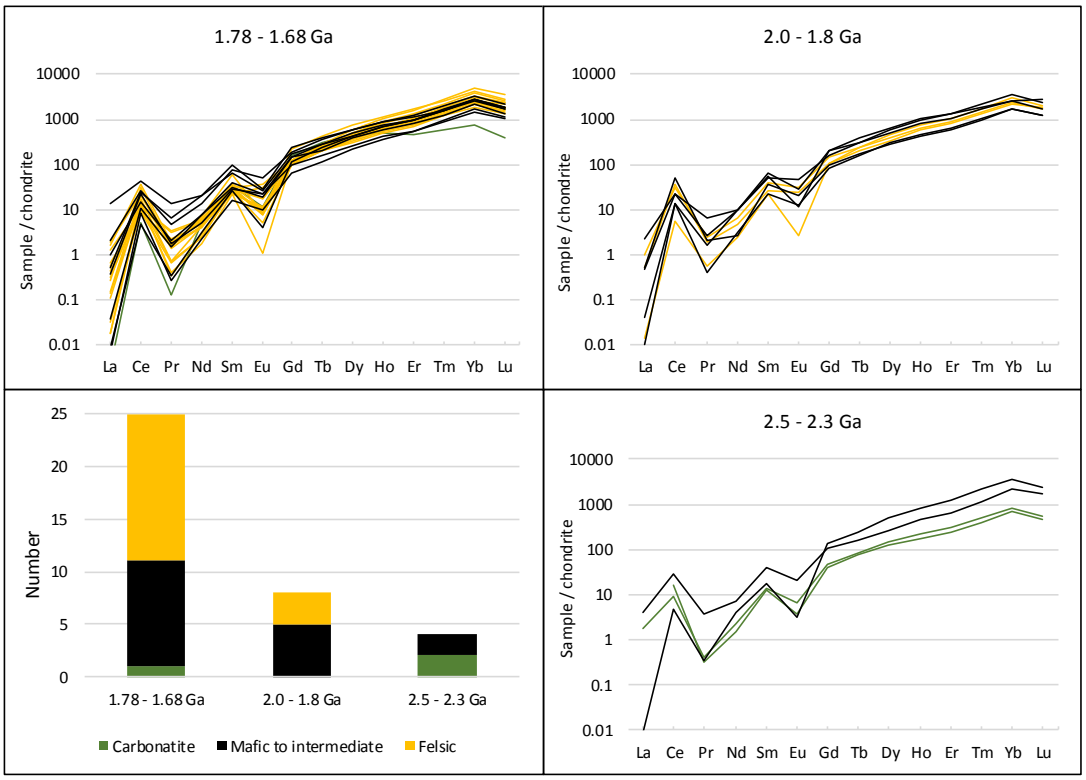

Figure 3.8. Protolith inferred from zircon trace element chemistry (following Belousova et al., 2002).

Table 3.1. LA-ICPMS analysis of detrital zircon

analysis	U ppm	Th ppm	Th/U	$^{206}Pb^*$ ppm	$^{206}Pb/^{204}Pb$	$^{206}Pb^*/^{207}Pb^*$	±1σ %	$^{207}Pb^*/^{235}U$	±1σ %	$^{206}Pb^*/^{238}U$	±1σ %	Corr. coeff.	Age $^{206}Pb^*/^{207}Pb^*$	± Ma	Disc. %
L 11	223	125	0.56	93	2257.8	9.301	1.2	4.81	4.0	0.325	3.8	0.951	1758	23	-3
L 13	83	40	0.49	32	2406.3	9.600	1.8	4.40	4.1	0.306	3.7	0.895	1700	34	-1
L 14	184	147	0.80	76	1870.0	9.339	1.8	4.47	4.0	0.303	3.6	0.890	1750	34	3
L 15	124	162	1.31	59	15937.8	9.435	2.4	4.60	5.4	0.315	4.8	0.899	1731	43	-2
L 16	131	51	0.39	55	1361.1	9.213	2.0	5.09	4.9	0.340	4.4	0.913	1775	36	-6
L 17	243	80	0.33	88	883.6	9.379	1.6	4.43	4.5	0.301	4.2	0.934	1742	30	3
L 2	280	215	0.77	112	7745.2	9.120	1.4	4.55	5.5	0.301	5.3	0.966	1794	26	5
L 20	323	218	0.67	128	2148.9	9.205	1.1	4.43	4.2	0.296	4.1	0.967	1777	20	6
L 22	169	134	0.79	122	15108.8	5.024	1.6	13.78	3.9	0.502	3.6	0.912	2818	26	7
L 23	517	281	0.54	161	9240.7	8.924	1.4	3.74	4.2	0.242	3.9	0.942	1833	25	24
L 25	250	138	0.55	89	1047.5	9.279	1.4	4.16	3.7	0.280	3.5	0.929	1762	25	10
L 27	164	96	0.59	69	5051.5	9.499	1.3	4.74	3.9	0.327	3.7	0.941	1719	24	-6
L 31	303	142	0.47	116	9211.3	9.567	1.7	4.49	5.2	0.311	5.0	0.947	1706	31	-2
L 34	172	144	0.84	71	1391.2	9.487	1.9	4.45	4.9	0.307	4.5	0.923	1721	35	0
L 36	262	195	0.74	102	5762.9	9.450	1.7	4.34	4.3	0.297	3.9	0.917	1729	31	3
L 39	288	111	0.38	98	1598.6	9.601	1.4	3.98	5.1	0.277	4.9	0.963	1700	25	7
L 4	281	163	0.58	102	3315.0	9.236	1.2	4.27	3.7	0.286	3.5	0.948	1771	22	8
L 41	180	109	0.61	75	2529.0	9.409	1.6	4.83	4.5	0.330	4.2	0.932	1737	30	-6
L 42	439	107	0.24	131	3292.6	9.432	1.2	3.74	3.6	0.256	3.4	0.937	1732	23	15
L 43	204	117	0.57	85	1435.0	9.333	1.4	4.76	4.6	0.322	4.4	0.955	1751	25	-3
L 44	226	153	0.68	104	1938.6	9.007	2.2	5.29	5.1	0.346	4.6	0.904	1816	40	-5
L 45	316	214	0.68	131	1508.8	9.587	1.9	4.46	5.5	0.310	5.1	0.937	1702	35	-2
L 48	345	109	0.31	145	23217.3	8.877	1.9	5.36	4.8	0.345	4.4	0.922	1843	34	-4
L 5	157	97	0.62	56	3671.6	9.548	1.4	3.96	3.9	0.275	3.7	0.932	1710	26	9
L 51	261	290	1.11	96	1565.8	9.663	1.7	3.78	4.0	0.265	3.6	0.909	1688	31	10
L 52	274	160	0.58	178	14350.4	5.983	1.2	11.15	3.6	0.484	3.4	0.940	2529	21	-1
L 55	216	80	0.37	77	1762.8	9.458	1.1	4.25	3.6	0.292	3.4	0.953	1727	20	4
L 57	275	194	0.71	107	1556.9	9.084	1.3	4.53	4.1	0.298	3.9	0.952	1801	23	7
L 6	460	202	0.44	129	1659.1	9.699	1.2	3.24	4.3	0.228	4.1	0.958	1681	23	21
L 62	154	114	0.74	96	1626.9	6.008	1.2	10.47	3.9	0.456	3.7	0.955	2522	19	4
L 8	392	302	0.77	193	1915.3	6.500	1.2	7.75	3.4	0.365	3.2	0.942	2389	20	16
L 9	227	261	1.15	95	749.4	7.980	1.7	5.21	3.8	0.302	3.4	0.895	2033	30	16
S 100	334	142	0.43	113	2316.1	9.368	1.6	4.01	3.9	0.273	3.5	0.913	1745	29	11
S 102	291	84	0.29	118	2128.4	8.099	1.5	5.68	3.9	0.334	3.6	0.920	2007	27	7
S 103	121	89	0.74	43	540.0	8.869	3.1	4.05	5.6	0.260	4.6	0.828	1844	56	19
S 104	292	75	0.26	108	3490.7	9.299	2.5	4.60	6.0	0.310	5.5	0.910	1758	46	1
S 105	273	135	0.49	103	2134.8	9.633	1.8	4.31	4.6	0.301	4.2	0.919	1693	34	0
S 110	153	122	0.80	64	1574.6	9.157	1.5	4.78	5.4	0.317	5.2	0.961	1786	27	1
S 111	181	154	0.85	81	1368.7	9.053	1.8	5.10	5.4	0.335	5.1	0.943	1807	33	-3
S 114	559	106	0.19	159	5317.4	9.039	1.4	3.69	4.5	0.242	4.3	0.948	1810	26	23
S 115	90	103	1.14	61	565.9	6.340	1.5	9.57	3.5	0.440	3.2	0.906	2432	25	3
S 64	242	203	0.84	99	1954.7	8.778	1.5	4.64	4.2	0.295	4.0	0.935	1863	27	10
S 66	293	182	0.62	109	2912.3	9.322	1.3	4.24	3.6	0.287	3.4	0.935	1754	23	7
S 67	236	115	0.49	116	8172.4	6.414	1.3	7.93	5.4	0.369	5.2	0.971	2412	22	16
S 68	92	78	0.85	46	4669.5	8.917	2.1	5.67	5.9	0.367	5.5	0.936	1834	38	-10
S 70	290	157	0.54	204	5418.2	4.706	1.6	14.90	4.3	0.509	4.0	0.929	2925	26	9
S 74	362	250	0.69	146	4307.1	8.699	2.3	4.71	5.1	0.297	4.6	0.898	1879	41	11
S 77	166	53	0.32	103	11640.8	6.251	1.6	10.96	4.8	0.497	4.5	0.940	2455	28	-6
S 78	315	218	0.69	135	8608.9	8.491	2.6	5.21	5.1	0.321	4.4	0.865	1923	46	7
S 79	233	122	0.52	92	1443.8	9.480	1.8	4.61	5.4	0.317	5.1	0.941	1723	33	-3
S 80	114	180	1.58	54	750.8	8.362	3.0	4.64	5.6	0.281	4.7	0.838	1950	54	18

analysis	U ppm	Th ppm	Th/U	$^{206}Pb^*$ ppm	$^{206}Pb/^{204}Pb$	$^{206}Pb^*/^{207}Pb^*$	±1σ %	$^{207}Pb^*/^{235}U$	±1σ %	$^{206}Pb^*/^{238}U$	±1σ %	Corr. coeff.	Age $^{206}Pb^*/^{207}Pb^*$	± Ma	Disc. %
S 82	195	106	0.55	95	2656.9	5.320	1.7	9.82	7.2	0.379	7.0	0.971	2724	28	24
S 84	221	154	0.70	91	25147.1	9.074	2.5	4.72	6.6	0.311	6.1	0.924	1803	46	3
S 85	251	255	1.02	92	1764.1	8.554	1.7	4.23	5.2	0.263	5.0	0.947	1909	30	21
S 86	275	178	0.65	106	8435.8	9.210	2.1	4.32	4.8	0.289	4.4	0.905	1776	37	8
S 88	246	169	0.69	143	2015.0	5.996	1.6	9.89	4.8	0.430	4.5	0.944	2525	27	9
S 89	134	56	0.42	74	14127.8	6.609	1.5	8.90	4.1	0.427	3.8	0.927	2361	26	3
S 91	217	234	1.08	146	2126.0	5.966	1.4	10.56	5.3	0.457	5.1	0.964	2534	23	4
S 93	281	185	0.66	103	2650.1	9.339	1.6	4.06	3.9	0.275	3.5	0.905	1750	30	10
S 95	311	150	0.48	118	11439.0	9.385	1.1	4.45	4.5	0.303	4.3	0.971	1741	19	2
S 97	252	360	1.43	88	1275.4	8.983	2.3	3.80	5.1	0.248	4.6	0.897	1821	41	22
S 98	165	88	0.53	69	10274.7	8.617	1.8	5.13	4.5	0.320	4.1	0.911	1896	33	6
S 119	112	152	1.36	50	834.1	8.780	2.3	5.34	4.5	0.340	3.9	0.863	1862	41	-1
S 124	151	94	0.62	56	19273.7	9.641	1.5	4.06	3.6	0.284	3.3	0.905	1692	28	5

Isotope ratios and ages are NOT corrected for initial common Pb. Isotope ratio and apparent age errors include systematic calibration errors of 0.33% (207Pb/206Pb) and 2.68% (206Pb/238U) (1 sigma). Ablation used a laser spot size of 25 microns, and a laser firing repetition rate of 10 Hz. Uncertainties are reported as 1σ.

Table 3.2. SHRIMP-II detrital zircon analyses

analysis	U ppm	Th ppm	Th/U	$^{206}Pb^*$ ppm	$^{206}Pb/^{204}Pb$	±1σ	f206 %	$^{206}Pb^*/^{207}Pb^*$	±1σ %	$^{207}Pb^*/^{235}U$	±1σ %	$^{206}Pb^*/^{238}U$	±1σ %	Corr. coeff.	age $^{206}Pb^*/^{207}Pb^*$	± Ma	Disc. %
719-1.1	495	237	0.49	113	51099.9	214	0.03	9.003	0.9	4.07	1.4	0.266	1.1	0.778	1817	16	18
719-4.1	313	92	0.30	93	18794.4	37	0.09	8.268	0.7	5.79	1.3	0.347	1.1	0.842	1970	13	3
719-5.1	465	248	0.55	113	6053.5	28	0.29	8.242	0.8	4.74	1.3	0.284	1.1	0.802	1976	14	21
719-6.1	485	300	0.64	156	68833.8	135	0.03	6.392	0.6	8.10	1.2	0.376	1.1	0.892	2418	9	17
719-11.1	352	162	0.48	93	11809.6	135	0.15	9.372	1.8	4.54	2.2	0.309	1.2	0.558	1744	33	1
719-14.1	399	290	0.75	101	19101.7	27	0.09	9.363	0.7	4.32	1.3	0.293	1.1	0.833	1746	13	6
719-16.1	306	138	0.47	75	4611.2	33	0.39	8.990	1.3	4.38	1.7	0.285	1.2	0.691	1820	23	13
719-35.1	556	227	0.42	99	4383.8	26	0.41	9.896	1.0	2.89	1.5	0.208	1.1	0.714	1644	19	28
719-2.1	120	66	0.57	32	-9311.5	53	-0.19	9.165	1.4	4.62	2.4	0.307	1.9	0.812	1785	25	4
719-3.1	153	84	0.57	41	16182.7	42	0.11	9.259	1.2	4.64	1.9	0.312	1.5	0.792	1766	22	1
719-36.1	143	164	1.19	39			0.00	9.368	1.3	4.65	1.8	0.316	1.3	0.703	1745	24	-2
719-33.1	462	225	0.50	147	65615.8	135	0.03	7.813	0.6	6.53	1.2	0.370	1.1	0.869	2071	11	2
719-31.1	461	244	0.55	145	40942.8	72	0.04	5.911	0.5	8.57	1.2	0.367	1.1	0.904	2549	9	24
719-32.1	152	115	0.78	67			0.00	5.333	0.8	13.22	1.5	0.511	1.3	0.840	2720	13	3
719-30.1	388	169	0.45	100	51600.0	50	0.03	9.382	0.8	4.41	1.3	0.300	1.1	0.822	1742	14	3

analysis	U ppm	Th ppm	Th/U	$^{206}Pb^*$ ppm	$^{206}Pb/^{204}Pb$	±1σ	f206 %	$^{206}Pb^*/^{207}Pb^*$	±1σ %	$^{207}Pb^*/^{235}U$	±1σ %	$^{206}Pb^*/^{238}U$	±1σ %	Corr. coeff.	age $^{206}Pb^*/^{207}Pb^*$	± Ma	Disc. %
719-29.1	116	202	1.80	36			0.00	7.987	1.2	6.24	1.8	0.361	1.3	0.730	2032	22	2
719-28.1	251	38	0.16	68			0.00	9.089	1.3	4.79	1.8	0.316	1.2	0.683	1800	24	2
719-25.1	388	338	0.90	99	32650.6	42	0.05	9.373	0.8	4.36	1.4	0.297	1.1	0.810	1744	15	4
719-23.1	274	151	0.57	70	7875.8	41	0.23	9.404	1.1	4.38	1.6	0.299	1.1	0.711	1738	21	3
719-20.1	232	130	0.58	60	14161.2	29	0.13	9.428	1.0	4.44	1.6	0.304	1.2	0.753	1733	19	1
719-17.1	55	28	0.53	15			0.00	8.546	1.8	5.24	2.4	0.325	1.6	0.653	1911	33	6
719-37.1	162	123	0.79	47	-4662.1	43	-0.38	8.524	1.5	5.45	2.0	0.337	1.3	0.637	1916	27	3
719-40.1	180	57	0.33	45	5046.43	27	0.35	9.271	1.3	4.31	1.8	0.290	1.2	0.676	1764	24	8
719-42.1	556	247	0.46	162	42647.3	36	0.04	7.816	0.6	6.00	1.4	0.340	1.2	0.910	2070	10	10
719-45.1	387	167	0.44	87	21684.0	31	0.08	9.405	0.8	3.83	1.4	0.261	1.1	0.796	1737	16	15
719-47.1	300	108	0.37	91	10752.6	25	0.17	6.579	0.7	7.38	1.8	0.352	1.7	0.924	2368	12	21
719-49.1	487	207	0.44	129	16400.3	44	0.11	9.086	0.8	4.68	1.3	0.308	1.1	0.821	1800	14	4
719-48.1	339	217	0.66	87	11691.2	28	0.15	9.252	0.9	4.46	1.4	0.299	1.1	0.788	1767	16	5
719-50.1	172	96	0.58	46	22231.1	50	0.08	9.375	1.2	4.56	1.8	0.310	1.4	0.760	1743	22	0
719-53.1	181	74	0.42	48	6019.46	31	0.30	9.430	1.3	4.48	1.8	0.306	1.2	0.677	1732	24	1
721-40.1	175	70	0.41	49	0.02052	73	-0.09	9.357	0.9	4.77	1.8	0.324	1.5	0.865	1747	16	-4
721-10.1	280	206	0.76	66	0.01510	38	0.08	9.378	0.5	4.05	1.6	0.276	1.5	0.940	1743	10	11
721-26.1	62	34	0.57	18	0.05490	297	-0.06	8.532	1.5	5.54	2.2	0.343	1.7	0.735	1914	27	1
721-31.1	186	94	0.52	51	0.01976	40	0.14	9.267	0.7	4.72	1.7	0.318	1.5	0.898	1764	13	-1
721-34.1_A	376	278	0.76	100	0.01001	36	0.07	9.321	0.7	4.57	1.7	0.309	1.6	0.916	1754	12	1
721-34.1	342	241	0.73	92	0.01085	60	0.02	9.346	0.5	4.63	1.6	0.314	1.5	0.952	1749	9	-1
721-42.1	138	116	0.87	35	0.02847	38	0.26	9.239	1.1	4.42	2.0	0.296	1.6	0.826	1770	20	6
721-8.1	177	77	0.45	48	0.02087	52	0.03	9.262	0.6	4.68	1.6	0.314	1.5	0.926	1765	11	0
721-32.1	195	70	0.37	43	0.02337	74	0.14	9.384	1.0	3.76	2.1	0.256	1.8	0.868	1741	19	18
721-7.1	380	284	0.77	89	0.01122	28	0.15	8.987	0.6	4.19	1.6	0.273	1.5	0.939	1820	10	16
721-39.1	236	124	0.54	92	0.01090	27	0.11	6.275	0.5	9.95	1.6	0.453	1.5	0.945	2449	9	2
721-4.1	289	117	0.42	125	0.00803	27	0.13	4.270	0.4	16.22	1.5	0.502	1.5	0.973	3081	6	18
721-28.1	387	69	0.18	106	0.00942	87	-0.05	9.392	0.7	4.69	2.0	0.319	1.9	0.939	1740	13	-3
721-19.1	95	52	0.57	25	0.04030	30	0.66	9.377	1.7	4.49	2.3	0.305	1.6	0.677	1743	31	2
721-13.1	442	274	0.64	113	0.00888	30	0.25	9.511	0.8	4.30	1.8	0.296	1.7	0.899	1717	15	3
721-30.1	197	94	0.49	56	0.01794	50	0.20	9.244	1.0	4.90	1.8	0.329	1.5	0.847	1769	18	-4
721-2.1	279	178	0.66	63	0.01599	28	0.23	9.297	0.7	3.88	1.7	0.261	1.5	0.912	1758	12	17
721-15.1	251	189	0.78	94	0.01058	164	0.12	6.263	1.2	9.63	1.9	0.438	1.5	0.778	2452	21	5
721-49.1	380	224	0.61	91	0.01104	21	0.63	9.417	1.2	4.06	1.9	0.277	1.5	0.799	1735	21	10
721-16.1	180	106	0.60	48	0.02100	34	0.39	9.425	1.1	4.49	1.9	0.307	1.5	0.798	1733	21	0
721-41.1	451	226	0.52	135	0.00742	24	0.31	9.298	0.8	5.16	1.7	0.348	1.5	0.878	1758	15	-11

analysis	U ppm	Th ppm	Th/U	$^{206}Pb^*$ ppm	$^{206}Pb/^{204}Pb$	±1σ	f206 %	$^{206}Pb^*/^{207}Pb^*$	±1σ %	$^{207}Pb^*/^{235}U$	±1σ %	$^{206}Pb^*/^{238}U$	±1σ %	Corr. coeff.	age $^{206}Pb^*/^{207}Pb^*$	± Ma	Disc. %
721-1.1	181	134	0.76	48	0.02104	20	0.80	9.345	1.3	4.52	2.0	0.306	1.5	0.759	1749	24	2
721-122.1	227	108	0.49	59	0.00010	26	0.19	0.106	0.8	4.43	1.5	0.302	1.3	0.863	1704	20	2
721-81.1	282	141	0.52	76	0.00010	33	0.18	0.109	0.7	4.69	1.5	0.311	1.3	0.878	1748	20	2
721-118.1	77	83	1.12	29	0.00014	18	0.27	0.168	0.8	10.30	1.7	0.445	1.5	0.876	2375	30	8
721-74.1	143	83	0.60	39	0.00000	2928	-0.01	0.115	1.3	4.99	2.0	0.316	1.6	0.785	1770	25	6
721-68.1	211	116	0.57	58	0.00010	34	0.18	0.113	0.7	4.95	1.6	0.318	1.4	0.881	1779	21	4
721-86.1	204	86	0.44	54	0.00007	39	0.12	0.107	0.7	4.56	1.5	0.310	1.3	0.867	1740	20	0
721-121.1	177	152	0.89	72	0.00009	66	0.17	0.165	0.7	10.86	1.5	0.476	1.4	0.896	2510	28	0
721-114.1	292	197	0.70	157	0.00001	37	0.02	0.245	0.3	21.07	1.3	0.624	1.3	0.974	3126	32	1
721-102.1	187	88	0.49	48	0.00018	31	0.34	0.107	1.0	4.41	1.6	0.300	1.3	0.792	1691	19	4
721-84.1	196	170	0.89	50	0.00009	41	0.17	0.107	0.8	4.40	1.5	0.299	1.3	0.847	1686	19	4
721-96.1	269	96	0.37	74	0.00011	33	0.21	0.106	0.7	4.68	1.5	0.319	1.3	0.874	1784	21	-3
721-98.1	147	102	0.72	41	0.00026	26	0.48	0.111	1.1	4.98	1.7	0.326	1.3	0.766	1820	21	-1
721-100.1	183	127	0.72	49	0.00013	32	0.24	0.107	0.9	4.59	1.6	0.311	1.3	0.838	1748	20	0
721-127.1	177	90	0.53	47	0.00016	31	0.30	0.106	0.9	4.52	1.6	0.308	1.3	0.811	1732	20	0
721-75.1	106	63	0.61	27	0.00017	41	0.32	0.106	1.3	4.32	1.9	0.294	1.3	0.723	1662	20	5
721-87.1	189	133	0.73	47	0.00030	23	0.55	0.103	1.2	4.15	1.8	0.291	1.3	0.745	1645	19	3
721-65.1	120	78	0.67	30	0.00011	21	0.20	0.107	0.9	4.29	1.7	0.291	1.4	0.837	1647	20	6
721-82.1	218	193	0.91	55	0.00011	58	0.20	0.106	1.1	4.32	1.7	0.295	1.3	0.766	1666	19	4
721-101.1	265	159	0.62	66	0.00006	66	0.12	0.108	0.8	4.31	1.5	0.290	1.3	0.854	1639	19	8
721-89.1	584	254	0.45	108	0.00078	9	1.42	0.108	1.0	3.22	1.6	0.216	1.3	0.776	1259	15	32
721-91.1	483	232	0.50	103	0.00016	22	0.30	0.105	0.7	3.59	1.5	0.249	1.3	0.893	1432	17	18
721-93.1	309	125	0.42	73	0.00016	39	0.29	0.107	1.0	4.04	1.6	0.274	1.3	0.795	1559	18	12
721-126.1	356	72	0.21	85	0.00015	41	0.27	0.108	0.9	4.12	1.6	0.278	1.3	0.811	1579	18	11
721-99.1	536	179	0.34	125	0.00017	18	0.31	0.111	0.5	4.15	1.4	0.272	1.3	0.919	1549	17	16
721-67.1	277	156	0.58	62	0.00012	31	0.22	0.113	0.7	4.04	1.5	0.259	1.3	0.871	1486	17	22
721-116.1	381	38	0.10	92	0.00006	75	0.10	0.107	0.7	4.15	1.5	0.281	1.3	0.865	1597	18	10
721-123.1	370	167	0.47	82	0.00030	21	0.55	0.104	1.0	3.71	1.6	0.259	1.3	0.789	1487	17	13
721-95.1	190	131	0.71	45	0.00036	21	0.65	0.104	1.2	3.99	1.8	0.277	1.4	0.738	1577	19	8
721-76.1	126	83	0.68	31	0.00033	25	0.61	0.108	1.4	4.21	2.0	0.283	1.4	0.714	1608	20	10
721-120.1	228	177	0.80	53	0.00002	136	0.04	0.106	0.9	3.95	1.6	0.269	1.3	0.840	1537	18	13

Isotope ratios and ages corrected for initial common Pb using the ^{204}Pb method. Surface blank was used as common Pb. Data reduction was done using squid 2.22. Uncertainties are reported as 1σ.

Table 3.3. Zircon chemistry

Zircon	P	Ti	Nb	La	Ce	Pr	Nd	Sm	Eu	Gd	Tb	Dy	Ho	Er	Tm	Yb	Lu	Y	U	Ta	Hf	Th	S.R.	age
L 52	176	11.9	1.3		10.0		0.7	2.0	0.2	7.8	2.8	31	9.5	39.3	10.3	118	11.8	274	274	0.7	8557	159.9	carb.	2529
L 62	248	4.5	0.8	1.0	16.7	0.4	3.3	6.2	1.2	21.3	5.9	67	25.4	110.2	29.9	361	44.4	717	154	0.6	8636	114.0	mafic	2522
S 77	644	12.1	0.5		2.9	0.0	1.9	2.6	0.2	27.8	9.0	129	47.4	210.8	56.5	602	62.7	1374	166	0.4	9201	52.9	mafic	2455
L 8	576	27.6	1.8	1.6	21.5	1.2	12.3	21.8	5.7	65.9	21.3	225	73.3	270.0	66.5	695	70.7	1859	392	0.8	7837	302.3	mafic	~~2389~~
S 89	110	8.1	1.4	0.4	5.7	0.0	1.1	2.1	0.4	9.3	3.0	38	12.8	51.6	12.6	135	13.7	338	134	0.9	7218	56.0	carb.	2361
S 102	240	2.9	2.0		12.7	0.0	0.7	3.3	0.4	16.3	6.3	74	26.2	115.6	30.6	348	36.5	699	291	1.2	7830	84.0	mafic	2007
S 80	215	36.7	1.6	0.4	56.1	1.4	22.8	25.6	8.0	63.2	14.3	124	33.0	112.6	25.7	260	26.6	953	114	0.7	6061	179.8	mafic	~~1950~~
S 78	512	20.2	2.8		8.4	0.2	4.4	8.4	0.7	43.2	14.1	161	56.9	227.7	55.7	592	61.7	1486	315	1.3	7335	218.2	mafic	1923
S 85	188	15.1	1.2	2.8	27.5	2.1	14.3	19.9	12.0	47.7	12.5	127	39.2	151.3	34.0	355	44.3	1123	251	0.6	8549	255.4	felsic	~~1909~~
S 98	297	12.6	1.4		8.3	0.0	1.5	3.3	0.7	17.0	6.1	75	25.5	104.3	26.1	294	30.9	650	165	1.0	7669	87.9	mafic	1896
S 74	342	5.4	1.9	0.1	8.2	0.4	6.4	12.1	1.4	56.7	19.1	209	71.5	271.7	66.4	671	69.4	1810	362	1.3	7655	250.0	mafic	~~1879~~
S 64	203	6.0	2.9	0.1	13.2	0.3	4.7	9.5	1.6	42.5	11.6	132	46.1	174.8	43.0	445	44.8	1143	242	1.6	7417	203.4	mafic	1863
L 48	372	8.0	1.7		3.3	0.1	1.2	3.3	0.2	21.9	8.7	102	36.8	142.3	36.7	409	42.2	978	345	1.2	8068	108.6	felsic	1843
L 23	258	7.4	7.7	1.9	18.3	1.0	8.1	9.7	2.6	38.8	14.8	163	56.2	230.5	56.0	603	61.7	1478	517	3.2	7661	280.9	mafic	~~1833~~
S 97	385	68.2	2.9	3.7	79.9	3.3	20.4	27.9	25.8	77.0	25.3	301	103.4	446.9	98.7	863	157.0	3184	252	1.0	7854	360.1	mafic	~~1821~~
S 111	206	9.5	1.8	0.1	29.7	0.2	1.3	5.4	1.2	19.6	6.2	72	23.8	101.0	24.5	279	32.0	675	181	1.3	7738	153.8	mafic	1807
S 84	376	11.1	2.4	0.2	18.2	0.2	3.1	6.0	1.7	31.2	8.8	118	41.9	170.5	43.0	496	52.7	1082	221	1.1	8185	153.9	felsic	1803
L 57	262	11.2	2.7	0.1	22.8	0.2	2.1	4.1	1.4	21.0	7.4	87	32.7	137.2	35.2	360	46.4	902	275	2.0	9539	194.1	felsic	1801
S 110	363	16.1	1.0		8.0	0.1	3.6	7.2	0.8	36.1	12.3	144	50.3	197.1	45.1	482	55.2	1298	153	0.9	7479	121.5	mafic	1786
L 20	250	10.0	2.0	0.1	19.4	0.1	3.0	4.8	0.5	19.9	7.5	88	30.3	127.2	31.2	367	36.7	820	323	1.6	8134	218.1	felsic	1777
S 86	216	4.9	2.8	0.1	13.9	0.2	2.3	4.5	1.3	20.2	6.0	63	23.9	92.6	23.9	289	29.1	630	275	1.7	7372	177.6	mafic	1776
L 16	603	17.0	0.6		3.0	0.0	1.5	4.1	0.2	24.0	9.2	109	40.7	164.9	42.1	482	45.9	1036	131	0.3	8570	50.7	mafic	1775
L 4	250	8.3	5.4	0.0	9.0	0.2	1.8	4.5	1.0	24.4	9.3	110	40.4	168.1	42.1	437	46.2	1074	281	2.7	8369	163.5	felsic	1771
S 104	756	6.7	1.6	0.1	7.0	0.3	2.5	4.7	2.2	26.3	10.4	149	57.4	262.0	71.2	829	87.5	1566	292	1.5	9194	74.8	felsic	1758
S 66	252	11.2	2.5	0.2	9.4	0.2	3.7	5.9	1.3	30.5	10.1	122	42.2	162.5	41.5	462	44.0	1078	293	1.7	7835	182.2	mafic	1754
L 43	749	14.4	1.1	0.0	6.2	0.1	3.4	9.2	0.5	44.3	16.2	188	65.7	272.1	65.9	719	73.6	1751	204	0.9	8571	116.9	felsic	1751
L 14	564	14.0	2.4	3.3	25.2	1.3	9.4	9.8	1.6	34.7	10.5	111	37.8	159.2	39.6	429	44.7	1031	184	1.2	7328	146.9	mafic	1750
S 93	401	12.8	1.5	0.5	15.8	0.4	6.3	12.1	2.9	38.7	13.0	153	50.5	200.6	52.7	562	56.8	1340	281	1.2	7924	185.3	mafic	1750
S 100	512	12.0	1.0	0.4	8.0	0.3	2.9	5.2	1.1	25.1	10.7	127	43.9	175.4	45.8	501	47.5	1135	334	0.7	8554	142.3	felsic	~~1745~~
L 17	534	11.2	0.9	0.2	5.1	0.2	2.2	3.3	1.8	22.9	9.5	122	46.5	200.9	50.1	579	58.7	1214	243	0.7	9735	80.2	felsic	1742

Zircon	P	Ti	Nb	La	Ce	Pr	Nd	Sm	Eu	Gd	Tb	Dy	Ho	Er	Tm	Yb	Lu	Y	U	Ta	Hf	Th	S.R.	age
L 41	421	14.2	1.4	0.0	9.4	0.0	1.4	3.9	0.6	25.5	9.7	116	39.8	175.7	42.6	455	55.7	1101	180	1.1	9057	108.6	felsic	1737
L 42	1001	9.1	1.8	0.2	4.9	0.3	2.9	10.2	1.9	62.1	20.5	248	78.6	309.0	72.7	765	76.6	2216	439	1.3	9068	107.4	felsic	~~1732~~
L 15	245	20.6	2.0	0.1	14.4	0.6	9.5	15.1	1.7	50.1	15.0	153	48.6	180.4	41.4	466	46.8	1244	124	0.9	7279	162.4	mafic	1731
L 36	262	9.4	3.3	0.4	22.7	0.2	2.6	5.1	0.6	20.8	7.8	91	34.1	138.2	33.4	362	40.5	864	262	2.0	10386	194.9	felsic	1729
L 55	214	4.3	1.4		3.2	0.0	2.4	5.3	0.7	32.3	11.0	117	27.4	75.2	15.2	129	10.3	791	216	0.6	9389	80.3	carb.	1727
S 79	425	11.8	2.9	0.5	13.9	0.1	2.1	3.3	0.7	21.0	8.2	112	39.9	174.1	47.8	519	58.1	1127	233	2.2	9255	121.8	felsic	1723
L 34	284	15.2	2.0	0.0	12.4	0.1	2.1	4.6	0.4	24.4	8.4	108	37.7	155.7	37.6	421	45.0	966	172	1.2	9557	144.1	felsic	1721
L 27	445	12.7	2.5		7.9	0.1	2.0	3.6	0.6	24.6	8.8	104	37.6	155.5	39.5	417	46.3	977	164	1.2	8615	96.5	felsic	1719
L 5	407	15.3	1.6	0.3	7.0	0.3	2.9	5.6	1.0	26.1	8.8	96	36.1	151.5	36.2	411	44.1	967	157	1.3	8442	97.4	felsic	1710
L 31	383	8.2	1.6	0.1	7.8		0.8	3.5	0.1	22.8	8.2	101	37.4	158.6	40.6	441	48.3	962	303	1.0	9907	141.7	felsic	1706
L 13	185	13.3	1.5		5.3	0.0	1.1	2.4	0.5	13.7	4.4	55	20.9	87.3	22.5	255	25.6	548	83	0.8	7299	40.4	mafic	1700
L 39	574	6.9	1.7	0.1	5.7	0.1	1.2	4.3	0.4	23.5	9.3	127	50.0	222.3	55.7	656	67.9	1289	288	1.2	9003	110.6	felsic	1700
S 105	205	8.1	2.5		10.8	0.1	1.2	3.9	0.3	19.6	7.4	80	28.5	114.0	30.5	323	34.1	741	273	1.4	8006	135.0	felsic	1693
L 6	784	16.7	3.0	2.6	16.0	1.6	13.0	18.7	9.3	67.5	20.9	240	80.2	309.6	74.6	802	80.7	2119	460	1.7	9584	201.8	felsic	~~1681~~
S 119	278	38.8	1.0	0.5	13.6	0.6	4.5	7.6	2.8	33.7	11.6	146	52.7	219.5	48.9	430	68.1	1427	112	0.8	7993	152.0	mafic	1862
S 124	272	13.3	1.2		6.8	0.1	3.4	4.6	1.1	29.3	7.6	99	32.1	133.3	31.9	362	35.3	868	151	0.9	7080	94.5	mafic	1692
S 87	493	21.3	3.4	5.1	43.3	3.4	24.0	34.0	20.9	95.0	25.2	220	57.8	181.1	42.0	424	40.4	1665	616	1.1	6478	445.1	mafic	~~2735~~
L 7	230	12.2	4.2	1.4	39.3	1.4	8.0	10.0	6.4	29.0	9.2	87	29.2	124.1	31.8	378	43.9	821	251	1.5	8393	139.1	felsic	~~2569~~
S 94	245	62.4	3.7	1.7	28.6	1.9	11.3	14.8	10.2	37.0	10.1	113	34.2	133.9	31.2	321	37.7	942	221	2.0	8260	266.9	felsic	~~2561~~
S 71	277	18.4	4.0	3.7	43.0	2.8	21.5	24.8	15.0	84.5	23.9	277	87.8	335.8	72.5	652	86.5	2453	366	1.7	8387	396.3	felsic	~~2546~~
S 101	480	35.2	2.8	4.2	27.1	2.7	18.5	23.2	17.0	63.1	18.3	177	51.8	202.3	56.8	663	66.3	1455	467	1.7	7558	175.0	mafic	~~2214~~
L 38	567	118.6	11.4	58.4	283.6	36.8	190.0	141.6	274.0	228.7	56.3	430	112.4	376.1	88.1	920	91.6	3176	1433	9.4	9868	959.4	felsic	~~2063~~
S 121	391	14.4	2.8	3.2	35.9	1.9	16.4	15.9	8.7	38.9	11.7	127	40.3	167.7	43.1	525	54.6	1077	362	1.8	8160	228.4	felsic	~~2062~~
L 26	602	33.0	2.9	0.9	16.9	0.9	8.6	16.5	4.6	52.3	17.8	185	61.0	241.3	56.5	607	67.0	1598	251	1.6	6778	204.1	mafic	~~1939~~
S 112	439	119.6	3.2	246.0	357.2	34.0	142.3	28.6	7.9	35.9	10.1	118	35.6	152.7	35.5	352	39.3	1032	198	0.9	5798	116.8	mafic	~~1911~~
L 53	218	24.2	1.1	3.2	16.1	1.8	11.0	14.8	11.4	44.4	11.2	81	21.3	69.9	14.3	129	10.2	588	484	0.2	9684	130.7	carb.	~~1892~~
S 92	541	22.8	3.3	2.6	34.4	3.0	24.1	40.2	26.5	134.5	32.2	289	76.5	262.9	56.1	534	58.0	2276	370	2.0	8543	234.2	felsic	~~1840~~
L 58	420	24.0	3.7	2.9	26.3	2.1	14.8	17.9	12.8	51.1	17.6	179	54.0	203.1	52.4	566	57.3	1487	488	1.8	9598	194.6	felsic	~~1822~~
S 76	225	31.2	2.8	3.4	38.9	2.1	13.4	12.9	16.2	29.2	9.8	101	35.6	154.2	42.4	457	60.6	1032	328	1.5	10530	264.4	felsic	~~1821~~
L 56	338	18.7	3.6	1.6	38.9	1.9	13.1	25.4	10.4	68.8	21.1	184	57.4	223.5	55.7	606	68.4	1607	565	1.5	8021	578.5	felsic	~~1784~~
L 30	337	82.3	4.5	3.7	68.3	2.7	16.6	21.3	19.4	65.2	19.3	220	76.2	324.7	75.3	727	105.7	2243	443	2.4	10933	432.3	felsic	~~1759~~
L 37	2071	26.7	6.9	48.1	151.4	21.7	122.6	92.5	32.6	155.5	46.0	368	82.7	278.1	65.4	654	61.0	2131	803	3.9	9471	337.4	felsic	~~1743~~
L 1	1290	17.3	2.2	17.8	38.7	6.0	28.3	24.2	20.4	69.0	28.1	347	130.3	545.7	139.8	1461	156.2	3312	736	1.6	11445	237.9	felsic	~~1731~~

All trace element data was collected with the mean count method. Analyses that intersected inclusions of other minerals were rejected based on time resolved P and Ti analyses and not included in this table. Backgrounds were monitored between sweeps 10 - 20. Sample counts integrated from sweeps 28 - 54. Radiometric ages with strike through are >10 % discordant and were not used in the characterization of the source rocks.

3.5.3. Hafnium isotopes

Table 3.4. Zircon hafnium isotope data

Sample	$^{176}Lu/^{177}Hf$	± 1σ	$^{176}Hf/^{177}Hf$	± 1σ	Age Ga	$^{176}Hf/^{177}Hf_T$	$^{176}Hf/^{177}Hf_{Ch}$	εHf_T	± 2σ	Tdm Ga
721-40.1	7.20E-04	4.10E-06	0.281528	3.50E-05	1.75	0.2815041	0.2816710	-5.92	2.51	2.48
721-26.1	3.97E-04	3.70E-05	0.281401	3.80E-05	1.91	0.2813866	0.2815626	-6.25	2.81	2.63
721-31.1	7.48E-04	1.40E-05	0.281674	4.40E-05	1.76	0.2816490	0.2816600	-0.39	3.17	2.22
721-39.1	3.33E-04	8.50E-06	0.281232	3.00E-05	2.45	0.2812164	0.2812130	0.12	2.17	2.73
721-13.1	1.07E-03	1.90E-05	0.281764	2.50E-05	1.72	0.2817292	0.2816905	1.37	1.83	2.10
721-1.1	1.05E-03	6.90E-06	0.28159	3.30E-05	1.75	0.2815551	0.2816697	-4.07	2.37	2.39
721-122.1	1.26E-03	1.60E-05	0.281561	4.60E-05	1.70	0.2815202	0.2816989	-6.34	3.31	2.47
721-82.1	7.02E-04	7.70E-06	0.281674	3.60E-05	1.67	0.2816518	0.2817235	-2.54	2.59	2.25
721-81.1	9.18E-04	9.20E-06	0.281623	3.70E-05	1.75	0.2815925	0.2816704	-2.76	2.66	2.33
721-114.1	1.58E-03	4.70E-05	0.280681	3.80E-05	3.13	0.2805861	0.2807657	-6.40	2.91	3.59
721-102.1	9.51E-04	1.00E-05	0.281612	3.70E-05	1.69	0.2815815	0.2817073	-4.47	2.66	2.37
721-96.1	7.95E-04	5.20E-06	0.281595	3.70E-05	1.78	0.2815681	0.2816470	-2.80	2.65	2.36
721-75.1	7.98E-04	5.10E-06	0.281624	3.90E-05	1.66	0.2815988	0.2817261	-4.52	2.79	2.35
721-127.1	6.40E-04	1.30E-05	0.281491	3.00E-05	1.73	0.2814700	0.2816807	-7.48	2.18	2.55
719-4.1	3.29E-04	2.80E-05	0.281086	2.70E-05	1.97	0.2810737	0.2815262	-16.07	2.01	3.16
719-11.1	2.81E-03	2.20E-04	0.281764	4.30E-05	1.74	0.2816710	0.2816730	-0.07	3.58	2.19
719-2.1	9.36E-04	2.60E-05	0.281569	3.00E-05	1.79	0.2815373	0.2816464	-3.87	2.21	2.41
719-3.1	7.91E-04	9.00E-06	0.281582	5.10E-05	1.77	0.2815555	0.2816587	-3.67	3.65	2.38
719-33.1	1.54E-03	1.70E-05	0.281518	2.70E-05	2.07	0.2814574	0.2814604	-0.10	1.98	2.45
719-30.1	9.22E-04	4.80E-05	0.281606	2.50E-05	1.74	0.2815755	0.2816743	-3.51	1.90	2.36
719-29.1	1.63E-03	2.00E-05	0.281508	3.30E-05	2.03	0.2814451	0.2814858	-1.44	2.41	2.48
719-25.1	1.12E-03	2.40E-05	0.281353	3.30E-05	1.74	0.2813159	0.2816730	-12.68	2.41	2.82
719-23.1	6.97E-04	2.40E-05	0.281335	4.30E-05	1.74	0.2813120	0.2816769	-12.95	3.12	2.82
719-20.1	8.40E-04	1.40E-05	0.281539	4.10E-05	1.73	0.2815114	0.2816801	-5.99	2.96	2.47
719-37.1	1.26E-03	7.10E-05	0.281494	2.80E-05	1.92	0.2814481	0.2815613	-4.02	2.19	2.52
719-49.1	9.41E-04	9.30E-06	0.281617	2.70E-05	1.80	0.2815848	0.2816367	-1.84	1.96	2.32
719-48.1	1.03E-03	9.40E-06	0.281497	2.90E-05	1.77	0.2814625	0.2816581	-6.94	2.10	2.55
719-50.1	8.07E-04	8.50E-06	0.281601	2.70E-05	1.74	0.2815743	0.2816736	-3.53	1.95	2.36
719-53.1	8.43E-04	5.00E-05	0.281605	3.00E-05	1.73	0.2815773	0.2816807	-3.67	2.26	2.36

εHf calculated using Söderlund et al. (2004) and Bouvier et al. (2008) for the lutetium decay constant and lutetium and hafnium chondrite data. $^{176}Hf/^{177}Hf_T$ = the $^{176}Hf/^{177}Hf$ value during zircon crystallization. $^{176}Hf/^{177}Hf_{Ch}$ = the chondritic $^{176}Hf/^{177}Hf$ value during zircon crystallization. εHf_T = the εHf signature during zircon crystallization. Model ages (Tdm) were calculated using a $^{176}Lu/^{177}Hf$ ratio of 0.01.

Hafnium isotope data were obtained on zircon that was analysed for U-Pb ages via SHRIMP-II and yielded $^{207}Pb/^{206}Pb$ ages that were < 5% discordant. All data are reported in Table 3.4. All of the grains have crystallization ages << model ages, consistent with derivation from an evolved source. For 29 of the zircon grains that were dated via SHRIMP εHf(t) ranges from 0 to – 16. Two-stage depleted mantle model ages for 18 zircons of 1.78 – 1.68 Ga ranges between 2.82 – 2.10 Ga. Two younger grains of 1.67 and 1.66 Ga have depleted mantle model ages of 2.25 and 2.35 Ga. Older grains are 3.13 – 1.79 Ga and have depleted mantle model ages of 3.59 – 2.32 Ga.

3.5.4. Whole rock geochemistry

Three samples of soft-sediment conglomerate were analysed for whole rock major and trace elements (Table 3.5). Trace element spectra overlap with values for average upper crust (Rudnick and Gao, 2014), with moderate depletion of Zn and Cu, and enrichment of Rb (Figure 3.9). Values of U and Ba are variable and moderately enriched to depleted. These variations are due to regolith formation, recent weathering, metasomatism, or a combination of these processes. The volatile content (loss on ignition, LOI) ranges from 6.18% - 12.15 % and appears to correlate with the abundance of veinlets.

Table 3.5. Whole rock geochemistry of soft-sediment conglomerate

Analyte (%)	SiO_2[1]	$Al2O_3$[1]	Fe_2O_3[1]	MnO[1]	MgO[1]	CaO[1]	Na_2O[1]	K2O[1]	TiO_2[1]	P_2O_5[1]	LOI[1]	S[3]	Total
Detection Limit	0.01	0.01	0.01	0.001	0.01	0.01	0.01	0.01	0.001	0.01		0.001	0.01
Absolute error	0.3	0.2	0.25	0.04	0.1	0.5	0.15	0.3	0.4	0		0.1	
Relative error (%)	1.5	1	1	6	1	1	2	11	12	1		1	
JV12-11-1-2A	57.52	7.69	4.85	0.424	5.6	7.36	0.1	3.56	0.418	0.22	12.15	0.076	99.9
JV12-14-ch	51.34	14.02	13.62	0.072	5.75	2.97	0.09	4.71	0.554	0.16	6.18	0.015	99.47
JV12-15m	53.08	12.06	9.35	0.126	5.75	4.81	0.26	5.03	0.551	0.15	9.18	0.024	100.4

Analyte (ppm)	Au[2]	Ag[2/3]	As[2]	Ba[1]	Be[1]	Bi[4]	Br[2]	Cd[3]	Co[2]	Cr[2]	Cs[4]	Cu[3]	Ga[4]
Detection Limit	0.001	0.5	1	1	1	0.1	0.5	0.5	0.1	0.5	0.1	1	1
Absolute error	n/a	n/a	2	2	1	1.5	n/a	0.5	1	3	0.3	2	1
Relative error (%)	n/a	n/a	5	4	2	1	n/a	1	4	10	3	4	1
JV12-11-1-2A	< 1	< 0.5	13	1966	2	0.2	< 0.5	< 0.5	9.2	28.8	2.1	2	10
JV12-14-ch	< 1	< 0.5	11	267	3	1.4	< 0.5	< 0.5	19.2	56	3.2	3	20
JV12-15m	0.003	< 0.5	11	399	2	0.4	< 0.5	< 0.5	17.3	55.6	3	< 1	16

Analyte (ppm)	Ge[4]	Hf[4]	Hg[2]	In[4]	Ir[2]	Mo[4]	Nb[4]	Ni[3]	Pb[3]	Rb[4]	Sb[2]	Sc[2]	Se[2]
Detection Limit	0.5	0.1	1	0.1	0.001	2	0.2	1	5	1	0.1	0.01	0.5
Absolute error	0.7	0.7	n/a	n/a	n/a	0.3	0.8	2	7	2	0.3	0.3	n/a
Relative error (%)	1	5	n/a	n/a	n/a	2.5	11	10	2	3	2	2	n/a
JV12-11-1-2A	1.6	2.3	< 1	< 0.1	< 1	< 2	6.2	17	< 5	137	8	7.6	< 0.5
JV12-14-ch	2.2	2.5	< 1	< 0.1	< 1	< 2	9.5	46	13	189	6.9	13.4	< 0.5
JV12-15m	1.8	3	< 1	< 0.1	< 1	< 2	9.1	28	< 5	195	6.5	10.9	< 0.5

Analyte (ppm)	Sn[4]	Sr[1]	Ta[4]	Th[4]	U[4]	V[1]	W[2]	Y[1]	Zn[2/3]	Zr[1]	La[4]	Ce[4]	Pr[4]
Detection Limit	1	2	0.01	0.05	0.01	5	1	1	1	1	0.05	0.05	0.01
Absolute error	1	2	0.3	1	0.5	1	n/a	3	5	2	2	3	0.2
Relative error (%)	0.5	2.5	2	7.5	3	5	n/a	7	9	7	11	11	8
JV12-11-1-2A	2	57	0.86	9.3	2.18	49	< 1	15	10	118	61.5	120	13.4
JV12-14-ch	3	24	0.97	15	8.49	100	< 1	18	39	125	57.6	103	10.9
JV12-15m	3	25	0.98	14.7	5.35	76	< 1	22	9	157	59	104	11.3

Analyte (ppm)	Nd[4]	Sm[4]	Eu[4]	Gd[4]	Tb[4]	Dy[4]	Ho[4]	Er[4]	Tl[4]	Tm[4]	Yb[4]	Lu[4]	
Detection Limit	0.05	0.01	0.005	0.01	0.01	0.01	0.01	0.01	0.05	0.005	0.01	0.002	
Absolute error	1.5	0.4	0.5	0.5	0.3	0.8	0.2	0.5	0.5	0.5	0.2	0.3	Mass[2]
Relative error (%)	4	6	1	16	7	4	5	5	8	1	4	1	(g)
JV12-11-1-2A	48.2	8.05	1.18	4.86	0.61	3.28	0.6	1.67	0.23	0.237	1.57	0.231	1.251
JV12-14-ch	37.4	6.42	1.61	5.07	0.88	4.5	0.89	2.46	0.26	0.366	2.27	0.332	1.176
JV12-15m	39.3	6.65	1.55	5.24	0.81	4.46	0.88	2.47	0.24	0.375	2.28	0.341	1.151

Analysed via [1]: Inductively coupled plasma mass spectrometry on diluted fused lithium meta-/tetraborate sample (using a Varian Vista ICP), [2]: Instrumental neutron activation analysis, [3]: Inductively coupled plasma mass spectrometry on (near) total digested sample, [4]: Inductively coupled plasma mass spectrometry on diluted fused lithium meta-/tetraborate sample (using a Perkin Elmer Sciex ICP/MS). Absolute and relative errors were assessed graphically using measurements of duplicates and standards error envelopes following Nielsen, 2011. N/a indicates a lack of data points to envelop. UTM NAD 1983 locations: JV12-11-1-2A: 636061E, 7217574N, JV12-14-ch: 578059E, 7182329N, JV12-15m: 577156E, 7180858N.

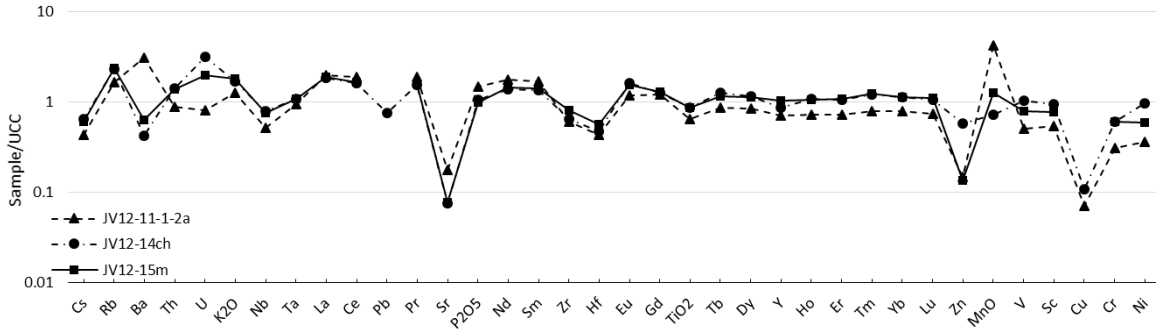

Figure 3.9. Selected elements and oxide concentrations normalized to average upper crust (Rudnick and Gao, 2014)

3.5.5. Neodymium isotopes

Three samples of soft-sediment conglomerate were analysed for samarium and neodymium isotopes. εNd_0 values range from –24.89 to -25.61 and εNd_i ranges from -5.32 to -5.68. Neodymium isotope model ages T_{DM} are 2.43 – 2.26 Ga with ε_{Ndi} = -5.32 to -5.68 for 1.6 Ga (Figure 3.10). The data are reported in Table 3.6. The εNd values indicate sediment derivation from evolved crust, and will be further discussed in the following section.

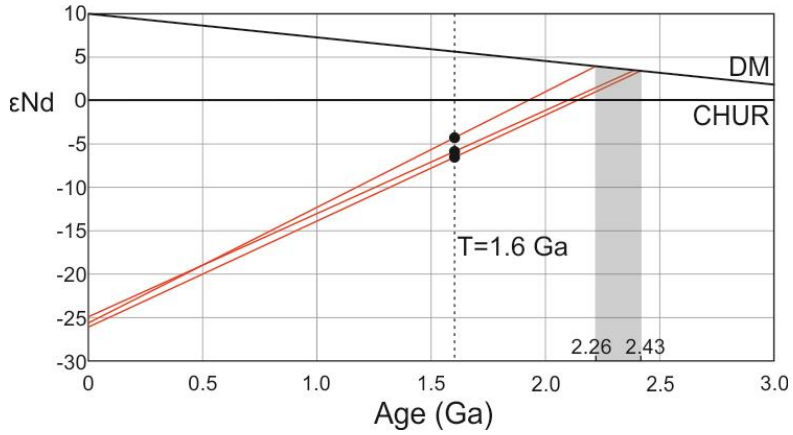

Figure 3.10. Sm-Nd isotope analysis indicates that the soft sediment conglomerate was at least in part derived from evolved crust. Sample locations provided in Table 3.5.

Table 3.6. Sm-Nd isotope ratios

Sample	Age (Ga)	Sm (ppm)	Nd (ppm)	$^{143}Nd/^{144}Nd$ measured	$^{147}Sm/^{144}Nd$ measured	$^{143}Nd/^{144}Nd$ initial	$^{143}Nd/^{144}Nd$ $CHUR_T$	$^{143}Nd/^{144}Nd$ $CHUR_{act}$	εNd_i	εNd_{act}	T_{DM}
11-1-2a	1.6	8.05	49.79	0.511325	0.0997	0.510297	0.510568	0.512638	-5.32	-25.61	2.26
15m	1.6	6.65	41.78	0.51130	0.1044	0.510288	0.510568	0.512638	-5.50	-26.10	2.43
14ch	1.6	6.42	37.68	0.511362	0.1059	0.510279	0.510568	0.512638	-5.68	-24.89	2.38

The current value for the chondritic uniform reservoir ($CHUR_{ACT}$) was taken from White (2009). Sm-Nd model ages (T_{DM}) were calculated following methods in DePaolo (1981). εNd_i refers to the initial εNd value, εNd_{act} refers to the current εNd value.

3.6. Discussion

3.6.1. Basin formation after Racklan Orogeny

The onset of WOUS deposition is bracketed in age between the end of the Racklan Orogeny at ca. 1.6 Ga (Furlanetto et al., 2013; 2016) and Wernecke Breccia formation at 1.599 Ga (Furlanetto et al., 2013). The well-bedded and fine-grained nature of the sediments indicates low-energy sedimentary environments, and restricted accommodation space or sediment supply. The character of the sediment is consistent with deposition in a lacustrine or shallow marine environment.

The soft sediment conglomerate formed from the unlithified sediments during brecciation. Large (>2m) well-bedded clasts of the WOUS grade into soft sediment conglomerate and then into hematitic breccia (Verbaas et al., 2014). In addition, this transitional boundary contains clasts derived from both the Wernecke Supergroup and Bonnetia. This transitional contact and the mixing of clasts within it indicates that the soft-sediment conglomerate formed where the fragments and fluidal patches of the WOUS descended into the breccia zones.

3.6.2. Lack of known proximal sources of 1.78 – 1.68 Ga zircon

The abundance of sub-angular zircon in the age range 1.78 – 1.68 Ga is consistent with a restricted proximal source of sediment with only minor addition of older sources.

Major detrital zircon populations from cratonic elements in Laurentia are present in the Wernecke Supergroup (Furlanetto et al., 2016) but are absent in the WOUS. Sources of 1.78 – 1.68 Ga zircon on Laurentia (Figure 3.11) include igneous rocks in the Yavapai orogen (cf. Whitmeyer and Karlstrom, 2007), the hypothetical Big White arc on southwestern Laurentia (Link et al., 2016), intrusive and extrusive rocks of the Kivalliq igneous suite (1.77 – 1.73 Ga) in the Thelon basin (Rainbird et al., 2003; Peterson et al., 2015) and metamorphic and magmatic units in the 1.71 – 1.62 Ga Labradorian orogen on the northeastern margin of Laurentia (Kamo et al., 1996).

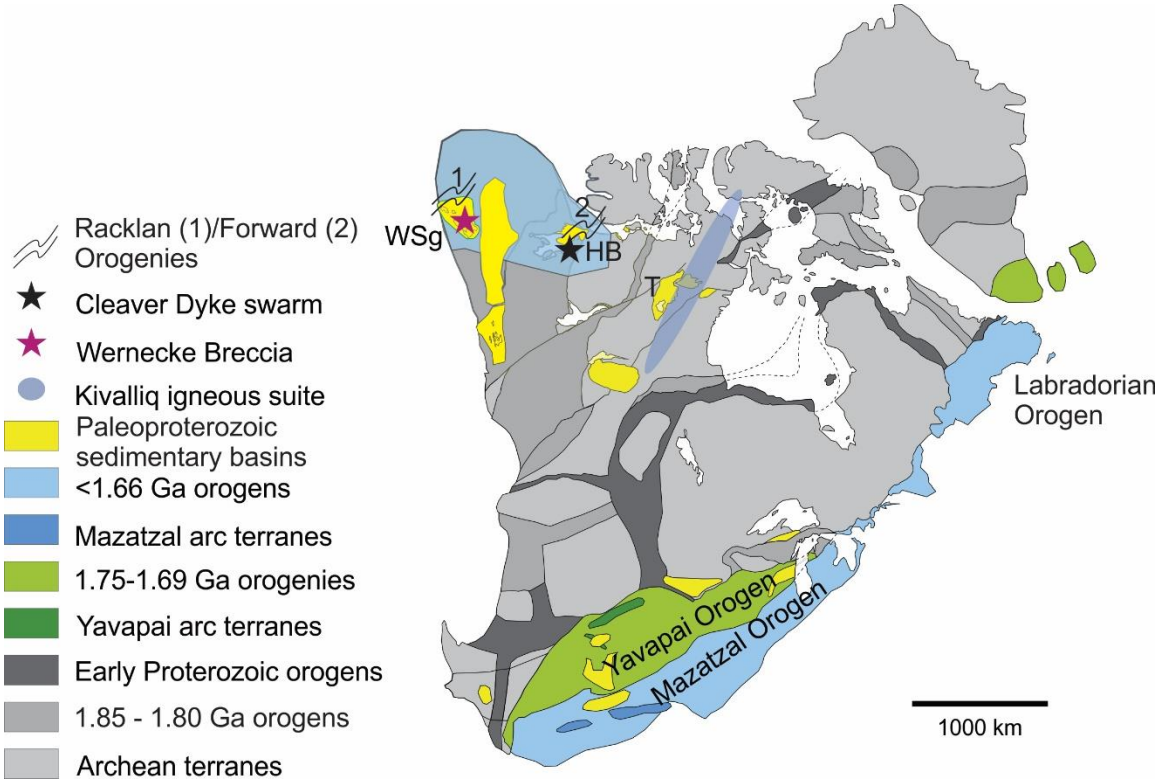

Figure 3.11. Location of Paleoproterozoic elements and Wernecke Breccia on Laurentia. HB: Hornby Bay basin, T: Thelon Basin, WSg: Wernecke Supergroup (modified from Hoffman, 1988; Furlanetto et al., 2016).

The Yavapai Orogeny resulted from the accretion of juvenile ca. 1.75 Ga crust to the southeastern margin of Laurentia (cf. Whitmeyer and Karlstrom, 2007). Based on Nd model ages and Pb isotopes the Yavapai terrane is juvenile (DePaolo, 1981; Aleinikoff, 1993) apart from local anomalies (Hill and Bickford, 2001). The juvenile character of Yavapai-derived zircon is inconsistent with the evolved hafnium signature of zircon in the WOUS. Additionally, it is unlikely that zircon traveled from the Yavapai orogeny or the

Labradorian orogeny, to northwestern Laurentia several thousand kilometres away without significant addition of zircon from other Laurentian sources. Zircon interpreted to be derived from the Yavapai terrane zircon are present within the Wernecke Supergroup (Furlanetto et al., 2016), but are notably more rounded and smaller than the zircon in the WOUS. In addition to Yavapai-derived zircons, small populations of zircon interpreted to be derived from Mazatzal arc rocks that accreted ca. 1.68 - 1.65 Ga in the southeastern US (Condie, 1992; Whitmeyer and Karlstrom, 2007) are present in the Wernecke Supergroup, but are also small and well-rounded (Furlanetto et al., 2016).

Link et al. (2016) proposed that a large magmatic arc, called the Big White arc, formed along southwestern Laurentia. The Big White arc was hypothesized to be a major source for sediment for parts of the Belt Basin (Link et al. 2016). They suggested that the arc was built upon the Yavapai and Mojave provinces prior to 1.7 Ga. The arc provided huge volumes of sediment with zircon ages predominantly from 1.78 – 1.71 Ga and with εHf(t) of +8 to -7, and was completely eroded in the process (Link et al. 2016). Detrital zircon of the Big White arc could also have been transported to northwestern Laurentia at ca. 1.6 Ga and could have contributed zircon to the WOUS. However, the εHf(t) of 0 to –12 of the WOUS makes the Big White Arc an unsuitable source. Furthermore, if zircon from that arc were transported >3000 km to northwestern Laurentia, zircon with a broader range of εHf(t) and crystallization ages would be expected from the addition of sediment from other Laurentian sources en route. Instead, the range of εHf(t) of zircon in the WOUS is smaller than that of the Big White Arc. In addition, preservation of subangular facets for the majority of zircon in the WOUS is not consistent with such a distal source. Nevertheless, the Big White arc serves as an example of a major source region that previously resided along the western margin of Laurentia but which is no longer present, and in that regard is similar to Bonnetia. It is possible that the Big White arc did not form on Laurentia but instead was part of Australia, Bonnetia or another intervening terrane.

The 1.77 – 1.73 Ga Kivalliq igneous suite (Rainbird et al., 2003; Peterson et al., 2015) is another potential source for the WOUS. However, this igneous suite is partially interlayered with strata of the Thelon basin (Rainbird et al., 2003). These strata contain major populations of Paleoproterozoic and Archean detrital zircon (Rainbird and Davis, 2007), that are notably absent in the WOUS. Hence the Kivalliq igneous suite can be ruled

out as a source of zircon for the WOUS. The Cleaver dyke swarm located on the Canadian Shield east of Great Bear Lake is dated at 1.74 Ga using U-Pb on baddeleyite (Irving et al., 2004). These dykes are not known to contain zircon, making them an unlikely source for zircon in the WOUS.

The WOUS formed prior to the Wernecke Breccia at 1.6 Ga. Hence there are no NAMG-aged (1.6 – 1.49 Ga) zircon in this succession which would signify a non-Laurentian source. However, the lack of local zircon sources for the 1.78 – 1.68 Ga detrital zircon peak in the WOUS may indicate a non-Laurentian source. NAMG-aged zircon are present in this area in the younger PR1 basin, which formed at approximately 1.45 Ga (Medig et al., 2014) and unconformably overlies the Wernecke Supergroup and Wernecke Breccia. The occurrence of zircon from non-Laurentian sources in the PR1 basin and the 1.78 – 1.68 Ga zircon peak in the WOUS imply that a non-Laurentian source of sediment was present along the western Laurentian margin for approximately 150 Myr, from ca.1.6-1.45 Ga.

3.6.3. Orogenic events on the margin of northwestern Laurentia

Because of the lack of suitable Laurentian sources of sediment, sources on other continents must be considered. Laurentian-derived sediments were deposited in the Wernecke Supergroup sometime during the interval 1.66-1.60 Ga (Furlanetto et al., 2016). The WOUS, with non-Laurentian derived zircon, is encased within the 1.599 Ga Wernecke Breccia, and hence a sediment source must have been introduced to Laurentia during the interval 1.66 Ga - 1.599 Ga. There were at least two contractional events on northwestern Laurentia that occurred close to the Paleo- to Mesoproterozoic boundary during which sedimentary sources may have been juxtaposed to the margin of Laurentia.

The first contractional event was the first phase of the Forward Orogeny. Most structures of the Forward Orogeny strike NNE-SSW and the principal horizontal stress was oriented ENE-WSW (Cook and Maclean, 1995). The Forward orogeny consisted of two phases of thick-skinned deformation and resulted in basin inversion of the Coppermine homocline, approximately 750 km ENE of our study area (Cook and Maclean, 1995). The first pulse of deformation occurred during eruption of the syn-tectonic 1663 Ma

Narakay volcanics (Bowring and Ross, 1985). The second contractional event includes the second phase of the Forward Orogeny in the Northwest Territories, and the Racklan Orogeny in Yukon (Furlanetto et al., 2016). The Racklan Orogeny occurred after sedimentation of the Wernecke Supergroup (>1.66 Ga, Furlanetto et al., 2013; 2016) and was apparently over by the time of Wernecke Breccia formation at 1.599 Ga (Furlanetto et al., 2013). The Forward Orogeny was complete by 1.59 Ga (Hamilton and Buchan, 2010).

The Racklan Orogeny deformed the Wernecke Supergroup and consisted of two pulses of deformation and fabric formation during greenschist facies metamorphism. Racklan deformation and metamorphism resulted from collisional tectonics along the northwestern margin of Laurentia (present day coordinates, Thorkelson et al., 2005; Furlanetto et al., 2013). The first pulse resulted in east-verging structures (Thorkelson, 2000). The second pulse of deformation resulted in south-verging structures (Thorkelson, 2000), and has been related to the obduction of Bonnetia (Furlanetto et al., 2013). The deposition of the Wernecke Supergroup, followed by orogenesis and terrane obduction indicates that, at the end of the late Paleoproterozoic, northwestern Laurentia changed from a passive margin to a collisional margin as a result of closure of an oceanic basin (Furlanetto et al., 2013; Nielsen et al., 2013; Thorkelson and Laughton, 2016).

3.6.4. Evidence for Paleoproterozoic to Mesoproterozoic Laurentia – Australia interactions

A Proterozoic connection between western Laurentia and another landmass during the existence of the supercontinent Columbia has been envisioned in several different configurations and at different times (e.g., Sears and Price, 1978; Bell and Jefferson, 1987; Ross et al., 1992; Thorkelson et al., 2001a; Zhao et al., 2004; Giles et al., 2004; Hou et al., 2008). Many researchers reconstruct Columbia with a connection between western Laurentia and Australia based on paleomagnetism, and coeval hydrothermal provinces, anorgenic granite provinces, orogenic events and sedimentation, and detrital zircon provenance (Thorkelson et al., 2001a; Zhao et al., 2002; Rogers and Santosh, 2002; Goodge et al., 2008; Payne et al., 2009; Evans and Mitchell, 2011; Pisarevsky et al., 2014; Furlanetto et al., 2016). Although numerous studies from Laurentia and

Australia/Antarctica demonstrate close intercontinental relations over hundreds of m.y., the exact nature and timing of convergence, divergence and other kinds of interactions remain uncertain (Goodge et al., 2017). The North Australia Craton, Gawler Craton of southern Australia and the Terre Adelie Craton of Antarctica were contiguous during the existence of the supercontinent Columbia and are collectively called the Mawson continent (Figure 3.12; Payne et al., 2009; Howard et al., 2011; Goodge and Fanning, 2010; 2016; Betts et al., 2016). Other proposed conjugates of western Laurentian include Siberia (Sears and Price, 1978, 2002) and north China (Hou et al., 2008). As noted in Boger and Hansen (2004), Betts et al. (2006, 2008) and Payne et al. (2009), the structural history of Australia/Antarctica is complicated and geographically variable. However, the similarities among different parts of Australia/Antarctica and Laurentia continue to provide compelling reasons to link the continents and to propose common belts of orogenic activity, even though details are not entirely understood (Dalziel, 2013; Gibson et al., 2017; Goodge et al., 2017)

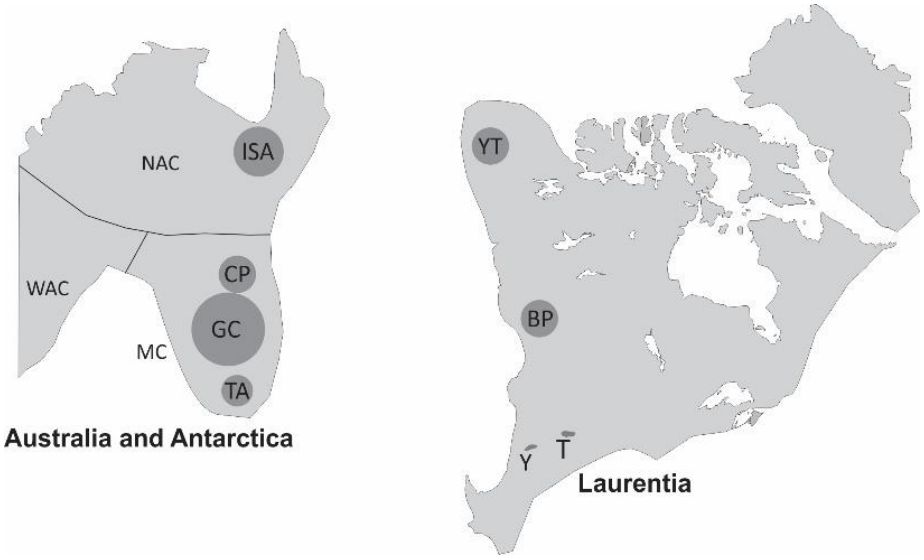

Figure 3.12. Regions containing Proterozoic rocks on Laurentia and Australia that are discussed in the text in dark grey. Abbreviations are NAC: North Australian Craton, ISA: the Mt. Isa Inlier. WAC: Western Australia Craton (not further discussed in the text). MC: Mawson Continent after Payne (2009), GC: Gawler Craton (Australia), CP: Curnamona Province (Australia), TA: Terre Adelie Craton (Antarctica) YT: Yukon Territory, BP: Belt Purcell basin, Y: Yankee Joe basin, T: Trampas basin.

Detrital zircon of the Belt Purcell Supergroup, Yankee Joe and Trampas Basin in the western and southern US and of sedimentary successions in Yukon have revealed non-Laurentian, likely Australian provenance around 1.45 Ga (Ross et al., 1992; Medig et al., 2014; Jones et al., 2015). Sediments deposited after 1.45 Ga have a Laurentian provenance (Jones et al., 2015; Medig et al., 2016), indicating that there was no sedimentary link between Australia and Laurentia after 1.45 Ga, at least until they were reconnected in Rodinia in the late Mesoproterozoic to Neoproterozoic (Moores, 1991; Li et al., 2008). How Australia and Laurentia were reconnected remains unclear but may relate to modest but widespread Grenville-age magmatic and metamorphic activity along western Laurentia (Milidragovic et al., 2011).

3.6.5. Sedimentary successions as clasts in hematitic breccias on Laurentia and the Gawler Craton

The Gawler Craton occurs in current southeastern Australia and hosts hydrothermal hematitic breccias within Paleo- Mesoproterozoic rocks (Skirrow et al., 2009). The similarity of the Wernecke Breccia zones to the Olympic Dam Breccia Complex on the Gawler Craton was noted by several researchers (Bell and Jefferson, 1987; Bell, 1989; Gandhi and Bell, 1990; Hitzman et al., 1992) and evidence for a continuous hydrothermal province at ca. 1.6 Ga was established by Thorkelson et al. (2001b). On the Gawler Craton, IOCG hydrothermal activity was present from 1604 ± 9 – 1567 ± 10 Ma (based on titanite and zircon U-Pb ages summarized in Reid et al., 2013). During this interval, the Olympic Dam Breccia Complex formed. At the time of brecciation, a sedimentary succession consisting of well-bedded green and red mudstone, conglomerate and sandstone is inferred to have overlain this part of the Gawler Craton (McPhie et al., 2011; 2016). The presence of this succession was based on clasts of sedimentary rock within the Olympic Dam Breccia Complex (McPhie et al., 2011). The source of sedimentary rock within the Olympic Dam Breccia Complex is here referred to as the “Olympic Dam strata.” McPhie et al. (2011, 2016) argued that clasts of the Olympic Dam strata foundered into the Olympic Dam Breccia Complex from an overlying succession.

The Olympic Dam strata consist of sandstone and red mudstone, green sandstone and mudstone, polymictic volcanic conglomerate, and well-sorted quartz-rich sandstone (McPhie et al., 2011; 2016). The former three units all contain a near unimodal detrital zircon population that was sourced from the 1.59 Ga Gawler Range Volcanics (McPhie et al., 2016). Detrital zircon from the well-sorted quartz-rich sandstone include large populations of ca. 1590 Ma, ca. 1740 Ma, and minor populations from 2100 – 1740 Ma and 2600 – 2400 Ma, and an absence of zircon from 2400 – 2100 Ma (McPhie et al., 2016). A small population of zircon older than 2600 Ma is also evident.

McPhie et al. (2016) interpreted detrital zircon from the well-sorted quartz-rich sandstone to be sourced from the Gawler Craton. In particular, the 2.6 – 2.4 Ga detrital zircon were sourced from the Sleaford and Mulgathing complexes on the Gawler Craton (Hand et al., 2007; McPhie et al., 2016). Potential zircon sources for the 1.78 – 1.68 Ga zircon are metasedimentary rocks in the Fowler domain, Mt. Woods domain, Nawa domain, Willyama Group, and Wallaroo Group (Page et al., 2005a, b; Payne et al., 2006; Jagodzinski et al., 2007; Hand et al., 2007; Chalmers et al., 2007; Fanning et al., 2007; Howard et al., 2011a; McPhie et al., 2016), and Archean and Paleoproterozoic igneous rocks on the Gawler Craton (Cowley and Fanning, 1991; Fanning et al., 2007).

A comparison of isotopic data reveals striking similarities between the WOUS and data compiled from the Gawler Craton. Hafnium isotope data is not available for the detrital zircon of the well-sorted sandstone clasts from the Olympic Dam Breccia Complex. However, many εHf(t) analyses from the Gawler Craton zircon are available and are displayed in Fig. 13A. The εHf(t) values from 1.78 – 1.68 Ga detrital zircon in Paleoproterozoic sedimentary successions on the Gawler Craton indicate a wide range of values from moderately juvenile to highly evolved (Belousova et al., 2006; 2009; Howard et al., 2009, 2011a,b; Szpunar, 2011). In order to enable a comparison of the εHf(t) and U-Pb data of zircon from the soft sediment conglomerate and those from the Gawler Craton, data from the WOUS are also plotted on Figure 3.13A. The εHf(t) values of 1.78 – 1.68 Ga zircon from the WOUS are also moderately juvenile to evolved. Additionally 2.0 – 1.8 Ga zircon and one 2.5 Ga zircon have εHf(t) that overlap with high abundances of similar zircon on the Gawler Craton. Whole rock Nd isotopic ratios are also similar to data compiled from the Gawler Craton (Figure 3.13B).

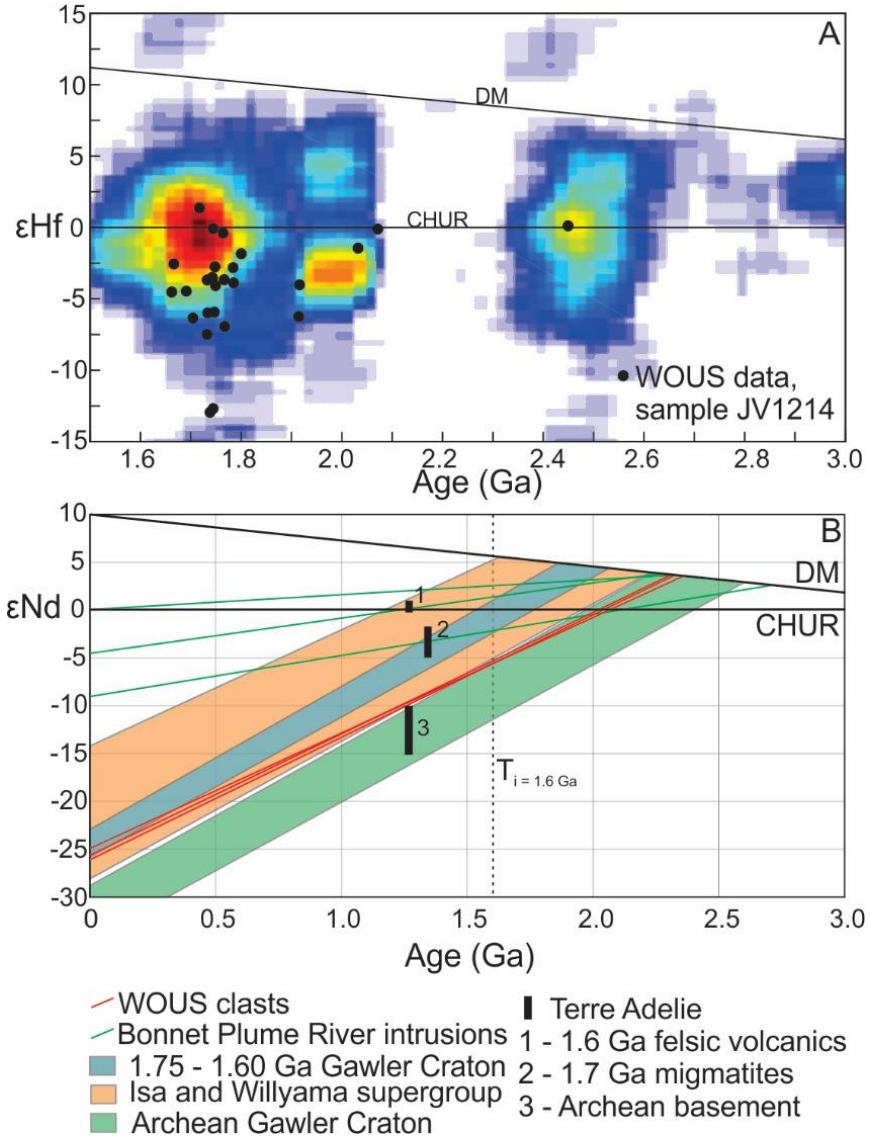

Figure 3.13. Density plot of zircon U-Pb and εHf of the Gawler Craton (data taken from Belousova et al., 2006; 2009; Howard et al., 2009, 2011a,b; Szpunar, 2011 and recalculated εHf using Lu-Hf chondrite values from Söderlund et al., 2004 and the decay constant from Bouvier et al., 2008). Density plot constructed using cell size of 20 m.y. in the X direction and 0.5 εHf in the Y direction, and smoothed using a moving average of 8 cell sizes. Data from the WOUS are plotted as black circles. B. Whole rock neodymium model ages of the WOUS, the Bonnet Plume River intrusions (Nielsen et al., 2013), average Gawler Craton (Howard et al., 2011b), the Isa and Willyama Supergroup (Barovich and Hand, 2008; Lambeck, 2012) and the Terre Adelie Craton (Peucat et al., 1999, 2002).

3.6.6. 1.6 Ga sedimentary successions on Yukon Territory and the Gawler Craton

The WOUS was deposited on Laurentia after the ca 1.6 Ga Racklan Orogeny and incorporated in the 1.599 Ga Wernecke Breccia. The WOUS consists of locally cross-bedded, well-bedded sandstone and mudstone, and soft sediment conglomerate deposited in a lacustrine or marine setting. On the Gawler Craton, the Olympic Dam strata were deposited after 1.59 Ga and incorporated in the Olympic Dam Breccia Complex (McPhie et al., 2011; 2016). The sedimentary facies consist of locally cross-bedded sandstone and red mudstone, green mudstone and sandstone and polymictic volcanic conglomerate that were deposited as turbidites (McPhie et al., 2016). Well-sorted quartz-rich sandstone also occurs within Olympic Dam Breccia Complex, but appears to have more fluvial characteristics, although bedforms are not clearly preserved (McPhie et al., 2016).

Does the WOUS correlate with the inferred sedimentary succession on the Gawler, and were these units deposited as an overlap succession between northwestern Laurentia and the Gawler Craton? To address this question we compare detrital zircon patterns of clasts from both regions. The patterns of detrital zircon ages are almost identical (Figure 3.14). The only notable difference is a large 1590 Ma zircon population in the Olympic Dam strata. This 1590 Ma peak coincides with the extrusion of the Gawler Range Volcanics prior to the formation of the Olympic Dam Breccia complex. The absence of a corresponding peak in the WOUS pattern is explained by a difference in the age of brecciation. The brecciation in Laurentia occurred at 1598.8 ± 1.0 Ma, whereas the brecciation in the Olympic Dam Breccia Complex occurred at ca. 1590 Ma (Johnson, 1993; Johnson and Cross, 1995; Jagodzinski, 2005). As such, the Olympic Dam Breccia Complex included clasts of strata which were up to 10 m.y. younger than those in the WOUS. Accordingly, sources of zircon in the Olympic Dam Breccia Complex clasts include younger units, i.e., the Gawler Range Volcanics. This age difference indicates that sedimentation on the Gawler Craton continued during the interval 1600 – 1590 Ma.

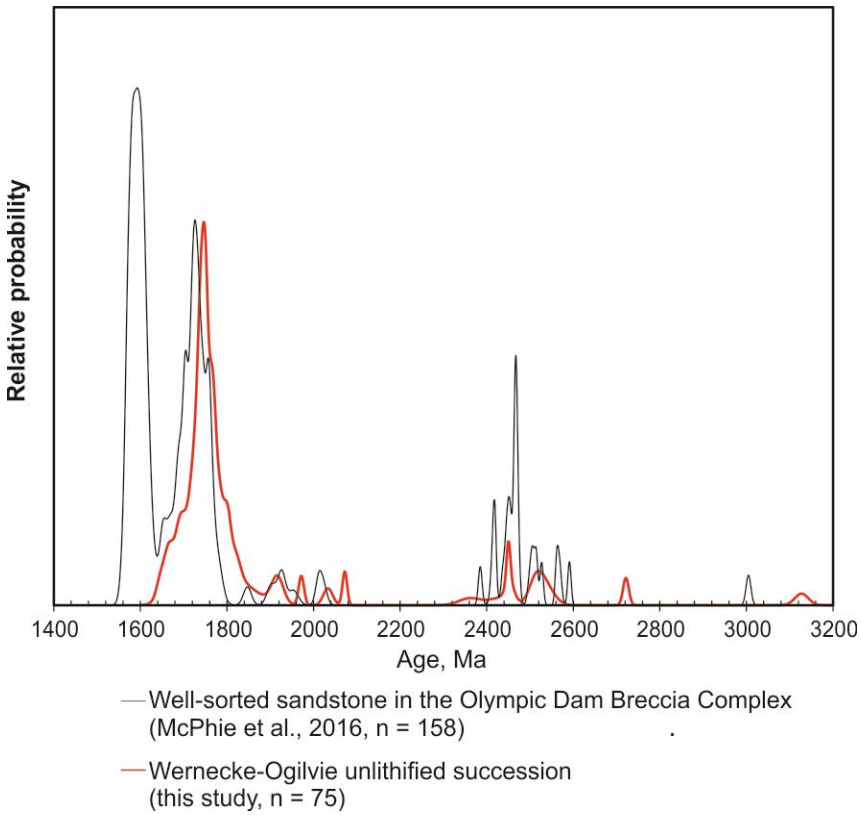

Figure 3.14. Detrital zircon data of the WOUS (zircon ages <5% discordant) compared with detrital zircon data of the well-sorted quartz-rich sandstone (zircon ages <10% discordant) in the Olympic Dam Breccia Complex.

Are sedimentary successions that belong to the overlap assemblage preserved? On Laurentia, no known strata correlate with the overlap assemblage; they were apparently eroded prior to deposition of unit PR1 of the Fifteenmile Group (Thompson, 1992). However, on Australia, three sedimentary successions may belong to the overlap assemblage: the Corunna Conglomerate, the Radium Creek Group and/or the Pandurra Formation.

The Corunna Conglomerate occurs on the Gawler Craton and is a sequence of fluvial to shallow marine conglomerate, sandstone and siltstone (Mcavaney and Reid, 2008). The Corunna Conglomerate contains detrital zircon with age profiles similar to the WOUS (Mcavaney and Reid, 2008). The Radium Creek Group is a <1595 Ma metasedimentary succession within the northwest Curnamona Province of Australia (Armit et al., 2014). This metasedimentary succession consists of micaceous psammite,

psammopelite, pelitic schist, phyllite, feldspathic quartzite and quartzofeldspathic gneiss (Armit et al., 2014). Detrital zircon preserved within the Radium Creek Group have similar age profiles and inferred provenance to the detrital zircon data of the WOUS (Armit et al., 2014). Other lines of evidence also suggest that the Curnamona Province and Gawler Craton were connected, such as concurrent igneous activity (Wade et al., 2012) and IOCG occurrences (Williams and Skirrow, 2000). Cherry et al. (2016) proposed that the overlying succession was the Pandurra Formation, a Mesoproterozoic fluvial succession of conglomerate, sandstone, and minor siltstone and shale, which crops out on the southern Gawler Craton, approximately 100 km west of Olympic Dam.

If the proposed correlations are correct, then the WOUS within Wernecke Breccia, the well-sorted sandstone within Olympic Dam Breccia, the Corunna Conglomerate, Radium Creek Group and/or the Pandurra Formation may have been part of a sedimentary overlap assemblage. These strata were apparently sourced from the same regions of the Gawler Craton, and were deposited around 1.6 – 1.59 Ga. The overlap assemblage was at least 500 x 50 km in size and extended across parts of an early Mesoproterozoic landmass which was subsequently divided into Australia and Laurentia.

3.6.7. The role of the Bonnetian arc

The Bonnetian arc accreted to the Laurentian margin prior to the formation of the Wernecke Breccia (Furlanetto et al., 2013) and is the arc from which the obducted terrane Bonnetia was derived. The age of Bonnetia is known from the Bonnet Plume River intrusions, which are preserved solely as megaclasts in Wernecke Breccia. U-Pb zircon dates on these megaclasts are 1705.9 ± 0.7, 1709.4 ± 1.4, 1711.1 ± 5.1, and 1713.6 ± 12.7 Ma (Thorkelson et al., 2001b). Rocks of the Bonnetian arc have Nd depleted mantle model ages of 2.43 – 2.26 Ga (Nielsen et al., 2013) which imply that Bonnetia was built on older crust. These model ages overlap with those of the WOUS, presented here, and with compiled data of the Gawler Craton (Figure 3.13B).

Thorkelson and Laughton (2016) proposed that the Bonnetian arc was built on the leading edge of eastern Australia, and flanked the Gawler Craton, North Australian Craton, and the Terre Adelie Craton of Antarctica. Detrital zircon provenance and Nd isotopes

indicate that the WOUS was derived from the Gawler Craton, and hence provide further evidence for a Laurentia-Bonnetia-Gawler Craton link. Thorkelson and Laughton (2016) further proposed that the Bonnetian arc was a source for airborne tephra or epiclastic sediment that elevated the εNd signature in sedimentary basins on eastern Australia (Lambeck et al., 2012). Part of the Bonnetian arc may have been uplifted and exposed as highlands during the Racklan Orogeny and prior to the formation of the Wernecke Breccia. In this scenario, the Bonnetian arc may have provided zircon to the WOUS and/or to Olympic Dam strata.

In the models of Gibson et al. (2008), Thorkelson and Laughton (2016) and Betts et al. (2016), westward subduction beneath Australia accommodated convergence between Australia and Laurentia. During this time, the Bonnetian arc developed and the Bonnet Plume River intrusions and other igneous rocks formed).

3.6.8. Paleogeographical reconstruction

At ca. 1.71 Ga, the Bonnet Plume River intrusions were emplaced within the volcanic arc Bonnetia (Thorkelson et al., 2001b; Furlanetto et al., 2013; Nielsen et al., 2013; Thorkelson and Laughton, 2016). From 1.73 – 1.69 Ga, the Kimban Orogeny affected the Gawler Craton (Payne et al., 2009). The Wernecke Supergroup is interpreted as a passive margin succession, and there is no evidence for subduction beneath northwestern Laurentia from 1.8 Ga to the mid-Paleozoic. Hence, convergence between Bonnetia, the Gawler Craton and Laurentia was accommodated by a west-dipping subduction zone. There is no 1.68 – 1.60 Ga zircon peak in the WOUS, which implies that there was no volcanic arc active during that time, or that igneous rocks of that age did not provide zircon to the WOUS after accretion. During this time, igneous and metamorphic activity occurred on the Gawler Craton (Morrissey et al., 2013). The passive margin of Laurentia was faulted and folded (Figure 3.15A), partially underthrust beneath the Gawler Craton (Figure 3.15B) and subjected to middle greenschist facies metamorphism during the Racklan Orogeny at 1.60 Ga (Thorkelson, 2000; Thorkelson et al., 2005; Furlanetto et al., 2013). Coeval orogenic events on the Gawler Craton and Curnamona Province are termed the Wartakan and Olarian Orogenies (Armit et al., 2012). According to Furlanetto et al., (2013) the first compressional stages of the Racklan Orogeny were concomitant

with erosion that exposed all three units of the Wernecke Supergroup at the surface prior to the obduction of Bonnetia. The collision between the Gawler Craton and northwestern Laurentia are herein depicted as one cycle of orogenesis, culminating in the east-directed obduction of Bonnetia. (Figure 3.15C).

The WOUS was deposited after collision between the Gawler Craton and Laurentia at ca. 1.6 Ga. At this time, Bonnetia is interpreted to have existed as a thrust nappe on Laurentia. Successor basins are deposited shortly after the collision of two continents (Eisbacher, 1974). Successor basins in young orogens are present in the Alps and the Zagros Mountains (Allen et al., 1991; Homke et al., 2009). Examples from other orogens include the Jurassic Bowser basin in the Canadian Cordillera (Ricketts et al., 1992) and the Ediacaran Bambuí foreland sequence on the São Fracisco Craton (Reis and Alkmim, 2015). Successor basin infills may include flysch and molasse such as those deposited in the Appalachians (Van Staal et al., 2014), Canadian Cordilleria (Coney and Evenchick, 1993) and in the North Alpine foreland basin (Allen et al., 1991), or fine-grained sediments such as in the Bambuí foreland sequence (Reis and Alkmim, 2015; Saura et al., 2015). The Gawler – northwestern Laurentia sedimentary overlap assemblage consists of mudstone, sandstone and polymictic volcanic conglomerate. These lithologies are consistent with deposition in a successor basin. However, there is insufficient paleogeographic information to uniquely identify the style and cause of basin formation.

The WOUS was deposited on the obducted terrane Bonnetia and perhaps other parts of Laurentia, over a minimum area of 250 x 50 km. The connection with sediments within the Olympic Dam Breccia Complex implies that the sedimentary basin extended from the Olympic Dam Breccia Complex to the margin of the Gawler Craton, an additional 150 km. If the sedimentary overlap assemblage also included the Radium Creek Group this distance increases to 250 km. If all possible correlations are correct then sedimentary overlap assemblage was deposited over a total area of at least 500 x 50 km. The overlap assemblage formed after the collision between the Gawler Craton and northwestern Laurentia at 1.6 Ga (Figure 3.15D). The sediment was largely sourced from metasedimentary formations on the Gawler Craton. It is unclear why a basin was created for sedimentation after continental collision, but it is possible that a period of erosion

separated the first pulse(s) of the Racklan Orogeny from the obduction of Bonnetia (Furlanetto et al., 2013), or that the region was subject to crustal extension and thinning.

At 1599 Ma, while the sedimentary overlap assemblage was still unlithified, the Wernecke Breccia formed within the crust and breached the surface (Figure 3.15E, Furlanetto et al., 2013). Fragments of unconsolidated sediment derived and the WOUS foundered into the breccia zones, together with clasts derived from the thrust nappe Bonnetia. Sedimentation continued until after the intrusion of the Hiltaba Suite and associated Gawler Range Volcanics at 1595 – 1592 Ma (Figure 3.15F, Figure 3.16). From this time onward, the detrital zircons shed into the basin were sourced largely from the recently formed Gawler Range Volcanics (McPhie et al., 2016). At ca. 1590 Ma, clasts of this part of the overlap succession foundered into Olympic Dam Breccia Complex during brecciation (Figure 3.15G, Figure 3.16, Figure 3.17). After a period of sinistral translation, the Mount Isa Inlier was juxtaposed to northwestern Laurentia (Medig et al., 2014; Figure 3.15H).

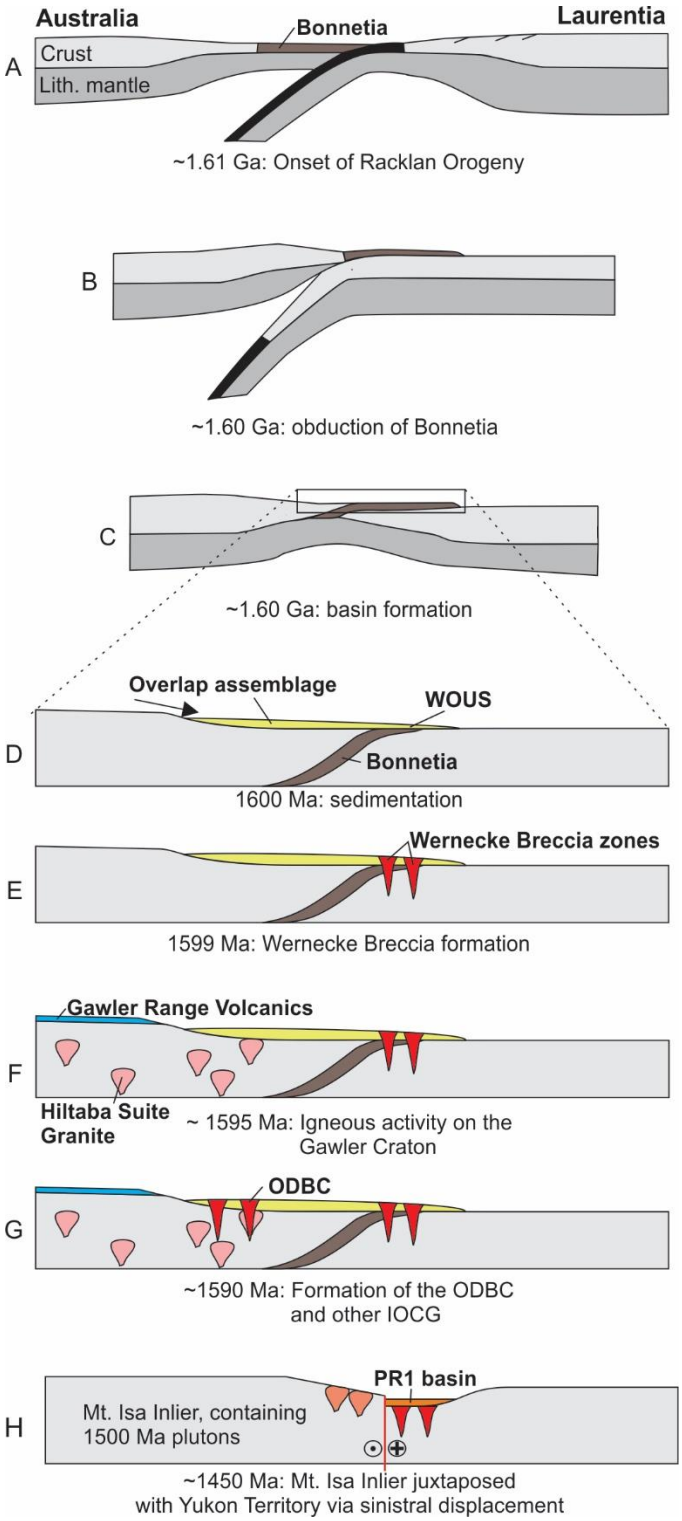

Figure 3.15. Schematic crustal cross sections depicting the collision between the Gawler Craton and northwestern Laurentia at ca. 1.6 Ga and the subsequent 100 m.y.

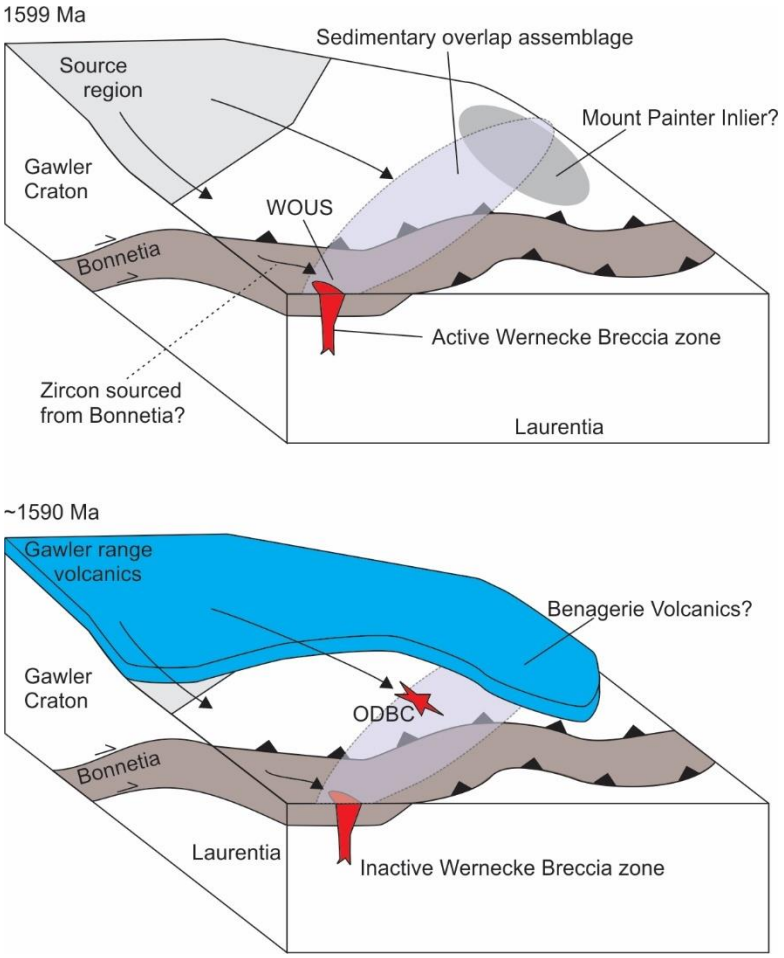

Figure 3.16. **Schematic block diagram of the area spanning the sedimentary overlap assemblage at 1599 Ma and ~1590 Ma. The Radium Creek Group on the Mount Painter Inlier is a potential correlative to the sedimentary overlap assemblage. The Benagerie Volcanics and Gawler Range Volcanics were proposed to be correlative by Armit et al. (2014). Bonnetia is here shown as a thrust slice on top of Laurentia and wedged in between the Gawler Craton and Laurentia, with thrust contacts on either side (see also Figure 15D).**

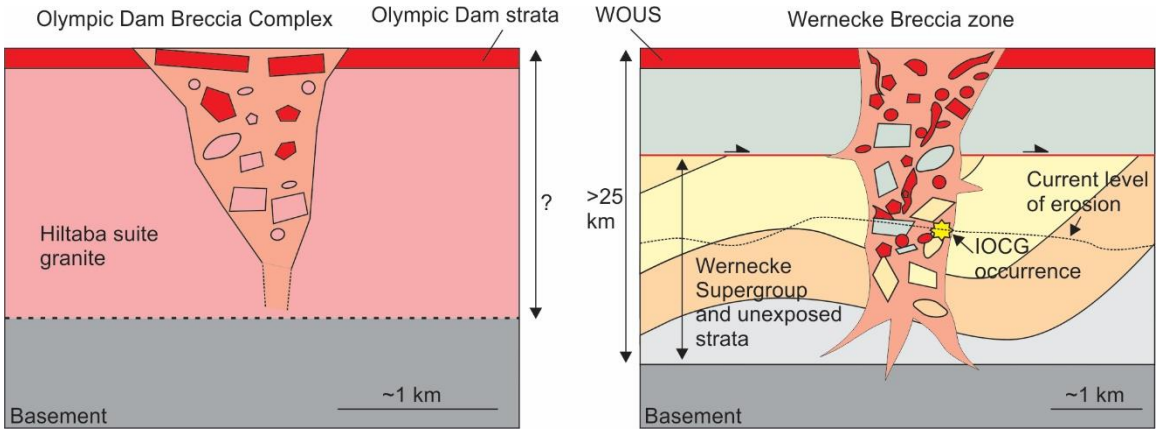

Figure 3.17. Crustal cross sections of the Olympic Dam Breccia Complex and a Wernecke Breccia zone. Both breccia zones contain foundered clasts of the overlying sedimentary material and of country rock. The nature of the continuation of the Wernecke Breccia into the basement is unclear. The Olympic Dam deposit grades into mafic alkaline magmas at depth (Johnson and Cross, 1995).

3.6.9. Southward translation of Australia along the Laurentian margin

After the collision of the Gawler Craton and northwestern Laurentia, a gap from 1.6 – 1.5 Ga exists in the rock record of northwestern Laurentia. At approximately 1.45 Ga, sediments with a distinct Australian provenance were shed into the PR1 basin (Medig et al., 2014) and the Belt-Purcell basin (Ross et al., 1992). These successions represent extension between Australia and Laurentia (Medig et al., 2014. The sediments in the PR1 basin were derived almost entirely from the Mt. Isa Inlier (Medig et al., 2014). In both of these reconstructions, the Gawler Craton is located far to the south of the Wernecke-Ogilvie area of northwestern Laurentia. In order for these reconstructions to be compatible with our model (Figure 3.18), Australia must have moved southwards relative to Laurentia sometime between 1.6 and 1.5 Ga. A southward motion of Australia was proposed by Betts et al. (2007) who recognized a hotspot track on Australia from 1.6 – 1.5 Ga. Similarly, the IOCG hydrothermal activity on the Gawler Craton and Yukon Territory at ca. 1.6 Ga has an expression at 1.55 – 1.50 Ga in the Mt. Isa Inlier, which may reflect southward motion of Australia. In some reconstructions, the Mt. Isa Inlier was still facing an oceanic basin after the Gawler-Laurentia collision at 1.6 Ga (Betts and Giles, 2006; Cawood and Korsch, 2008; Payne et al., 2009). In other scenarios, Australia and Laurentia were fully

connected at 1.6 Ga (Gibson et al., 2008; 2012; Thorkelson and Laughton, 2016). The southward translation and reorganization placed the Mt. Isa Inlier next to northwestern Laurentia prior to ca. 1.47 Ga (Medig et al., 2014). This allowed sediments from a broad swath of Australia to be deposited in Mesoproterozoic basins throughout western Laurentia (Ross, 1992; Blewett et al., 1998; Shufeldt et al., 2010; Doe et al., 2012; Medig et al., 2014; Figure 3.18) and a continuous granite-rhyolite province to be emplaced on Laurentia and the Mawson Continent (Goodge et al., 2008).

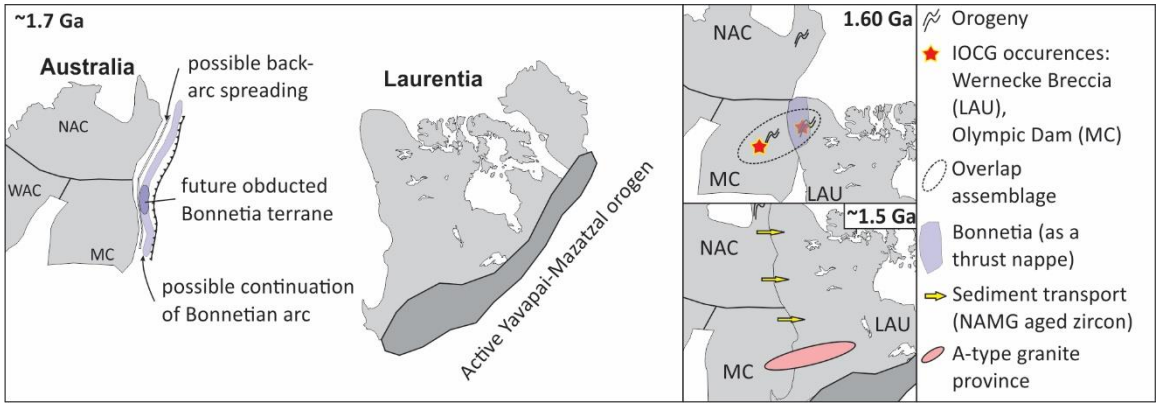

Figure 3.18. ~1.71 Ga. The Bonnetian arc originates on the leading edge of the Gawler Craton (part of the Mawson Continent, abbreviated MC) and possibly extends along the eastern Australian margin (NAC = North Australian Craton, WAC = Western Australian Craton). Convergence between Laurentia (LAU) and Australia is accommodated by westdipping subduction underneath the Bonnetian arc and Australia (modified from Thorkelson and Laughton, 2016). 1.60 Ga. Collision between Laurentia and the Gawler Craton leads to the obduction of Bonnetia over the Laurentian margin. The Wernecke Breccia forms on Laurentia, the Olympic Dam deposit forms on Australia. A sedimentary overlap assemblage is deposited on northwestern Laurentia and the Gawler Craton. ~1.5 Ga. Widespread transfer of sediment from Australia to Laurentia occurs after southward translation of Australia (modified from Medig et al., 2014).

3.7. Conclusions

Sedimentary clasts and ribbons with soft-sediment textures are present in zones of 1.60 Ga Wernecke Breccia in northwest Laurentia. The soft-sediment material includes well-bedded red to pink mudstone and sandstone, soft-sediment conglomerate, and green mudstone, all derived from non-lithified strata. The inferred source of these fragments is herein named the Wernecke-Ogilvie unlithified succession (WOUS). The WOUS was an

extensive well-bedded succession of sandstone and mudstone deposited over at least 250 x 50 km based on the distribution of clasts within Wernecke Breccia zones. The succession was deposited after the Racklan Orogeny at ca. 1.6 Ga and before the formation of the Wernecke Breccia at 1.599 Ga. The WOUS was deposited on Bonnetia, an oceanic terrane that was obducted onto the Laurentian margin between ca. 1.65 and 1.60 Ga.

Zircon from the WOUS are dominated by a population with ages of 1.78 – 1.68 Ga with evolved εHf(t) of 0 to -12. Other significant age populations range from 2.1 – 1. 78 Ga and 2.55 – 2.45 Ga. A small proportion of the grains fall outside of these ranges and have Paleoproterozoic to Archean ages. Most of the grains, including those in the 1.78 – 1.68 Ga age-range, display smooth crystal faces and rounded edges and corners, and are consistent with derivation from a proximal source. However, there are no known local Laurentian sources for this zircon population and we propose that the majority of the grains were sourced from the Gawler Craton, which has yielded similar detrital zircon ages and Hf and Nd isotopic ratios, and which collided with the Laurentian margin in the late stages of the Racklan orogeny (Furlanetto et al., 2013). In addition, the Bonnetian arc may have provided zircon to the WOUS. In this model, the obducted terrane Bonnetia is interpreted as the leading edge of the Gawler Craton, or a fringing terrane, which was obducted onto the margin of Laurentia during late Paleoproterozoic collision of Australia with Laurentia.

On the basis of lithological similarity, depositional timing and provenance, we correlate the WOUS to the Olympic Dam strata that were deposited on the Gawler Craton (McPhie et al., 2011; 2016). These sediments are interpreted as remnants of an intercontinental sedimentary overlap assemblage that was deposited after the collision of Australia and Laurentia and obduction of Bonnetia. The Corunna Conglomerate, Pandurra Formation on the Gawler Craton and the Radium Creek Group on the Curnamona Province are tentatively included in this overlap assemblage.

The proposed overlap assemblage strengthens the paleogeographic reconstruction of Thorkelson et al. (2001a) which places northwestern Laurentia adjacent to the Gawler Craton at 1.6 Ga. During the interval 1.6 – 1.5 Ga, Australia was sinistrally translated along the margin of Laurentia to allow for a more southerly fit at 1.5 Ga (Medig

et al., 2014) and the juxtaposition of northwestern Laurentia with the Mt Isa inlier. During this time, the WOUS and Bonnetia were eroded, and the only known remnants of these units are now present as foundered fragments within the Wernecke Breccia. Correlatives of the WOUS may remain on Australia as the Pandurra and Radium Creek successions.

3.8. Acknowledgements

Funding was provided by NSERC grants to DJT. The Yukon Geological Survey provided logistical support in 2012. This is a contribution to IGCP Project 648. We thank J. Payne and an anonymous reviewer for numerous helpful comments.

3.9. References

Aitken, A. R. A., Betts, P. G., Young, D. A., Blankenship, D. D., Roberts, J. L., & Siegert, M. J. (2016). The Australo-Antarctic Columbia to Gondwana transition. Gondwana Research, 29(1), 136–152. http://doi.org/10.1016/j.gr.2014.10.019

Aleinikoff, J. N., Reed, J. C., Jr., & Wooden, J. L. (1993). Lead isotopic evidence of the origin of Paleo- and Mesoproterozoic rocks of the Colorado province, U.S.A.: Precambrian Research, 63, p. 97-122.

Allen, P. A., Crampton, S. L., & Sinclair, H. D. (1991). The inception and early evolution of the north Alpine foreland basin, Switzerland. Basin Research, 3(3), 143–163. http://doi.org/10.1111/j.1365-2117.1991.tb00124.x

Armit, R. J., Betts, P. G., Schaefer, B. F., & Ailleres, L. (2012). Constraints on long-lived Mesoproterozoic and Paleozoic deformational events and crustal architecture in the northern Mount Painter Province, Australia. Gondwana Research, 22(1), 207–226. http://doi.org/10.1016/j.gr.2011.11.003

Armit, R. J., Betts, P. G., Schaefer, B. F., Pankhurst, M. J., & Giles, D. (2014). Provenance of the Early Mesoproterozoic Radium Creek Group in the northern Mount Painter Inlier: Correlating isotopic signatures to inform tectonic reconstructions. Precambrian Research, 243, 63–87. http://doi.org/10.1016/j.precamres.2013.12.022

Barovich, K., & Hand, M. (2008). Tectonic setting and provenance of the Paleoproterozoic Willyama Supergroup, Curnamona Province, Australia: Geochemical and Nd isotopic constraints on contrasting source terrain components. Precambrian Research, 166(1–4), 318–337. http://doi.org/10.1016/j.precamres.2007.06.024

Bell, R. T., & Jefferson, C. W. (1987). An hypothesis for an Australian-Canadian connection in the Late Proterozoic and the birth of the Pacific Ocean. Pacific Rim Congress 87 Conference Proceedings, 39-50

Bell RT (1989) A conceptual model for development of megabreccias and associated mineral deposits in Wernecke Mountains, Canada, Copperbelt, Zaire, and Flinders Range, Australia. In: Uranium resources and geology of North America: proceedings of a technical committee meeting, organized by the Internal Atomic Energy Agency held in Saskatoon, Canada, 1987, 149–169

Belousova, E.A., Griffin, W.L., O'Reilly, S.Y., and Fisher, N.I. (2002) Igneous zircon: trace element composition as an indicator of source rock type: Contributions to Mineralogy and Petrology, 143, 602–622, doi: 10.1007/s00410-002-0364-7.

Belousova, E. A., Preiss, W. V., Schwarz, M. P., & Griffin, W. L. (2006). Tectonic affinities of the Houghton Inlier, South Australia: U – Pb and Hf-isotope data from zircons in modern stream sediments. Australian Journal of Earth Sciences, 53(October), 971–989. http://doi.org/10.1080/08120090600880875

Belousova, E. A., Reid, A. J., Griffin, W. L., & O'Reilly, S. Y. (2009). Rejuvenation vs. recycling of Archean crust in the Gawler Craton, South Australia: Evidence from U-Pb and Hf isotopes in detrital zircon. Lithos, 113(3–4), 570–582. http://doi.org/10.1016/j.lithos.2009.06.028

Giles, D., Betts, P. G., Aillères, L., Hulscher, B., Hough, M., & Lister, G. S. (2006). Evolution of the Isan Orogeny at the southeastern margin of the Mt Isa Inlier. Australian Journal of Earth Sciences, 53(1), 91–108. http://doi.org/10.1080/08120090500432470

Betts, P.G., Giles, D., Mark, G., Lister, G.S., Goleby, B.R., and Aillères, L. (2006) Synthesis of the proterozoic evolution of the Mt Isa Inlier: Australian Journal of Earth Sciences, 53, 187–211, doi: 10.1080/08120090500434625.

Betts, P. G., Giles, D., & Schaefer, B. F. (2008). Comparing 1800-1600 Ma accretionary and basin processes in Australia and Laurentia: Possible geographic connections in Columbia. Precambrian Research, 166(1–4), 81–92. http://doi.org/10.1016/j.precamres.2007.03.007

Betts, P. G., & Giles, D. (2006). The 1800-1100 Ma tectonic evolution of Australia. Precambrian Research, 144(1–2), 92–125. http://doi.org/10.1016/j.precamres.2005.11.006

Betts, P.G., Giles, D., Schaefer, B.F., and Mark, G. (2007) 1600-1500 Ma hotspot track in eastern Australia: Implications for Mesoproterozoic continental reconstructions: Terra Nova, 19, p. 496–501, doi: 10.1111/j.1365-3121.2007.00778.x.

Betts, P. G., Giles, D., Foden, J., Schaefer, B. F., Mark, G., Pankhurst, M. J., Hills, Q. (2009). Mesoproterozoic plume-modified orogenesis in eastern Precambrian Australia. Tectonics, 28(3). http://doi.org/10.1029/2008TC002325

Betts, P. G., Armit, R. J., Stewart, J., Aitken, A. R. A., Ailleres, L., Donchak, P., Giles, D. (2016). Australia and Nuna. Geological Society, London, Special Publications, 424(1), 47–81. http://doi.org/10.1144/SP424.2

Blewett, R. S., Black, L. P., Sun, S. S., Knutson, J., Hutton, L. J., & Bain, J. H. C. (1998). U-Pb zircon and Sm-Nd geochronology of the Mesoproterozoic of North Queensland: Implications for a Rodinian connection with the Belt Supergroup of North America. Precambrian Research, 89(3–4), 101–127. http://doi.org/10.1016/S0301-9268(98)00030-8

Boger, S. D., & Hansen, D. (2004). Metamorphic evolution of the Georgetown Inlier, northeast Queensland, Australia; evidence for an accreted Paleoproterozoic terrane? Journal of Metamorphic Geology, 22(6), 511–527. http://doi.org/10.1111/j.1525-1314.2004.00528.x

Bouvier, A., Vervoort, J. D., & Patchett, P. J. (2008). The Lu-Hf and Sm-Nd isotopic composition of CHUR: Constraints from unequilibrated chondrites and implications for the bulk composition of terrestrial planets. Earth and Planetary Science Letters, 273(1–2), 48–57. http://doi.org/10.1016/j.epsl.2008.06.010

Bowring, S. A., & Ross, G. M. (1985). Geochronology of the Naraka Volcanic Complex: implications for the age of the Coppermine Homocline and Mackenzie igneous events. Canadian Journal of Earth Sciences, 22, 774–781. http://doi.org/10.1139/e85-082

Cawood, P. A., & Korsch, R. J. (2008). Assembling Australia: Proterozoic building of a continent. Precambrian Research, 166(1–4), 1–35. http://doi.org/10.1016/j.precamres.2008.08.006

Chalmers, N. C. (2007). Mount Woods Domain: Proterozoic Metasediments and intrusives. South Australia. Department of Primary Industries and Resources, Report Book 2007(20)

Cherry, A. R., Kamenetsky, V. S., Ehrig, K., McPhie, J., Kamenetsky, M., & Apukhtina, O. (2016). Sedimentary facies within the Olympic Dam Breccia Complex: A potential metal source. Australian Earth Sciences Convention 2016, conference abstracts

Condie, K.C. (1992) Proterozoic Terranes and Continental Accretion in Southwestern North America, Developments in Precambrian Geology, 10, 477

Coney, P.J., and Evenchick, C.A. (1994) Consolidation of the American Cordilleras: Journal of South American Earth Sciences, 7, 241–262, doi: 10.1016/0895-9811(94)90011-6.

Cook, F.A., Hall, K.W., and Lynn, C.E. (2005) The edge of northwestern North America at similar to 1.8 Ga: Canadian Journal of Earth Sciences, 42, 983–997, doi: 10.1139/e05-039.

Cook, F.A., Van Der Velden, A.J., Hall, K.W., and Roberts, B.J., (1998) Tectonic delamination and subcrustal imbrication of the Precambrian lithosphere in northwestern Canada mapped by LITHOPROBE: Geology, 26, 1998, 839–842, doi: 10.1130/0091-7613(1998)026<0839:TDASIO>2.3.CO;2.

Cook, D. G., & MacLean, B. C. (1995). The intracratonic Paleoproterozoic Forward orogeny, and implications for regional correlations, Northwest Territories, Canada. Canadian Journal of Earth Sciences, 32(11), 1991–2008. http://doi.org/10.1139/e95-152

Cowley, W.M. and Fanning, C.M., (1991). Low-grade Archaean metavolcanics in the northern Gawler Craton. Quarterly Geological Notes - Geological Survey of South Australia, 119: 2-17.

Crawford, B. L., Betts, P. G., & Aillères, L. (2010). An aeromagnetic approach to revealing buried basement structures and their role in the Proterozoic evolution of the Wernecke Inlier, Yukon Territory, Canada. Tectonophysics, 490(1–2), 28–46. http://doi.org/10.1016/j.tecto.2010.04.025

Dalziel, I. W. D. (2013). Antarctica and supercontinental evolution: clues and puzzles. Earth and Environmental Science Transactions of the Royal Society of Edinburgh, 3–16. http://doi.org/10.1017/S1755691012000096

Delaney, G. D. (1981). The mid-Proterozoic Wernecke Supergroup, Wernecke Mountains, Yukon Territory. In Campbell, F.H.A. (Ed.), Proterozoic Basins of Canada (pp. 1–24).

DePaolo, D. J. (1981). Neodymium isotopes in the Colorado Front Range and crust–mantle evolution in the Proterozoic. Nature, 291(5812), 193–196. http://doi.org/10.1038/291193a0

Doe, M. F., Jones, J. V., Karlstrom, K. E., Thrane, K., Frei, D., Gehrels, G., & Pecha, M. (2012). Basin formation near the end of the 1.60-1.45 Ga tectonic gap in southern Laurentia: Mesoproterozoic Hess Canyon Group of Arizona and implications for ca. 1.5 Ga supercontinent configurations. Lithosphere, 4(1), 77–88. http://doi.org/10.1130/L160.1

Eisbacher, G.H. (1974). Evolution of successor basins in the Canadian Cordillera. Society of economic paleontologists and mineralogists. Special publication, SP19

Ernst, R. E., Wingate, M. T. D., Buchan, K. L., & Li, Z. X. (2008). Global record of 1600-700 Ma Large Igneous Provinces (LIPs): Implications for the reconstruction of the proposed Nuna (Columbia) and Rodinia supercontinents. Precambrian Research, 160(1–2), 159–178. http://doi.org/10.1016/j.precamres.2007.04.019

Ernst, R. E., Bleeker, W., Söderlund, U., & Kerr, A. C. (2013). Large Igneous Provinces and supercontinents: Toward completing the plate tectonic revolution. Lithos, 174, 1–14. http://doi.org/10.1016/j.lithos.2013.02.017

Evans, D. A. D., & Mitchell, R. N. (2011). Assembly and breakup of the core of Paleoproterozoic-Mesoproterozoic supercontinent Nuna. Geology, 39(5), 443–446. http://doi.org/10.1130/G31654.1

Fanning, C. M., Reid, A., & Teale, G. (2007). A geochronological framework for the Gawler Craton, South Australia. South Australia Geological Survey Bulletin (Vol. 55).

Fanning, C. M., Link, P. K., Woodhead, J. & Hergt, J. (2009). Provenance of unique Mesoproterozoic sedimentary basins in Australia and North America; U-Pb and Lu-Hf isotopic data for detrital zircons and the implications for Rodinia reconstructions. Abstracts, Geological Society of London Fermor Meeting, Rodinia: Supercontinents, Superplumes and Scotland

Furlanetto, F., Thorkelson, D. J., Rainbird, R. H., Davis, W. J., Gibson, H. D., & Marshall, D. D. (2016). The Paleoproterozoic Wernecke Supergroup of Yukon, Canada: Relationships to orogeny in northwestern Laurentia and basins in North America, East Australia, and China. Gondwana Research, 39, 14–40. http://doi.org/10.1016/j.gr.2016.06.007

Furlanetto, F., Thorkelson, Rainbird, R. H., Davis, W. J., D. J., Gibson, H. D., Marshall, D. D. (2013). Late Paleoproterozoic terrane accretion in northwestern Canada and the case for circum-Columbian orogenesis. Precambrian Research, 224, 512–528. http://doi.org/10.1016/j.precamres.2012.10.010

Gibson, G., Henson, P., Neumann, N. L., Southgate, P. N., & Hutton, L. J. (2012). Paleoproterozoic-earliest Mesoproterozoic basin evolution in the Mount Isa region, northern Australia and implications for reconstructions of the Nuna and. Episodes, 35(1), 131–141.

Gibson, G. M., Hutton, L. J., & Holzschuh, J. (2017). Basin inversion and supercontinent assembly as drivers of sediment-hosted Pb – Zn mineralization in the Mount Isa region, northern Australia. Journal of the Geological Society 174, 773–786.

Gibson, G.M., Rubenach, M.J., Neumann, N.L., Southgate, P.N., and Hutton, L.J. (2008) Syn- and post-extensional tectonic activity in the Palaeoproterozoic sequences of Broken Hill and Mount Isa and its bearing on reconstructions of Rodinia: Precambr. Res., 166, 350–369, doi: 10.1016/j.precamres.2007.05.005

Giles, D., Betts, P. G., & Lister, G. S. (2004). 1.8-1.5-Ga links between the North and South Australian Cratons and the Early-Middle Proterozoic configuration of Australia. Tectonophysics, 380(1–2), 27–41. http://doi.org/10.1016/j.tecto.2003.11.010

Goodge, J. W., Fanning, C. M., Fisher, C. M., & Vervoort, D. (2017). Proterozoic crustal evolution of central East Antarctica: Age and isotopic evidence from glacial igneous clasts, and links with Australia and Laurentia. Precambrian Research, (July). http://doi.org/10.1016/j.precamres.2017.07.026

Goodge, J. W., & Fanning, C. M. (2010). Composition and age of the East Antarctic shield in eastern Wilkes Land determined by proxy from Oligocene-Pleistocene glaciomarine sediment and beacon supergroup sandstones, Antarctica. Bulletin of the Geological Society of America, 122(7–8), 1135–1159. http://doi.org/10.1130/B30079.1

Goodge, J. W., & Fanning, C. M. (2016). Mesoarchean and Paleoproterozoic history of the Nimrod Complex, central Transantarctic Mountains, Antarctica: Stratigraphic revisions and relation to the Mawson Continent in East Gondwana. Precambrian Research, 285, 242–271. http://doi.org/10.1016/j.precamres.2016.09.001

Goodge, J. W., Vervoort, J. D., Fanning, C. M., Brecke, D. M., Farmer, G. L., `Williams, I. S., DePaolo, D. J. (2008). A positive test of East Antarctica-Laurentia juxtaposition within the Rodinia supercontinent. Science (New York, N.Y.), 321(2008), 235–240. http://doi.org/10.1126/science.1159189

Hall, K.W., and Cook, F.A. (1998) Geophysical transect of the Eagle Plains foldbelt and Richardson Mountains anticlinorium, northwestern Canada: Bulletin of the Geological Society of America, v. 110, 1998, 311–325, doi: 10.1130/0016-7606(1998)110<0311:GTOTEP>2.3.CO;2.

Hand, M., Reid, A., & Jagodzinski, L. (2007). Tectonic framework and evolution of the Gawler Craton, Southern Australia. Economic Geology, 102(8), 1377–1395. http://doi.org/10.2113/gsecongeo.102.8.1377

Hamilton, M.A., and Buchan, K.L. (2010), U-Pb geochronology of the Western Channel Diabase, northwestern Laurentia: Implications for a large 1.59Ga magmatic province, Laurentia's APWP and paleocontinental reconstructions of Laurentia, Baltica and Gawler craton of southern Australia: Precambr. Res., 183, 463–473, doi: 10.1016/j.precamres.2010.06.009.

Heatherington, A. L., & Mueller, P. A. (1991). Geochemical evidence for Triassic rifting in southwest Florida. Tectonophysics, 188, 291–302.

Hill, B.M., and Bickford, M.E. (2001) Paleoproterozoic rocks of central Colorado: Accretedarcs or extended older crust? Geology, 29, 1015–1018.

Hitzman, M.W., Oreskes, N., and Einaudi, M.T. (1992) Geological characteristics and tectonic setting of proterozoic iron oxide (CuUAuREE) deposits: Precambr. Res., 58, 241–287, doi: 10.1016/0301-9268(92)90121-4.

Hoffman, P.F. (1988) United plates of America, the birth of a craton; Early Proterozoicassembly and growth of Laurentia. Ann. Rev. Earth Planet. Sci. 16, , 543–603

Homke, S., J. Vergés, J. Serra-Kiel, G. Bernaola, I. Sharp, M. Garcés, I. Montero-Verdú, R. Karpuz, and M. H. Goodarzi, (2009), Late Cretaceous-Paleocene formation of the proto-Zagros foreland basin, Lurestan Province, SW Iran, Geol. Soc. Am. Bull., 121(7/8), 963–978, doi:10.1130/B26035.26031.

Hou, G., Santosh, M., Qian, X., Lister, G. S., & Li, J. (2008). Configuration of the Late Paleoproterozoic supercontinent Columbia: Insights from radiating mafic dyke swarms. Gondwana Research, 14(3), 395–409. http://doi.org/10.1016/j.gr.2008.01.010

Howard, K. E., Hand, M., Barovich, K. M., Reid, A., Wade, B. P., & Belousova, E. A. (2009). Detrital zircon ages: Improving interpretation via Nd and Hf isotopic data. Chemical Geology, 262(3–4), 293–308. http://doi.org/10.1016/j.chemgeo.2009.01.029

Howard, K. E., Hand, M., Barovich, K. M., & Belousova, E. (2011a). Provenance of late Paleoproterozoic cover sequences in the central Gawler Craton: exploring stratigraphic correlations in eastern Proterozoic Australia using detrital zircon ages, Hf and Nd isotopic data. Australian Journal of Earth Sciences, 58(5), 475–500. http://doi.org/10.1080/08120099.2011.577753

Howard, K. E., Hand, M., Barovich, K. M., Payne, J. L., & Belousova, E. A. (2011b). U-Pb, Lu-Hf and Sm-Nd isotopic constraints on provenance and depositional timing of metasedimentary rocks in the western Gawler Craton: Implications for Proterozoic reconstruction models. Precambrian Research, 184(1–4), 43–62. http://doi.org/10.1016/j.precamres.2010.10.002

Hunt, J., Baker, T., and Thorkelson, D.J. (2005) Regional-scale Proterozoic IOCG-mineralized breccia systems: Examples from the Wernecke Mountains, Yukon, Canada: Mineralium Deposita, 40, 492–514, doi: 10.1007/s00126-005-0019-5.

Hunt, J. A., Baker, T., & Thorkelson, D. J. (2007). A review of iron oxide copper-gold deposits, with focus on the Wernecke Breccias, Yukon Canada, as an example of a non-magmatic end member and implications for IOCG genesis and classification. Exploration and Mining Geology, 16(3–4), 209–232. http://doi.org/10.2113/gsemg.16.3-4.209

Irving, E., Baker, J., Hamilton, M., & Wynne, P. J. (2004). Early Proterozoic geomagnetic field in western Laurentia: Implications for paleolatitudes, local rotations and stratigraphy. Precambrian Research, 129(3–4), 251–270. http://doi.org/10.1016/j.precamres.2003.10.002

Jagodzinski, E. (2005). Compilation of SHRIMP U-Pb geochronological data, Olympic Domain, Gawler Craton, South Australia, 2001-2003. Geoscience Australia, Record 2005/020, 197 p.

Jagodzinski, E. A., Reid, A. J., Chalmers, N. C., Swain, G., Frew, R. A., & Foudoulis, C. (2007). Compilation of SHRIMP U-Pb geochronological data for the Gawler Craton, South Australia, 2007. South Australia. Department of Primary Industries and Resources, Report Book 2007/21

Johnson, J.P., and Cross, K.C. (2005) U-Pb geochronological constraints on the genesis of the Olympic Dam Cu-U-Au-Ag deposit, South Australia: Economic Geology, 90, 1995, 1046–1063.

Johson, J.P. (1993). The geochronology and radiogenic isotope systematics of the Olympic Dam uranium-copper-gold-silver deposit, South Australia: PhD thesis, Canberra, The Australian National University, 251 p.

Jones, J. V., Daniel, C. G., & Doe, M. F. (2015). Tectonic and sedimentary linkages between the Belt-Purcell basin and southwestern Laurentia during the Mesoproterozoic, ca. 1.60–1.40 Ga. Lithosphere, 7(4), 465–472. http://doi.org/10.1130/L438.1

Kamo, S.L., Wasteneys, H., Gower, C.F., and Krogh, T.E. (1996), U-Pb geochronology of Labradorian and later events in the Grenville Province, eastern Labrador: Precambr. Res., 80, 239–260, doi: 10.1016/S0301-9268(96)00017-4.

Lambeck, A., Barovich, K., Gibson, G., Huston, D., & Pisarevsky, S. (2012). An abrupt change in Nd isotopic composition in Australian basins at 1655Ma: Implications for the tectonic evolution of Australia and its place in NUNA. Precambrian Research, 208–211, 213–221. http://doi.org/10.1016/j.precamres.2012.01.009

Lane, R. A. (1990). Geologic setting and petrology of the Proterozoic Ogilvie Mountain breccias of the Coal Creek Inlier, Southern Ogilvie Mountains, Yukon Territory. M.Sc. thesis. The University of British Columbia.

Li, Z. X., Li, X. H., Li, W. X., & Ding, S. (2008). Was Cathaysia part of Proterozoic Laurentia? - New data from Hainan Island, South China. Terra Nova, 20(2), 154–164. http://doi.org/10.1111/j.1365-3121.2008.00802.x

Link, P.K., Fanning, C.M., Lund, K.I., and Aleinikoff, J.N., (2007), Detrital zircons, correlation and provenance of Mesoproterozoic Belt Supergroup and correlative strata of east-central Idaho and southwest Montana: in Link, P.K., and Lewis, R.S., eds., SEPM Special Publication 86, Proterozoic geology of western North America and Siberia, p. 101-128.

Link, P. K., Stewart, E. D., Steel, T., Sherwin, J.-A., Hess, L. T., and McDonald, C., 2016, Detrital zircons in the Mesoproterozoic upper Belt Supergroup in the Pioneer, Beaverhead and Lemhi Ranges, Montana and Idaho: The Big White arc: in MacLean J.S, and Sears, J.W. eds., Belt Basin: Window to Mesoproterozoic Earth: Geological Society of America Special Paper 522, p. 163-183, doi:10.1130/2016.2522(03)

MacLean, B.C., and Cook, D.G. (2004), Revisions to the Paleoproterozoic Sequence A, based on reflection seismic data across the western plains of the Northwest Territories, Canada: Precambrian Research, 129, 271–289, doi:10.1016/j.precamres.2003.10.008.

Ludwig, K. (2003). SQUID 2: A User's Manual. Berkeley Geochronology Center Special Publication No. 5.

Mcavaney, S., and Reid, A., (2008), The Corunna Conglomerate, Gawler Craton : a review of the sedimentology and new U – Pb zircon geochronology, Report book 2008/3, Government of South Australia, Primary industries and resources SA

McPhie, J., Kamenetsky, V., Allen, S., Ehrig, K., Agangi, A., & Bath, A. (2011). The fluorine link between a supergiant ore deposit and a silicic large igneous province. Geology, 39(11), 1003–1006. http://doi.org/10.1130/G32205.1

McPhie, J., Orth, K., Kamenetsky, V., Kamenetsky, M., & Ehrig, K. (2016). Characteristics, origin and significance of Mesoproterozoic bedded clastic facies at the Olympic Dam Cu-U-Au-Ag deposit, South Australia. Precambrian Research, 276, 85–100. http://doi.org/10.1016/j.precamres.2016.01.029

Medig, K. P. R., Thorkelson, D. J., Davis, W. J., Rainbird, R. H., Gibson, H. D., Turner, E. C., & Marshall, D. D. (2014). Pinning northeastern Australia to northwestern Laurentia in the Mesoproterozoic. Precambrian Research, 249, 88–99. http://doi.org/10.1016/j.precamres.2014.04.018

Medig, K. P. R., Turner, E. C., Thorkelson, D. J., & Rainbird, R. H. (2016a). Rifting of Columbia to form a deep-water siliciclastic to carbonate succession: The Mesoproterozoic Pinguicula Group of northern Yukon, Canada. Precambrian Research, 278, 179–206. http://doi.org/10.1016/j.precamres.2016.03.021

Medig, K.P.R., Thorkelson, D.J., Davis, W.J., Rainbird, R.H., Turner, E.C., Gibson, H.D., Marshall, D.D. (2016b). Mesoproterozoic basins of Laurentia and their possible connection to Australia. GAC-MAC 2016: Margins through time, Whitehorse. Abstract.

Milidragovic, D., Thorkelson, D. J., Davis, W. J., Marshall, D. D., & Gibson, H. D. (2011). Evidence for late Mesoproterozoic tectonism in northern Yukon and the identification of a Grenville-age tectonothermal belt in western Laurentia. Terra Nova, 23(5), 307–313. http://doi.org/10.1111/j.1365-3121.2011.01015.x

Moores, E. M. (1991). Southwest U.S.-East Antarctic (SWEAT) connection: A Hypothesis. Geology, 19, 425–428.

Morrissey, L. J., Hand, M., Wade, B. P., Szpunar, M., Hand, M., Wade, B. P., & Early, M. S. (2013). Early Mesoproterozoic metamorphism in the Barossa Complex, South Australia: links with the eastern margin of Proterozoic Australia Australian Journal of Earth Sciences, 60(0), 769–795. http://doi.org/10.1080/08120099.2013.860623

Mueller, P. A., Kamenov, G. D., Heatherington, A. L., & Richards, J. (2008). Crustal Evolution in the Southern Appalachian Orogen: Evidence from Hf Isotopes in Detrital Zircons. The Journal of Geology, 116(4), 414–422. http://doi.org/10.1086/589311

Nielsen, A. B. (2011). The Wernecke igneous clasts in Yukon, Canada: evidence for a Paleoproterozoic volcanic arc terrane at 1.7 Ga and its obduction onto ancestral North America. M.Sc. Thesis, Simon Fraser University, 115 p.

Nielsen, A. B., Thorkelson, D. J., Gibson, H. D., & Marshall, D. D. (2013). The Wernecke igneous clasts in Yukon, Canada: Fragments of the Paleoproterozoic volcanic arc terrane Bonnetia. Precambrian Research, 238, 78–92. http://doi.org/10.1016/j.precamres.2013.09.017

Page, R. W., & Sun, S. (1998). Aspects of geochronology and crustal evolution in the Eastern Fold Belt, Mt Isa Inlier. Australian Journal of Earth Sciences, 45(3), 343–361. http://doi.org/10.1080/08120099808728396

Page, R. W., Conor, C. H. H., Stevens, B. P. J., Gibson, G. M., Preiss, W. V., & Southgate, P. N. (2005a). Correlation of Olary and Broken Hill domains, Curnamona Province: Possible relationship to Mount Isa and other north Australian Pb-Zn-Ag-bearing successions. Economic Geology, 100(4), 663–676. http://doi.org/10.2113/gsecongeo.100.4.663

Page, R. W., Stevens, B. P. J., & Gibson, G. M. (2005b). Geochronology of the sequence hosting the Broken Hill Pb-Zn-Ag orebody, Australia. Economic Geology, 100(4), 633–661. http://doi.org/10.2113/gsecongeo.100.4.633

Payne, J. L., Barovich, K. M., & Hand, M. (2006). Provenance of metasedimentary rocks in the northern Gawler Craton, Australia: Implications for Paleoproterozoic reconstructions. Precambrian Research, 148(3–4), 275–291. http://doi.org/10.1016/j.precamres.2006.05.002

Payne, J. L., Hand, M., Barovich, K. M., Reid, a., & Evans, D. A. D. (2009). Correlations and reconstruction models for the 2500-1500 Ma evolution of the Mawson Continent. Geological Society, London, Special Publications, 323(1), 319–355. http://doi.org/10.1144/SP323.16

Peterson, T. D., Scott, J. M. J., LeCheminant, A. N., Jefferson, C. W., & Pehrsson, S. J. (2015). The Kivalliq Igneous Suite: Anorogenic bimodal magmatism at 1.75Ga in the western Churchill Province, Canada. Precambrian Research, 262, 101–119. http://doi.org/10.1016/j.precamres.2015.02.019

Peucat, J. J., Ménot, R. P., Monnier, O., & Fanning, C. M. (1999). The Terre Adelie basement in the East-Antarctica Shield: Geological and isotopic evidence for a major 1.7 Ga thermal event; comparison with the Gawler Craton in South Australia. Precambrian Research, 94(3–4), 205–224. http://doi.org/10.1016/S0301-9268(98)00119-3

Peucat, J. J., Capdevila, R., Fanning, C. M., Ménot, R. P., Pécora, L., & Testut, L. (2002). 1.60 Ga felsic volcanic blocks in the moraines of the Terre Adélie Craton, Antarctica: Comparisons with the Gawler Range Volcanics, South Australia. Australian Journal of Earth Sciences, 49(5), 831–845. http://doi.org/10.1046/j.1440-0952.2002.00956.x

Pisarevsky, S. A., Elming, S. Åke, Pesonen, L. J., & Li, Z. X. (2014). Mesoproterozoic paleogeography: Supercontinent and beyond. Precambrian Research, 244, 207–225. http://doi.org/10.1016/j.precamres.2013.05.014

Rainbird, R.H., and Davis, W.J. (2007), U-Pb detrital zircon geochronology and provenance of the late Paleoproterozoic Dubawnt Supergroup: Linking sedimentation with tectonic reworking of the western Churchill Province, Canada: Bulletin ofthe Geological Society of America, 119, 2007, 314–328, doi: 10.1130/B25989.1

Rainbird, R. H., Hadlari, T., Aspler, L. B., Donaldson, J. A., LeCheminant, A. N., & Peterson, T. D. (2003). Sequence stratigraphy and evolution of the Paleoproterozoic intracontinental Baker Lake and Thelon basins, western Churchill Province, Nunavut, Canada. Precambrian Research, 125(1–2), 21–53. http://doi.org/10.1016/S0301-9268(03)00076-7

Reid, A., Smith, R. N., Baker, T., Jagodzinski, E. A., Selby, D., Gregory, C. J., & Skirrow, R. G. (2013). Re-Os dating of molybdenite within hematite breccias from the vulcan Cu-Au prospect, olympic Cu-Au province, South Australia. Economic Geology, 108(4), 883–894. http://doi.org/10.2113/econgeo.108.4.883

Reis, H. L. S., & Alkmim, F. F. (2015). Anatomy of a basin-controlled foreland fold-thrust belt curve: The Três Marias salient, São Francisco basin, Brazil. Marine and Petroleum Geology, 66, 711–731. http://doi.org/10.1016/j.marpetgeo.2015.07.013

Ricketts, B.D., Evenchick, C.A., Anderson, R.G., and Murphy, D.C., (1992), Bowser Basin, northern British Columbia: constraints on the timing of initial subsidence and Stikinia-North America terrane interactions: Geology, 20, 1992, 1119–1122, doi: 10.1130/0091-7613 020<1119:BBNBCC>2.3.CO;2

Rogers, J. J. W., & Santosh, M. (2002). Configuration of Columbia, a Mesoproterozoic Supercontinent. Gondwana Research, 5(1), 5–22. http://doi.org/10.1016/S1342-937X(05)70883-2

Ross, G.M., Parrish, R.R., and Winston, D. (1992), Provenance and UPb geochronology of the Mesoproterozoic Belt Supergroup (northwestern United States): implications for age of deposition and pre-Panthalassa plate reconstructions: Earth and Planetary Science Letters, 113, 57–76, doi: 10.1016/0012-821X(92)90211-D

Ross, G. M., & Villeneuve, M. (2003). Provenance of the Mesoproterozoic (1.45 Ga) Belt basin (western North America): Another piece in the pre-Rodinia paleogeographic puzzle. Bulletin of the Geological Society of America, 115(10), 1191–1217. http://doi.org/10.1130/B25209.1

Ross, G. M., Parrish, R. R., & Winston, D. (1992). Provenance and UPb geochronology of the Mesoproterozoic Belt Supergroup (northwestern United States): implications for age of deposition and pre-Panthalassa plate reconstructions. Earth and Planetary Science Letters, 113(1–2), 57–76. http://doi.org/10.1016/0012-821X(92)90211-D

Rudnick, R. L., & Gao, S. (2014). Composition of the Continental Crust. Treatise on Geochemistry: Second Edition (2nd ed., Vol. 4). Elsevier Ltd. http://doi.org/10.1016/B978-0-08-095975-7.00301-6

Saura, E., Garcia-Castellanos, D., Casciello, E., Parravano, V., Urruela, A., and Vergés, J., (2015), Modeling the flexural evolution of the Amiran and Mesopotamian foreland basins of NW Zagros (Iran-Iraq): Tectonics, 34, 377–395, doi: 10.1002/2014TC003660.

Sears, J. W., & Price, R. A. (1978). The Siberian Connection: A case for Precambrian separation of the North American and Siberian cratons. Geology, 6, 267–270.

Sears, J. W., & Price, R. A. (2002). The Hypothetical Mesoproterozoic Supercontinent Columbia: Implications of the Siberian-West Laurentian Connection. Gondwana Research, 5(1), 35–39. http://doi.org/10.1016/S1342-937X(05)70885-6

Shufeldt, O. P., Karlstrom, K. E., Gehrels, G. E., & Howard, K. E. (2010). Archean detrital zircons in the Proterozoic Vishnu Schist of the Grand Canyon, Arizona: Implications for crustal architecture and Nuna supercontinent reconstructions. Geology, 38(12), 1099–1102. http://doi.org/10.1130/G31335.1

Skirrow, R. G., Bastrakov, E. N., Barovich, K. M., Creaser, R. A., Fanning, C. M., Raymond, O. L., & Davidson, G. J. (2007). Timing of Iron Oxide Cu-Au-(U) Hydrothermal Activity and Nd Isotope Constraints on Metal Sources in the Gawler Craton, South Australia. Economic Geology, 102, 1441–1470.

Sláma, J., Košler, J., Condon, D. J., Crowley, J. L., Gerdes, A., Hanchar, J. M., Whitehouse, M. J. (2008). Plešovice zircon - A new natural reference material for U-Pb and Hf isotopic microanalysis. Chemical Geology, 249(1–2), 1–35. http://doi.org/10.1016/j.chemgeo.2007.11.005

Söderlund, U., Patchett, P. J., Vervoort, J. D., & Isachsen, C. E. (2004). The 176Lu decay constant determined by Lu-Hf and U-Pb isotope systematics of Precambrian mafic intrusions. Earth and Planetary Science Letters, 219(3–4), 311–324. http://doi.org/10.1016/S0012-821X(04)00012-3

Stern, R. A. (1997). The GSC Sensitive High-Resolution Ion Microprobe (SHRIMP): analytical techniques of zircon V-Th-Pb age determinations and performance evaluation. Natural Resources Canada, 1–33. http://doi.org/10.1126/science.ns-6.149S.521-a

Stern, R. A., & Amelin, Y. (2003). Assessment of errors in SIMS zircon U-Pb geochronology using a natural zircon standard and NIST SRM 610 glass. Chemical Geology, 197(1–4), 111–142. http://doi.org/10.1016/S0009-2541(02)00320-0

Szpunar, M., Hand, M., Barovich, K., Jagodzinski, E., & Belousova, E. (2011). Isotopic and geochemical constraints on the Paleoproterozoic Hutchison Group, southern Australia: Implications for Paleoproterozoic continental reconstructions. Precambrian Research, 187(1–2), 99–126. http://doi.org/10.1016/j.precamres.2011.02.006

Thompson, R. I., Roots, C. F., & Mustard, P. S. (1992). Geology of Dawson map area (116B, C) (northeast of Tintina Trench). Geological Survey of Canada, Open File 2849.

Thorkelson, D. J. (2000). Geology and mineral occurrences of the Slats Creek, Fairchild Lake and ``Dolores Creek'' areas, Wernecke Mountains (106D/16, 106C/13, 106C/14), Yukon Territory. Exploration and Geological Services Division, Yukon Region, Bulletin (Vol. 10).

Thorkelson, D. J., Abbott, J. G., Mortensen, J. K., Creaser, R. A., Villeneuve, M. E., Mcnicoll, V. J., & Layer, P. W. (2005). Early and Middle Proterozoic evolution of Yukon, Canada. Canadian Journal of Earth Sciences, 42, 1045–1071. http://doi.org/10.1139/E04-075

Thorkelson, D. J., & Laughton, J. R. (2016). Paleoproterozoic closure of an Australia-Laurentia seaway revealed by megaclasts of an obducted volcanic arc in Yukon, Canada. Gondwana Research, 33(May 2016), 115–133. http://doi.org/10.1016/j.gr.2015.01.004

Thorkelson, D.J., Mortensen, J.K., Davidson, G.J., Creaser, R.A., Perez, W.A., and Abbott, J.G., (2001a) Early Mesoproterozoic intrusive breccias in Yukon, Canada: The role of hydrothermal systems in reconstructions of North America andAustralia: Prec. Res., 111, 2001a, p. 31–55, doi: 10.1016/S0301-9268(01)00155-3.

Thorkelson, D. J., Mortensen, J. K., Creaser, R. A., Davidson, G. J., & Abbott, G. J. (2001b). Early Proterozoic magmatism in Yukon, Canada: constraints on the evolution of northwestern Laurentia. Canadian Journal of Earth Sciences, 38(10), 1479–1494. http://doi.org/10.1139/cjes-38-10-1479

van Staal, C. R., Zagorevski, A., McNicoll, V. J., & Rogers, N. (2014). Time-Transgressive Salinic and Acadian Magmatism and Old Red Sandstone Sedimentation in Newfoundland. Geoscience Canada, 41, 138–163.

Verbaas, J., Thorkelson, D. J., Gibson, H. D., Marshall, D. D., & Milidragovic, D., 2014, Soft sediment textures in clasts in Wernecke Breccia: Reconstruction of an eroded late Paleoproterozoic succession in northern Yukon. In MacFarlane, K.E., Nordling, M.G., Sack, P.J. (Ed), Yukon Exploration and Geology 2014, Yukon Geological Survey, 145-146.

Wade, C. E., Reid, A. J., Wingate, M. T. D., Jagodzinski, E. A., & Barovich, K. (2012). Geochemistry and geochronology of the c. 1585 Ma Benagerie Volcanic Suite, southern Australia: Relationship to the Gawler Range Volcanics and implications for the petrogenesis of a Mesoproterozoic silicic large igneous province. Precambrian Research, 206–207, 17–35. http://doi.org/10.1016/j.precamres.2012.02.020

Whitmeyer, S. J., & Karlstrom, K. E. (2007). Tectonic model for the Proterozoic growth of North America. Geosphere, 3(4), 220. http://doi.org/10.1130/GES00055.1

Williams, P. J., & Skirrow, R. G. (2000). Overview of iron oxide-copper-gold in the Curnamona province and Cloncurry district (Eastern Mount Isa), Australia. In Porter, T.M., Ed., Hydrothermal Iron Oxide Copper-Gold Related Deposits: A Global Perspective: Adelaide, PGC Publishing, 1(105–122).

Woodhead, J., Hergt, J., Shelley, M., Eggins, S., & Kemp, R. (2004). Zircon Hf-isotope analysis with an excimer laser, depth profiling, ablation of complex geometries, and concomitant age estimation. Chemical Geology, 209(1–2), 121–135. http://doi.org/10.1016/j.chemgeo.2004.04.026

Zhang, S., Li, Z. X., Evans, D. A. D., Wu, H., Li, H., & Dong, J. (2012). Pre-Rodinia supercontinent Nuna shaping up: A global synthesis with new paleomagnetic results from North China. Earth and Planetary Science Letters, 353–354, 145–155. http://doi.org/10.1016/j.epsl.2012.07.034

Zhao, G., Cawood, P. A., Wilde, S. A., & Sun, M. (2002). Review of global 2.1-1.8 Ga orogens: Implications for a pre-Rodinia supercontinent. Earth-Science Reviews, 59(1–4), 125–162. http://doi.org/10.1016/S0012-8252(02)00073-9

Zhao, G., Sun, M., Wilde, S. A., & Li, S. (2004). A Paleo-Mesoproterozoic supercontinent: Assembly, growth and breakup. Earth-Science Reviews, 67(1–2), 91–123. http://doi.org/10.1016/j.earscirev.2004.02.003

Chapter 4.

Formation of the Wernecke Breccia

This chapter has not been published. A modified version will be prepared for publication.

4.1. Abstract

The Wernecke Breccia is a set of 1.599 Ga hematitic megabreccias in Yukon, northern Canada. The breccias crosscut the Paleoproterozoic Wernecke Supergroup and are distributed over an area of 48,000 km^2. Locally, the breccias host iron oxide copper gold (IOCG) mineralization. The Wernecke Breccia contains clasts of up to 800 metres in size that foundered at least several kilometres deep into the breccia zones. The breccia set is extensive and intensely altered and lacks evidence of concurrent magmatism. Despite considerable study by academic researchers, geological survey geologists and economic geologists, the exact processes that formed the Wernecke Breccia remain unclear. Previously proposed models include formation by mud diapirism, evaporite diapirism and surging hydrothermal fluids. Boundary conditions for breccia formation are outlined and previously proposed and new models for their formation are evaluated. It is concluded that the Wernecke Breccia formed from surging hydrothermal fluid with a significant gaseous component (possibly CO_2 and/or N_2) followed by aqueous metasomatism. The ascending fluid expanded dramatically near the surface, caused extensive brecciation and vented. The aqueous phase consisted of metamorphic waters, formational waters and/or meteoric water. A possible source of gas is CO_2 exsolved from carbonatitic melts at depth.

4.2. Introduction

Many iron oxide copper and gold deposits are hosted within large hydrothermal breccia zones. The scale and extent of brecciation has been termed a defining characteristic of IOCG deposits (Groves et al., 2010). IOCG deposits are perhaps the most

complex deposit type and their formation has been extensively debated. The majority of IOCG deposits are characterized by magnetite and/or hematite alteration, concurrent magmatism, and rare earth element (REE) enrichment (Hitzman et al., 1992; Williams, 2005; Groves et al., 2010). Accordingly, many are regarded as products of magmatism and related hydrothermal activity. However, some IOCGs are not demonstrably related to concurrent magmatism and their origins require other explanations. One set of IOCG occurrences that has not been directly tied to magmatism is hosted by the Wernecke Breccia, a set of hematitic breccias in northwestern Canada (Thorkelson et al., 2001a; Hunt et al., 2007). Determining the processes that formed these breccias is important for the understanding of the IOCG mineral deposit class.

The Wernecke Breccia is a 1.6 Ga set of IOCG-bearing breccias in northern Yukon, Canada (Archer and Schmidt, 1978; Laznicka and Edwards, 1979; Bell, 1986a, b; Thorkelson, 2000; Thorkelson et al., 2001a). The breccias crop out in an area of 300 x 150 km and host numerous IOCG occurrences that have attracted mineral exploration for several decades (Archer et al., 1977; Archer and Schmidt, 1978; Hitzman et al., 1992; Thorkelson, 2000; Thorkelson et al., 2001a; Thorkelson et al., 2005). Neither the Wernecke Breccia nor the surrounding rock exhibits evidence for concurrent magmatism (Thorkelson et al., 2001a, Hunt et al., 2007, 2011). Researchers have suggested several mechanisms for the formation of the breccias including mud diapirism (Lane, 1990), evaporite diapirism (Bell, 1986b; Hunt et al., 2005), fault brecciation (Delaney, 1985), diatreme emplacement (Bell and Delaney, 1977; Archer et al., 1977; Bell, 1978; Tempelman-Kluit, 1981) and hydrothermal fluid surges (Hitzman et al., 1992.; Thorkelson et al., 2001a; Furlanetto et al., 2013; Nielsen et al., 2013; Thorkelson and Laughton, 2016). The hydrothermal and diatreme explanations have been broadly linked to possible but undocumented magmatism (Archer et al., 1977; Archer and Schmidt, 1978; Thorkelson et al., 2001a; Kendrick et al., 2008). However, igneous rocks within the breccia province are now known to be separated in age by at least 100 m.y. than the breccias, and the nearest known coeval igneous rocks are located hundreds of km away (Hunt and Thorkelson, 2006; Hamilton and Buchan; 2010). Other indirect evidence for magmatism around 1.6 Ga is present 350 km to the southwest in the McKenzie Mountains in the form of a zircon inheritance age in a xenolith of the Coates Lake Diatreme (1.6 ± 0.25 Ga, Jefferson and

Parrish, 1989) and as a 1565 ± 1 Ma zircon xenocryst in the Little Dal Basalts (Milton et al., 2014).

In this chapter, previously proposed and new models for Wernecke Breccia formation are described and evaluated. Field relations, geochemistry and geochronology are used to constrain the processes that formed the breccias. Some models of formation are rejected and others are considered plausible under specific geological conditions. These models may be applicable to other breccia provinces and prove to be valuable for mineral exploration.

4.3. Location, extent, and country rock

The Wernecke Breccia consists of numerous individual breccia zones that occur in the Ogilvie, the Wernecke, and the southern Richardson mountains in northern Yukon, Canada (Thorkelson et al., 2005). Individual breccia zones range in size from 0.1 – 10 km^2 and occur over an area of approximately 48 000 km^2 (Thorkelson et al., 2001a; Thorkelson et al., 2005).

The Wernecke Breccia is hosted by the Wernecke Supergroup (Figure 4.2., Delaney, 1981; Thorkelson, 2001a), a Paleoproterozoic succession of >13 km of metasedimentary rock that is interpreted as a passive margin succession (Thorkelson et al., 2005; Furlanetto et al., 2013). The base of the Wernecke Supergroup is not exposed (Delaney, 1981; Thorkelson, 2000). Based on gravity and seismic data, 5 – 9 km of stratified rocks underlie the exposed Wernecke Supergroup (Hall and Cook, 1998; Crawford et al., 2010; Furlanetto et al., 2016). The Wernecke Supergroup formed after 1.66 Ga, constrained by detrital zircon geochronology (Furlanetto et al., 2013). Sedimentation of the Wernecke Supergroup was terminated at ~1.61 Ga by the Racklan Orogeny (Furlanetto et al., 2013). The Racklan Orogeny involved basin inversion, thrusting and folding, and middle greenschist facies metamorphism at 15 – 25 km depth (Thorkelson, 2000; Thorkelson et al., 2005; Furlanetto et al., 2013). The Wernecke Supergroup and the unexposed strata below were deposited on crystalline basement (Furlanetto et al., 2016). Although not exposed, the basement is likely attenuated igneous and metamorphic crust of the Canadian Shield (Thorkelson et al. 2005).

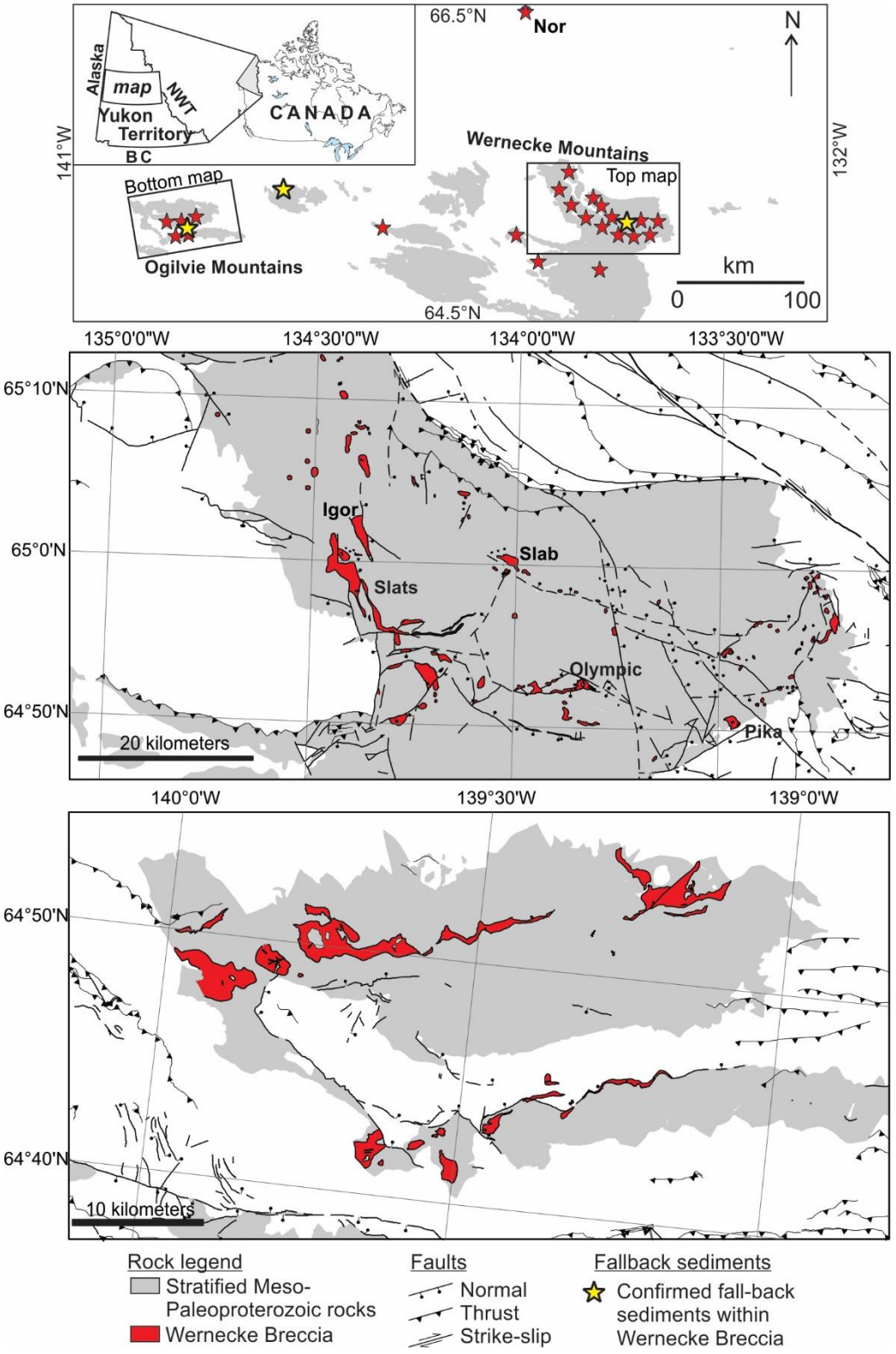

Figure 4.1. Location of the Wernecke Breccia and mineral occurrences discussed in the text.

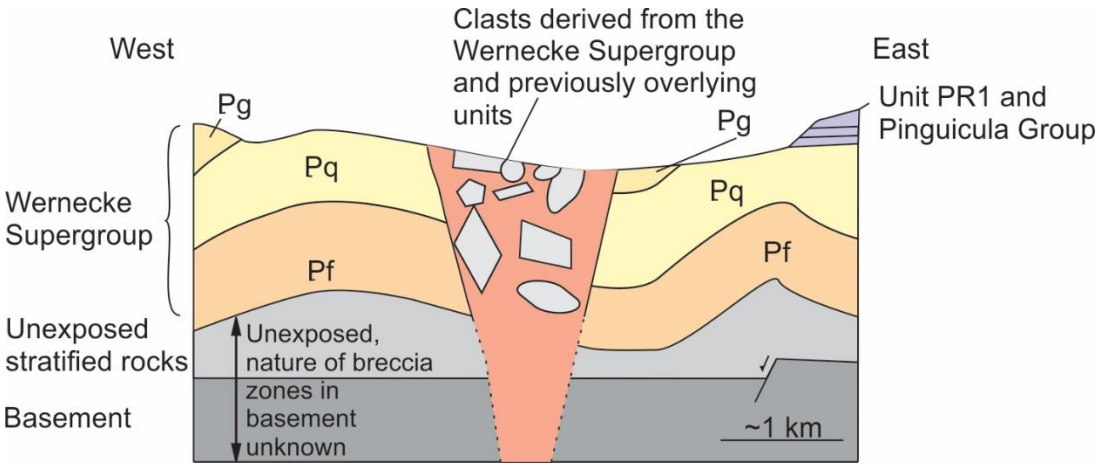

Figure 4.2. Schematic geological cross section for Wernecke Breccia localities in the Wernecke and Ogilvie mountains (vertical exaggeration approximately 10x). The Wernecke Supergroup is subdivided into the Fairchild Lake Group (Pf), Quartet Group (Pq) and the Gillespie Lake Group (Pg). In some parts of the study area, the Fairchild Lake Group is exposed at the surface. The age and nature of subsurface strata are uncertain. The age of crystalline basement may be ca. 1.85 Ga (Thorkelson et al., 2005). The maximum depth of breccia zones is unknown.

The Wernecke Breccia is composed of angular to sub-angular clasts within a metasomatic matrix (Figure 4.3A, Thorkelson et al., 2001a). The clasts range in size from a few millimetres to 800 x 300 x 30 m (Nielsen et al., 2013) and are predominantly clasts from the Wernecke Supergroup. The Wernecke Breccia crosscuts metamorphic fabrics and strata of the Wernecke Supergroup (Figure 4.3C). The random orientation of the schistose clasts and the crosscutting nature of the Wernecke Breccia indicate the Wernecke Supergroup was deformed and metamorphosed prior to brecciation (Figure 4.3B, Thorkelson et al., 2001a). The boundary with the country rock ranges from sharp to gradational over several tens of metres (Thorkelson et al., 2001a). Locally, intrusive, plutonic, and sedimentary rocks of other affinities are present within the Wernecke Breccia zones (Figure 4.3D, Thorkelson et al., 2001a, b; Nielsen et al., 2013; Furlanetto et al., 2013).

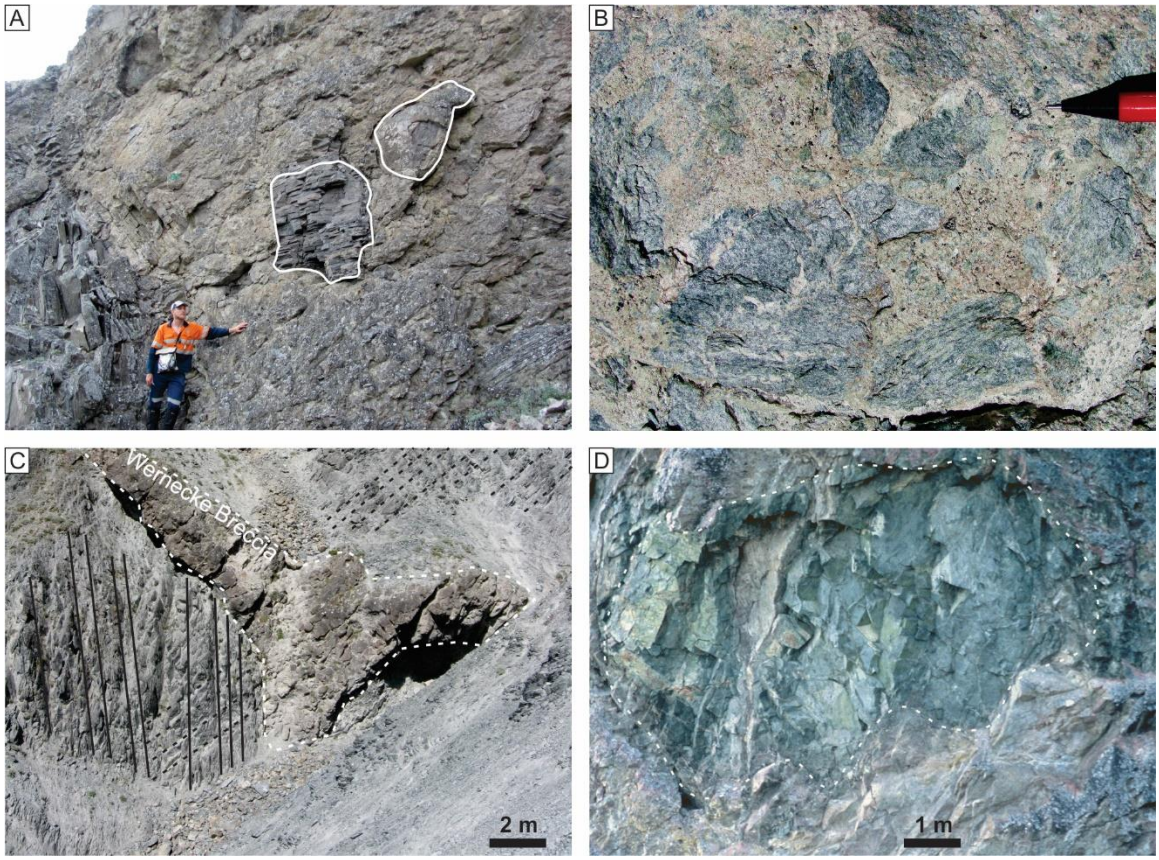

Figure 4.3. **A. Angular and rounded clasts within a sodically altered breccia zone at the Slab mineral occurrence. B. Randomly oriented schistose clasts of the Wernecke Supergroup encased in hydrothermal matrix. C. Wernecke Breccia near the Slab mineral occurrence crosscuts at least two metamorphic fabrics (solid and dashed lines) developed within chloritoid-garnet schist of the Fairchild Lake Group. D. Large clast of Bonnet Plume River intrusion near the Slab mineral occurrence, outlined by dashed white line.**

4.4. Crustal column at the time of brecciation

At the time of breccia formation, the crust contained several units that are currently unexposed or removed by erosion. Our understanding of the crust at that time is largely based on the diversity of clasts within the Wernecke Breccia. Most clasts were derived from the Wernecke Supergroup, and a minority of clasts were derived from units that were positioned above the Wernecke Supergroup (Thorkelson et al., 2001a; Furlanetto et al., 2013; Nielsen et al., 2013). Some of these clasts represent an obducted terrane named

Bonnetia (Furlanetto et al., 2013; Nielsen et al., 2013; Thorkelson and Laughton, 2016), and others represent an overlying sedimentary succession (Verbaas et al., 2014).

4.4.1. Accretion of an oceanic arc

Clasts interpreted to have been derived from the obducted terrane, Bonnetia, occur within many of the breccia zones throughout the region. The Bonnetian clasts include plutonic and volcanic lithologies named the Bonnet Plume River intrusions, the Devil volcanics and the Slab volcanics, and range up to 900 x 300 x 30 metres in size (Nielsen et al., 2013; Thorkelson and Laughton, 2016). Clasts from the Bonnet Plume River intrusions were dated via U-Pb on zircon at ca. 1.71 Ga (Thorkelson et al., 2001b). The plutonic and volcanic lithologies have chemical compositions consistent with derivation from a calc-alkaline to weakly tholeiitic oceanic arc that was modified by plume or slab window processes (Nielsen et al., 2013; Thorkelson and Laughton, 2016). Bonnetia was interpreted as part of an oceanic volcanic arc that was obducted onto the Wernecke Supergroup during the Racklan Orogeny (Chapter 3; Furlanetto et al., 2013; Nielsen et al., 2013; Thorkelson and Laughton, 2016). Bonnetia was completely eroded after the formation of the Wernecke Breccia at 1599 Ma and before Mesoproterozoic deposition of the Pinguicula Group and unit PR1 (Figure 4.2). It is preserved only as clasts that foundered into Wernecke Breccia (Furlanetto et al., 2013).

4.4.2. An overlap assemblage on the Gawler Craton and Yukon Territory

Locally, sedimentary clasts within Wernecke Breccia display soft-sediment textures, suggesting these clasts were originally unlithified when they were incorporated into the Wernecke Breccia. These clasts represent an unlithified succession termed the Wernecke-Ogilvie unlithified succession (WOUS) that was deposited on northwestern Laurentia during the formation of the Wernecke Breccias (Chapters 2, 3). Clasts of the WOUS foundered into the breccia zones alongside igneous clasts derived from Bonnetia and the Wernecke Supergroup. The WOUS clasts include well-bedded sandstone to mudstone, a tightly packed conglomerate of sandstone and mudstone “rip up” clasts, and fluidally deformed mudrock. Locally these lithologies encase or coat clasts of the

Wernecke Supergroup and Bonnetia and are interpreted to have been lithified after descending into the breccia zones (Verbaas et al., 2014)

Based on detrital zircon geochronology, whole rock geochemistry, and field relations, the WOUS is interpreted as part of an overlap assemblage that was deposited on top of the Gawler Craton and Mount Painter Inlier of Australia, and northwestern Laurentia (Chapter 3). Notably, similar sedimentary lithologies have been described within the Olympic Dam Breccia Complex on the Gawler Craton in South Australia (McPhie et al., 2011a; 2016), which has been correlated with the Wernecke Breccia (Thorkelson et al., 2001a). Both breccias formed at approximately 1.6 Ga and are characterized by hematite alteration and associated IOCG mineralization (Figure 4.4; Johnson and Cross, 1995; Thorkelson et al., 2001a).

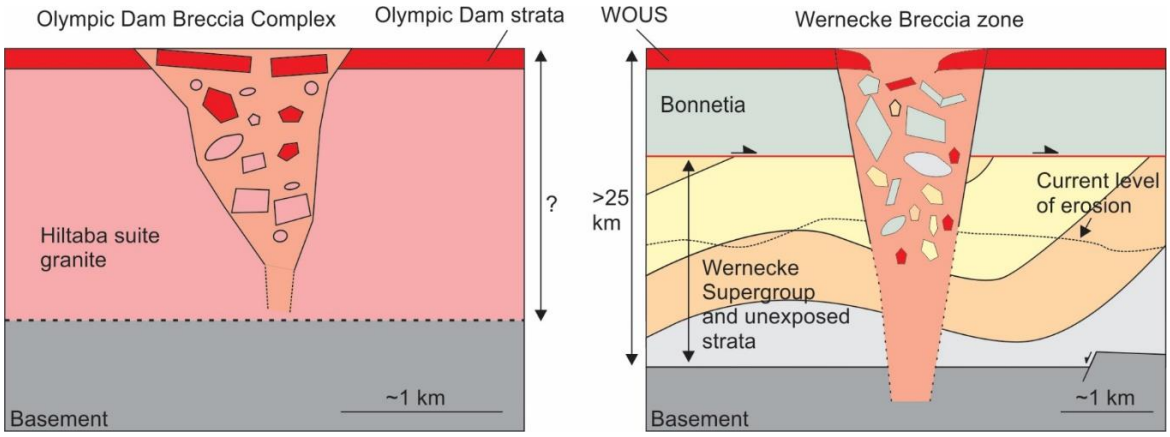

Figure 4.4. Schematic cross section at the time of brecciation (modified from Thorkelson and Laughton, 2016). Thicknesses of units after Delaney et al., 1981; Thorkelson, 2000; Nielsen et al., 2013; Furlanetto et al., 2016. The obduction is considered to have occurred after erosion of the Racklan orogen. The nature of the breccia zones in the basement is unknown.

4.4.3. Paleogeographic context

Western Laurentia, Australia and East Antarctica were closely associated with one another during the existence of the supercontinent Columbia (also termed Nuna), from ca. 1.9- 1.45 Ga (Goodge et al., 2008; Zhang et al., 2012; Furlanetto et al., 2016). The rock record on all three continents is consistent with continental collisions and subsequent adjustments involving extension, contraction, magmatism, basin formation and sediment

transport (Young et al., 1979; Ross et al., 1992; Thorkelson et al., 2005; Betts and Giles, 2006; Gibson et al., 2008; 2012; Medig et al., 2014; Furlanetto et al., 2016; Thorkelson and Laughton, 2016). One of these adjustments involved extension between Australia and Laurentia starting between 1.8 and 1.75 Ga, and led to passive-margin deposition of the Wernecke Supergroup on Laurentia between ca. 1.66 and 1.61 Ga (Furlanetto et al., 2013).

Deposition of the Wernecke Supergroup was followed by convergence between Australia and Laurentia (Furlanetto et al., 2013; Nielsen et al., 2013; Thorkelson and Laughton, 2016). Bonnetia, which had grown as an oceanic arc along the margin of Australia (Thorkelson and Laughton, 2016; Chapter 3) became wedged between Australia and Laurentia during closure of the intervening ocean and was obducted during the Racklan Orogeny. After the Racklan Orogeny, Bonnetia existed as an allochthon on the Wernecke Supergroup (Figure 4.4). Following obduction of Bonnetia, the WOUS was deposited on the Gawler Craton and northwestern Laurentia (Chapter 3). The Wernecke Breccia formed during deposition of this overlap assemblage and contains clasts of the Wernecke Supergroup, the allochthon Bonnetia, and the overlap assemblage (Figure 4.4).

Wernecke brecciation was followed by a 150 m.y. interval of apparent quiescence on Laurentia. This interval of stability was terminated by renewed rifting of Australia and Laurentia as indicated by sedimentation and magmatism (Ross et al., 1992; Thorkelson et al., 2005). Between ca. 1.5 and 1.4 Ga, sediments of Australian provenance were deposited on the margin of Laurentia in the PR1, Belt-Purcell, Trampass and Hess Canyon basins (Ross and Villeneuve, 2003; Doe et al., 2012; Daniel et al., 2013; Medig et al., 2014). The provenance of the sediments shifted rapidly from Australian to Laurentian sources, and contiguity between the two continents appears to have ended by ca. 1.45 Ga (Jones et al., 2015). Localized magmatism on Laurentia at 1.47 Ga (Anderson and Davis, 1995) and 1.38 Ga (Doughty and Chamberlain, 1996; Thorkelson et al., 2005) was coeval with sedimentation. Widespread magmatism in northern Laurentia occurred at 1.27 Ga (LeCheminant and Heaman, 1989; Schwab et al., 2004). The continents were reattached during formation of the supercontinent Rodinia (Moores et al., 1981; Dalziel et al., 1991; Li et al., 2008).

4.5. Wernecke Breccia field relations

4.5.1. Breccia occurrence and composition

The Wernecke Breccia is exposed over 48 000 km^2, spanning more than 300 km from east to west and 150 km from north to south (Thorkelson et al., 2001a). At 1.6 Ga, the Wernecke Breccia and Gawler Olympic IOCG province formed a continuous 120 000 km^2 hydrothermal province (Thorkelson et al., 2001a; Chapter 3). Individual breccia zones range from a few tens of metres to several km across, and vary from nearly circular to elongate. They occur in curvilinear patterns although subsequent faulting largely controls this distribution, particularly in the Ogilvie Mountains where the trends are most pronounced (Lane and Godwin, 1992).

The Wernecke Breccia formed in all levels of the Wernecke Supergroup and in the overlying terrane Bonnetia. Within the Wernecke Supergroup, the breccias developed within a broad range of lithologies including meta-siltstone, fine-grained quartzite, slate, phyllite, schist, dolostone and marble. Within Bonnetia, the breccias developed mainly within diorite, gabbro, and mafic volcanic rocks.

Contacts between breccia zones and the Wernecke Supergroup are sharp, or gradational over several metres, and crosscut both primary sedimentary and secondary structural features (Thorkelson, 2000). Commonly, the degree of brecciation gradually decreases outward into the country rock (Lane, 1990; Thorkelson, 2001a; Hunt et al., 2005). The breccias range from clast- to matrix-supported. The clasts are typically angular but are locally rounded (Figure 4.3A). The rounded clasts may reflect clast milling, abrasion, and hydrothermal dissolution (Thorkelson et al., 2001a). The clast/matrix ratio ranges from 30 – 70 % and is highly variable.

Breccia clasts are typically metasomatized and typically display variable colours and growth of secondary hematite, quartz, carbonate, chlorite, scapolite and a variety of other minerals (Figure 4.3B). As with brecciation, the effects of metasomatism may end abruptly at the breccia margin, but they more commonly grade into the country rock for metres or tens of metres. The metasomatism has variably affected different beds and laminae of the Wernecke Supergroup, locally yielding a variegated mottled or striped

appearance in both the clasts and the marginal country rock (Figure 4.5A, B). In the plutonic clasts derived from Bonnetia, the metasomatism is largely manifested as disseminations of hematite and magnetite, and veins of hematite quartz, epidote and carbonate, typically flanked by potassic alteration haloes (Figure 4.5C, D).

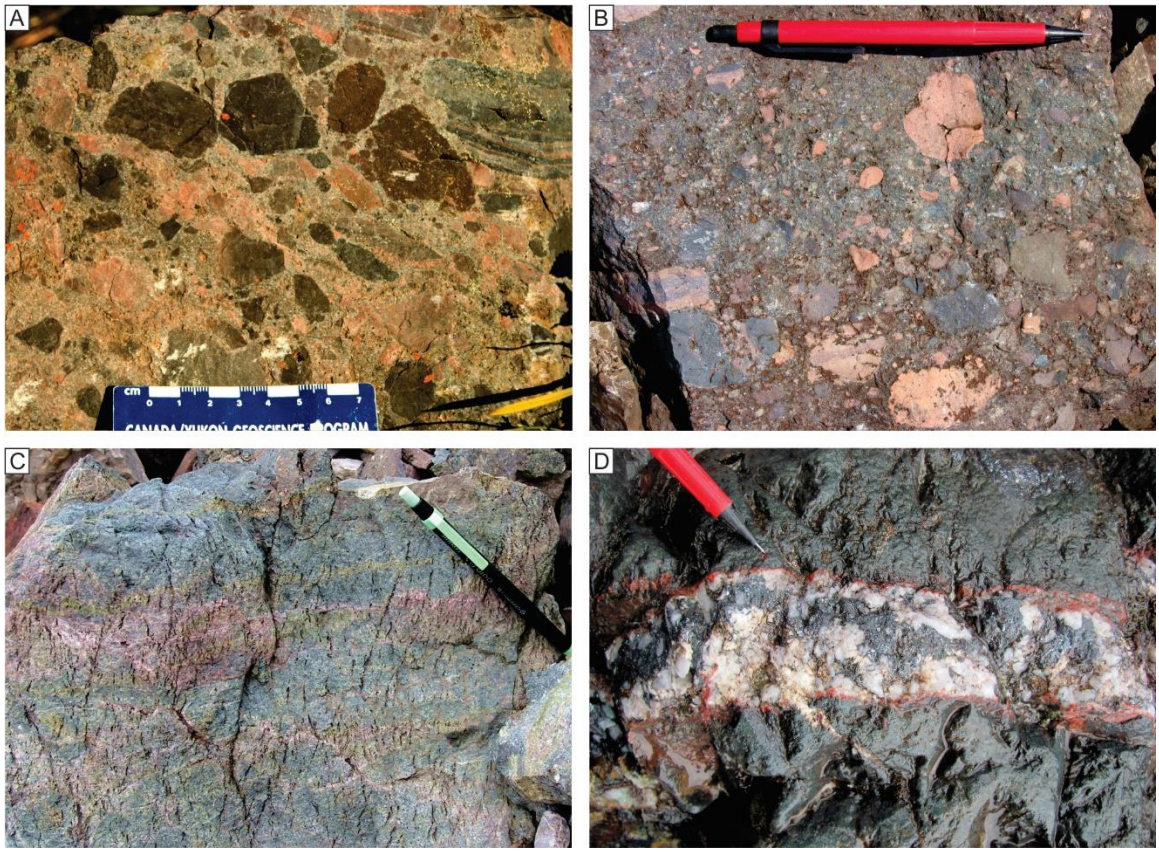

Figure 4.5 **A. Wernecke Breccia with a variety of siltstone and dolostone clasts displaying discoloration and mottling within a mainly silicate-hematite matrix. B. Hematitic matrix displaying potassic discolouration of clasts at the Pika mineral occurrence. C. Epidote (green) and hematite-potassic feldspar (pink) and carbonate (brown) veins in a Bonnet Plume River Intrusion clast, Sihota mineral occurrence D. Specular hematite-quartz-carbonate vein with potassic selvage in Bonnet Plume River Intrusion clast, Yukon Olympic mineral occurrence.**

The clasts are cemented by a variety of silicate minerals. One prominent breccia at Slab Mountain in the Wernecke Mountains is cemented by a granular assemblage of quartz, hematite, magnetite, albite, microcline, phlogopite and titanite (Thorkelson et al., 2001a). Other breccia zones contain similar cement assemblages and include minerals

such as muscovite, scapolite and carbonate. Chlorite is locally common but may represent mineral growth under retrograde conditions. Carbonate minerals (calcite, dolomite and ankerite) and sulphide minerals (notably pyrite and chalcopyrite) occur mainly in disseminations, patches and veins that developed late in the history of breccia formation and mineralization (Hunt et al., 2005).

The history of brecciation in many breccia zones was polygenetic (Thorkelson et al, 2001a). Laznicka and Gaboury (1988) argued for at least ten pulses of re-brecciation at one breccia locality. At another, Hunt et al. (2001) showed that there were at least two pulses of brecciation with the second yielding crosscutting, tabular zones characterized by rounded clasts and hosted by a more angular-clast breccia.

4.5.2. Post-orogenic timing of brecciation

The Wernecke Breccia postdates regional deformation and metamorphism of the Racklan Orogeny (Thorkelson et al., 2000, 2001a, 2005; Furlanetto et al., 2013). The breccias crosscut deformational and metamorphic fabrics of the Racklan Orogeny (Thorkelson et al., 2000, 2001a). These fabrics include schistosity, crenulations and kink bands developed in the lower stratigraphic levels of the Wernecke Supergroup. Randomly oriented clasts of slate, phyllite and schist of the Wernecke Supergroup occur within many of the breccia zones (Thorkelson et al., 2001a), indicating that the Wernecke Supergroup was deformed and metamorphosed prior to brecciation. The orogenesis is likely to have eliminated original formational waters from within the Wernecke Supergroup strata, leaving them fully lithified with little pore space.

Wernecke Breccia was dated at 1598.8 ± 1 Ma via U-Pb on fragments of two metasomatic titanite grains of a single breccia zone at the Slab mineral occurrence (Furlanetto et al., 2013). A similar U-Pb date of 1595 ± 5 Ma on metasomatic titanite from the same breccia zone was published by Thorkelson et al. (2001b). The Racklan Orogeny was dated by Lu-Hf on garnet, with the best isochron yielding an age of 1593 ± 67 Ma (Furlanetto et al., 2013). Although the age-ranges overlap, the aforementioned field relations clearly indicate that the Wernecke Breccia formed after peak metamorphism of the Racklan Orogeny.

In the model proposed by Furlanetto et al. (2013), the deformation of the Wernecke Supergroup and the obduction of Bonnetia were discrete phases of the Racklan orogeny, separated by an interval of erosion and denudation. This interpretation explains the occurrence of all three groups of the Wernecke Supergroup at the surface prior to obduction, the disparity in fluid inclusion temperatures and pressures within the Wernecke Breccia (Hunt et al., 2011), and the temperature and associated depth of the peak metamorphism of the Wernecke Supergroup (Furlanetto et al., 2013). Although this model is self-consistent, it does not identify the tectonic drivers for the phases of Racklan Orogeny. The landmasses that are currently recognized to have collided with the northwestern margin of Laurentia at ca. 1.6 Ga are Bonnetia and Australia (Thorkelson et al., 2001a; Betts and Giles, 2006; Furlanetto et al., 2013; Medig et al., 2014; Thorkelson and Laughton, 2016; Gibson et al., 2017). The pre-obduction deformation may have been generated by the arrival of Bonnetia and its accretion to the Laurentian margin. Bonnetia could have been subsequently obducted during collision between Australia and Laurentia. Other explanations, including collisions between Laurentian and unidentified terranes, remain possible.

The Wernecke Breccia formed in the northern Wernecke Mountains, the Ogilvie Mountains and the Richardson Mountains where the Racklan deformation of the Wernecke Supergroup is known to have occurred (Chapter 5). Racklan deformation is not evident in the southern Wernecke and southeastern Ogilvie mountains (Abbott, 1997; Moroskat, 2009; Chapter 5), and neither are zones of Wernecke Breccia. In the Gawler Olympic IOCG province, brecciation was restricted to rocks of greenschist grade (Hand et al., 2007). It is possible that the combined Gawler-Yukon IOCG hydrothermal province was limited to previously deformed and metamorphosed rocks, although how such tectonism may have contributed to brecciation is unknown.

4.5.3. Alteration, mineralogy and fluid inclusions

The Wernecke Breccia is mainly potassically altered, although a large subset in the Wernecke Mountains are sodically altered (Laughton et al., 2003). Albite, scapolite, calcite, dolomite, orthoclase, ankerite, sericite and barite comprise the main alteration minerals (Hunt et al., 2005). Both alteration types are locally overprinted by chloritic and

carbonate alteration in the form of disseminations and veins. Hitzman (1992) developed a model in which different alteration types were correlated to depth of breccia formation. However, as noted by Thorkelson et al. (2001a), this interpretation was based upon the incorrect premise that the Wernecke Breccia formed prior to deformation of the Wernecke Supergroup, a situation in which stratigraphic position could be equated to crustal depth. Hunt et al. (2005, 2011) related the host rock chemistry to the type of alteration, however, this interpretation is dependent on the presence of (meta-)evaporites in the Wernecke Supergroup for which there is no independent evidence. Carbon, sulfur, hydrogen, and oxygen isotopes appear to be buffered by the immediate country rock (Hunt et al., 2011). A large variation exists between the alteration at different mineral occurrences, which has been explained as varying halite dissolution, input of different fluids including magmatic and meteoric waters, and depth of formation (Hitzman, 1992; Kendrick et al., 2008; Gillen, 2010; Hunt et al., 2011).

Three studies on mineralized Wernecke Breccia occurrences focused on the chemistry of fluid inclusions. The data obtained from these studies include noble gas and halogen isotopes (Kendrick et al., 2008), chemical compositions of fluid inclusions (Gillen, 2010; Hunt et al., 2011) and stable isotope ratios (Hunt et al., 2011). The mineralizing fluids of the Wernecke Breccia are saline NaCl-CaCl-H_2O brines (15 – 45 wt. % NaCl equiv.; Gillen et al., 2010; Hunt et al., 2011). Gillen (2010) hypothesized bittern brines to be the dominant fluid type, but also noted one sample bearing possibly primary, single-phase CO_2 inclusions among larger aqueous inclusions. A high $^{40}Ar/^{36}Ar$ in some fluid inclusions, notably those in the Igor occurrence, were interpreted by Kendrick et al., (2008) to represent mixing of magmatic water with the bittern brines. Gillen (2010) argued against the presence of any surface-derived water and concluded that formational water was salinized by evaporites in the Wernecke Supergroup. In contrast, Hunt et al., (2011) inferred that the fluids represent either formational or hydrothermal waters and argued against the input of any magmatic fluids.

Models for the formation of Wernecke Breccia must be able to account for 1) high salinities of metasomatising fluids and 2) dominantly H_2O and minor CO_2 inclusions. Although the exact sources of the fluids are debated, all authors invoke mixing of different

types of aqueous metasomatising fluids (Kendrick et al., 2008; Gillen, 2010; Hunt et al., 2011).

4.5.4. Foundering of igneous clasts within the breccia zones

Clasts within Wernecke Breccia were not all sourced from the immediate country rock, i.e., the Wernecke Supergroup. In several breccia zones, igneous clasts represent the dominant clast type. At many localities, the breccias include abundant igneous rocks derived from Bonnetia (Nielsen et al., 2013). This abundance implies that many of the clasts moved downward through the breccia zones, coming to rest hundreds of metres, or perhaps kilometres, from their points of origin (Furlanetto et al., 2013; Nielsen et al., 2013). As such, the Wernecke breccias are regarded as transported breccias (Laznicka, 1988).

The settling of clasts within the breccia zones must have been accompanied by creation of accommodation space (transient open space). Field relations at the Olympic, Slab and Pika mineral occurrences in Yukon provide a basis for the accommodation space required for the settling of clasts within the Wernecke Breccia. At the Olympic mineral occurrence, which hosts abundant clasts from the Bonnet Plume River intrusions, clasts larger than 10 m constitute about 30% of the breccia zone (Figure 4.6A, Thorkelson et al., 2000; Nielsen et al., 2013). At the Slab mineral occurrence, a 160 x 380 m clast of the Slab volcanics occurs near the edge of a large Wernecke Breccia zone. Other plutonic and volcanic clasts occur throughout the breccia zone (Laughton et al., 2005; Hunt et al., 2002) but not all are not mapped in detail. At the Pika mineral occurrence, Bonnet Plume River intrusion clasts are the dominant clast type (Figure 4.6B). The largest igneous clast at this occurrence is at least 800 x 300 x 30 m in size.

A model of formation needs to be consistent with the foundering of very large clasts within the breccia zones. Before clasts came to rest, the Wernecke Breccia zones were filled with a medium that was less dense than the clasts themselves, such as air, hydrothermal fluid, evaporites, or mud. The removal of rock and creation of accommodation space may have occurred through dissolution, elutriation (the removal of fine particles around larger fragments during brecciation), ejection, dilation or a combination of these mechanisms.

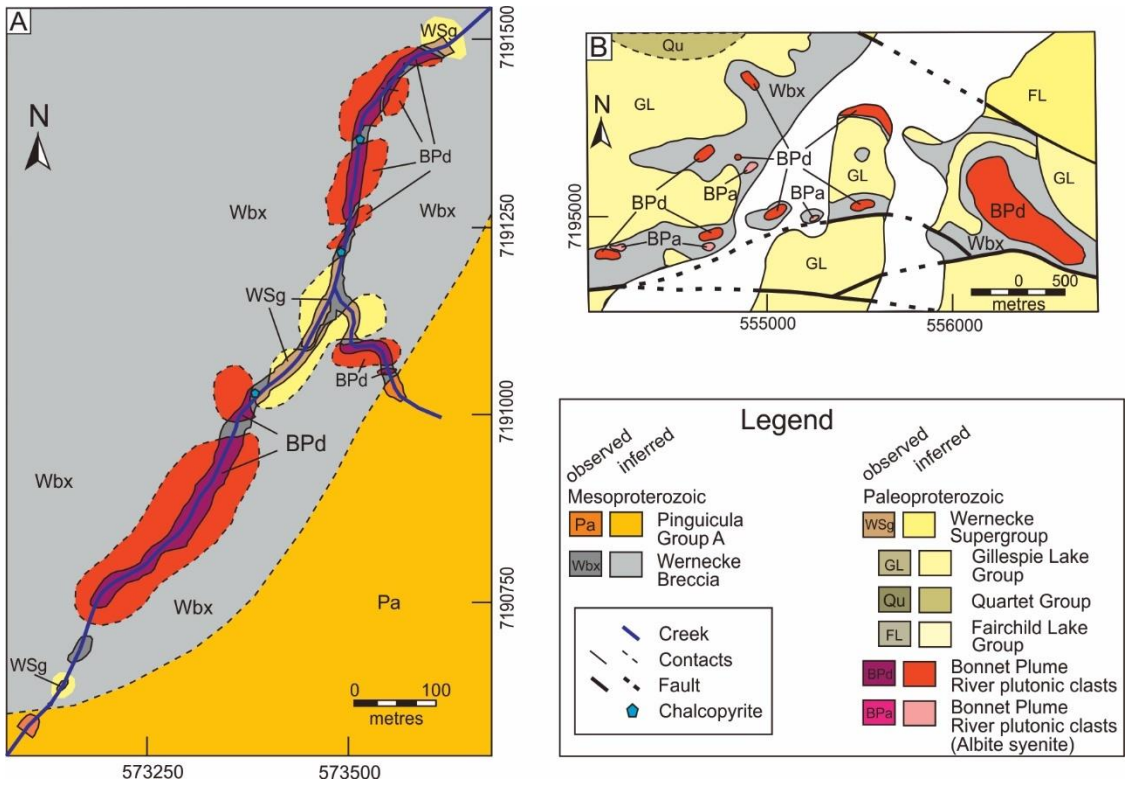

Figure 4.6. Mapping around the Pika (A) and Olympic (B) mineral occurrences (After Nielsen et al., 2013).

4.5.5. Quantifying depth of clast foundering

The Wernecke Breccia zones were emplaced at significant depth. The mineralogy of the breccia zones lacks significant clay grade alteration (Thorkelson et al., 2001a). Furlanetto et al. (2013) and Nielsen et al. (2013) noted that all of the igneous clasts from Bonnetia must have foundered deep into the breccia zones in order for the clasts to now lie adjacent to the Wernecke Supergroup. Fluid inclusion studies indicate that the breccia zones were emplaced at 6 to 11 km depth (Gillen, 2010; Hunt et al., 2011). Considering these depth estimates together with the interpretation that some rocks were sourced from the former overlying terrane Bonnetia, an attempt is made here to establish the depth of clast foundering.

Following the model proposed by Furlanetto (2013), Nielsen (2013) and Thorkelson and Laughton (2016) published comprehensive studies on the plutonic and volcanic clasts within Wernecke Breccia. Nielsen et al. (2013) used the fluid inclusion

studies by Hunt et al. (2011) in order to estimate the thickness of Bonnetia at 4-9 km. However, if fluids in the breccia zones were hotter than within the adjacent wall-rock this thickness, and the resulting depth of clast foundering may be overestimated. Given that plutonic and volcanic clasts could have been derived from short distances above the thrust contact between Bonnetia and the Wernecke Supergroup, Nielsen et al. (2013), estimated a depth of clast foundering of 2 km.

The WOUS soft-sediment material which is preserved in some of the breccia zones must have been derived from at or near the Earth's paleosurface. Hence the WOUS material must have foundered all the way from the surface, through Bonnetia, to where it lithified and is currently preserved. Although fluid inclusion studies were not undertaken on the breccia zones that are confirmed to contain WOUS material, the mineralogical characteristics of these breccia zones are similar across the entire breccia province, indicating that they all formed at similar depths. Using a thickness for Bonnetia of 4-9 km, as proposed by Nielsen et al. (2013), for the entire obducted terrane, the minimum depth of foundering for the WOUS soft-sediments would have been 5 km (4 km plus the current relief). However, the mineralogy of the breccia cement, as listed above, is more consistent with depths >5 km and perhaps deeper than 10 km.

4.5.6. Magmatism at depth?

The hydrothermal IOCG province that encompassed the Wernecke Breccia and the Olympic Dam deposit was accompanied by voluminous magmatism on the Gawler Craton (Reynolds, 2000; Skirrow et al., 2002, 2007) and Curnamona Province (Conor and Preiss, 2008; Wade et al., 2012) and, 50 – 100 m.y. later, in the Cloncurry district of the Mount Isa Inlier (Williams and Skirrow, 2000). However, surficial 1.6 Ga magmatism is not present proximal to the Wernecke Breccia, instead, the nearest coeval igneous rock is that of the 1.59 Ga Western Channel diabase, approximately 500 km east-northeast of the Wernecke Breccia (Hamilton and Buchan, 2010). In their paleomagnetic reconstruction of the Gawler Craton, Curnamona province and northwestern Laurentia, Hamilton and Buchan (2010) placed the Wernecke Breccia zones between the Benagerie Volcanics of the Curnamona Province and Gawler Range Volcanics on the Gawler Craton, 500 km to the west, and the Western Channel diabase 500 km to the east. Approximately 1600 km

to the south of the Wernecke Breccia, a 1.6 Ga dyke is exposed (Rogers et al., 2016). It is possible that the Western Channel diabase and the dyke dated by Rogers et al. (2016) are distal expressions of the extensive volcanism on the Gawler Craton. Inherited zircon in the Coates Lake diatreme, 350 km southeast of the Wernecke Breccia (Jefferson and Parrish, 1989), provides additional evidence for an igneous event at ca. 1.6 Ga. Was the Laurentian lithosphere beneath Yukon Territory also affected by magmatism at depth but not in the upper crust?

Several researchers have hypothesized that the Wernecke Breccia formed concurrently with emplacement of unexposed intrusions (Jefferson and Parrish, 1989; Hitzman et al., 2000; Thorkelson et al., 2001b; Kendrick et al., 2008). However, field relations and age determinations have not yielded any evidence that the Wernecke Breccia formed as the result of a magmatic process. The Bonnet Plume River intrusions and Slab volcanics were originally thought to have been emplaced concurrently with the breccias (Thorkelson et al., 2001a; Laughton, 2005), but subsequent age determinations (Furlanetto et al., 2013) revealed that the Bonnet Plume River intrusions are 110 m.y. older than the Wernecke Breccia. Hunt et al. (2011) interpreted fluid compositions to reflect a mix of formational waters and evaporitic waters, although the $\delta^{18}O$ and δD values of one sample overlap with those of primary magmatic waters. On the basis of noble gas isotopes, particularly high $^{40}Ar/^{36}Ar$ ratios, Kendrick et al. (2008) argued that fluid sourced from a deep-seated but not necessarily contemporaneous intrusion was important in some Wernecke Breccia occurrences.

4.5.7. Breccia formation model constraints

The hydrothermal province in which the Wernecke Breccia formed was larger than 48 000 km^2. The combined Gawler Olympic IOCG – Wernecke Breccia province was much larger still and spans 120 000 km^2. Individual Wernecke Breccia zones range in width from several metres to several kilometres and likely extended from the surface to depths of at least 5 km, and likely >10 km. Clasts range in size from several millimetres to hundreds of metres across. Unlithified sandy mud from the WOUS foundered from the surface to >5 km deep prior to lithification.

The Wernecke Breccia formed after contractional deformation and metamorphism, and after the obduction of the volcano-plutonic terrane Bonnetia. A shallow sea or large lake was present on top of Bonnetia at the time of brecciation (Chapters 2, 3) and may have contributed to the metasomatizing fluids. The breccia system and its immediate wallrock were affected by metasomatism and localized IOCG mineralization. There was no volcanism or plutonism in the upper crust at the time of brecciation within the Wernecke Breccia province. Hence metasomatism was facilitated by non-igneous sources of aqueous fluid that contained minor components of CO_2 and N_2.

4.5.8. Tectonic environment of formation

The Wernecke Breccia formed in a specific tectonic environment that may have occurred at other times and places during Earth evolution. Constraining this tectonic environment may be valuable to plate reconstructions, hydrothermal system analysis, and mineral exploration. Of particular interest is the nature and origin of the combined Gawler Olympic IOCG province and the Wernecke Breccia province, which were likely caused by similar processes at approximately the same time (Thorkelson et al., 2001a; Chapter 3).

The Wernecke Breccia formed after collision between Australia and Laurentia (Chapter 3), and after peak metamorphism of the Racklan Orogeny, during which Wernecke Supergroup was subjected to greenschist facies metamorphism. Australia and Laurentia were connected until ~1.45 Ga or later, when intracontinental rift basins formed on Laurentia (Medig et al., 2014). The absence of 1.6 Ga sedimentary successions or extensional fault systems is consistent with breccia formation in a convergent setting.

The Wernecke Breccia formed without concurrent magmatism at the same crustal level. It is possible that magmatism occurred in deeper levels of the crust. On the Gawler Craton, IOCG deposits formed coeval with a siliceous large igneous province (SLIP) with minor mafic volcanism (the Gawler Range Volcanics; Allen et al., 2003). Although there is a lack of magmatic fluids within the Wernecke Breccia, whether the Wernecke Breccia could have formed without any input from magmatism remains unclear.

4.6. Previous and new hypotheses

4.6.1. Assessment of model viability

Several models for the origin of Wernecke Breccia have been previously proposed, and additional hypotheses are described herein. Each of these ideas is evaluated by analyzing if it conforms to the boundary conditions outlined in the previous sections. The models and hypotheses taken into consideration are mud volcanism (Lane, 1990), evaporite diapirism (Bell, 1986b), rock dissolution (Bell, 1986b; Hunt et al., 2005), phreatic and phreatomagmatic activity (Ernst et al., 2009), hydrothermal eruption cratering (Laughton et al., 2003), diatreme activity (Tempelman-Kluit, 1981), fault brecciation (Bell, 1978; Laznicka and Edwards, 1979; Delaney, 1985), hydrothermal brecciation (Laznicka and Edwards, 1979; Hitzman et al., 1992; Thorkelson et al., 2001a; Laughton et al., 2003), and impact brecciation. The summarized assessments are tabulated in Table 4.1. Breccia formation by hydrothermal fluid surges is most consistent with the boundary conditions. However, the mechanism through which fluids surged from depth is an impediment to this model. A new hypothesis that invokes expansion of CO_2 as the main cause of brecciation is presented.

Table 4.1. Evaluation of formational processes and boundary conditions of the Wernecke Breccia

	Boundary condition → / Model ↓	Removal of material from sub-surface	Fall-back of clasts to >5 km depth	Compatible with metasedimentary and igneous host rock	Amagmatic process	Fluid inclusion constraints
Slow	Evaporite diapirism	***Removal of evaporites***	*No space generated until dissolution*	*salt is commonly removed durng burial prior to orogeny*	***Yes***	***Yes***
	Mud diapirism	***Removal of water-laden clay***	*No space generated*	*Dewatering occurs during burial, prior to orogeny*	***Yes***	*No*
	Rock dissolution	***Yes***	***Yes***	*Inconsistent with variety of host lithologies*	***Yes***	*Possibly*
	Fault brecciation	*No*	*No*	***Yes***	***Yes***	***Yes***
	Phreatic and phreatomagmatic eruptions	***Removal by ejection and elutriation***	*Unlikely but possible with multiple eruptions and subsidence*	***Yes***	*No*	*No*
	Hydrothermal eruptions	***Removal by ejection and elutriation***	*Deepest phreatic eruption ejected material from ~500m*	***Yes***	*Amagmatic but in volcanic fields*	*No*
	Kimberlitic volcanism	***Removal by ejection and elutriation***	***Possibly in cases of multiple eruptions and crater floor subsidence***	***Yes***	*No*	*No*
	Amagmatic hydrothermal fluid surges	***Removal by ejection and elutriation***	***Yes***	***Yes***	***Yes***	*gas under-represented*
Fast	Impact brecciation	***Removal by ejection***	*No*	***Yes***	*If impact does not cause melting*	*No*

4.6.2. Diapirism and dissolution

Mud diapirism

Lane (1990) proposed a genetic model involving mud diapirism based on the presence of soft-sediment deformation textures in clasts within the Wernecke Breccia. In a mud volcano or diapir, mud and its entrained clasts flow to the surface and accumulate in a volcano-like mound. The ascension of mud is driven by a density inversion resulting from a high proportion of water in mud within unlithified sediments, and the maximum depth of mud mobilization is estimated to be on the order of a few kilometres (Kopf, 2002). The mud would typically contain abundant water-bearing minerals of the smectite, kaolinite, and vermiculite mineral groups (Rakhmanov, 1987; Kopf, 2002). Lane (1990) concluded that the mud originated in the Fairchild Lake Group, i.e., beneath the Quartet and Gillespie Lake groups, and became mobile during faulting.

Lane's (1990) model was based on the possibility that the Wernecke Breccia formed prior to lithification and orogenesis. However, the breccias locally contain randomly oriented clasts of schist derived from the Fairchild Lake Group (Thorkelson et al., 2001a). The mineral assemblage of the schist is quartz-muscovite-chlorite-biotite-chloritoid +/- garnet. Biotite-garnet geothermometry and garnet Lu-Hf geochronology indicates a peak temperature of ~500 °C, corresponding to a depth of 15 – 25 km, at ca. 1.6 Ga (Furlanetto et al., 2013). The presence of clasts of schist derived from the Wernecke Supergroup in the breccia demonstrates that brecciation occurred in metasedimentary rock, not mud, and that the Wernecke Breccia was not caused by mud diapirism.

The clasts with soft-sediment textures described by Lane are reinterpreted to have been sourced from the WOUS, which was an unconsolidated surface deposit at the time of brecciation (Chapter 3), rather than the Fairchild Lake Group. Furthermore, the matrix of the Wernecke Breccia is commonly metasomatic (Thorkelson et al., 2001a), except in rare localities where green mud of the WOUS encapsulates clasts of Wernecke Breccia (Verbaas et al., 2014; Chapter 3).

Evaporite diapirism

Models of breccia formation involving evaporites were first invoked by Bell (1986b) and later by other workers (Hunt et al., 2005, 2011; Kendrick et al., 2008; Gillen, 2010). In an evaporite diapirism model, clasts of country rock would have initially become entrained in a rising lobe or diapir of evaporite. Subsequently, as the evaporitic material dissolved, a cavity in the crust would form, the wallrock would fracture and break, and a mix of clasts would settle into the developing cavity (Bell, 1986b). Potential indicators for former evaporitic beds in the Wernecke Supergroup are scapolite grains in the Wernecke Breccia and the Fairchild Lake Group (Hunt et al., 2005; 2011), as well as high salinity fluid inclusions (Gillen, 2010; Hunt et al., 2011), and high-Mg biotite (Hunt et al., 2005). The high salinity of the metasomatising fluids in Wernecke Breccia is consistent with salinity control by evaporites or connate waters (Hunt et al., 2011; Yardley and Graham, 2002), but may also be explained by a magmatic fluid component.

The deposition of evaporites occurs when evaporation exceeds recharge in rift basins that have a restricted or no connection to the ocean. Hence, evaporite diapirism is not uncommon in passive margin sequences (Michaelovitch de Mahiques et al., 2017). However, the evaporitic source beds typically lie below the passive margin strata (Rowan, 2014). Evaporites tend to become upwardly mobile at depths of a few kilometres, but can be buried up to depths of 15 km, such as in the Gulf of Mexico (Peel et al., 1995; Hudec and Jackson, 2006). Mobile evaporites are capable of piercing strata and transporting kilometre-sized clasts (Warren, 2016).

Recognizing evaporite diapirism in ancient rocks is difficult because eventually all evaporites dissolve completely, leaving behind only specific structures, minerals, breccias and fluids (Warren, 2016). The dissolution of evaporites leads to several types of breccia such as collapse breccia (Waltham et al., 2005; Gutierrez, 2010), solution collapse breccia (Warren, 2016) and breccia pipes and chimneys (Quinlan, 1978). Clasts from both deeper levels and higher levels in the crusts can occur in an evaporite generated breccia chimney because evaporites initially transport clasts from deeper levels upward, and upon dissolution clasts from higher levels can founder into the space formerly occupied by the evaporites.

In Namibia, halokinesis (evaporite movement) in the Duruchaus Formation was triggered by overthrusting of the Kudis Thrust Nappe (Schmidt-Mumm et al., 1987). The overpressure provided by the thrust nappe generated widespread halokinesis and associated brecciation. The evaporites were sourced from more than a kilometre of sabkha sediments, and the halokinetic breccias are associated with abundant scapolite and dravitic tourmaline (Behr et al., 1983; Schmidt-Mumm et al., 1987). In Sweden, meta-evaporites are present in the Sitka Formation as layers of magnesite, scapolite and halokinetic breccias over a 30 m stratigraphic interval in an amphibolite facies thrust nappe (Svenningsen, 1974).

In the Wernecke Supergroup, scapolite occurs as discrete layers of 5 mm up to 30 cm thick in a >50 m thick sequence of chloritoid-garnet schist of the Fairchild Lake Group (Hunt et al., 2005). However, there are no characteristic stratabound breccias that indicate removal of large quantities of evaporites within that section of the crust. Other mineralogical indicators of evaporites such as magnesite (Svenningsen, 1974) and dravite-tourmaline (Behr et al., 1983; Schmidt-Mumm et al., 1987; Warren, 2016), within either the Wernecke Breccia or the Wernecke Supergroup have not been reported. The evidence for meta-evaporites in the Wernecke Supergroup is especially limited in comparison to other meta-evaporites in the world (Serdyuchenko, 1975), such as in the Duruchaus Formation in Namibia, and in the Sitka Formation in Sweden.

Furlanetto et al. (2016) showed that approximately 5-9 km of strata underlie the Wernecke Supergroup. Is it possible that evaporites were present in these strata? The Wernecke Supergroup has been interpreted as a passive margin sequence (Thorkelson et al., 2000; Furlanetto et al., 2013; Furlanetto et al., 2016). Evaporites are therefore not expected to have been part of the Wernecke Supergroup, but may have been present below the currently exposed strata in rift-related sediments. If abundant evaporites were present below the exposed base of the Wernecke Supergroup, halokinesis likely occurred during burial, considering the Wernecke Supergroup is >13 km thick. Evidence from the Wernecke Supergroup, or the Wernecke Breccia does not indicate syn-depositional evaporite movement, nor significant removal of evaporites (Delaney, 1981; Thorkelson, 2000).

The analogue between the Wernecke Supergroup and the Duruchaus Formation in Namibia seems attractive because both successions were overthrust by an allochthonous terrane. However, peak metamorphism of the Racklan Orogeny preceded the formation of the Wernecke Breccia. The Fairchild Lake Group was buried to 9 – 13 km depth during sedimentary burial and then to 15-25 km and 500 °C during peak metamorphism of the Racklan Orogeny. If halokinesis originated within the Fairchild Lake Group or deeper layers then diapirism would have likely been triggered during sedimentary burial, and before the onset of metamorphism. Other field relations are also inconsistent with a model involving evaporite diapirism. Clasts within Wernecke Breccia have all been transported downwards or remained at the same level within the crust (Thorkelson et al., 2001a), instead of transported both upwards and downwards. Furthermore, solution breccia, the dominant breccia type in evaporite-generated breccia zones, is a rare breccia type within the Wernecke Breccia (Hunt et al., 2005). An additional difficulty with the evaporite model is that the overlying terrane Bonnetia was largely composed of plutonic and volcanic rock units. If evaporite piercement and dissolution were the causes of brecciation, then evaporite diapirs must have risen through the entire obducted terrane of Bonnetia. Considering the strength and cohesiveness of plutonic and volcanic rock, this scenario appears unlikely.

Rock dissolution

The dissolution of rock can form cavities that eventually collapse (Laznicka, 1988). Bell (1986) and Hunt (2005) hypothesized that dissolution and collapse of evaporites were partly responsible for the formation of the Wernecke Breccia. Thorkelson et al. (2001a) noted that many clasts in the Wernecke Breccias were embayed and apparently corroded. Hunt (2005) suggested that rock dissolution was a significant cause of brecciation at some localities.

A dissolution cavity can cave in to form a collapse breccia with clasts derived from slightly higher levels in the crust. Rocks that are especially susceptible to dissolution are evaporites and carbonates. Collapse breccias are therefore most common in association with 1) karst environments (Osborne, 2013), 2) Mississippi Valley Type (MVT) deposits (Leach, 2010), and 3) evaporite diapirism (as discussed previously). Dissolution of limestone can form caves in the uppermost crust that are kilometres in size (Osborne,

2013). Flowing water in caves commonly leads to sedimentation and the formation of flowstone. Sedimentary structures and ore mineral textures that indicate open space are also common in MVT deposits (Leach et al., 2010). Silicate rock is far more chemically resistant than carbonate rock, but can be dissolved in high-temperature hydrothermal vents, such as those in the Yellowstone caldera (Guidry and Chafetz, 2003; Vandemeulebrouck et al., 2013), or under conditions of high acidity. Fluid reservoirs that feed geysers, where host rock is dissolved, can reach 20 metres in size (Vandemeulebrouck et al., 2013). Acid-caused silicate rock dissolution and collapse from high concentrations of HF, on the basis of F-rich fluid inclusions, has been proposed for the Olympic Dam breccia complex (McPhie et al., 2011b).

Rock dissolution can create caverns similar in size to zones of Wernecke Breccia. However, certain features of Wernecke Breccia are inconsistent with rock dissolution as the main cause of breccia formation and open space development. First, the size of Wernecke Breccia zones does not vary significantly among the various types of Wernecke Supergroup host rock. Specifically, the breccia zones within the Gillespie Lake Group, which is dominantly dolostone, are no larger than the zones within the Quartet and Fairchild Lake groups, which are dominantly meta-siltstone. Thus, the tendency of corrosive fluids to preferentially dissolve carbonate over silicic rocks is not reflected in corresponding breccia zone size differences. Furthermore, mass dissolution of the meta-siliciclastic rocks would likely require corrosion by hydrofluoric acid, but this option is unlikely considering that fluorine was not a significant component of the metasomatizing fluids in Wernecke Breccia (Kendrick et al., 2008; Gillen, 2010; Hunt et al., 2011b) and fluorite is scarce within the Wernecke Breccia. A third point is that Wernecke Breccia zones are up to thousands of metres across and extended from the surface to deeper than 5 km, far deeper than currently known hydrothermal vents, karst zones and MVT deposits (Guidry and Chafetz, 2003; Leach et al., 2010; Osborne, 2013). finally, the formation of flowstone in the breccia zones, even in those that are hosted by carbonate rock, has not been observed, casting further doubt on the possibility of karst-style dissolution and cavern development.

4.6.3. Fault brecciation

A spatial connection between regional patterns of faulting and breccia zone distribution was recognized by many researchers including Bell (1986a), Hitzman et al. (1992), Lane (1990), Thorkelson (2000) and Hunt (2005). In particular, strands of the Richardson Fault Array in the Richardson and Wernecke mountains (Norris, 1981) and prominent faults in the Ogilvie Mountains (Thompson, 1992) coincide with many of the breccia zones. In addition, many breccia zones are elongated along the faults. These connections led Bell (1978), Laznicka and Edwards (1979) and Delaney (1985) to propose that faulting was the principal cause of brecciation. In contrast, Thorkelson et al. (2001a) noted that many of the breccia zones are not located along faults and Hunt et al., (2005) suggested that the connection between faults and breccia zones was due to the breccias exploiting crustal weaknesses produced by previous faulting. The Richardson Fault Array and other regional faults in the area were active in Cenozoic (Norris and Dyke, 1997), and some strands remain active; other strands may have been active at earlier times, perhaps as far back as the Proterozoic.

Under brittle conditions, the interior of a fault is commonly characterized by fault breccia, gouge and cataclasite, and under ductile conditions by mylonite. Planar and linear fabrics are common, with clast sizes and orientations reflecting the fault kinematics. Clasts within fault breccias can only be sourced from lithologies present a maximum of one throw above (in the footwall) or below (in the hanging wall) the location of the fault breccia. Dilational jogs and void collapse structures have been well documented and can be tens of metres wide (Woodcock et al., 2006; Melosh et al., 2014). However, dilational jogs and void collapse structures are not open to the surface and commonly contain clasts directly sourced from within the fault or from adjacent country rock. In some fault systems clasts have been transported significant distances. In the Minas Fault zone of Nova Scotia, Canada, clasts derived from near surface conditions are mixed with granulite clasts derived from 35 km depth (Gibbons et al., 1995; 1996).

Planar and linear fabrics are rarely present in the Wernecke Breccia, as most of the clasts show little organization in terms of orientation and size distribution. Instead, the clasts typically occur as disordered shattered rocks that display no planar or linear fabric. At rare locations, cataclastic faulting is evident but is attributable to localized post-breccia

fault motion (Thorkelson et al., 2001a). Some of the clasts within Wernecke Breccia were transported for at least 5 kilometres within the breccia zones. If the Wernecke Breccia formed from faulting, this distance constrains the minimum movement along the fault to 5 km. The near-absence of fault breccia, cataclasite or mylonite, and the lack of significant offset along many of the breccia-coincident faults, are inconsistent with faulting as the primary mechanism for breccia formation.

4.6.4. Kimberlite diatremes

The Wernecke Breccias have been described as kimberlite-related diatremes (Bell and Delaney, 1977; Archer et al., 1977) and as diatremes of unspecified affinity (Tempelman-Kluit, 1981). Kimberlitic diatremes form by explosive volcanism (White and Ross, 2011), and are characterized by narrow, conical craters, commonly called pipes. The diatremes are interpreted to form from the rapid exsolution of volatiles as the kimberlitic magma nears the surface (Sparks, 2013), or from the expansion of CO_2 exsolved at greater depth from a carbonatitic/kimberlitic parental magma (Russell et al., 2012). The brecciation and excavation is caused principally by expansion of magmatic CO_2 according to some researchers (Wilson and Head, 2007; Russell et al., 2012). The diatremes can extend to several kilometres in depth (Wilson and Head, 2007; White and Ross, 2011; Sparks, 2013), form independent of host rock lithology and excavate significant zones of country rock. Shortly after excavation they are infilled by fallback material. Diatreme deposits typically contain fragments of local country rock, lower crust and upper mantle, including eclogite and peridotite (Kwon and Sohn, 2008; Kurszlaukis and Lorenz, 2008). Diatreme deposits are broadly subdivided into massive and layered facies (Sparks et al., 2013). The layered facies occur in the upper part of the kimberlite pipe and consists of layered pyroclastic and/or sedimentary rocks. The massive facies comprise a chaotic mix of kimberlite and country rock fragments and commonly occurs below the layered facies. Clasts within the massive facies commonly range up to several metres in size (Hetman et al., 2004; Brown et al., 2009).

The Wernecke Breccia contains a chaotic mix of fragments, but no layered facies. Abundant fallback material occurs within the Wernecke Breccia. However, there is no

evidence of kimberlitic or carbonatitic magmatism within or around the Wernecke Breccia zones.

4.6.5. Impact brecciation

The genesis of Wernecke Breccia from a nearby impact of a comet or meteorite is an unpublished hypothesis which provides a possible explanation for some of the features of Wernecke Breccia. Two options are worth considering: 1) brecciation caused by a single large impactor, or 2) by a set of smaller ones. In both cases, the central idea is that the high energy of the impact(s) may have been sufficient to cause rapid processes such as crater excavation, intense seismicity, deep fracturing, crustal brecciation and long-lived hydrothermal activity. In shallow marine settings, such as those proposed for the Wernecke Breccia case, tsunami-like resurge into the impact crater and/or downpouring of seawater into deep, transient fracture systems are also contemplated. Fractures at locations directly beneath the crater, and also in peripheral areas (e.g., ring fractures) are worth consideration. In general, such processes may be able to explain some of the characteristics of Wernecke Breccia such as the deep descent of megaclasts into the crust and the high salinity of fluid inclusions.

The structure and variety of lithologies found in an impact crater are dependent on the impactor and the target structure and composition, the size of the impactor, and the velocity and angle of the impact (French and Koeberl, 2010). Impacts generally excavate relatively wide and shallow bowl-shaped depressions with depth to width ratio of ~3:1 (Barnouin et al., 2011), Shock metamorphism, a circular structure and remnants of the impactor are the most diagnostic features of impact cratering (French and Koeberl, 2010). Other features include brecciated rock, and pseudotachylite (from shock and frictional melting), but these can also occur in other geological environments. Impact melts are considered to be generated during or shortly after impact, with the main products being 1) an aerosol of droplets in the crater and surrounding ejecta blanket (Stähle, 1972), and 2) a lens of magma within the upper crust (Barton, 2014). Impact craters are excavated in seconds to minutes (Kenkmann et al., 2010). Fractures around the impact are both radial and concentric and may extend through the entire crust and into the mantle directly below

the impact crater (Kumar and Kring, 2008; Christeson et al., 2009). Post-impact hydrothermal activity has occurred on both Earth and Mars (Osinski et al., 2012).

Two types of breccia are common beneath crater floors, with pseudotachylitic breccia predominant in large impacts craters and clastic-matrix breccias in smaller ones (Dressler and Reimold, 2004). Both types tend to be polymictic and occur in near-vertical dyke-like bodies with widths >10 m and lengths >1000 m (Dressler and Reimold, 2004). Monomictic clastic-matrix breccias also occur distal to some impact craters (Dressler and Reimold, 2004). Pseudotachylitic breccia is commonly flanked by clastic-matrix breccia. In the Sudbury impact complex, clastic-matrix breccias form irregular bodies up to 100 m wide and contain comminuted and rounded clasts of the adjacent country rock (Lafrance et al., 2008). The country rock contains shock metamorphic features that extend several kilometres beyond the clastic-matrix breccia bodies (Dressler, 1984; Krogh et al., 1984).

Resurge breccias are sedimentary deposits in impact craters that formed in marine or lacustrine basins. These breccias form from a post-impact resurge of water into an impact crater and contain centimetre to metre-sized clasts, as documented for the Lockne impact crater (Sturkell, 1992; Azad et al., 2015). The resurge breccia of the Lockne impact is 156 m thick and overlies ca. 100 m monomictic breccia formed as rock avalanche or scree, sourced directly from the impacted rock (cf. Azad et al., 2015). These units host minimal ejecta and impact melt and are restricted to the uppermost crust.

No evidence of shock deformation or impact melts has been recorded in or around the Wernecke Breccia, and there is no evidence for concurrent melting that could be related to an impact melt sheet or pseudotachylitic breccia. However, the current level of erosion could be below the base of a former melt sheet and pseudotachylite. An origin as clastic-matrix breccias is possible but given the lack of shock metamorphic features is considered unlikely. Additionally, the largest impact-related clastic-matrix breccia zones are much smaller than the largest Wernecke Breccias. If the Wernecke Breccia zones formed as resurge breccias, they probably would have all been connected to one another within a bowl-shaped crater. On the contrary, the Wernecke Breccia zones are narrow and deep, and are not connected at the current level of erosion. The only rocks which display

abundant textures of sediment shaking and disaggregation and that may have been affected by resurge are the WOUS clasts.

Breccia zones of the IOCG province that spanned both the Gawler Craton and northwestern Laurentia were formed over a span of roughly 20 m.y. from ~1605 to 1585 Ma (Thorkelson et al., 2001a; Reid et al., 2013). If all of these breccia-hosted IOCG occurrences were produced by several impacts caused by atmospheric breakup of a larger bolide they would have been coeval instead of spanning 20 m.y. One way to accommodate this discrepancy is if much of the brecciation and mineralization occurred significantly after impact. If the impact occurred at the initiation of the breccia province, at 1605 Ma (Mortimer et al., 1988), and created a deep network of fractures on both continents, then these fractures could have been exploited by hydrothermal activity and related brecciation (Pirajno, 2009) over the next several m.y. In the shared Laurentia-Gawler IOCG breccia province, the individual breccia zones would not have formed at the same time, and may have occurred below, above or beside the site of the impact. However, to produce a hydrothermal field of that size, the impact crater would likely have had a diameter of >250 km and the impactor would have been >10 km across (Collins et al., 2005). It seems problematic that such a large impactor would have struck the Earth without leaving shock metamorphic features in a region that later became a massive impact-hydrothermal breccia province. Additionally, a ~1.6 Ga impact crater has not been described in Yukon Territory or South Australia.

4.6.6. Phreatomagmatic and phreatic eruptions

Phreatomagmatic eruptions involve ejections of steam, country rock and magma as a result from groundwater interaction with magma (White and Ross, 2001) and eruptions of gas following the degassing of volatile-rich host rock (Ernst et al., 2009; Polozov et al., 2016). If no magma is ejected the eruption is considered phreatic, and if magma is ejected the eruption is considered phreatomagmatic (Browne and Lawless, 2001). Phreatomagmatic eruptions commonly result in volcanic breccia pipes and/or crater lakes (maars; White and Ross, 2001). Some of the best studied examples of volcanic pipes resulting from groundwater-magma interactions are in the Eifel volcanic field in Germany (Schminke, 2009; Lutz and Lorenz, 2013). Magma-groundwater interaction

cannot produce a crater that is substantially deeper than the groundwater itself. Phreatomagmatic craters can be kilometres deep and originate via explosive activity caused by magmas intruding into strata containing abundant pore water such as shales and evaporites (Ernst et al., 2009). Prerequisites for explosivity are the availability of pore water, brines or groundwater that can interact with the magma (White and Ross, 2001; Grunewald et al., 2007). Numerous phreatomagmatic craters occur above deep sill complexes associated with large igneous provinces (LIPs). One example are the 2-4 km deep Tunguska breccia pipes belonging to the Siberian Traps LIP (Polozov et al., 2016).

No coeval igneous rocks, nor fragments of juvenile magma, are exposed within the Wernecke Breccia province. The absence of synchronous igneous activity eliminates phreatic or phreatomagmatic behavior as the cause of breccia formation. However, even if concurrent magmatism did occur, it is unlikely that it would have had an explosive effect on the Wernecke Supergroup or the overlying terrane Bonnetia. A phreatomagmatic origin would have required an abundance of pore water in addition to an intruding magma. In the Wernecke Supergroup, porosity would have been very low because the rocks were converted from sedimentary protoliths to metamorphic rocks, eliminating almost all pore space in the process (Furlanetto et al., 2013). Bonnetia was dominated by volcanic and plutonic rocks with little pore space. Hence, any breccia-concurrent plutons would not have been able to release a large volume of volatiles from the country rock. Furthermore, the only evidence for the possible involvement of magma are interpretations of fluid inclusion data that permit, but do not require, a small contribution from igneous-equilibrated fluids (Kendrick et al., 2008; Hunt et al., 2011). Younger sills emplaced within the Wernecke Supergroup, including the 1.38 Ga Hart River sills (chapter 5), and the 1.27 Ga Bear River dykes, produced narrow contact metamorphic aureoles but little or no breccia (Thorkelson, 2000; Schwab and Thorkelson, 2004).

4.6.7. Hydrothermal brecciation from crustal fluids

Shallow sourced hydrothermal brecciation

A hydrothermal eruption occurs when the confining pressure of an active hydrothermal system with near-boiling fluids is lowered to the point that the boiling fluids flash to vapor (Browne and Lawless, 2001; Morgan et al., 2009). As a result, the fluids

catastrophically increase in volume. During the initial eruption, rock and gas are expelled from the top of the hydrothermal system which effectively lowers the pressure and boiling point for the hydrothermal fluids deeper in the system. The eruption propagates downwards because of the progressive release of confining pressure. The pressure on a hydrothermal system may be released by a variety of mechanisms, including removal of overburden (Muffler et al., 1971; Morgan et al., 2009), or subsurface hydraulic fracturing (Grindley and Browne, 1976).

All known hydrothermal eruption craters are associated with concurrent volcanic activity (Browne and Lawless, 2001). The Mary Bay hydrothermal eruption crater in the Yellowstone caldera is the largest hydrothermal eruption crater documented and is 2.5 km in diameter (Wold et al., 1977) and was at least 500 m deep during eruption (Browne et al., 1994; Clark, 1999; Morgan et al., 2009). Other well documented hydrothermal eruption craters occur in for example New Zealand and Iceland (Browne and Lawless, 2001). The size of a hydrothermal eruption is controlled by "the extent of existing alteration, the extent of inter-connected fluid filled voids and fractures, host rock lithology, and amount of readily available boiling water" (Morgan et al., 2009).

Laznicka and Edwards (1979) appealed to a combination of non-explosive hydrothermal activity, faulting and igneous intrusion as the main causes of brecciation and alteration in Wernecke Breccia. Hitzman et al. (1992), in a seminal compilation of information on IOCG deposits, considered the Wernecke Breccias to have been generated by near-surface hydrothermal activity, and speculated that the fluids were derived from igneous intrusions that may have been emplaced into the underlying crystalline basement. Thorkelson et al. (2001b) demonstrated that the volcanic and plutonic rocks within the breccia zones were ~100 Ma older than the breccias themselves, and appealed to hydrothermal activity along the previous igneous pathways as the cause of brecciation. All of these works emphasized the importance of hydrothermal activity to brecciation, alteration and economic mineral precipitation. However, the need to explain deep brecciation and foundering of megaclasts to >5 km in a post-orogenic setting had not been fully recognized. Utilizing new information on rock ages and structural deformation, Laughton et al. (2005) showed that the Wernecke Breccia formed after plutonism and orogenesis from a series of intense hydrothermal eruptions that breached the Earth's

surface. In their model, the hydrothermal eruptions led to excavation of deep vents in the uppermost crust and ejection of clasts onto the surface. Immediately afterward, blocks of wallrock “tumbled into the vent from above and became enveloped by a steaming mass of milling, settling breccia.” Foundering of megaclasts was thereby invoked, but was considered to be limited to a few hundred metres depth.

Deep-sourced hydrothermal brecciation

Hydrothermal activity as the cause of brecciation continued to be explored by later workers, but under a new set of tectonic conditions in which brecciation was preceded by the obduction of Bonnetia (Furlanetto et al., 2013). With Bonnetia as the newly recognized source of igneous clasts in the breccias, Furlanetto et al. (2013), Nielsen et al. (2013) and Thorkelson and Laughton (2016) hypothesized that the hydrothermal fluid surges were caused by overpressurization of the Laurentian crust as a result of the obduction of Bonnetia, leading to violent bursts of hydrothermal activity. These surges occurred across northwestern Laurentia, leading to the formation of the Wernecke Breccia. Importantly, this hypothesis emphasized the need for a breccia-forming process that led to accommodation space that allowed clasts from Bonnetia to founder well below the obduction surface, becoming lodged in breccia zones flanked by the underlying Wernecke Supergroup. The great depth of foundering is underscored by the presence of WOUS sediments that descended from the surface through the entire thickness of Bonnetia, and came to rest alongside the Wernecke Supergroup. According to fluid inclusion and stable isotope work of Hunt et al. (2011), the breccias were developed at depths of up to 10 km. The idea of tectonic overpressurization is also consistent with the lack of concurrent magmatism as noted earlier by Thorkelson et al. (2001a) and the absence of a notable igneous component in the fluids as determined by fluid inclusion studies (Kendrick et al., 2008; Gillen, 2010; Hunt et al., 2011).

The hypothesis of overpressurization accords with a general understanding of orogenic dewatering (McCaig, 1989) and “seismic pumping” in which fluids are expelled from the crust during intervals of loading or compression. Considering the relatively low tensile strength of rock, a high fluid pressure is an effective way to crack rocks and create a fluid-filled fracture network (Ague, 2014). In order for a fluid to surge from depth to the surface, it must be significantly overpressurized, a common situation for upper crustal

water that is sealed at depth by a relatively impermeable layer. Above the seal, the water is typically at hydrostatic pressure but below the seal it is commonly above hydrostatic pressure, but below lithostatic pressure (Deming, 2001). If the pressure increases, and/or the seal is breached, the water will flow upwards until pressure equilibrium is attained, or until the seal becomes impermeable again, a process referred to as crack-and-seal. This process is commonly invoked for hydrothermal veins (Sibson, 2000) and related mineral deposits. For each burst, the mass of upward surging water will be limited by the amount of overpressurized water trapped beneath the seal. In orogenic dewatering, the widths of fluid channels may range up to a few cm, although these channels may anastomose into wider zones in dense fracture networks, or along faults and shear zones (Ague, 2014).

Although hydrothermal surges related to the obduction of Bonnetia may be an attractive way to form Wernecke Breccia, in detail the hypothesis is problematic. Normal crack and seal (vein-related) processes appear to be insufficient to generate the high volumes of fluid flow needed to form kilometre-sized breccia zones that host downdropped megaclasts up to 100s of metres in size. Large volumes of overpressurized hydrothermal fluid would need be stored in the crust and then tapped rapidly during an upsurge. However, the location and style of the storage reservoir within the crust remains a significant impediment to the model. Furlanetto (2016) noted that pore space within the Wernecke Supergroup is extremely low. Expulsion and metamorphic reaction of the original formational water within the Wernecke Supergroup and concomitant loss of porosity likely occurred during Racklan orogeny, prior to Wernecke Breccia formation. To store large volumes of water would require the existence of secondary porosity such as dissolution cavities or fractures. Possibly, the fluids were stored in a vast network of crustal fractures that opened during orogenesis and obduction. Why such a network would generate anomalously voluminous and vigorous surges remains unexplained. Moreover, veining within the Wernecke Supergroup adjacent to the breccia zones is modest, so the crust at this level appears to have been uninvolved in the storage and expulsion of large volumes of postmetamorphic fluid.

Boiling of aqueous fluid is an important consideration for any model based on hydrothermal surging and rock brecciation. Liquid water is close to incompressible, and without a phase change from liquid to gas during boiling, the volume increase of the fluid

as it rises is negligible. Fluid uprise in the crust may persist simply because liquid water is significantly less dense than crustal rocks. However, fluids that boil have the ability to act explosively as water turns to steam, a process that is particularly cogent in systems that undergo crack-and-seal. However, studies of fluid inclusions in quartz within zones of Wernecke Breccia do not indicate boiling (Kendrick et al., 2008; Gillen, 2010; Hunt et al., 2011). Thus, in the case of Wernecke Breccia, it is unlikely that non-boiling hydrothermal solutions could have provided enough energy to brecciate enormous columns of the crust, develop large amounts of open space, and forcefully eject material at the surface.

Despite an absence of evidence for fluid boiling, we note that an interval of boiling may have occurred prior to the growth of the quartz grains that hosts the fluid inclusions. As such, the fluid inclusions within the quartz may provide information on relatively cool and quiescent conditions within the breccia zones but not on earlier, catastrophic events involving boiling, gas expansion and crustal brecciation. The growth of the quartz and other mineral phases, and the concurrent entrapment of the fluid inclusions, may reflect fluid and rock behavior at conditions closer to those of the ambient crust. The fluid inclusion data may thereby record breccia cementation during thermal retrogression.

4.6.8. Hydrothermal brecciation from degassing carbonatite

The genesis of Wernecke Breccia through some kind of fluid activity remains a possibility although, as noted above, certain aspects remain problematic. Some impediments to a model with a fluid sourced from the crust include: 1) an absence of evidence for concomitant magmatism, particularly in the upper crust; 2) dehydration of the crust due to the Racklan Orogeny and hence an uncertain origin of the fluid source; 3) a lack of understanding of how large volumes of fluid could be stored and then catastrophically released, and 4) a need for consistency of conditions and processes to form a remarkably uniform set of breccias distributed over tens of thousands of square kilometres.

Here, we explore the possibility that the fluids were generated by igneous activity within the mantle (Verbaas and Thorkelson, 2017). Although speculative, the hypothesis addresses some of the outstanding issues of breccia formation including fluid source and

storage, rock brecciation and regional distribution. The idea hinges on the involvement of a highly volatile fluid with the potential to expand and shatter rocks from the surface to depths of several kilometres.

Gases are highly compressible, and will undergo a large volume increase as pressure decreases en route to the surface. Hence, fluids that rise up through the crust are expected to fracture rocks and erupt more forcefully if they contain a large proportion of highly volatile components such as CO_2 (Phipps Morgan et al., 2004; Wilson and Head, 2007; Bosshard-Stadlin et al., 2014). In principle, such expansion could produce forceful ejections of rock and generate deep craters that subsequently become infilled with fragments of country rock (Figure 4.7). Previous authors have termed the surface expressions of CO_2-dominated gas expansion as “Verneshots” (Nicolayson and Ferguson, 1990; Phipps Morgan et al., 2004). The identification and depiction of these features are not widely accepted in the geological literature but the underlying process of deep-sourced volatiles remains an intriguing analogue for Wernecke Breccia. Importantly, the description of Verneshots is broadly similar to other processes involving gas expansion, including kimberlite eruptions. The outcome of vent excavation and fragment fall-back for Verneshots is broadly consistent with the Laughton et al. (2003) and Nielsen et al. (2013) model for Wernecke Breccia formation, except that the processes of rupture, brecciation and open space development would need to extend to greater depths. A summary of research on Verneshots and of other types of cryptoexplosions is provided in Appendix B.

The most likely volatile to be involved in Verneshot explosions is CO_2 (Phipps Morgan et al., 2004). CO_2 is common in both igneous and hydrothermal systems and can be exsolved from carbonatitic melts in the deep lithosphere. Carbonatitic magmas are mixtures of liquid carbonate and silicate, and can be formed from low degrees of partial melting of the continental lithospheric mantle (Hammouda and Keshav, 2015). Carbonatite melts can release large amounts of CO_2 in response to the assimilation of silicate minerals, especially orthopyroxene (Russell et al., 2012). If CO_2 exsolves but does not fully separate from the magma, the magma may rise through the crust as a low-density froth and, if it nears the surface, will expand explosively to form a kimberlite diatreme (Wilson and Head, 2007; Russell et al., 2012). Alternatively, it is possible for the magma and gas to fully separate at depth, and for the magma to stall within the lithosphere as a result of reduced

buoyancy and/or increased viscosity. The viscosity may also increase because the assimilation of silicate minerals will lower the melts temperature and increase its silica content (Mien et al., 1982). It is further possible that the magma could solidify completely, and expel most of its remaining volatiles (Candela, 1997; Oppenheimer et al., 2014). If the separated CO_2 rises through the lithosphere along a tight fracture network that allows its pressure to be retained, the gas will expand rapidly upon reaching the surface and create a crater of typically 3 km deep in 10 seconds (Wilson and Head, 2007; Sparks, 2013). Gaseous CO_2 is unable to carry xenoliths upwards due to the density difference between the rock and gas (Wilson and Head, 2007). Whether the crater can extend to depths of 5 or even 10 km is uncertain.

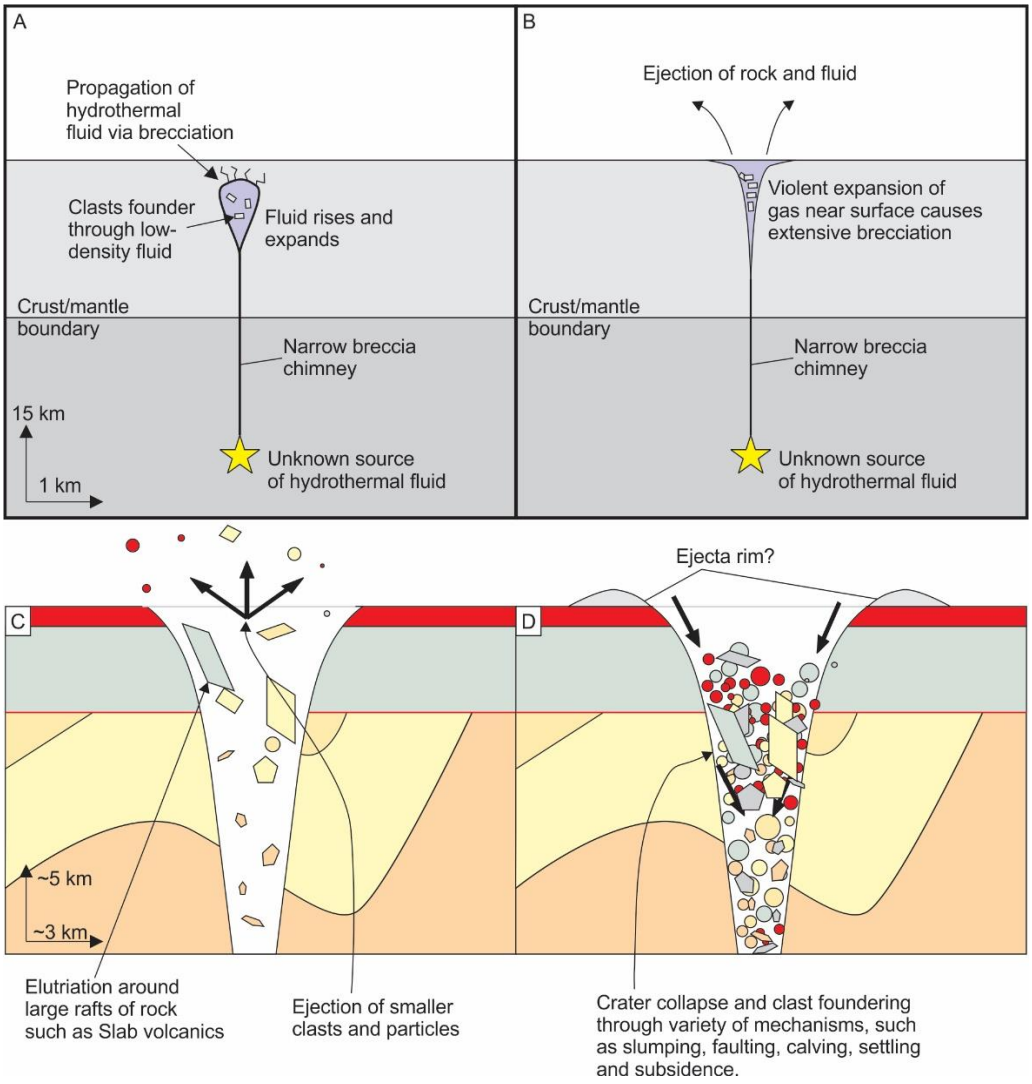

Figure 4.7. Verneshot model for a zone of Wernecke Breccia. (A) Fluid is generated in the mantle, possibly by reaction between carbonatite magma and peridotite. Rising carbonatite-generated fluid with a significant gaseous phase causes extensive brecciation. (B) Fluid rises along a narrow fracture network. Minor brecciation may be concurrent, but wallrock clasts are too dense to be carried upward by the fluid. (C) Upon venting, violent expansion of the gaseous phase causes elutriation and ejection of rock and fluid, creating short-lived open space. (D) Walls of breccia zone collapse, and clasts founder to depths of >5 km. Hydrous metasomatising fluids from a variety of sources (formational, metamorphic and meteoric) invaded the breccia zone, leading to alteration, IOCG mineralization and precipitation of cement.

Evidence for a gaseous component within Wernecke Breccia is present at the Igor and Olympic mineral occurrences, where rare but possibly primary CO_2 and $N_2 \pm CO_2$

inclusions are present in quartz (Gillen, 2010). However, in the carbonatite model, CO_2 and/or N_2 must have formed a larger component of the brecciating fluid than is currently apparent from fluid inclusion studies. The initial brecciating fluid may have either fully vented, or initial gaseous fluids in mineral inclusions were replaced by aqueous fluids. Some of the CO_2 may have formed carbonate minerals upon venting, a possibility that is consistent with the δC^{13} values of syn-breccia carbonate (Hunt et al., 2011), although most carbonate mineralization occurred late in the mineral paragenesis (Hunt et al., 2005).

The size and scale of brecciation of Wernecke Breccia and Olympic Dam type IOCG deposits is comparable to that of large kimberlite pipes (Groves et al., 2010). This similarity is expected if both Olympic Dam type IOCG deposits and kimberlite pipes form as the result of carbonatite-associated CO_2 degassing (i.e. IOCG deposits in the absence of magma, and kimberlite volcanism in the presence of magma). A Verneshot eruption would be able to account for many of the physical features of a Wernecke Breccia zone. However, on its own, it would be unable to account for the intense hydrothermal alteration, hydrous mineral precipitation and localized IOCG mineralization within and adjacent to the breccia. Major aqueous metasomatism is also required. The formation of a highly permeable conduit that extended from the surface to >10 km depth allowed for mixing of meteoric, formational, and hydrothermal waters derived from the crust (Kendrick et al., 2008; Gillen, 2010; Hunt et al., 2011). The required fluid convection may have been related to crustal thickening and overpressurization by the Racklan Orogeny and the obduction of Bonnetia (Furlanetto et al., 2013; Nielsen et al., 2013; Thorkelson and Laughton, 2016).

A requirement of the degassing-carbonatite hypothesis for Wernecke Breccia is that carbonatite magmatism must have been widespread beneath the breccia province, and that none of the magmas penetrated the upper crust. Carbonatites could have been generated by either an extensive mafic underplate with associated carbonatitic melts or a wide zone of low-percentage partial melting that yielded only carbonatitic melts. Carbonatites are commonly associated with rift settings (Pirajno, 2015) and may be emplaced peripherally to mantle plumes (Ernst and Bell, 2010; Pirajno, 2015). Magmatism on the Gawler Craton of Australia at 1.59 Ga has been interpreted as the result of a mantle plume (Campbell et al., 1998; Betts et al., 2007). The Gawler Craton and northwestern

Laurentia were likely connected at that time, so the carbonatitic melts beneath northwestern Laurentia may have been distal manifestations of the Gawler mantle plume.

If carbonatitic magmatism at depth indeed led to the Wernecke Breccia event, then (some) IOCG occurrences, carbonatite magmatism and kimberlite volcanism are genetically related (Russell et al., 2012). The type of mantle, depth of origin, and thickness of the crust and mantle lithosphere may be the controlling factors regarding how carbonatitic magmas at depth are expressed at the surface. Hence, this hypothesis brings a new perspective on the possible link between IOCG deposits, alkaline magmatism and hybrid carbonatite-IOCG hybrid deposits (Vielreicher et al., 2000; Groves and Vielreicher, 2001; Goff et al., 2004; Williams et al., 2005; Groves et al., 2010)

4.6.9. Summary of model viability

The physical, petrologic and geochemical attributes of Wernecke Breccia enable the assessment of the foregoing hypotheses for breccia formation. Mud diapirism as a mechanism of breccia formation (Lane, 1990) explains the presence of soft sedimentary material that in some cases serves as a matrix for breccia clasts. Evaporite diapirism, dissolution and collapse (Bell, 1986) is able to explain the presence of very large clasts. However, diapirism of either type is viable only for pre-orogenic conditions whereas the Wernecke Breccias occurred after deformation and metamorphism of the Racklan Orogeny.

Fault activity (Laznicka and Edwards, 1979) has the potential to yield breccias at a range of depths, but is precluded because fault textures are largely absent and many breccia zones are not associated with faults. Phreatic, phreatomagmatic, hydrothermal eruption and kimberlite diatreme origins are appealing because they provide a mechanism for fluid flow and metasomatism. These mechanisms are untenable because there is no evidence for concurrent volcanism (Thorkelson et al., 2001a, b).

An impact origin for the Wernecke Breccia is consistent with the size of clasts in the Wernecke Breccia, occurring as a post-orogenic brecciation, and possibly accounts for the extent of brecciation. However, it is difficult to explain clast foundering to significant depth because open space is commonly not generated below impact craters (Dressler

and Reimold, 2004). In addition, the Wernecke Breccia zones differ markedly from impact-generated breccias such as resurge and clastic-matrix breccias.

Brecciation as a result from deep hydrothermal fluid surges is consistent with post orogenic brecciation, the foundering of large clasts into the breccia zones and is potentially an amagmatic process. In the models of Furlanetto et al. (2013), Nielsen et al. (2013), and Thorkelson and Laughton (2016), the fluid is interpreted to be metamorphic and formational water that was overpressurized during the obduction of Bonnetia. The low pore space in the Wernecke Supergroup (Furlanetto et al. 2016) and the lack of fluid inclusions that indicate boiling (signifying a phase change and accompanying change in fluid volume) are impediments to this model. In addition, the obduction is hypothesized to have taken place on northwestern Laurentia but not on the Gawler Craton whereas the hydrothermal event that generated the Wernecke Breccia may also have encompassed breccias of the same age on the Gawler Craton (Chapter 3). It is thereby unlikely that obduction could be the only cause of brecciation. Nevertheless, obduction, crustal thickening and fluid entrapment may have been important contributors to the formation of the Wernecke Breccias.

In a new hypothesis (this thesis), the breccia zones formed by CO_2 degassing of carbonatite in the mantle. This process is similar to that proposed for Verneshots (Nicolayson and Ferguson, 1990; Phipps Morgan et al., 2004). The venting of CO_2 and excavation of the breccia zones by ejection and elutriation potentially explains brecciation but not hydrothermal alteration. A secondary flux of metamorphic, formational, and meteoric waters would have followed the ascent of CO_2 and metasomatized the breccia zones, aided by the initial high permeability of the Wernecke Breccia zone compared to the host rock, and the potential overpressure of fluids related to the obduction of Bonnetia. The breccia zones would have initially provided a permeable conduit from the surface to >10 km depth that allowed for fluid mixing of meteoric, hydrothermal and formational waters (Kendrick et al., 2008; Gillen, 2010; Hunt et al., 2011). An obvious impediment to this model is that CO_2 with a mantle signature has not been described within Wernecke Breccia. It is however possible that all the gas from the mantle vented, or that the gaseous fluids related to venting were all replaced by later aqueous fluids. Another problem with the model is that there is no carbonatite or kimberlite volcanism expressed at 1.6 Ga. It is

possible that all of the carbonatite magmas stalled in the mantle or deep crust, although why their retention at depth would have taken place beneath the entire Wernecke Breccia province, and potentially the coeval hydrothermal field on the Gawler Craton, remains unaddressed.

4.7. Conclusions

The Wernecke Breccia is a set of amagmatic, post-orogenic, 1598.8 ± 1 Ma hematitic breccia zones (Thorkelson et al., 2001a, Hunt et al., 2007; Furlanetto et al., 2013). Large blocks of wallrock, up to hundreds of metres in size, foundered kilometres deep into the breccia zones (Thorkelson et al., 2001a; Nielsen et al., 2013; Thorkelson and Laughton, 2016). The breccias display mainly potassic and locally sodic and calcic alteration that was caused largely by hydrothermal activity. Locally, the breccia zones host iron oxide copper and gold (IOCG) mineralization (Hitzman et al., 1992). The Wernecke Breccia province may be part of a larger hydrothermal field that extended onto the Gawler Craton of Australia (Thorkelson et al., 2001a; Chapter 3).

The process of formation of Wernecke Breccia requires deep excavation of zones in the crust and development of transient open space. The excavations were likely caused by the ascent of volatile-rich fluids and violent venting of rock and gas (Laughton et al., 2005). CO_2 may have been a major component of the fluid and could have been derived from a carbonatitic magma within the mantle or deep crust in a manner similar to that proposed for Verneshots (Nicolayson and Ferguson, 1990; Phipps Morgan et al., 2004). Voluminous hydrothermal activity following brecciation led to the metasomatism of clasts and wallrock and hydrothermal cementation. Terrane obduction and contractional deformation may have contributed to the environment of breccia formation through fluid entrapment and overpressurization. Other new and previously proposed and hypotheses such as mud diapirism and evaporite diapirism, rock dissolution, kimberlite volcanism and fault activity are rejected as main causes of breccia formation.

4.8. Acknowledgements

This chapter benefited from discussion with many geologists within academia and industry and their contributions are gratefully acknowledged.

4.9. References

Abbott, G. (1997). Geology of the Upper Hart River Area, Eastern Ogilvie Mountains, Yukon Territory (116A/10, 116A/11).

Ague, J.J. (2014). Fluid flow in the deep crust. In: *Treatise on Geochemistry (second edition),* volume 3, 203-247. Elsevier

Acevedo, R. D., Ponce, J. F., Rocca, M., Rabassa, J., & Corbella, H. (2009). Bajada del Diablo impact crater-strewn field: The largest crater field in the Southern Hemisphere. *Geomorphology*, *110*(3–4), 58–67. http://doi.org/10.1016/j.geomorph.2009.03.026

Acevedo, R. D., Rabassa, J., Corbella, H., Orgeira, M. J., Prezzi, C., Ponce, J. F., Subías, I. (2014). Comment on “Impact structures in Africa: A review” by Reimold and Koeberl [J. Afr. Earth Sci. 93 (2014) 57-175]. *Journal of African Earth Sciences*, *100*, 755–756. http://doi.org/10.1016/j.jafrearsci.2014.07.020

Acevedo, R. D., Rabassa, J., Ponce, J. F., Martínez, O., Orgeira, M. J., Prezzi, C., Vásquez, C. (2012). The Bajada del Diablo astrobleme-strewn field, central Patagonia Argentina: Extending the exploration to surrounding areas. *Geomorphology*, *169–170*, 151–164. http://doi.org/10.1016/j.geomorph.2012.04.020

Acevedo, R. D., Rabassa, J., Rocca, M., González-Guillot, M., Martínez, O., Subías, I., Ponce, J. F. (2016). Further comment to “Reply to Comment on impact structures in Africa: A review (Short Note)” by Reimold and Koeberl [J. Afr. Earth Sci. 100 (2014) 757–758]. *Journal of African Earth Sciences*, *118*, 315–316. http://doi.org/10.1016/j.jafrearsci.2015.02.004

Allen, P. A., Crampton, S. L., and Sinclair, H. D., (1991). The inception and early evolution of the North Alpine Foreland Basin, Switzerland: Basin Research, v. 3, p. 143–163.

Allen, S.R., Simpson, C.J., McPhie, J., and Daly, S.J., (2003). Stratigraphy, distribution and geochemistry of widespread felsic volcanic units in the Mesoproterozoic Gawler Range Volcanics, South Australia. *Australian Journal of Earth Sciences,* v. 50, p. 97–112, doi: 10.1046/j.1440-0952.2003.00980.x.

Amstutz, G. C. (1964). Impact, cryptoexplosion, or diapiric movements? *Kansas Academy of Science Transactions*, *67*, 343–356.

Anderson, H. E., & Davis, D. W. (1995). U-Pb geochronology of the Moyie sills, Purcell Supergroup, southeastern British Columbia: implications for the Mesoproterozoic geological history of the Purcell (Belt) Basin. *Canadian Journal of Earth Sciences*, *32*, 1180–1193.

Archer, A., Bell, R. T., Delaney, G. D., & Godwin, C. I. (1977). Mineralized breccias of Wernecke Mountains Yukon. *Geological Association of Canada, Program with Abstracts 2:5*.

Archer, A., & Schmidt, U. (1978). Mineralized breccias of early Proterozoic age, Bonnet Plume River district, Yukon Territory. *Canadian Mining and Metallurgical Bulletin*, *71*, 53–58.

Azad, A. S., Dypvik, H., & Kalleson, E. (2015). Sedimentation in marine impact craters - Insight from the Ritland impact structure. *Sedimentary Geology*, *318*, 97–112. http://doi.org/10.1016/j.sedgeo.2015.01.001

Barnouin, O.S., Ernst, C.M., Heinick, J.T., Sugita, S., Cintala, M.J., Crawford, D.A., Matsui, T. (2011). Experimental results investigating impact velocity effects on crater growth and the transient depth-to-diameter ratio. In: *42nd Lunar and Planetary Science Conference*. Abstract 2258.f.

Barton, M.D., (2014), Iron oxide(–Cu–Au–REE–P–Ag–U–Co) systems, in Scott, S.D., ed., Treatise on Geochemistry (second edition, volume 13): Amsterdam, Elsevier, p. 515–541.

Behr, H. J., Ahbrendt, H., Martin, H., Porada, H., Rohrs, J., & Weber, K. (1983). Sedimentology and mineralogy of Upper Proterozoic playa-lake deposits in the Damara orogen. In H. Martin & F. W. Eder (Eds.), *Intracontinental Fold Belts* (pp. 577–610). Springer-Verlag, Berlin.

Bell, R. T. (1986a). Geological map of northeastern Wernecke Mountains, Yukon Territory. *Geological Survey of Canada*, Open File 1207.

Bell, R. T. (1986b). Megabreccias in northeastern Wernecke Mountains, Yukon Territory. *Current Research, Part A. Geological Survey of Canada*, *Paper 1986*, 375–384.

Bell, R. T. (1978). Breccias and uranium mineralization in the Wernecke Mountains, Yukon Territory - a progress report. *Current Research, Part A. Geological Survey of Canada*, Paper 78-1A, 317-322.

Bell, R. T., & Delaney, G. D. (1977). Geology of some uranium occurrences in Yukon Territory. *Report of Activities, Part A, Geological Survey of Canada*, *Paper 1-77*, 33–37.

Bertelli, M., & Baker, T. (2010). A fluid inclusion study of the Suicide Ridge Breccia Pipe, Cloncurry district, Australia: Implication for Breccia Genesis and IOCG mineralization. *Precambrian Research*, *179*(1–4), 69–87. http://doi.org/10.1016/j.precamres.2010.02.016

Betts, P. G., Giles, D., Schaefer, B. F., & Mark, G. (2007). 1600-1500 Ma hotspot track in eastern Australia: Implications for Mesoproterozoic continental reconstructions. Terra Nova, 19(6), 496–501. http://doi.org/10.1111/j.1365-3121.2007.00778.x

Betts, P. G., & Giles, D. (2006). The 1800-1100 Ma tectonic evolution of Australia. Precambrian Research, 144(1–2), 92–125. http://doi.org/10.1016/j.precamres.2005.11.006

Bosshard-Stadlin, S. A., Mattsson, H. B., & Keller, J. (2014). Magma mixing and forced exsolution of CO2 during the explosive 2007–2008 eruption of Oldoinyo Lengai (Tanzania). Journal of Volcanology and Geothermal Research, 285, 229–246. http://doi.org/10.1016/j.jvolgeores.2014.08.017

Brown, K. M. (1990). Nature and hydrogeologic significance of mud diapirs and diatremes for accretionary systems. *Journal of Geophysical Research*, *95*, 8969–8982.

Brown, R. J., Tait, M., Field, M., & Sparks, R. S. J. (2009). Geology of a complex kimberlite pipe (K2 pipe, Venetia Mine, South Africa): Insights into conduit processes during explosive ultrabasic eruptions. *Bulletin of Volcanology*, *71*(1), 95–112. http://doi.org/10.1007/s00445-008-0211-4

Browne, P. R. L., & Lawless, J. V. (2001). Characteristics of hydrothermal eruptions, with examples from New Zealand and elsewhere. *Earth Science Reviews*, *52*(4), 299–331. http://doi.org/10.1016/S0012-8252(00)00030-1

Bucher, W. H. (1965). The largest so-called meteorite scars in three continents as demonstrably tied to major terrestrial structures. *New York Academy of Sciences Annals*, *123*, 897–903.

Bucher, W. H. (1963). Cryptoexplosion structures caused from without or from within the earth? (“astroblemes” or “geoblemes?”). *American Journal of Science*, *261*(Summer), 597–649.

Campbell, I.H., (1998), The mantle’s chemical structure: insights from the melting products of mantle plumes, in Jackson, I.N.S. (ed.), The Earth’s mantle: Composition, structure and evolution. Cambridge University Press, Cambridge, p. 259-310.

Candela, P. A. (1997). A Review of Shallow, Ore-related Granites: Textures, Volatiles, and Ore Metals. Journal of Petrology, 38(12), 1619–1633.

Christeson, G. L., Collins, G. S., Morgan, J. V, Gulick, S. P. S., Barton, P. J., & Warner, M. R. (2009). Mantle deformation beneath the Chicxulub impact crater. Earth and Planetary Science Letters, 284(1–2), 249–257. http://doi.org/10.1016/j.epsl.2009.04.033

Clark, J.P., (1999). Thermal evolution along the southern Paeroa fault, between the Orakei Korako and Te Kopia geothermal areas, Taupo Volcanic Zone, New Zealand. MSc thesis, Geology Department, University of Auckland, pp. 124

Conor, C. H. H., & Preiss, W. V. (2008). Understanding the 1720-1640 Ma Palaeoproterozoic Willyama Supergroup, Curnamona Province, Southeastern Australia: Implications for tectonics, basin evolution and ore genesis. *Precambrian Research*, *166*(1–4), 297–317. http://doi.org/10.1016/j.precamres.2007.08.020

Collins, G. S., Melosh, H. J., & Marcus, R. A. (2005). Earth Impact Effects Program: A Web-based computer program for calculating the regional environmental consequences of a meteoroid impact on Earth, 840(6), 817–840.

Daniel, C. G., Jones, J. V., Andronicos, C. L., & Gray, M. B. (2013). Making the case for the Picuris orogeny: Evidence for a 1500 to 1400 Ma orogenic event in the southwestern United States. *Field Guides*, *33*(7), 205–235. http://doi.org/10.1130/2013.0033(07)

Delaney, G. D. (1985). *The Middle Proterozoic Wernecke Supergroup, Wernecke Mountains, Yukon Territory*. Doctoral Thesis, University of Western Ontario.

Delaney, G. D. (1981). The Mid-Proterozoic Wernecke Supergroup, Wernecke Mountains, Yukon Territory. In F. H. A. Campbell (Ed.), *Proterozoic Basins of Canada* (p. 23). Geological Survey of Canada, Paper 81-10.

Deming, D. (2001). Abnormal fluid pressures. *In: Introduction to hydrogeology.* McGraw-Hill Science

Dietz, R. S. (1963). Cryptoexplosion structures: A discussion. *American Journal of Science*, *262*, 650–654.

Doe, M. F., Jones, J. V., Karlstrom, K. E., Thrane, K., Frei, D., Gehrels, G., & Pecha, M. (2012). Basin formation near the end of the 1.60-1.45 Ga tectonic gap in southern Laurentia: Mesoproterozoic Hess Canyon Group of Arizona and implications for ca. 1.5 Ga supercontinent configurations. *Lithosphere*, *4*(1), 77–88. http://doi.org/10.1130/L160.1

Doughty, P. T., & Chamberlain, K. R. (1996). Salmon River Arch revisited: new evidence for 1370 Ma rifting near the end of deposition in the Middle Proterozoic Belt basin. *Canadian Journal of Earth Sciences*, *33*(7), 1037–1052. http://doi.org/10.1139/e96-079

Dressler, B. O. (1984). The effects of the Sudbury event and the intrusion of the Sudbury Igneous Complex on the footwall rocks of the Sudbury structure. In E. G. Pye, A. J. Naldrett, & P. E. Giblin (Eds.), *The Geology and Ore Deposits of the Sudbury Structure. Ontario Geological Survey Special Volume 1* (pp. 97–136).

Dressler, B. O., & Reimold, W. U. (2004). Order or chaos? Origin and mode of emplacement of breccias in floors of large impact structures. Earth-Science Reviews, 67(1–2), 1–54. http://doi.org/10.1016/j.earscirev.2004.01.007Ernst, R. E. (2009). Vent Complexes above Dolerite Sills in Phanerozoic LIPs. *2009 American Geophysical Union Spring meeting abstracts*

Eyster, A. E., Fu, R. R., Strauss, J. V, Weiss, B. P., Roots, C. F., Halverson, G. P., Macdonald, F. A. (2016). Paleomagnetic evidence for a large rotation of the Yukon block relative to Laurentia: Implications for a low-latitude Sturtian glaciation and the breakup of Rodinia, (Xx), 1–21. http://doi.org/10.1130/B31425.1

Hörz, F., H. (1968). Statistical measurements of deformation structures and refractive indices in experimentally shock loaded quartz. In B. M. French & N. M. Short (Eds.), *Shock Metamorphism of Natural Materials* (pp. 243–253). Mono Book Corp, Baltimore, MD.

French, B. M. (1990). 25 years of the impact-volcanic controversy. *EOS Transactions, American Geophysical Union*, *82*, 2869–2890.

French, B. M. (1998). Traces of Catastrophe: A handbook of shock metamorphic effects in terrestrial meteorite impact structure. *Lunar and Planetary Institute, NASA*, (954), 120.

French, B. M., & Koeberl, C. (2010). The convincing identification of terrestrial meteorite impact structures: What works, what doesn't, and why. *Earth-Science Reviews*, *98*(1–2), 123–170. http://doi.org/10.1016/j.earscirev.2009.10.009

Furlanetto, F., Thorkelson, D. J., Rainbird, R. H., Davis, W. J., Gibson, H. D., & Marshall, D. D. (2016). The Paleoproterozoic Wernecke Supergroup of Yukon, Canada: Relationships to orogeny in northwestern Laurentia and basins in North America, East Australia, and China. *Gondwana Research*, *39*, 14–40. http://doi.org/10.1016/j.gr.2016.06.007

Furlanetto, F., Thorkelson, D. J., Daniel Gibson, H., Marshall, D. D., Rainbird, R. H., Davis, W. J., Vervoort, J. D. (2013). Late Paleoproterozoic terrane accretion in northwestern Canada and the case for circum-Columbian orogenesis. *Precambrian Research*, *224*, 512–528. http://doi.org/10.1016/j.precamres.2012.10.010

Gibbons, W., & Murphy, J. B. (1995). Mylonitic mafic granulite in fault megabreccia at Clarke Head, Nova Scotia: A sample of Avalonian lower crust? *Geological Magazine*, *132*, 81–90.

Gibbons, W., Doig, R., Gordon, T., Murphy, B., Reynolds, P., & White, J. C. (1996). Mylonite to megabreccia: Tracking fault events within a transcurrent terrane boundary in Nova Scotia, Canada. *Geology*, *24*(5), 411–414. http://doi.org/10.1130/0091-7613(1996)024<0411:MTMTFE>2.3.CO;2

Gibson, G. M., Hutton, L. J., & Holzschuh, J. (2017). Basin inversion and supercontinent assembly as drivers of sediment-hosted Pb – Zn mineralization in the Mount Isa region, northern Australia, 174, 773–786.

Gillen, D. (2010). A study of IOCG-related hydrothermal fluids in the Wernecke Mountains, Yukon Territory, Canada. *Chapter 1 - 3*, *James Cook*.

Glikson, A. (2005). Asteroid/comet impact clusters, flood basalts and mass extinctions: Significance of isotopic age overlaps. *Earth and Planetary Science Letters*, *236*(3–4), 933–937. http://doi.org/10.1016/j.epsl.2005.05.007

Goff, B. H., Weinberg, R., Groves, D. I., Vielreicher, N. M., & Fourie, P. J. (2004). The giant Vergenoeg fluorite deposit in a magnetite/fluorite/fayalite REE pipe: a hydrothermally-altered carbonatite-related pegmatoid? *Mineralogy and Petrology*, *80*(3–4), 173–199. http://doi.org/10.1007/s00710-003-0012-6

Grindley, G. W., & Browne, P. R. L. (1976). Structural and hydrological factors controlling the permeability of some hot water fields. *Proceedings of the 2nd U.N. Symposium on Development and Use of Geothermal Resources, San Francisco*, *1*, 377–386.

Grunewald, U., Zimanowski, B., Buttner, R., Phillips, L.F., Heide, K., Buchel, G., 2007. MFCI experiments on the influence of NaCl-saturated water on phreatomagmatic explosions. J. Volcanol. Geotherm. Res. 159, 126–137. http://dx.doi.org/10.1016/j.jvolgeores.2006.06.016.

Groves, D. I., Bierlein, F. P., Meinert, L. D., & Hitzman, M. W. (2010). Iron Oxide Copper-Gold (IOCG) Deposits through Earth History: Implications for Origin, Lithospheric Setting, and Distinction from Other Epigenetic Iron Oxide Deposits. *Economic Geology*, *105*(3), 641–654. http://doi.org/10.2113/gsecongeo.105.3.641

Groves, D. I., & Vielreicher, R. M. (2000). The Phalaborwa (Palabora) Deposit and its Potential Connection to Iron-Oxide Copper-Gold Deposits of Olympic Dam Type. In T. M. Porter (Ed.), *Hydrothermal Iron Oxide Copper-Gold and Related Deposits, A Global Perspective, Volume 1* (pp. 321–329). PGC publishing, Adelaide.

Groves, D. I., & Vielreicher, N. M. (2001). The Phalabowra (Palabora) carbonatite-hosted magnetite-copper sulfide deposit, South Africa: An end-member of the iron-oxide copper-gold-rare earth element deposit group? *Mineralium Deposita*, *36*(2), 189–194. http://doi.org/10.1007/s001260050298

Guidry, S. A., & Chafetz, H. S. (2003). Anatomy of siliceous hot springs: Examples from Yellowstone National Park, Wyoming, USA. Sedimentary Geology, 157(1–2), 71–106. http://doi.org/10.1016/S0037-0738(02)00195-1

Gutierrez, F. (2010). Hazards associated to karst. In I. Alcántara-Ayala & A. S. Goudie (Eds.), *Geomorphological Hazards and Disaster Prevention* (pp. 161–176).

Hall, K. W., & Cook, F. A. (1998). Geophysical transect of the Eagle Plains foldbelt and Richardson Mountains anticlinorium, northwestern Canada. *Bulletin of the Geological Society of America*, *110*(3), 311–325. http://doi.org/10.1130/0016-7606(1998)110<0311:GTOTEP>2.3.CO;2

Hamilton, M. A., & Buchan, K. L. (2010). U-Pb geochronology of the Western Channel Diabase, northwestern Laurentia: Implications for a large 1.59Ga magmatic province, Laurentia's APWP and paleocontinental reconstructions of Laurentia, Baltica and Gawler craton of southern Australia. *Precambrian Research*, *183*(3), 463–473. http://doi.org/10.1016/j.precamres.2010.06.009

Hand, M., Reid, A., & Jagodzinski, L. (2007). Tectonic framework and evolution of the Gawler craton, Southern Australia. Economic Geology, 102(8), 1377–1395. http://doi.org/10.2113/gsecongeo.102.8.1377

Hetman, C. M., Scott Smith, B. H., Paul, J. L., & Winter, F. (2004). Geology of the Gahcho Kué kimberlite pipes, NWT, Canada: Root to diatreme magmatic transition zones. *Lithos*, *76*(1–4 SPEC. ISS.), 51–74. http://doi.org/10.1016/j.lithos.2004.03.051

Higgins, G. E., & Saunders, J. B. (1974). Mud volcanoes - Their nature and origin. *Verhandlungen Naturforschen Gesellschaft Basel*, *85*, 101–152.

Hitzman, M. W. (2000). Iron Oxide-Cu-Au Deposits: What, Where, When and Why. In T. M. Porter (Ed.), *Hydrothermal Iron Oxide Copper-Gold and Related Deposits, A Global Perspective, Volume 12* (pp. 9–25). PGC publishing, Adelaide.

Hitzman, M. W., Oreskes, N., & Einaudi, M. T. (1992). Geological characteristics and tectonic setting of Proterozoic iron oxide (Cu U Au REE) deposits. *Precambrian Research*, *58*, 241–287. http://doi.org/10.1016/0301-9268(92)90121-4

Hudec, M. R., & Jackson, M. P. A. (2006). Advance of Allochthonous salt sheets in passive marigns and orogens. *American Association of Petroleum Geologists Bulletin2*, *90*, 1535–1564.

Hunt, J. A., Baker, T., & Thorkelson, D. J. (2007). A review of iron oxide copper-gold deposits, with focus on the Wernecke Breccias, Yukon Canada, as an example of a non-magmatic end member and implications for IOCG genesis and classification. *Exploration and Mining Geology*, *16*(3–4), 209–232. http://doi.org/10.2113/gsemg.16.3-4.209

Hunt, J. A., Baker, T., Cleverley, J., Davidson, G. J., Fallick, A. E., & Thorkelson, D. J. (2011). Fluid inclusion and stable isotope constraints on the origin of Wernecke Breccia and associated iron oxide – copper – gold mineralization, Yukon. *Canadian Journal of Earth Sciences*, *48*(10), 1425–1445. http://doi.org/10.1139/e11-044

Hunt, J.A., Laughton, J.R., Brideau, M-A., Thorkelson, D.J., Brookes, M.L. and Baker, T. (2002). New mapping around the Slab iron oxide-copper-gold occurrence, Wernecke Mountains (parts of NTS 106C/13, 106D/16, 106E/1 and 106F/4), Yukon. In: D.S. Emond, L.H. Weston and L.L. Lewis (Ed.), *Yukon Exploration and Geology 2002,* Exploration and Geological Services Division, Yukon Region, Indian and Northern Affairs Canada, p. 125-138.

Hunt, J., Baker, T., & Thorkelson, D.J. (2005). Regional-scale Proterozoic IOCG-mineralized breccia systems: Examples from the Wernecke Mountains, Yukon, Canada. *Mineralium Deposita*, *40*(5), 492–514. http://doi.org/10.1007/s00126-005-0019-5

Jefferson, C. W., & Parrish, R. R. (1989). Late Proterozoic stratigraphy, U–Pb zircon ages, and rift tectonics, Mackenzie Mountains, northwestern Canada. *Canadian Journal of Earth Sciences*, *26*(9), 1784–1801. http://doi.org/10.1139/e89-151

Johnson, J. P., & Cross, K. C. (1995). U-Pb geochronological constraints on the genesis of the Olympic Dam Cu-U-Au-Ag deposit, South Australia. *Economic Geology and the Bulletin of the Society of Economic Geologists*, *90*, 1046–1063.

Jones, J. V., Daniel, C. G., & Doe, M. F. (2015). Tectonic and sedimentary linkages between the Belt-Purcell basin and southwestern Laurentia during the Mesoproterozoic, ca. 1.60–1.40 Ga. *Lithosphere*, *7*(4), 465–472. http://doi.org/10.1130/L438.1

Kendrick, M. A., Honda, M., Gillen, D., Baker, T., & Phillips, D. (2008). New constraints on regional brecciation in the Wernecke Mountains, Canada, from He, Ne, Ar, Kr, Xe, Cl, Br and I in fluid inclusions. *Chemical Geology*, *255*(1–2), 33–46. http://doi.org/10.1016/j.chemgeo.2008.05.021

Kenkmann, T., Poelchau, M. H., & Wulf, G. (2014). Structural geology of impact craters. *Journal of Structural Geology*, *62*, 156–182. http://doi.org/10.1016/j.jsg.2014.01.015

Keulen, N., Garde, A. A., & Jørgart, T. (2014). Shock melting of K-feldspar and interlacing with cataclastically deformed plagioclase in granitic rocks at Toqqusap Nunaa, southern West Greenland: Implications for the genesis of the Maniitsoq structure. *Tectonophysics*, *662*, 328–344. http://doi.org/10.1016/j.tecto.2015.07.028

Kiilsgaard, T. H., Heyl, A. V., & Brock, M. R. (1962). The Crooked Creek disturbance, southeast Missouri. *U.S. Geological Survey Professional Paper*, *450 E*(2), 75–89.

Kopf, A. J. (2002). Significance of mud volcanism. *Reviews of Geophysics*, *40*(May), 1005. http://doi.org/10.1029/2000RG000093

Krogh, T. E., Davis, D. W., & Corfu, F. (1984). Precise U-Pb zircon and baddeleyite ages for the Sudbury area. In E. G. Pye, A. J. Naldrett, & P. E. Giblin (Eds.), *The Geology and Ore Deposits of the Sudbury Structure. Ontario Geological Survey Special Volume 11* (pp. 431–446).

Kumar, P. S., & Kring, D. A. (2008). Impact fracturing and structural modification of sedimentary rocks at Meteor Crater, Arizona. Journal of Geophysical Research E: Planets, 113(9), 1–17. http://doi.org/10.1029/2008JE003115

Kurszlaukis, S., & Lorenz, V. (2008). Formation of “Tuffisitic Kimberlites” by phreatomagmatic processes. *Journal of Volcanology and Geothermal Research*, *174*(1–3), 68–80. http://doi.org/10.1016/j.jvolgeores.2007.12.047

Kvasnytsya, V., Wirth, R., Dobrzhinetskaya, L., Matzel, J., Jacobsen, B., Hutcheon, I., Kovalyukh, M. (2013). New evidence of meteoritic origin of the Tunguska cosmic body. *Planetary and Space Science*, *84*, 131–140. http://doi.org/10.1016/j.pss.2013.05.003

Kwon, C. W., & Sohn, Y. K. (2008). Tephra-filled volcanic neck (diatreme) of a mafic tuff ring at Maegok, Miocene Eoil Basin, SE Korea. *Geosciences Journal*, *12*(4), 317–329. http://doi.org/10.1007/s12303-008-0032-7

Lafrance, B., Legault, D., & Ames, D. E. (2008). The formation of the Sudbury breccia in the North Range of the Sudbury impact structure. *Precambrian Research*, *165*(3–4), 107–119. http://doi.org/10.1016/j.precamres.2008.06.004

Lane, R. A. (1990). Geologic setting and petrology of the Proterozoic Ogilvie Mountain breccias of the Coal Creek Inlier, Southern Ogilvie Mountains, Yukon Territory. *M.Sc. thesis, The University of British Columbia*.

Lane, R. A., Godwin, C. I. (1992). Geology of the Ogilvie Mountains Breccias Coal Creek Inlier (NTS 116B/11, 13, 14) Yukon Territory

Laughton, J. R., Thorkelson, D. J., Brideau, M.-A., Hunt, J. A., & Marshall, D. D. (2005). Early Proterozoic orogeny and exhumation of Wernecke Supergroup revealed by vent facies of Wernecke Breccia, Yukon, Canada. *Canadian Journal of Earth Sciences*, *42*(6), 1033–1044. http://doi.org/10.1139/e04-085

Laznicka, P., & Edwards, R. J. (1979). Dolores Creek, Yukon – A disseminated copper mineralization in sodic metasomatites. *Economic Geology*, *74*, 1352–1370.

Laznicka, P., & Gaboury, D. (1988). Wernecke Breccias and Fe, Cu, U mineralization: Quartet Mountain-Igor area (NTS 106E). *Yukon Geology, Exploration and Geological Services Division, Indian and Northern Affairs Canada.*, 44–50.

Laznicka, P. (1988). Breccias and coarse fragmentites: petrology, environments, associations, ores. Volume 25, Developments in Economic Geology. Elsevier. 832 pp.

Leach, D., Taylor, R., Fey, D., & Diehl, S. (2010). A Deposit Model for Mississippi Valley-Type Lead-Zinc Ores. *Mineral Deposit Models for Resource Assessment*, *Chapter A*, 1–43.

LeCheminant, A. N., & Heaman, L. M. (1989). Mackenzie igneous events, Canada: Middle Proterozoic hotspot magmatism associated with ocean opening. *Earth and Planetary Science Letters*, *96*(1–2), 38–48. http://doi.org/10.1016/0012-821X(89)90122-2

Li, Z. X., Bogdanova, S. V., Collins, A. S., Davidson, A., De Waele, B., Ernst, R. E., Vernikovsky, V. (2008). Assembly, configuration, and break-up history of Rodinia: A synthesis. *Precambrian Research*, *160*(1–2), 179–210. http://doi.org/10.1016/j.precamres.2007.04.021

Luczaj, J. (1998). Argument supporting explosive igneous activity for the origin of “cryptoexplosion” structures in the midcontinent, United States. *Geology*, *26*(4), 295–298. http://doi.org/10.1130/0091-7613(1999)027<0279:ASEIAF>2.3.CO;2

Lutz, H., & Lorenz, V. (2013). Early volcanological research in the Vulkaneifel, Germany, the classic region of maar-diatreme volcanoes: The years 1774-1865. Bulletin of Volcanology, 75(8), 1–16. http://doi.org/10.1007/s00445-013-0743-0

McCall, G. J. H. (1964). Are cryptovolcanic structures due to meteoric impact? *Nature*, *201*, 251–254.

McPhie, J., Kamenetsky, V. S., Chambefort, I., Ehrig, K., & Green, N. (2011a). Origin of the supergiant Olympic Dam Cu-U-Au-Ag deposit, South Australia: Was a sedimentary basin involved. *Geology*, *39*(8), 795–798. http://doi.org/10.1130/G31952.1

McPhie, J., Kamenetsky, V., Allen, S., Ehrig, K., Agangi, A., & Bath, A. (2011b). The fluorine link between a supergiant ore deposit and a silicic large igneous province. *Geology*, 39(11), 1003–1006. http://doi.org/10.1130/G32205.1

McPhie, J., Orth, K., Kamenetsky, V., Kamenetsky, M., & Ehrig, K. (2016). Characteristics, origin and significance of Mesoproterozoic bedded clastic facies at the Olympic Dam Cu-U-Au-Ag deposit, South Australia. Precambrian Research, 276, 85–100. http://doi.org/10.1016/j.precamres.2016.01.029

McCaig, A.M., Wickham, S.M., and Taylor, H.P. (1990). Deep fluid circulation in alpine shear zones, Pyrenees, France: field and oxygen isotope studies. Contributions to Mineralogy and Petrology, Canadian Journal of Earth Sciences. Vol. 37, 2000 106: 41–60.

Medig, K. P. R., Thorkelson, D. J., Davis, W. J., Rainbird, R. H., Gibson, H. D., Turner, E. C., & Marshall, D. D. (2014). Pinning northeastern Australia to northwestern Laurentia in the Mesoproterozoic. *Precambrian Research*, *249*, 88–99. http://doi.org/10.1016/j.precamres.2014.04.018

Melosh, B. L., Rowe, C. D., Smit, L., Groenewald, C., Lambert, C. W., & Macey, P. (2014). Snap, crackle, Pop: Dilational fault breccias record seismic slip below the brittle-plastic transition. *Earth and Planetary Science Letters*, *403*, 432–445. http://doi.org/10.1016/j.epsl.2014.07.002

Michaelovitch, M., Mahiques, D., Schattner, U., Lazar, M., Sumida, P. G. S., de Souza, L. A. P. (2017). An extensive pockmark field on the upper Atlantic margin of Southeast Brazil: spatial analysis and its relationship with salt diapirism. *Heliyon*, (February), e00257. http://doi.org/10.1016/j.heliyon.2017.e00257

Milton, J.E., M., Hickey, K. E., & Gleeson, S. A. (2014). New U-Pb constraints on gunbarrel volcanism and the break-up of Rodinia: the 775 Ma Little Dal basalts. In *Geological Association of America. Conference abstract*

Morgan, L.A., Shanks III, W.C., Pierce, K. L. (2009). Hydrothermal processes above the Yellowstone magma chamber. *Geological Society of America*, *Special Paper*, 97.

Moroskat, M. J. A. (2009). On the genesis of the Blende Zn-Pb-Ag deposit, Wernecke Mountains, Yukon: Structural and geochemical evidence. *University of Alberta M.Sc. thesis*

Mortimer, G.E., Cooper, J.A., Paterson, H.L., Cross, K., Hudson, G.R.T., and Uppill, R.K., 1988, Zircon U-Pb dating in the vicinity of Olympic Dam Cu- U-Au deposit, Roxby Downs, South Australia: *Economic Geology*, v. 83, p. 694–709.

Muffler, L. J. P., White, D. E., & Truesdell, A. H. (1971). Hydrothermal explosion craters in Yellowstone National Park. *Geological Society of America Bulletin 1*, *82*, 723–740.

Nicolayson, L.O., & Ferguson, J. (1990). Cryptoexplosion structures, shock deformation and siderophile concentration related to explosive venting of fluids associated with alkaline ultramafic magmas. *Tectonophysics*, *171*, 303–335.

Nielsen, A. B., Thorkelson, D. J., Gibson, H. D., & Marshall, D. D. (2013). The Wernecke igneous clasts in Yukon, Canada: Fragments of the Paleoproterozoic volcanic arc terrane Bonnetia. *Precambrian Research*, *238*, 78–92. http://doi.org/10.1016/j.precamres.2013.09.017

Nold, J. L., Dudley, M. A., & Davidson, P. (2014). The Southeast Missouri (USA) Proterozoic iron metallogenic province-Types of deposits and genetic relationships to magnetite-apatite and iron oxide-copper-gold deposits. *Ore Geology Reviews*, *57*, 154–171. http://doi.org/10.1016/j.oregeorev.2013.10.002

Norris, D.K., (1981). Wind River. Geological Survey of Canada, Map 1528A, 1:250 000 scale.

Norris, D.K., Dyke, L.D., (1997). Proterozoic. In: Norris, D.K. (Ed.), The geology, mineral and hydrocarbon potential of northern Yukon Territory and northwestern District of Mackenzie. Geological Survey of Canada, pp. 65–84.

Oppenheimer, C., Fischer, T.P., & Scaillet, B. (2014). Volcanic degassing: process and impact. *In: Treatise on geochemistry*, 2nd edition, 2014. Elsevier

Osborne, R. A. L. (2013). 6.9 Preservation and Burial of Ancient Karst. In *Treatise on Geomorphology* (pp. 95–103). http://doi.org/10.1016/B978-0-12-374739-6.00132-9

Osinski, G. R., Tornabene, L. L., Banerjee, N. R., Cockell, C. S., Flemming, R., Izawa, M. R. M., … Southam, G. (2013). Impact-generated hydrothermal systems on Earth and Mars. Icarus, 224(2), 347–363. http://doi.org/10.1016/j.icarus.2012.08.030

Paillou, P., Elbarkooky, a, Barakat, a, Malezieux, J., Reynard, B., Dejax, J., & Heggy, E. (2004). Discovery of the largest impact crater field on Earth in the Gilf Kebir region, Egypt. *Comptes Rendus Geosciences*, *336*(16), 1491–1500. http://doi.org/10.1016/j.crte.2004.09.010

Paillou, P., Reynard, B., Malézieux, J. M., Dejax, J., Heggy, E., Rochette, P., … Colin, J. P. (2006). An extended field of crater-shaped structures in the Gilf Kebir region, Egypt: Observations and hypotheses about their origin. *Journal of African Earth Sciences*, *46*(3), 281–299. http://doi.org/10.1016/j.jafrearsci.2006.05.006

Peel, F. J., Travis, C. J., & Hossack, J. R. (1995). Genetic structural provinces and salt tectonics of the Cenozoic offshore U.S. Gulf of Mexico: a preliminary analysis. In M. P. A. Jackson, D. G. Roberts, & S. Snelson (Eds.), *Salt tectonics: a global perspective* (pp. 153–175). Tulsa OK, American Association Petroleum Geologists Memoir, v. 65.

Phipps Morgan, J., Reston, T. J., & Ranero, C. R. (2004). Contemporaneous mass extinctions flood basalts and "impact signals": are mantle plume-induced lithospheric gas explosions the causal link? *Earth and Planetary Science Letters*, *217*, 263–284.

Pirajno F. (2009) Hydrothermal Processes Associated with Meteorite Impacts. In: Hydrothermal Processes and Mineral Systems. Springer, Dordrecht

Pirajno, F. (2015). Intracontinental anorogenic alkaline magmatism and carbonatites, associated mineral systems and the mantle plume connection. *Gondwana Research*, *27*(3), 1181–1216. http://doi.org/10.1016/j.gr.2014.09.008

Polozov, A. G., Svensen, H. H., Planke, S., Grishina, S. N., Pristad, K. E., & Jerram, D. A. (2016). The basalt pipes of the Tunguska Basin (Siberia, Russia): High temperature processes and volatile degassing into the end-Permian atmosphere. *Palaeogeography, Palaeoclimatology, Palaeoecology*, 441, 51–64.

Prezzi, C. B., Orgeira, M. J., Acevedo, R. D., Ponce, J. F., Martinez, O., Rabassa, J. O., Subías, I. (2012). Geophysical characterization of two circular structures at Bajada del Diablo (Patagonia, Argentina): Indication of impact origin. *Physics of the Earth and Planetary Interiors*, *192–193*, 21–34. http://doi.org/10.1016/j.pepi.2011.12.004

Quinlan, J. F. (1978). Types of karst, with emphasis on cover beds in their classification and development: *University of Texas PhD thesis*

Rampino, M. R., & Volk, T. (1996). Multiple impact event in the Paleozoic; collision with a string of comets or asteroids? *Geophysical Research Letters*, *23*(1), 49–52.

Reid, A., Smith, R. N., Baker, T., Jagodzinski, E. A., Selby, D., Gregory, C. J., & Skirrow, R. G. (2013). Re-Os dating of molybdenite within hematite breccias from the vulcan Cu-Au prospect, olympic Cu-Au province, South Australia. *Economic Geology*, *108*(4), 883–894. http://doi.org/10.2113/econgeo.108.4.883

Reimold, W. U., & Koeberl, C. (2014). Reply to "Comment on impact structures in Africa: A review (Short Note)" by Acevedo, R.D. et al. *Journal of African Earth Sciences*, *100*, 757–758. http://doi.org/10.1016/j.jafrearsci.2014.08.012

Reimold, W. U. (2007). The Impact Crater Bandwagon (Some problems with the terrestrial impact cratering record). *Meteoritics & Planetary Science*, *42*(9), 1467–1472. http://doi.org/10.1111/j.1945-5100.2007.tb00585.x

Reimold, W. U., & Koeberl, C. (2014). Impact structures in Africa: A review. *Journal of African Earth Sciences*, *93*, 57–175. http://doi.org/10.1016/j.jafrearsci.2014.01.008

Reynolds, L. J. (2000). Geology of the Olympic Dam Cu-U-Au-Ag REE deposit. In T. M. Porter (Ed.), *Hydrothermal Iron Oxide Copper-Gold and Related Deposits, A Global Perspective, Volume 1* (pp. 93–104). PGC publishing, Adelaide.

Rhakmanov, R. R. (1987). Mud Volcanoes and Their Importance in Forecasting of Subsurface Petroleum potential (In Russian), *Nedra. Moscow*.

Rogers, R. L., Ernst, R. E., Cousens, B., Söderlund, U., Hamilton, M., Harlan, S. (2016). Newly recognized 1550 – 1590 Ma Tobacco Root Western Channel LIP, and Further evidence for bringing Australia back home to western Laurentia. *Geological association of Canada – Mineralogical association of Canada general meeting.* Abstract volume

Rogers, R. L., Mackinder, A., Ernst, R. E., Cousens, B. (2016) Mafic magmatism in the Belt-Purcell Basin and Wyoming Province of western Laurentia. Geological Society of America Special Paper 522, 243 – 260

Rowan, M. G. (2014). Passive-margin salt basins: Hyperextension, evaporite deposition, and salt tectonics. *Basin Research*, *26*(1), 154–182. http://doi.org/10.1111/bre.12043

Russell, J. K., Porritt, L. a., Lavallée, Y., & Dingwell, D. B. (2012). Kimberlite ascent by assimilation-fuelled buoyancy. *Nature*, *481*(7381), 352–356. http://doi.org/10.1038/nature10740

Schmidt-Mumm, A., Behr, H. J., & Horn, E. E. (1987). Fluid systems in metaplaya sequences in the Damara Orogen (Namibia): evidence for sulfur-rich brines-general evolution and first results. *Chemical Geology*, *61*, 135–145.

Schminke, H. (2009) Vulkane der Eifel, Aufbau, Entstehung, und heutige Bedeutung. *Spektrum Akademischer Verlag*

Serdyuchenko, D. P. (1974). Some Precambrian scapolite-bearing rocks evolved from evaporites. *Lithos*, *8*, 1–7.

Sharpton, V. L., & Grieve, R. A. F. (1990). Meteorite impact, cryptoexplosion, and shock metamorphism; A perspective on the evidence at the K/T boundary. In V. Sharpton & P. Ward (Eds.), *Global Catastrophes in Earth history; an interdisciplinary conference on impacts, volcanism and mass mortality: Geological Society of America Special Paper 247* (pp. 301–318).

Sibson, R. H. (2000). Fluid involvement in normal faulting. *Journal of Geodynamics 29, 469 - 499*

Skirrow, R. G., E., B., Davidson, G., Raymond, O. L., & Heithersay, P. (2002). The Geological Framework, Distribution and Controls of Fe-Oxide, Cu-Au Mineralisation in the Gawler Craton, South Australia: Part II: Alteration and Mineralisation. In T. M. Porter (Ed.), *Hydrothermal Iron Oxide Copper-Gold and Related Deposits, A Global Perspective, Volume 2* (pp. 33–47). PGC publishing, Adelaide.

Skirrow, R., Bastrakov, E. N., & Barovich, K. (2007). Timing of Iron Oxide Copper-Gold Hydrothermal Activity and Isotope Constraints on Metal Sources in the Gawler Craton, South Australia Prospect : Timing of Iron Oxide Cu-Au- (U) Hydrothermal Activity and Nd Isotope Constraints. *Economic Geology*, *102*(1995), 1441–1470. http://doi.org/10.2113/gsecongeo.102.8.1441

Smeraglia, L., Berra, F., Billi, A., Boschi, C., Carminati, E., & Doglioni, C. (2016). Origin and role of fluids involved in the seismic cycle of extensional faults in carbonate rocks. *Earth and Planetary Science Letters*, *450*, 292–305. http://doi.org/10.1016/j.epsl.2016.06.042

Snyder, F. G. (n.d.). Structural Lineaments and mineral deposits, eastern United States. In D. O. Rausch & B. C. Mariacher (Eds.), *Mining and Concentration of Lead and Zinc* (pp. 76–94). American Institute of Mining, Metallurgical and Petroleum Engineers Vol. 1.

Snyder, F. G., & Gerdemann, P. E. (1965). Explosive igneous activity along an Illinois-Missouri-Kansas axis. *American Journal of Science*, *263*, 465–493.

Sparks, R. S. J. (2013). Kimberlite Volcanism. *Annual Review of Earth and Planetary Sciences*, *41*(1), 497–528. http://doi.org/10.1146/annurev-earth-042711-105252

Stähle, V. (1972). Impact glasses from the suevite of the Nördlinger Ries. Earth and Planetary Science Letters, 17, 275–293.

Stöffler, D. (1972). Deformation and transformation of rock-forming minerals by natural and experimental shock processes: I. Behavior of minerals under shock compression. *Fortschritte Mineralogie*, *49*, 50–113.

Sturkell, E. F. F. (1992). Resurge morphology of the marine Lockne impact crater, Jämtland, central Sweden. *Geological Magazine*, *1*, 171–177.

Svenningsen, O. M. (1994). Tectonic significance of the meta-evaporitic magnesite and scapolite deposits in the Seve Nappes, Sarek Mts., Swedish Caledonides. *Tectonophysics*, *231*, 33–44.

Tempelman-Kluit, D. J. (1981). Nor, summary of assessment work and description of mineral properties. In *Yukon Geology and Exploration, 1979-1980, Exploration and Geological Services Division, Yukon Indian and Northern Affairs Canada* (pp. 300–301).

Thompson, R. I., Roots, C. F., & Mustard, P. S. (1992). *Geology of Dawson map area (116B, C) (northeast of Tintina Trench). Geological Survey of Canada, Open File 2849*.

Thorkelson, D. J. (2000). *Geology and mineral occurrences of the Slats Creek, Fairchild Lake and ``Dolores Creek'' areas, Wernecke Mountains (106D/16, 106C/13, 106C/14), Yukon Territory*. *Exploration and Geological Services Division, Yukon Region, Bulletin* (Vol. 10).

Thorkelson, D. J., Abbott, J. G., Mortensen, J. K., Creaser, R. A., Villeneuve, M. E., Mcnicoll, V. J., & Layer, P. W. (2005). Early and Middle Proterozoic evolution of Yukon, Canada. *Canadian Journal of Earth Sciences*, *42*, 1045–1071. http://doi.org/10.1139/E04-075

Thorkelson, D. J., & Laughton, J. R. (2016). Paleoproterozoic closure of an Australia-Laurentia seaway revealed by megaclasts of an obducted volcanic arc in Yukon, Canada. *Gondwana Research*, *33*(May 2016), 115–133. http://doi.org/10.1016/j.gr.2015.01.004

Thorkelson, D. J., Mortensen, J. K., Creaser, R. A., Davidson, G. J., & Abbott, G. J. (2001). Early Proterozoic magmatism in Yukon, Canada: constraints on the evolution of northwestern Laurentia. *Canadian Journal of Earth Sciences*, *38*(10), 1479–1494. http://doi.org/10.1139/cjes-38-10-1479

Thorkelson, D. J., Mortensen, J. K., Davidson, G. J., Creaser, R. A., Perez, W. A., & Abbott, J. G. (2001). Early Mesoproterozoic intrusive breccias in Yukon, Canada: The role of hydrothermal systems in reconstructions of North America and Australia. *Precambrian Research*, *111*(1–4), 31–55. http://doi.org/10.1016/S0301-9268(01)00155-3

Vandemeulebrouck, J., Roux, P., & Cros, E. (2013). The plumbing of Old Faithful Geyser revealed by hydrothermal tremor. *Geophysical Research Letters*, *40*(10), 1989–1993. http://doi.org/10.1002/grl.50422

Vannucchi, P., Morgan, J. P., Della Lunga, D., Andronicos, C. L., & Morgan, W. J. (2015). Direct evidence of ancient shock metamorphism at the site of the 1908 Tunguska event. *Earth and Planetary Science Letters*, *409*, 168–174. http://doi.org/10.1016/j.epsl.2014.11.001

Verbaas, J., Thorkelson, D. J., Gibson, H. D., Marshall, D. D., & Milidragovic, D., (2014), Soft sediment textures in clasts in Wernecke Breccia: Reconstruction of an eroded late Paleoproterozoic succession in northern Yukon. In MacFarlane, K.E., Nordling, M.G., Sack, P.J. (Ed), Yukon Exploration and Geology 2014, Yukon Geological Survey, 145-146.

Verbaas, J., and Thorkelson, D. J., (2016). The Wernecke Breccia: mega-breccia formed from the venting of hydrothermal fluid. Geological Association of Canada, GAC Cordilleran Section Exploration Breakfast Series Early Stage Active Projects

Vernette, G., Mauffret, A., Bobier, C., Briceno, L., & Gayet, J. (1992). Mud diapirism, fan sedimentation and strike-slip faulting, Caribbean Colombian Margin. *Tectonophysics*, *202*(2–4), 335–349. http://doi.org/10.1016/0040-1951(92)90118-P

Wade, C. E., Reid, A. J., Wingate, M. T. D., Jagodzinski, E. A., & Barovich, K. (2012). Geochemistry and geochronology of the c. 1585Ma Benagerie Volcanic Suite, southern Australia: Relationship to the Gawler Range Volcanics and implications for the petrogenesis of a Mesoproterozoic silicic large igneous province. *Precambrian Research*, *206–207*, 17–35. http://doi.org/10.1016/j.precamres.2012.02.020

Waltham, T., Bell, F., & Culshaw, M. (2005). *Sinkholes and Subsidence: Karst and Cavernous Rocks in Engineering and Construction*. Springer Praxis Books, Berlin Heidelberg.

Warren, J. K. (2016). *Evaporites a geological compendium* (2nd edition). Springer Berlin Heidelberg.

White, J. D. L., & Ross, P. S. (2011). Maar-diatreme volcanoes: A review. *Journal of Volcanology and Geothermal Research*, *201*(1–4), 1–29. http://doi.org/10.1016/j.jvolgeores.2011.01.010

Wilkinson, J. J. (2014). *Sediment-Hosted Zinc-Lead Mineralization: Processes and Perspectives: Processes and Perspectives*. *Treatise on Geochemistry: Second Edition* (2nd ed., Vol. 13). Elsevier Ltd. http://doi.org/10.1016/B978-0-08-095975-7.01109-8

Williams, P. A. J. W. (2005). Iron Oxide Copper-Gold Deposits: Geology, Space-Time Distribution, and Possible Modes of Origin. *Economic Geology*, *100th Anniversary Volume*, 371–405.

Williams, P. J., & Skirrow, R. G. (2000). Overview of Iron Oxide-Copper-Gold Deposits in the Curnamona Province and Cloncurry District (Eastern Mount Isa Block), Australia. In T. Porter (Ed.), *Hydrothermal Iron Oxide Copper-Gold and Related Deposits, A Global Perspective, Volume 1* (pp. 105–122). PGC publishing, Adelaide.

Wilson, L., & Head Iii, J. W. (2007). An integrated model of kimberlite ascent and eruption. *Nature*, *447*(7140), 53–57. http://doi.org/10.1038/nature05692

Wold, R.J., Mayhew, M.A., Smith, R.B., (1977). Bathymetric and geophysical evidence for a hydrothermal explosion crater in Mary Bay, Yellowstone Lake, Wyoming. Journal of Geophysical Research. 82, 226., 3733–3738.

Woodcock, N. H., Omma, J. E., & Dickson, J. a. D. (2006). Chaotic breccia along the Dent Fault, NW England: implosion or collapse of a fault void? *Journal of the Geological Society*, *163*(3), 431–446. http://doi.org/10.1144/0016-764905-067

Yardley, B. W. D., & Graham, J. T. (2002). The origins of salinity in metamorphic fluids. *Geofluids*, *2*(4), 249–256. http://doi.org/10.1046/j.1468-8123.2002.00042.x

Young, G.M., Jefferson, C.W., Delaney, G.D., and Yeo, G.M., 1979, Middle and late Proterozoic evolution of the northern Canadian Cordillera and Shield: Geology, v. 7, p. 125–128.

Zhang, S., Li, Z. X., Evans, D. A. D., Wu, H., Li, H., & Dong, J. (2012). Pre-Rodinia supercontinent Nuna shaping up: A global synthesis with new paleomagnetic results from North China. *Earth and Planetary Science Letters*, *353–354*, 145–155. http://doi.org/10.1016/j.epsl.2012.07.034

Chapter 5.

1.38 Ga magmatism in northwestern Laurentia: the Hart River sills

This chapter will be prepared for publication in Lithos and will be submitted in 2018.

5.1. Abstract

The Hart River sills are a set of mafic to intermediate intrusions that occur in northern Yukon, Canada. The largest sills are up to 500 metres thick and over 200 km long. New U-Pb dates of 1382.15 ± 0.39 Ma and 1382.14 ± 0.36 Ma were obtained via chemical abrasion thermal ionization mass spectrometry on zircon. Whole rock initial neodymium isotopic compositions of the Hart River sills are juvenile and have εNd_i from +1.5 to +4.0. The primary mineralogy of the Hart River sills is dominated by clinopyroxene and plagioclase. Geochemical modeling indicates that the Hart River sills lie on a common liquid line of descent defined by a fractionating assemblage of plagioclase, clinopyroxene and minor olivine. The Hart River sills have rare earth element and high field strength abundances similar to normal mid-ocean ridge basalts and are enriched in large ion lithophile elements. The Nb/Ta ratio of the sills varies from 0.5 to 17.9 and indicates either enrichment of their mantle source by an Nb-rich melt/fluid (such as carbonatite) or, more likely, low pressure fractionation of Ti-rich minerals. The Sm/Yb and Dy/Zr ratios indicate >8% partial melting of spinel-bearing mantle. During the emplacement of the Hart River sills, western Laurentia was juxtaposed with Australia and eastern Antarctica within the supercontinent Columbia. The degree of partial melting, similarity to N-MORB, and juvenile isotopic signature are consistent with an episode of rifting at 1.38 Ga. Coeval magmatism and intracontinental rift basins farther south on Laurentia provide additional evidence for rifting of supercontinent Columbia at 1.38 Ga.

5.2. Introduction

Large igneous provinces (LIPs) provide valuable information on both mantle processes and plate tectonics (Halls, 1982; Bleeker and Ernst, 2006; Ernst et al., 2008, Ernst et al., 2013; Ernst et al., 2014). LIPs have the potential to be correlated from one continental block to another and help constrain paleogeographic reconstructions (Bleeker and Ernst, 2006; Ernst et al., 2008, Ernst et al., 2013). LIPs are generally regarded as large intraplate magmatic provinces with an igneous volume >0.1 Mkm^3 that are emplaced within 35 m.y. in one or more short magmatic pulses (Bryan and Ernst, 2008, Ernst and Bleeker, 2010; Ernst and Youbi, 2017). The origin of LIPs is varied, and may involve mantle plumes, delamination of lithosphere, or impact events (Campbell and Kerr, 2007; Ernst and Bleeker, 2010). The ages of LIPs on continental blocks effectively produce a 'barcode' that can be correlated from one continental block to another (Bleeker, 2003; Ernst and Bleeker, 2010; Ernst et al., 2013). In addition to these 'barcodes', radiating dyke swarms associated with many LIPs may be correlated from one continental block to another, providing useful paleogeographic constraints (Bleeker and Ernst, 2006; Ernst et al., 2013).

The Hart River sills are a set of intermediate to mafic intrusions that have been dated by U-Pb zircon at 1.38 Ga (Abbott, 1997; Thorkelson et al., 2005). The sills are voluminous and were included in the global LIP database by Ernst et al. (2008) as a possible LIP remnant. The Hart River sills were emplaced into the Paleoproterozoic Wernecke Supergroup in the Ogilvie and Wernecke mountains of Yukon, northern Canada (Green, 1972; Abbott, 1997; Thorkelson, 2000). Determining the magmatic and tectonic environment of the Hart River sills is critical because they are potentially associated with other magmatic events of similar age on Laurentia (Doughty and Chamberlain, 1998), Antarctica (Lanyon et al., 1993) and Siberia (Ernst et al., 2000). Combined, these magmatic events may reflect a LIP of key importance to the tectonic history of Laurentia and its neighbours (Ernst et al., 2008; Evans and Mitchell, 2011; Puchkov et al., 2013). Western Laurentia was proximal to Siberia (Sears and Price, 1978, 2002; David et al., 2016; Ernst et al., 2016), Australia (Bell and Jefferson, 1987; Moores, 1991; Thorkelson et al., 2001; Medig et al., 2014; chapter 3), and Antarctica (Goodge et al., 2008) during the Mesoproterozoic.

Precise new U-Pb zircon ages were obtained from the Hart River sills using U-Pb chemical abrasion thermal ionization mass spectrometry (CA-TIMS). These ages are coupled with whole rock elemental and isotopic (Sr, Nd, and Pb) geochemistry on major, minor and trace elements. Together, the data are used to confirm the widespread distribution of the sills and to provide a petrogenetic model. In addition, the sills are compared to other igneous complexes of similar age, and are considered in the context of a dynamic Mesoproterozoic Earth.

5.3. The Hart River sills

5.3.1. Geological context

The Hart River sills crop out over an area of approximately 180 x 80 km in northern Yukon, Canada. Most of the sills are exposed in a narrow curvilinear belt. They were mapped by Green (1972) at a scale of 1:250,000 and by Abbott (1997) at 1:50,000. Three U-Pb zircon dates on the sills have been published from the Hart River area: 1385.8 ± 1.9 Ma, 1383.0 +5.9/-5.2 Ma, 1380.2 +4.0/-3.8 Ma (Abbott, 1997). One additional intrusion in the northern Wernecke Mountains was dated by Thorkelson et al. (2005) at 1381.9 +5.3/-3.7. Two additional higher precision ages of 1382.15 ± 0.39 Ma and 1382.14 ± 0.36 Ma are provided herein.

Exposures of the Hart river sills are mainly restricted to the southern Wernecke Mountains. However, the sills likely extend in the subsurface to more northern regions, including the northern Wernecke Mountains and the southern Richardson Mountains (Figure 5.1). This extent is evident from sites of crustal reheating as revealed by growth of garnet in the host rock to the sills in the Wernecke Mountains at 1362 ± 35 Ma and in the Richardson Mountains at 1372 ± 31 Ma (Furlanetto, 2013), and growth of rutile at 1383 ± 7 Ma in the Slab Volcanics (Thorkelson et al., 2001a). Similarly, based on rutile and zircon ages Davis (1997) concluded that the 1.27 Ga McKenzie event extends far beyond its current exposure. The Hart River event may also have included sheets of mafic magma within or at the base of the Laurentian crust.

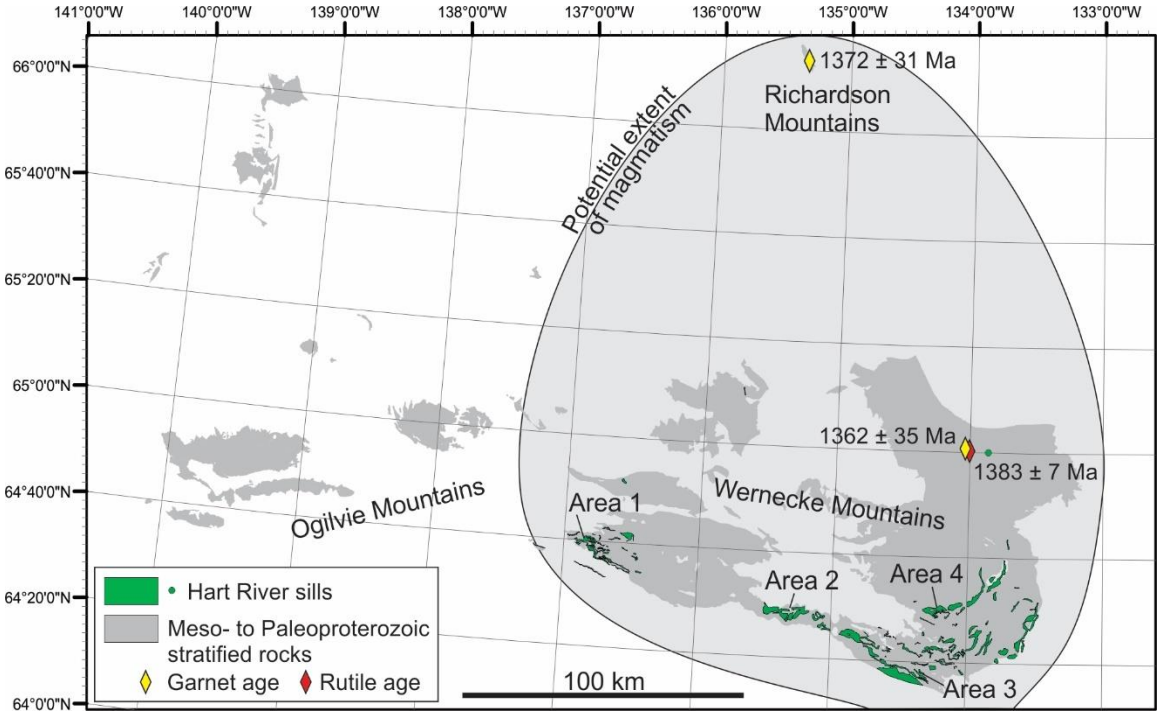

Figure 5.1. Extent of the Hart River sills and the potential extent of magmatism in the subsurface based on garnet and rutile ages of Thorkelson et al. (2001) and Furlanetto et al. (2013). Sampling areas are shown in more detail in figure 5.2.

The Hart River sills were emplaced into the Wernecke Supergroup, a passive margin succession deposited between 1.66 and 1.60 Ga (Furlanetto et al., 2013; 2016). Underlying the Wernecke Supergroup are approximately 5-9 km of unexposed strata (Furlanetto et al., 2016). Most of the sills occur in the southern Wernecke and Ogilvie mountains where they were emplaced into dolostone of the Gillespie Lake Group, the highest unit of the Wernecke Supergroup. Others were emplaced into lower strata of the Wernecke Supergroup, and possibly at deeper structural levels.

Regional deformation and metamorphism of the Wernecke Supergroup during the 1.6 Ga Racklan Orogeny is recorded in the western Ogilvie Mountains and northern Wernecke Mountains (Eisbacher, 1978; Mercier, 1989; Thorkelson, 2000; Thorkelson et al., 2005; Furlanetto et al., 2013). Racklan deformation and metamorphism was focused to the northwest in current coordinates (Thorkelson, 2000). The Racklan Orogeny does not appear to have affected the southern Wernecke Mountains and the southeastern Ogilvie Mountains (Abbott, 1997; Moroskat, 2009). There, the Hart River sills are thick and

continuous and appear to have been emplaced in undeformed strata. In the northern Wernecke Mountains the Hart River sills intruded in deformed and metamorphosed strata. In this area, the sills are present as smaller but less continuous stocks (Thorkelson, 2000). In these deformed and metamorphosed strata, magma was not able to intrude as long tabular bodies and hence sills in the northern Wernecke Mountains are smaller in size and not as continuous.

The Wernecke Supergroup is overlain by unit PR1 of the Fifteenmile Group (Thompson, 1992; Medig et al., 2014) and the Pinguicula Group (Medig et al., 2016). The PR1 basin contains sedimentary rocks with a distinctive Australian provenance and was deposited at approximately 1.45 Ga (Medig et al., 2014). The Pinguicula Group is a siliciclastic and carbonate succession that was deposited in a tectonically active basin sometime during the interval 1.38 – 1.0 Ga (Thompson, 1992; Medig et al., 2016).

A set of volcanic rocks was termed the 'Hart River volcanics' and correlated to the Hart River sills by Abbott (1997), based on spatial association and geochemical character. However, our field investigation in 2013 showed that the Hart River volcanics are not as extensive as previously mapped and are limited to a few pillow basalt flows in a succession of fine grained sedimentary rocks. Based on geochemical results presented in Appendix C this assemblage is reinterpreted to be Neoproterozoic or younger.

5.3.2. Paleogeographic context

Recent tectonic syntheses postulate that Laurentia and Australia underwent a Wilson cycle (Wilson, 1968) followed by sinistral translation (Furlanetto et al., 2016; Thorkelson et al., 2016) during the existence of the supercontinent Columbia at ca. 1.8 - 1.45 Ga (Zhang et al., 2012). Laurentia and Australia were proximal at 1.75 Ga, although their exact orientation remains unclear (Pisarevsky et al., 2014; Furlanetto et al., 2016). Antarctica was connected to southern Australia from the Paleo- or early Mesoproterozoic until the Neoproterozoic (Payne et al., 2009; Goodge and Fanning, 2016). It is unclear how Laurentia, Australia and Antarctica were connected prior to 1.75 Ga, but lithospheric extension within Laurentia and Australia is evident as early as 1.7 Ga (Rainbird and Davis, 2007; Gibson, 2008), and separation of Laurentia from Australia probably occurred at

ca.1.66 Ga (Furlanetto et al., 2016). However, by 1.6 Ga, the intervening oceanic lithosphere had been consumed and collision between northwestern Laurentia and the Australia is interpreted to have resulted in the Racklan Orogeny (Chapter 3). A sedimentary overlap succession was deposited (Chapter 3) and hematitic hydrothermal breccias formed on both continents (Thorkelson et al., 2001).

During the interval ca. 1.60 - 1.45 Ga, Australia and Antarctica were translated along the margin of Laurentia, leading to a more southerly fit during deposition of the PR1 basin (Medig et al., 2014; Chapter 3). Renewed rifting of Australia and Laurentia occurred at roughly 1.45 Ga when sediments of Australian provenance were deposited in the PR1 basin of northern Laurentia, as well as the Purcell, Trampass and Hess Canyon basins of central and southwestern Laurentia (Ross and Villeneuve, 2003; Doe et al., 2012; Daniel et al., 2013; Medig et al., 2014; Jones et al., 2015). Concurrently, the Moyie sills were emplaced on the margin of western Laurentia at 1468 ± 2 Ma (Anderson and Davis, 1995; Rogers et al., 2016). The PR1 basin was deposited between 1.46 and 1.42 Ga during exhumation and erosion of its proposed source batholiths in eastern Australia (Spikings et al., 2001; Medig et al., 2014). The absence of an Australian flux of sediment onto Laurentia after 1.45 Ga suggests that Australia and Laurentia were fully separated by this time (Jones et al., 2015; Medig et al., 2016). Rifting may be represented by magmatism along the margin of western Laurentia at 1.38-1.37 Ga (Doughty and Chamberlain, 1996; Abbott, 1997; Thorkelson et al., 2005) and throughout much of northern Laurentia at 1.27 Ga (LeCheminant and Heaman, 1989). Australia and Laurentia were later reattached during formation of the supercontinent Rodinia (Li et al., 2008).

5.3.3. Location and sampling

Sixteen samples of the Hart River sills were collected from 4 areas in Yukon Territory (

Table 5.1, Figure 5.2). Three of the thickest sills were sampled at different levels in order to identify possible magmatic layering.

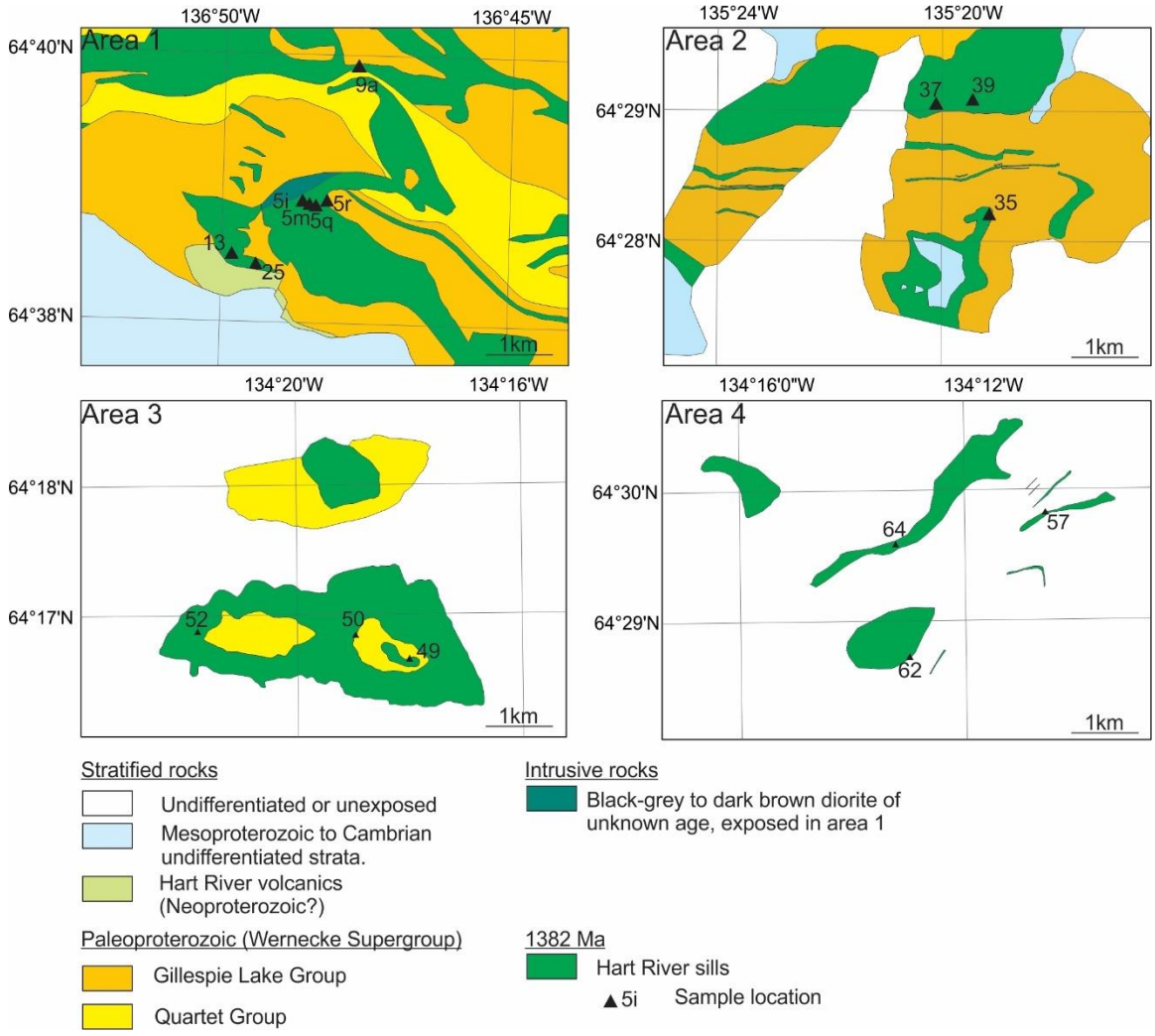

Figure 5.2. Detailed maps of the 4 sampled areas. Samples are indicated with the last two digits of the full sample name. The sample areas are indicated on Figure 5.1. (The map of Area 1 is modified from Abbott, 1997).

Table 5.1. List of Hart River sill samples

Sample	Rock type	Area	UTM Easting[4]	UTM Northing[4]	Use[2]	Reference
JV13-2-5i	Gabbro	1	413502	7170518		
JV13-2-5k	Gabbro	1	413595	7170477		
JV13-2-5m	Gabbro	1	413687	7170453	RI, MC	
JV13-2-5q	Gabbroic diorite	1	413839	7170519	RI, MC	
JV13-3-9a	Gabbro	1	414286	7172369	MC	
JV13-4-13	Gabbro	1	412521	7169793		
JV13-6-25	Gabbro	1	412851	7169628		
JV13-11-35	Gabbro	2	484591	7149412		
JV13-12-37	Gabbroic diorite	2	483834	7150985	MC	
JV13-12-39	Gabbro	2	484355	7151043	AD, RI	
JV13-12-49	Gabbro	3	533887	7128138		
JV13-16-50	Gabbroic diorite	3	533108	7128457		
JV13-16-52	Gabbro	3	530844	7128520	AD, RI	
JV13-18-57	Gabbro	4	539582	7152671	RI, MC	
JV13-19-62	Gabbro	4	537651	7150606	AD, RI	
JV13-20-64	Gabbroic diorite	4	537444	7152209	RI	
GA4-2	Gabbro	1[1]				Abbot, 1997 (TON93-4-2)[3]
GA4-3	Gabbro	1[1]				Abbott, 1997 (TON93-4-3)[3]
GA6-3	Gabbro	1[1]				Abbott, 1997 (TOA95-6-3)[3]
GA6-5	Gabbro	1[1]				Abbott, 1997 (TOA95-6-5)[3]

[1]Sample chemistry taken from Abbott (1997); exact location not reported.
[2]Sample use: all samples were analysed for major, minor and trace elements. RI: radiogenic isotopes, MC: mineral chemistry (electron microprobe), AD: age determination.
[3]Original sample name assigned by Abbott (1997)
[4]UTM NAD 1983

5.3.4. Field relations and petrology

The Hart River sills range in thickness from several metres to more than 500 metres (Figure 5.3A). Exposure lengths range from several metres up to 200 kilometres. The sills are dark gray to light green and weather dark grey to dark brown. They range from gabbro to diorite and are locally plagioclase-phyric (Figure 5.3B). Thick sills (>100 metres) are commonly accompanied by smaller sills, dikes and apophyses that are up to 10 metres across. The Hart River sills host up to three joint sets. One joint set is commonly parallel to the orientation of the sills. Locally a second and third perpendicular joint set are present. Primary mineralogical variations are commonly obscured by alteration and

metamorphic mineral assemblages. A clearly visible metasomatic margin is present where the dikes and sills intruded carbonate-rich rocks of the Wernecke Supergroup. This metasomatic margin is light grey to white and consists of several decimetres to metres of dolomitized wall rock. The sills and their metasomatic margins are typically more resistant to weathering than the host rock.

The primary mineralogy of the sills is dominated by plagioclase (Figure 5.3C), clinopyroxene, hornblende (Figure 5.3D), interstitial ilmenite (Figure 5.3E), and ilmenite in colloidal FeO_x after titaniferous magnetite (Figure 5.3D), and minor interstitial quartz. Plagioclase occurs as elongate twinned crystals and as lamellar and globular symplectites in granophyres and is commonly altered to fine-grained sericite. Clinopyroxene occurs as inclusions in hornblende or is rimmed by hornblende. Both clinopyroxene and hornblende are variably metamorphosed to chlorite. Sericite, amphibole and chlorite are locally present as veinlets. Trace minerals include epidote, clinozoisite, zircon and rutile.

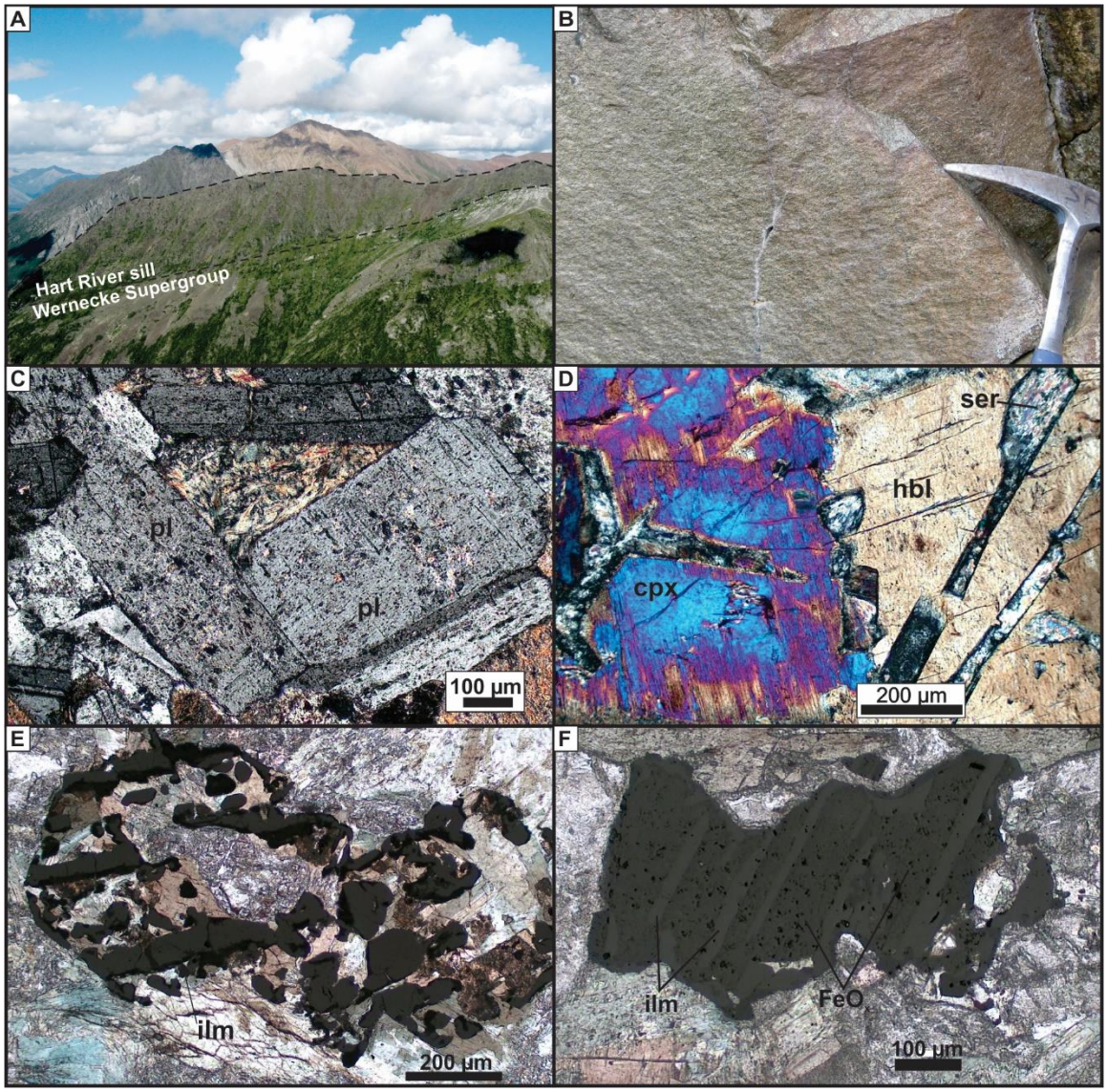

Figure 5.3. **A. Thick (> 400 metres) Hart River sill exposed within the Wernecke Supergroup. B. Dark green to brown Hart River sill. C. Twinned plagioclase with interstitial alteration minerals (predominantly sericite). D. Clinopyroxene partially altered to hornblende with sericitized laths of early formed plagioclase. E. Interstitial ilmenite. F. Skeletal ilmenite in a colloid(?) FeO_x matrix (dark grey). This grain is interpreted as a former grain of titaniferous magnetite that exsolved ilmenite. The magnetite was subsequently altered to a colloid.**

Several samples contain medium-grained euhedral plagioclase and medium to small subhedral to anhedral pyroxene-amphibole grains with well defined grain boundaries. Plagioclase is commonly overgrown by pyroxene-amphibole, or forms a

network of laths with pyroxene-amphibole in the interstices. However, in several samples plagioclase has overgrown clinopyroxene-amphibole grains. Ilmenite and rutile commonly occur as anhedral interstitial minerals and as skeletal overgrowths over titaniferous magnetite.

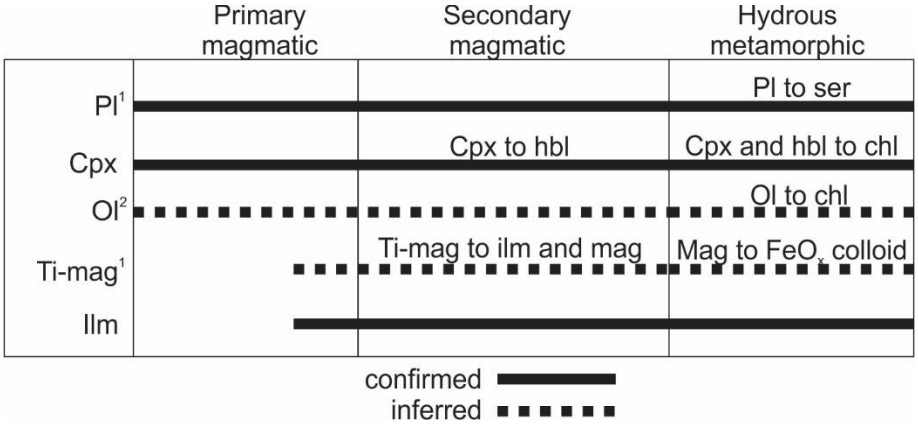

Figure 5.4. Mineral paragenesis of the Hart River sills. [1]Locally accumulated. [2]The presence of olivine is inferred from results presented in section 5.6.3 and 5.6.4

The relation between plagioclase and clinopyroxene indicates cotectic crystallization (Figure 5.4). The alteration of clinopyroxene to hornblende represents a high-temperature mineral-melt reaction (Bowen, 1956; Deer et al., 1966). The occurrence of inclusions of hornblende in clinopyroxene is inconsistent with amphibolite facies metamorphism. Titaniferous magnetite and primary ilmenite crystallized as interstitial phases. Secondary ilmenite later exsolved from titaniferous magnetite and the magnetite subsequently altered to a FeO_x colloid. Several samples appear to have accumulated titaniferous magnetite. Alteration to sericite and chlorite occurred during lower greenschist facies hydrous metamorphism.

5.4. Analytical techniques

Whole rock major, minor and trace elements were analyzed at Activation Laboratories, Ontario, Canada. Samples were fused in a lithium metaborate/tetraborate bead to ensure full digestion and subsequently dissolved in weak nitric acid. Samples were then analyzed using a combination of inductively coupled plasma mass

spectrometry, inductively coupled plasma optical emission spectra and instrumental neutron activation analyses (Appendix C).

Seven powdered sill samples were used for whole rock radiogenic isotope analyses at the University of Florida Centre for Isotope Geoscience. Sm-Nd isotope ratios were determined by isotope dilution on whole rock powders following the methods of Ingle et al. (2003) and Heatherington and Mueller (1991). Rb-Sr isotope ratios were determined following the methods of Heatherington and Mueller (1991). Pb-Pb isotope ratios were determined following the methods of Kamenov et al. (2005).

Zircon crystals were separated from sill samples using standard crushing, milling and magnetic separation techniques at Simon Fraser University. The zircon crystals were mounted on epoxy and imaged by cathode luminescence to select suitable crystals and analyses spots at Boise State University. Subsequently the zircon crystals were analyzed at Boise State University using laser ablation inductively coupled mass spectrometry (LA-ICPMS) on three samples. Zircon rare earth element chemistry was analyzed concurrently with U-Pb isotope ratios. Suitable zircon crystals of these samples were selected for subsequent chemical abrasion thermal ionization mass spectrometry (CA-TIMS) in order to minimize the uncertainty on the crystallization age. Full methods and results for LA-ICPMS and full methods for CA-TIMS are reported in Appendix C.

5.5. Major, minor and trace element geochemistry

5.5.1. Whole rock major, minor and trace element geochemistry

Whole rock major elements were recalculated to anhydrous compositions with all iron as Fe^{2+}, reported as FeO*. The samples have a restricted range of SiO_2 content, from 46.6– 52.5 wt %. Mg is more variable and MgO ranges from 2.24 – 10.18 wt. %. The Mg number (Mg# = Mg / (Mg+Fe^{2+}) ranges from 20.52 – 72.02. Major oxides are plotted versus MgO in Fenner plots (Figure 5.5). The FeO*, P_2O_5 and TiO_2 concentration increase with decreasing MgO content. The Al_2O_3 concentration decreases with decreasing MgO content. Na_2O ranges from 1.84 – 4.60 wt %. And K_2O from 0.60 – 2.88 wt. %. Na_2O, K_2O and Na_2O/K_2O versus MgO display significant scatter. The CaO concentration ranges from

5.49 - 11.29 wt. % and CaO versus MgO also displays significant scatter. Geochemical data tables are presented in Appendix C. Whole rock major oxide data of four samples from Abbott (1997) are included in the data treatment. Samples are subdivided into potassically altered, sodically altered, and least altered groups (defined in Section 5.5.2).

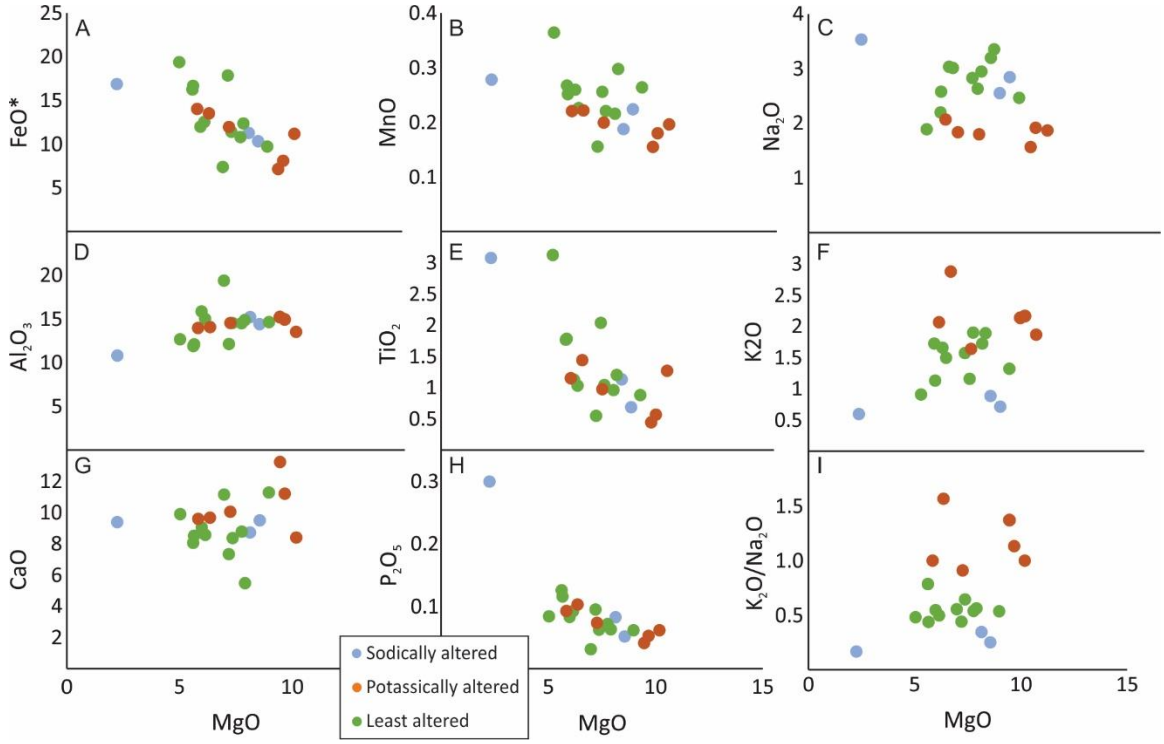

Figure 5.5. Fenner plots of major element oxides. Samples are divided into sodically altered, a potassically altered, and least altered groups (alteration groupings are established in section 5.6.1). Stonergram modeling (Section 5.7.3.) argues against variably sodic and potassic magma sources.

Trace element abundances

The Hart River sills have trace element abundances that are similar to normal mid-oceanic ridge basalts (N-MORB) with the exception of large ion lithophile elements (LILE) such as Ce, K and Ba (Figure 5.6) which are significantly elevated. The pattern is flat from Nb-Lu. The REE patterns range from flat to light rare earth element (LREE) enriched, and Eu anomalies vary from 0.70 – 1.20 (Eu anomalies were calculated as $Eu_{ch}^* = Eu_{CN} / (Sm_{CN} + Gd_{CN} / 2)$). Sample JV13-20-64 has especially abundant REE. The compatible trace elements Zn, Mn and V range from slightly depleted to moderately enriched. The Ta/Nb ratio of the Hart River sills ranges from 0.5 to 17.9.

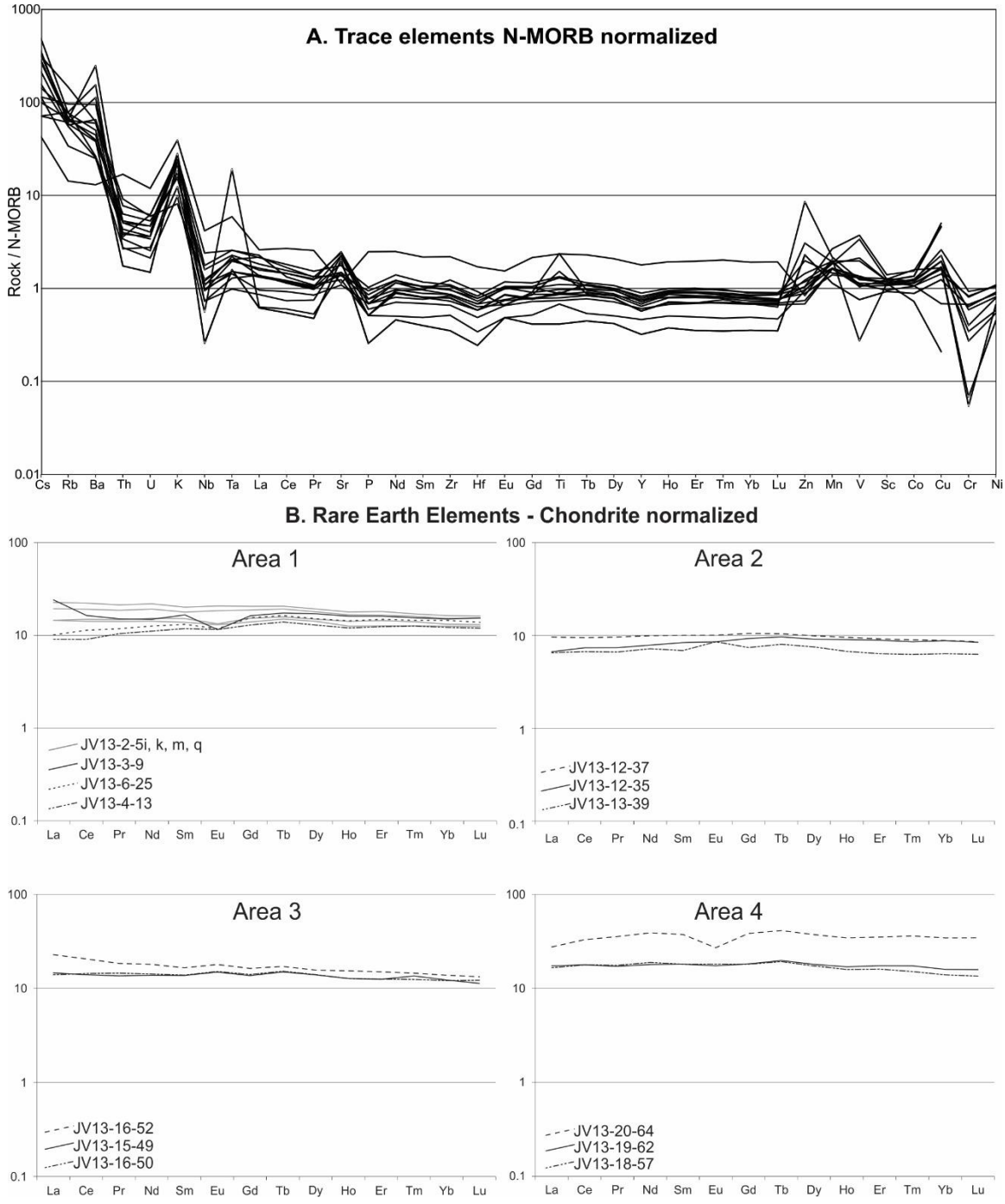

Figure 5.6. A. Trace elements normalized to N-MORB show enrichment in light ion lithophile elements, and high field-strength and rare earth elements similar to N-MORB. B. Chrondrite-normalized REE plots display flat profiles with minor variation in enrichment.

Samples from Area 1 fall into two categories. The first consists of samples JV13-2-5i to 5q, which represent different samples of one thick sill. The second category includes different sills and dykes. Some of these sills and dykes may be apophyses of the larger sill. The sills in this area have variable LREE, from 9 – 25 times chondritic values. Samples of area 3 and 4 are enriched in REE with overall flat profiles. An exception is sample JV13-20-64, which is highly enriched in REE. Samples of area 2 are more primitive and therefore less enriched than those of other areas.

Chemical classification and tectonic discrimination diagrams

The Hart river sills plot as gabbro to gabbroic diorite on the total alkali – SiO_2 classification (Figure 5.7A) of LeBas et al. (1986) and the Zr/Ti vs. Nb/Y diagram (Figure 5.7B) of Winchester and Floyd (1977), and are thereby identified as subalkaline. On the FeO^*/MgO – SiO_2 diagram (Figure 5.7C) of Miyashiro (1974), the data display ambiguity between a tholeiitic and calc-alkaline signature. However, on the ternary plot of FeO*, MgO and total alkalis (Figure 5.7D) of Irvine and Baragar (1971) the data display a clear tholeiitic trend. All samples are metaluminous.

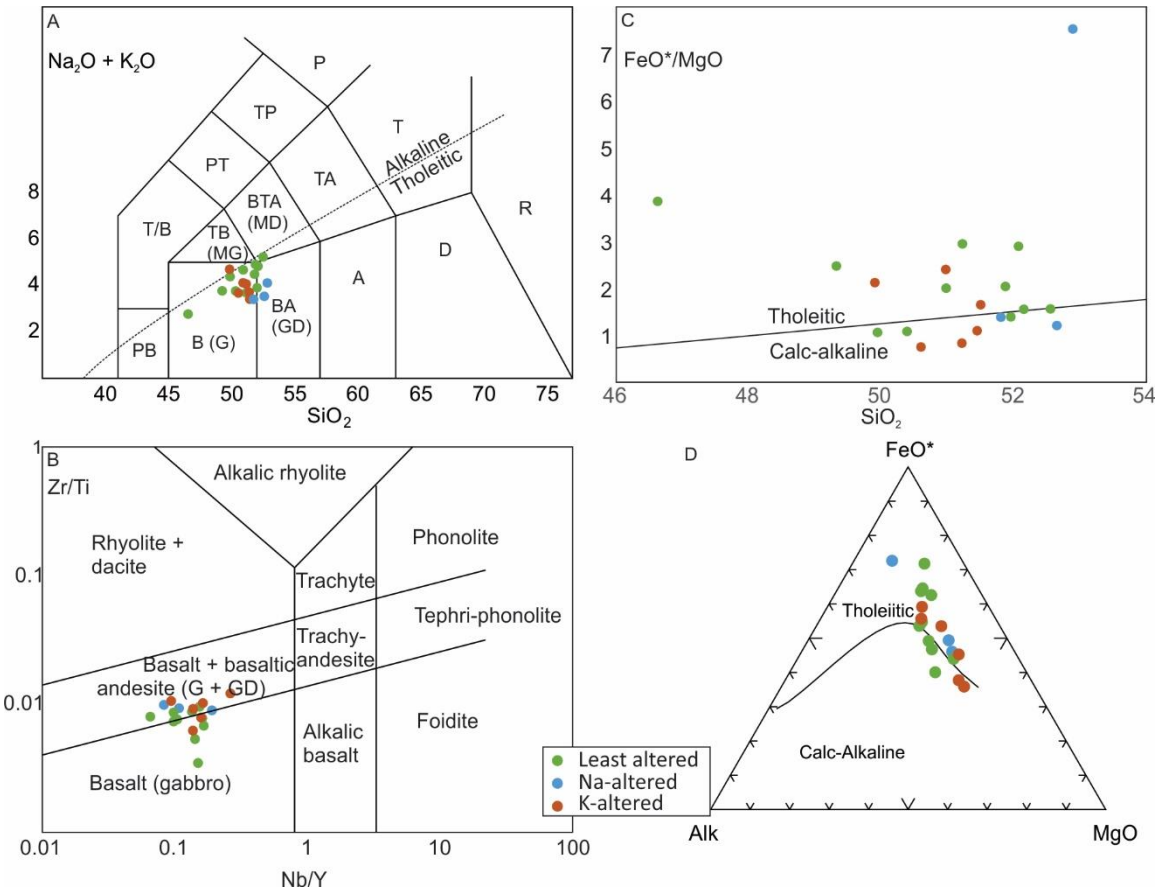

Figure 5.7. A, B. Chemical classification diagrams based on major and trace elements indicate the Hart River sills are gabbros to gabbroic diorites (LeBas et al., 1986; Irvine and Barager, 1971; Winchester and Floyd, 1977). C-D. Major elements indicate the Hart River sills represent a tholeiitic magma series (Miyashiro, 1974, Irvine and Baragar, 1971).

Using an Nb/La versus $(Sm/La)_N$ classification (John et al., 2003) the data display similarity to mid-oceanic ridge basalts (Figure 5.8A). On the Yb-normalized Th and Nb MORB array (Figure 5.8B) of Pearce (2008), the data plot above the MORB-OIB mantle array and display a relative enrichment in Th relative to N-MORB. Using an N-MORB normalized Th and Nb classification as proposed by Saccani (2015), the data fall on the edges of the backarc, intra-oceanic arc, and oceanic subduction-unrelated & rifted margin fields (Figure 5.8C).

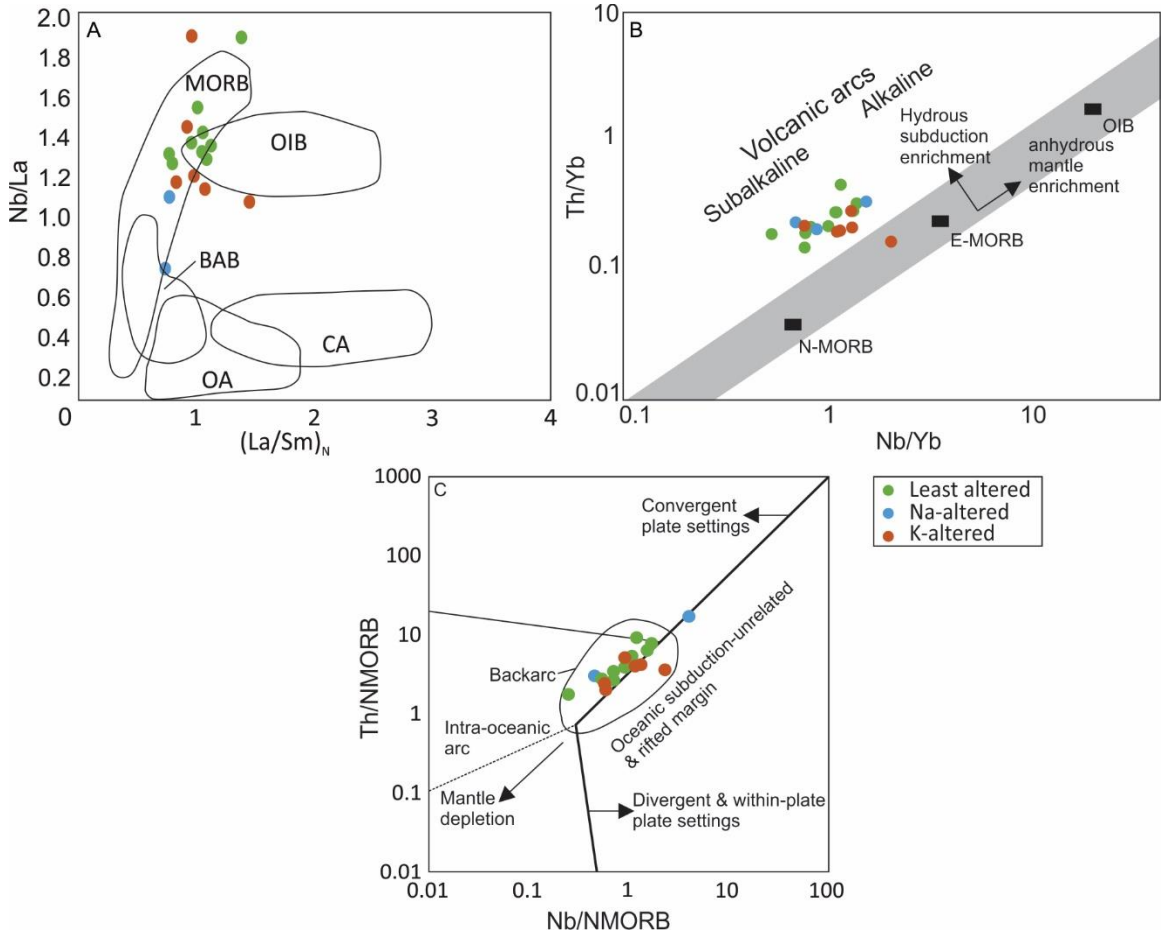

Figure 5.8. **A. Tectonic discrimination based on Nb/La and $(La/Sm)_N$ indicates similarity to mid-oceanic ridge basalt (John et al., 2003). B. The Hart River sills fall above the MORB-OIB array (Pearce, 2008) and are enriched in Th. C. NMORB normalized Th vs. Nb plot after Saccani, 2015. The Hart River sills plot on the margin of the convergent-divergent, and oceanic-continental field, and all but one sample fall in the backarc field.**

The trace element pattern of the Hart River sills illustrates the high enrichment of light ion lithophile elements Cs, Rb, Ba and K, and of the elements Zn – Cu (Figure 5.9). These elements are more abundant in the Hart River sills than in any other typical magma such oceanic island basalt and continental arc basalts. Apart from these elements, the abundance of the trace elements is most similar with that of E-MORB.

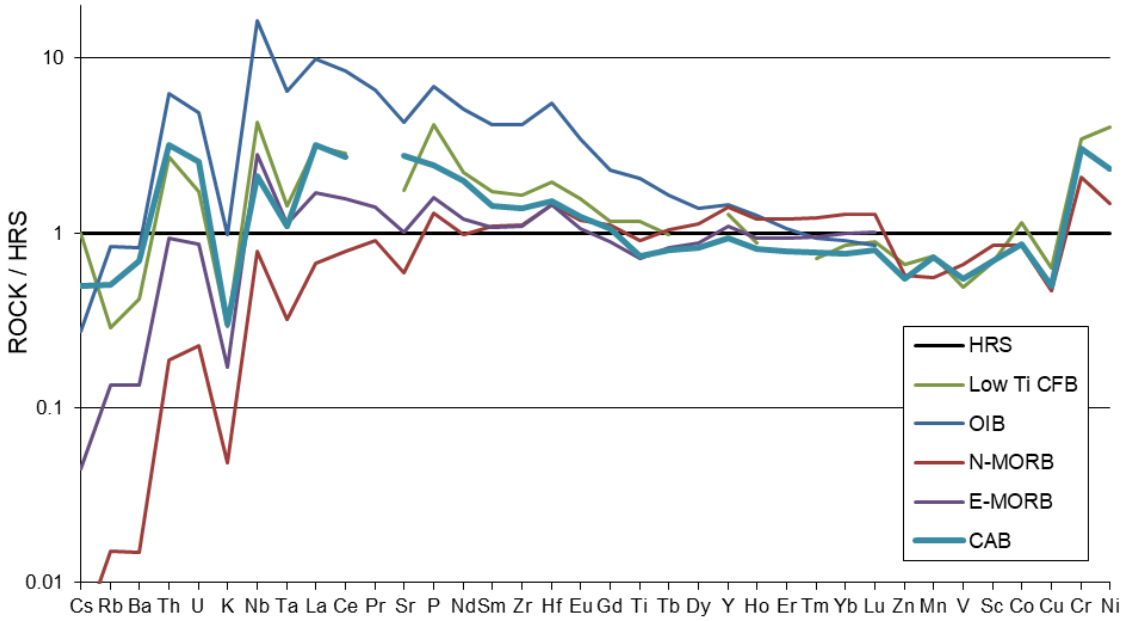

Figure 5.9. Trace element patterns of the Hart River sills (HRS, with a value of 1) compared to low Ti continental flood basalt (CFB; data from Farmer et al., 2014), oceanic island basalt (OIB), normal mid-oceanic ridge basalt (N-MORB), enriched mid-oceanic ridge basalt (E-MORB), data from Sun & McDonough (1989), Pearce and Parkinson, (1993), and Thorkelson (unpublished), and continental arc basalt (CAB; data from Kelemen et al., 2014)

5.5.2. Alkali Alteration

The mineralogy of the Hart River sills is largely secondary, and the most ubiquitous mineral phases are hydrothermal and metamorphic in origin. Metamorphism is evident from abundant chlorite overgrowths on amphibole and clinopyroxene. Hydrothermal alteration is evident from sericitic overgrowths on plagioclase, amphibole and other veinlets (Abbott, 1997). The extent of alteration of the most mobile major elements, potassium and sodium is here quantified following Nielsen (2013) and Thorkelson and Laughton (2016). K_2O vs. Na_2O display significant scatter (Figure 5.10A). The ratio K_2O/Na_2O against MgO also displays significant scatter (Figure 5.10B). During fractional crystallization, both K_2O and Na_2O are expected to increase as MgO decreases, because both are incompatible. If magmatic processes govern the abundances of Na_2O and K_2O these oxides should plot on a clear positive trend. Instead, the scatter of data is evidence

for significant remobilization of K_2O and Na_2O. The K_2O/Na_2O ratios of the Hart River sills range from 0.17 – 1.57.

The Hart River sills are here subdivided into three groups based on their K_2O/Na_2O ratio (Figure 5.10) in order to show the degree to which samples have undergone alkali metasomatism. The purpose of this discrimination is to identify samples which are most likely to have preserved their original igneous geochemical compositions. The variation in the K_2O/Na_2O ratio is best visualized as a histogram (Figure 5.10C). Least altered samples have ratios K_2O/Na_2O ratios from 0.40 to 0.80. Although this subdivision is perhaps not entirely correct (all samples likely have undergone some degree of alteration), it allows for the difference in K_2O/Na_2O to be visualized and the relative amounts and types of alteration to be assessed.

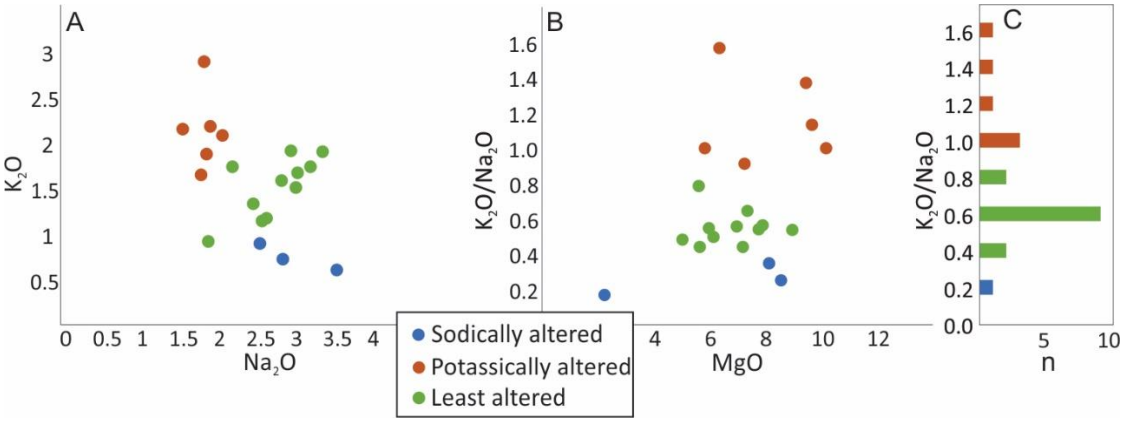

Figure 5.10. A. K_2O vs. Na_2O. B. K_2O/Na_2O vs. MgO. C. Histogram of K_2O vs. Na_2O. Samples with $0.4 < K_2O/Na_2O < 0.8$ are chosen to represent a least altered sample suite.

5.6. Isotope geochemistry

5.6.1. Whole rock Sm-Nd, Pb-Pb, and Rb-Sr isotope ratios

Nd, Pb and Sr isotope ratios were acquired to determine the source characteristics of the Hart River sills and reported in Table 5.2. Because of the ubiquitous alteration of the Hart River sills the isotope data may not reflect a primary magmatic signature. We show that different isotope systems represent varying degrees of alteration using major and trace elements.

All of the Nd isotope ratios are juvenile compared to the chondritic uniform reservoir (CHUR; DePaolo and Wasserburg, 1976). These Nd isotope ratios are consistent with no to minor crustal enrichment. The εNd was recalculated to initial values of 1.5 to 4.0. The Sr isotope ratios are highly variable and all are evolved compared to CHUR. The Sr isotope ratios $^{87}Sr/^{86}Sr$ were recalculated to initial values of $^{87}Sr/^{86}Sr_i$ from 0.703 to 0.725. A plot of $\varepsilon Nd_{1.38}$ versus $^{87}Sr/^{86}Sr_i$ displays a weak negative trend (Figure 5.11A). Because the absolute Pb abundance is only known for three samples, the abundance of Pb for other samples was calculated from that of sample JV13-20-64 (using Rayleigh fractionation based on PER, see also Section 5.7.2 and 5.7.3) because it represents a refractory melt with good Pb analyses and is mineralogically fresh. The initial values all plot close to the 1.38 Ga geochron and are consistent with no to minor crustal enrichment (Figure 5.11B).

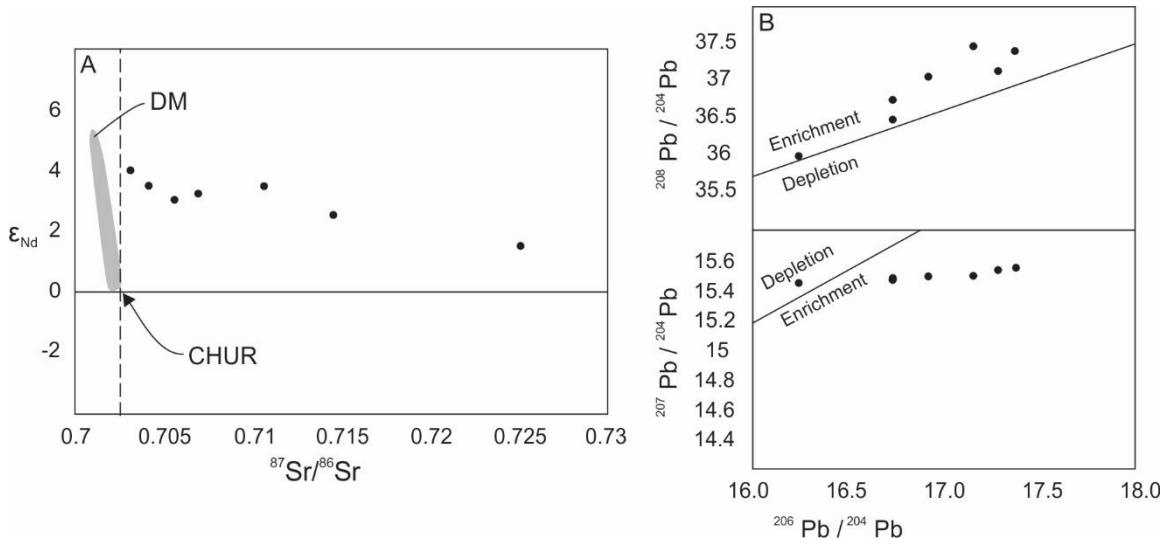

Figure 5.11. A. Initial ε_{Nd} is juvenile whereas $^{87}Sr/^{86}Sr$ is evolved. Indicated in light grey is the mantle array, which indicates expected ε_{Nd} and $^{87}Sr/^{86}Sr$ values for melts extracted from depleted mantle (DM) through to CHUR. B. Initial Pb isotope are consistent with results from Nd isotopes and plotted with the 1.38 Ga geochron.

The Nd and Sr isotope analyses yield contradictory results. The Nd isotope analyses yield a mostly juvenile signature, whereas the Sr isotope analyses yield a variable signature from juvenile to highly evolved. The Pb isotope data yields similar results to the Nd isotope data. In order to clarify the results of the different isotope systems, the parent elements of both isotope systems (Sm and Rb) are plotted against MgO and

the daughter elements Nd and Sr (Figure 5.12). Sm versus MgO and versus Nd displays linear trends that are consistent with closed system fractionation. Plots of Rb versus MgO and Sr display no obvious correlation and Rb appears to correlate to the Na_2O/K_2O ratio. This relationship supports the possibility that these elements were remobilized during alteration.

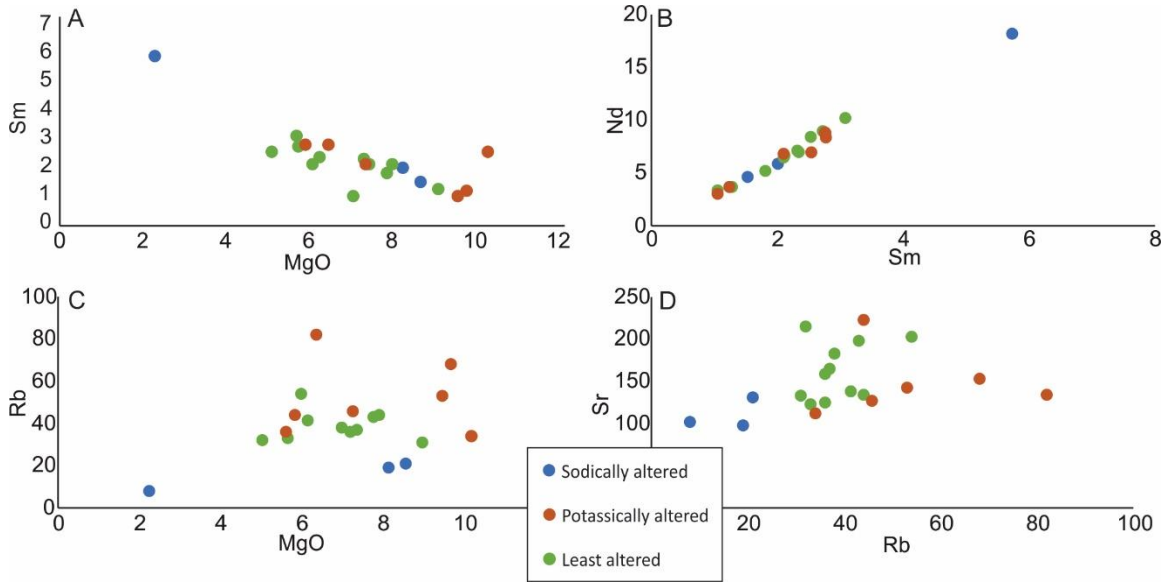

Figure 5.12. A. Nd vs MgO display a negative correlation that is consistent with incompatible behaviour of Nd. B: Nd vs Sm display a strong positive linear correlation that is consistent with incompatible behaviour of both elements in mafic magmatic systems. C-D: Rb vs MgO and Rb vs Sr show scattered patterns that appear to be partly controlled by degree of alkali alteration

The Nd ratios are juvenile except for sample JV13-12-52, which has a slightly more evolved initial Nd isotope ratio of εNd_i = +1.52 (Figure 5.12). This sample was taken on the margin of a sill. The evolved signature may have been caused by wallrock assimilation of isotopically enriched Wernecke Supergroup (Furlanetto et al., 2016).

Table 5.2. Whole rock radiogenic isotope data.

	Nd (ppm)	Sm (ppm)	$\frac{^{143}Nd}{^{144}Nd}$	$\frac{^{147}Sm}{^{144}Nd}$	εNd_0	$\varepsilon Nd_{1.38}$	T_{DM}[1]
JV13-19-62	9.2	3.0	0.51283	0.19853	3.8	3.5	2.08
JV13-20-64	19.9	6.5	0.51279	0.19886	2.9	2.5	2.72
JV13-2-5q	7.3	2.4	0.51279	0.19528	3.0	3.2	2.06
JV13-2-5m	7.9	2.5	0.51277	0.19445	2.6	3.0	2.12
JV13-18-57	9.8	3.1	0.51281	0.19353	3.4	4.0	1.69
JV13-16-52	9.2	2.8	0.51257	0.18117	-1.2	1.5	2.18
JV13-12-39	3.7	1.3	0.51288	0.20322	4.6	3.5	2.47

	Pb ppm	$\frac{^{206}Pb}{^{204}Pb}$	$\frac{^{207}Pb}{^{204}Pb}$	$\frac{^{208}Pb}{^{204}Pb}$	$\frac{^{206}Pb}{^{204}Pb_i}$	$\frac{^{207}Pb}{^{204}Pb_i}$	$\frac{^{208}Pb}{^{204}Pb_i}$
JV13-19-62	3.5[2]	18.023	15.586	37.954	16.942	15.491	37.060
JV13-20-64	7	17.597	15.563	37.435	16.258	15.445	35.989
JV13-2-5q	2.7[2]	18.379	15.600	38.623	17.172	15.494	37.468
JV13-2-5m	3.0[2]	18.259	15.598	38.049	16.980	15.485	36.939
JV13-18-57	3.5[2]	18.085	15.602	37.839	17.299	15.533	37.136
JV13-16-52	9	17.918	15.595	38.022	17.391	15.548	37.404
JV13-12-39	25	16.805	15.485	36.524	16.760	15.481	36.484

	Rb (ppm)	Sr (ppm)	$\frac{^{87}Sr}{^{86}Sr}$	error	$\frac{^{87}Sr}{^{86}Sr_i}$
JV13-19-62	44	223	0.722	1.4E-05	0.711
JV13-20-64	8	102	0.719	2.6E-05	0.715
JV13-2-5q	37	165	0.720	2.6E-05	0.707
JV13-2-5m	36	125	0.722	2.1E-05	0.706
JV13-18-57	82	134	0.737	2.2E-05	0.703
JV13-16-52	32	215	0.733	1.6E-05	0.725
JV13-12-39	38	183	0.716	1.7E-05	0.704

[1]Acccording to methods outlined in DePaolo (1981)

[2]Lead values recalculated using assumed ideal Rayleigh Fractionation of lead, fit to sample JV13-20-64. The percentage of fractionation was estimated using ideal fractionation of Sm, which is well defined for all samples

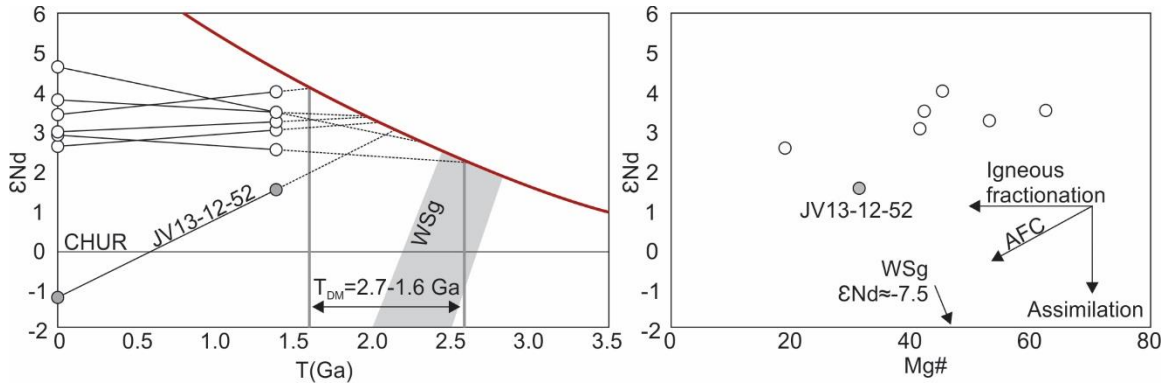

Figure 5.13. Nd isotopes are predominantly juvenile, except for sample JV13-12-52. The more evolved Nd isotope ratio of this sample may reflect assimilation of evolved crust, and/or Wernecke Supergroup (WSg).

5.6.2. Zircon U-Pb age determinations and zircon chemistry

Two geochronology samples have been analysed with CA-TIMS. These samples were taken from area 2 and 3, which previously lacked well defined ages. Zircon crystals of a sample taken from area 4 were analyzed via LA-ICPMS and yielded similar ages (Appendix C). CA-TIMS age determinations are reported in Table 5.3. All selected zircon crystals range from tabular subhedral to anhedral with sharp terminations and jagged edges and are 50 – 150 µm in size (Figure 5.14). Seven zircon crystals from JV13-53 (Figure 5.15) yielded equivalent $^{207}Pb/^{206}Pb$ ages (0.05-0.30% discordance). A weighted mean date of 1382.15 ± 0.39 Ma (MSWD = 1.1, probability of fit = 0.35) is the interpreted igneous crystallization age (Figure 5.15A). Seven zircon crystals from JV13-61 (Figure 5.15) were analyzed via CA-TIMS, all of which yielded equivalent $^{207}Pb/^{206}Pb$ ages (0.01-0.36% discordance). A weighted mean date of 1382.14 ± 0.36 Ma (MSWD = 1.4, probability of fit = 0.23) is the interpreted igneous crystallization age (Figure 5.15B).

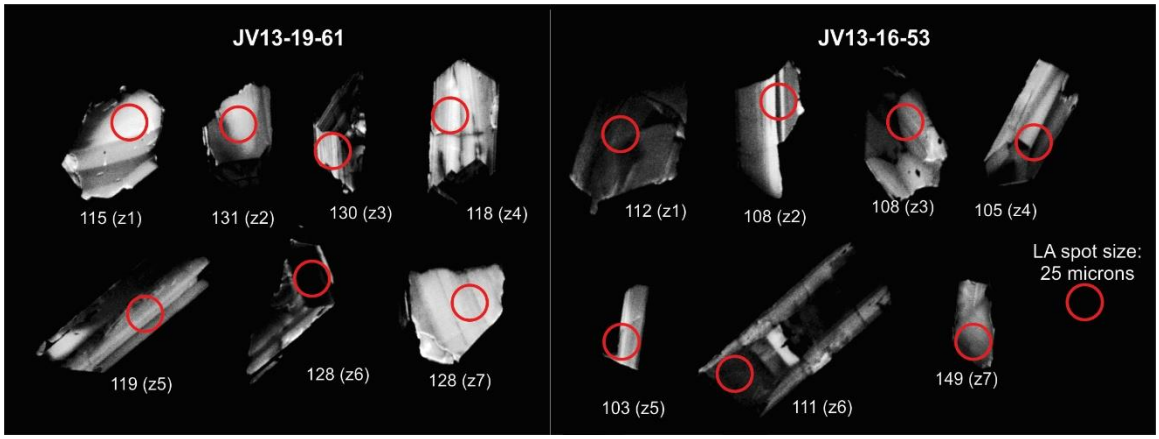

Figure 5.14. CL images of zircon from the Hart River sill selected for CA-TIMS analyses after LA-ICPMS (red circles indicate spot locations).

Ti in zircon thermometry indicates that sample JV13-12-39 crystallized zircon at higher temperatures (Ca. 750 – 850 °C) than sample JV13-16-53 and JV13-19-62 (Ca. 670 – 750 °C). Sample JV13-12-39 was taken in the centre of a thick sill, and samples JV13-16-53 and JV13-19-62 were taken on the margins of sills. Sample JV13-12-39 also has a higher Eu* anomaly than other samples (Figure 5.15C). Zircon REE abundances are shown in (Figure 5.15D). Zircon chemistry and U-Pb isotope ratios obtained via LA-ICPMS are reported in Appendix C.

Table 5.3. CA-TIMS zircon U-Pb analyses

						Radiogenic Isotope Ratios										Isotopic Dates					
	$\frac{Th}{U}$	$^{206}Pb^*$ x 10^{-13} mol	mol % $^{206}Pb^*$	$\frac{Pb^*}{Pb_c}$	Pb_c (pg)	$\frac{^{206}Pb}{^{204}Pb}$	$\frac{^{208}Pb}{^{206}Pb}$	$\frac{^{207}Pb}{^{206}Pb}$	% err	$\frac{^{207}Pb}{^{235}U}$	% err	$\frac{^{206}Pb}{^{238}U}$	% err	corr. coef.	$\frac{^{207}Pb}{^{206}Pb}$	±	$\frac{^{207}Pb}{^{235}U}$	±	$\frac{^{206}Pb}{^{238}U}$	±
(a)	(b)	(c)	(c)	(c)	(c)	(d)	(e)	(e)	(f)	(e)	(f)	(e)	(f)		(g)	(f)	(g)	(f)	(g)	(f)
JV13-16-53																					
z1	0.747	8.6209	99.96%	765	0.30	42375	0.223	0.088083	0.066	2.896159	0.128	0.238574	0.069	0.957	1383.44	1.26	1380.91	0.97	1379.28	0.85
z2	0.925	9.9797	99.97%	1094	0.26	58174	0.276	0.088050	0.071	2.896270	0.130	0.238674	0.069	0.932	1382.71	1.36	1380.94	0.98	1379.80	0.86
z3	0.990	31.4495	99.99%	3078	0.29	161391	0.295	0.088007	0.040	2.895105	0.086	0.238694	0.052	0.959	1381.77	0.76	1380.64	0.65	1379.90	0.64
z4	1.041	11.1745	99.97%	1153	0.28	59833	0.310	0.088006	0.062	2.897830	0.126	0.238921	0.068	0.972	1381.76	1.19	1381.35	0.95	1381.08	0.85
z5	0.959	10.6345	99.96%	889	0.34	46951	0.286	0.088012	0.062	2.894400	0.127	0.238623	0.070	0.969	1381.87	1.18	1380.45	0.96	1379.53	0.87
z6	1.064	17.4165	99.98%	1623	0.31	83782	0.317	0.088020	0.041	2.895633	0.087	0.238702	0.052	0.955	1382.06	0.78	1380.77	0.66	1379.94	0.64
z7	0.997	11.8222	99.94%	573	0.59	30042	0.297	0.088035	0.064	2.897759	0.127	0.238837	0.068	0.966	1382.38	1.22	1381.33	0.96	1380.65	0.85
JV13-19-61																					
z1	0.874	9.2180	99.95%	686	0.37	36899	0.261	0.088043	0.064	2.894960	0.127	0.238583	0.068	0.968	1382.57	1.22	1380.60	0.96	1379.33	0.85
z2	0.958	15.2586	99.97%	1221	0.35	64462	0.286	0.087968	0.061	2.895918	0.126	0.238867	0.069	0.970	1380.92	1.18	1380.85	0.95	1380.80	0.86
z3	1.039	8.1996	99.95%	643	0.37	33401	0.310	0.088040	0.065	2.890473	0.129	0.238223	0.069	0.965	1382.49	1.26	1379.43	0.98	1377.45	0.85
z4	1.021	19.7754	99.98%	1595	0.36	83091	0.304	0.088042	0.041	2.899892	0.087	0.238994	0.052	0.953	1382.54	0.79	1381.88	0.66	1381.46	0.65
z5	1.023	33.2333	99.98%	2144	0.45	111636	0.305	0.088003	0.041	2.895290	0.087	0.238721	0.051	0.956	1381.68	0.78	1380.69	0.65	1380.04	0.64
z6	2.041	13.8182	99.97%	1353	0.36	57795	0.608	0.088028	0.042	2.895284	0.088	0.238651	0.052	0.949	1382.23	0.80	1380.68	0.66	1379.68	0.65
z7	0.887	14.5917	99.97%	1046	0.39	56146	0.264	0.088044	0.060	2.899829	0.125	0.238984	0.068	0.976	1382.57	1.16	1381.87	0.95	1381.41	0.85

a) z1, z2, etc. are labels for analyses composed of single zircon grains that were annealed and chemically abraded (Mattinson, 2005).

b) Model Th/U ratio calculated from radiogenic $^{208}Pb/^{206}Pb$ ratio and $^{207}Pb/^{235}U$ date.

c) Pb* and Pbc are radiogenic and common Pb, respectively. mol % $^{206}Pb^*$ is with respect to radiogenic and blank Pb.

d) Measured ratio corrected for spike and fractionation only. Fractionation correction is 0.18 ± 0.03 (1σ) % /(atomic mass unit) for single-collector Daly analyses, based on analysis of EARTHTIME ^{202}Pb-^{205}Pb tracer solution

e) Corrected for fractionation, spike, common Pb, and initial disequilibrium in $^{230}Th/^{238}U$. Common Pb in analyses was assigned to the zircon with a composition determined by Stacey and Kramers (1975), except for 0.3 µg that was assigned to laboratory blank with a composition of $^{206}Pb/^{204}Pb$ = 18.04 ± 0.61%; $^{207}Pb/^{204}Pb$ = 15.54 ± 0.52%; $^{208}Pb/^{204}Pb$ = 37.69 ± 0.63% (1σ). $^{207}Pb/^{206}Pb$ ratios corrected for initial disequilibrium in $^{230}Th/^{238}U$ using Th/U_{magma} = 3.0 ± 0.3 (1σ).

f) Errors are 2σ, propagated using algorithms of Schmitz and Schoene (2007) and Crowley et al. (2007).

g) Calculations based on the decay constants of Jaffey et al. (1971). $^{206}Pb/^{238}Pb$ and $^{207}Pb/^{206}Pb$ dates corrected for initial disequilibrium in $^{230}Th/^{238}U$ using Th/U_{magma} = 3.0 ± 0.3 (1σ)

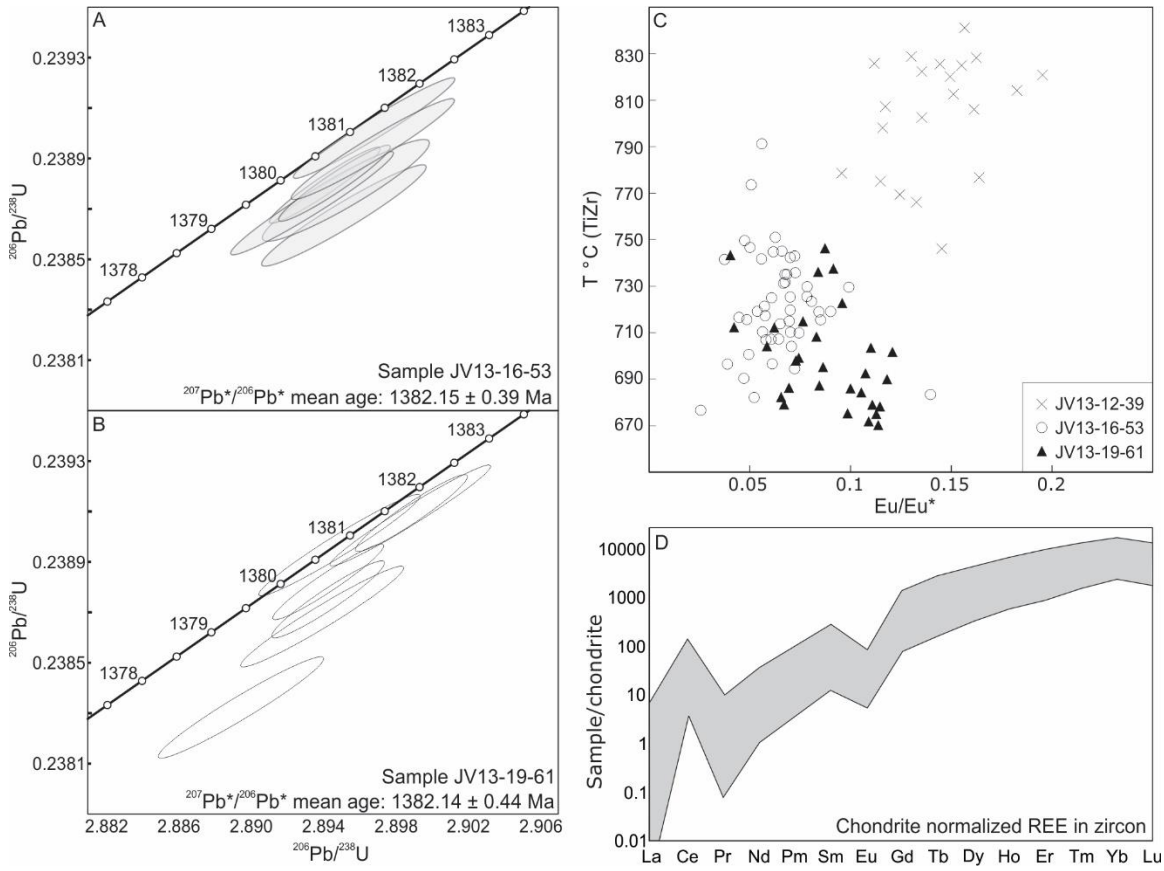

Figure 5.15. A. Sample JV13-16-53 zircon U-Pb ratios obtained via CA-TIMS plotted in a Wetherill concordia diagram. B. Sample JV13-19-61 zircon U-Pb ratios obtained via CA-TIMS plotted in a Wetherill concordia diagram. C. Ti in zircon thermometry plotted against the Eu anomaly in zircon (obtained via LA-ICPMS, Appendix C). D. Rare earth element concentrations in zircon obtained via LA-ICPMS (Appendix C).

5.7. Petrogenetic modeling

Several methods are used in order to determine the petrogenesis of the Hart River sills. Pearce element ratio (PER) modeling is used in order to assess igneous processes using the compositions of all samples on single diagrams. Stonergram modeling is used to determine whether all samples can be related to a common parent, and which minerals were involved in magma differentiation. Alphamelts modeling (Ghiorso and Sack, 1995; Smith and Asimow, 2005) is used to assess the ambient conditions of mantle melting.

5.7.1. Mineral chemistry

Electron microprobe (EMP) data was obtained at the electron microscopy lab of the University of British Columbia. Qualitative mineralogy and quantitative mineral chemistry of clinopyroxene and oxide minerals in six thin section sample were analyzed using a Cameca SX50 electron microprobe. Data were rejected if the analyses did not sum to 98 – 102 %, if calculated total cations fell outside the range 99 – 101%, and/or if the charge balance varied by more than 1 %.

Pyroxene compositions are reported in appendix C. All measured pyroxene is augite with constant calcium content (range) and a variable Fe/Mg ratio (also range) (Figure 5.16). The Fe/Mg of clinopyroxene increases with decreasing MgO content of samples. Analyzed augite has on average ~23% Fe_2O_3. Measured oxides were skeletal ilmenite and trace rutile. Skeletal ilmenite occurs within and around a FeO_x colloid after magnetite. This colloid was not successfully analyzed.

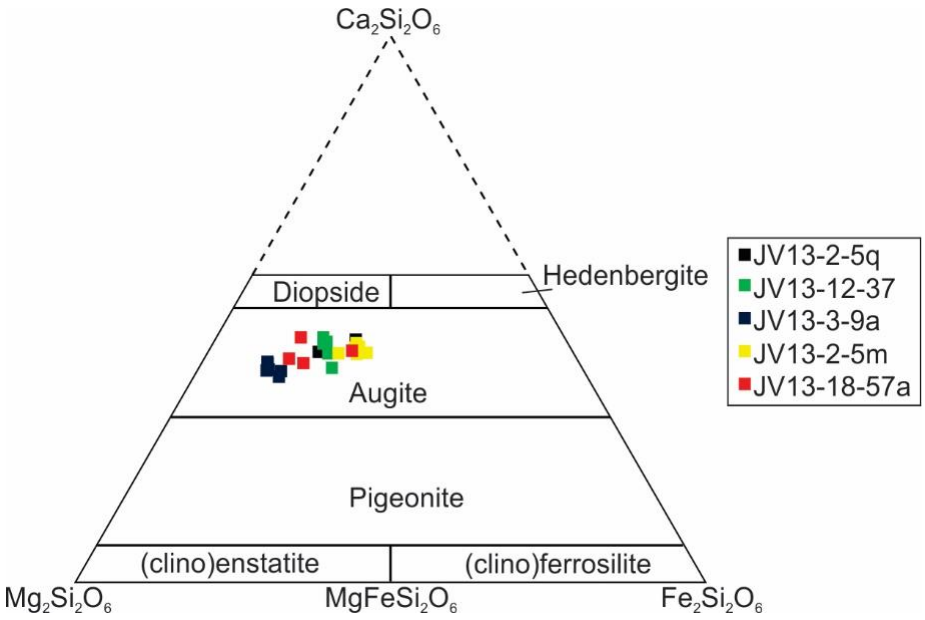

Figure 5.16. All measured clinopyroxenes are augite.

5.7.2. Pearce Element Ratios

Pearce element ratio diagrams are normalized bivariate plots that can aid in the identification of minerals that were involved in magma differentiation, particularly closed-

system processes such as crystal fractionation and accumulation (Russell and Nichols, 1988; Ernst et al., 1988; Russel and Stanley, 1990; Nichols and Russell, 2016). Ratios are constructed by dividing molar concentrations of major oxides affected by fractionation or accumulation by abundances of an element that, ideally, has been precisely determined and is both “conserved” and “immobile.” A conserved element is one which has not been appreciably included in the minerals that grew during magma crystallization (such elements are also termed “highly incompatible elements”). An immobile element is one which has not been appreciably affected by post-magmatic processes such as metamorphism and weathering. The resulting graphs allow displays of data to be compared to “control lines” with slopes that are related to mineral stoichiometry. For example, if only the mineral anorthite ($CaAl_2Si_2O_8$) has fractionated from a silicate melt, the resulting slope on a normalized Al-Si diagram will be 1. Here, Sm used for the normalization because the Sm analysis has a low uncertainty, and is expected to behave both as an incompatible and conserved element in mafic to intermediate systems. Samarium exhibits linear to curvilinear trends on bivariate plots with MgO (negative slope), and incompatible elements such as Zr, Hf, Ce, Er (positive slopes, Figure 5.17), which further suggests that it behaved consistently and predictably during magma differentiation and remained immobile. Using a different conserved element such as Ce, Er, Hf or Zr for the normalization yields similar results.

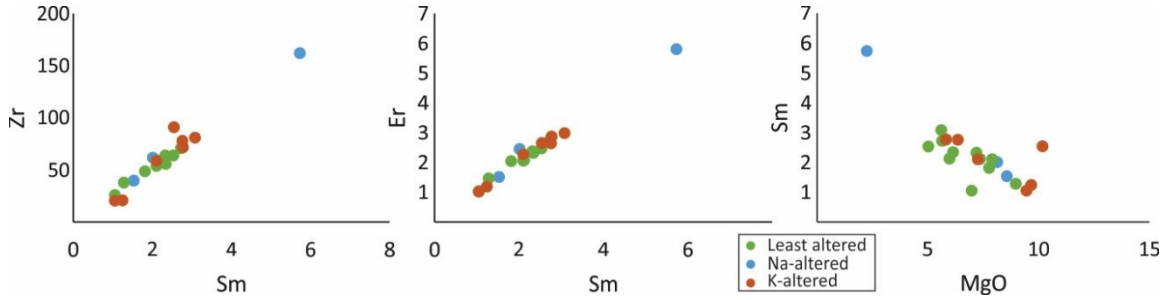

Figure 5.17. Samarium exhibits normal refractory behavior. Zirconium and Er exhibit similar behaviour.

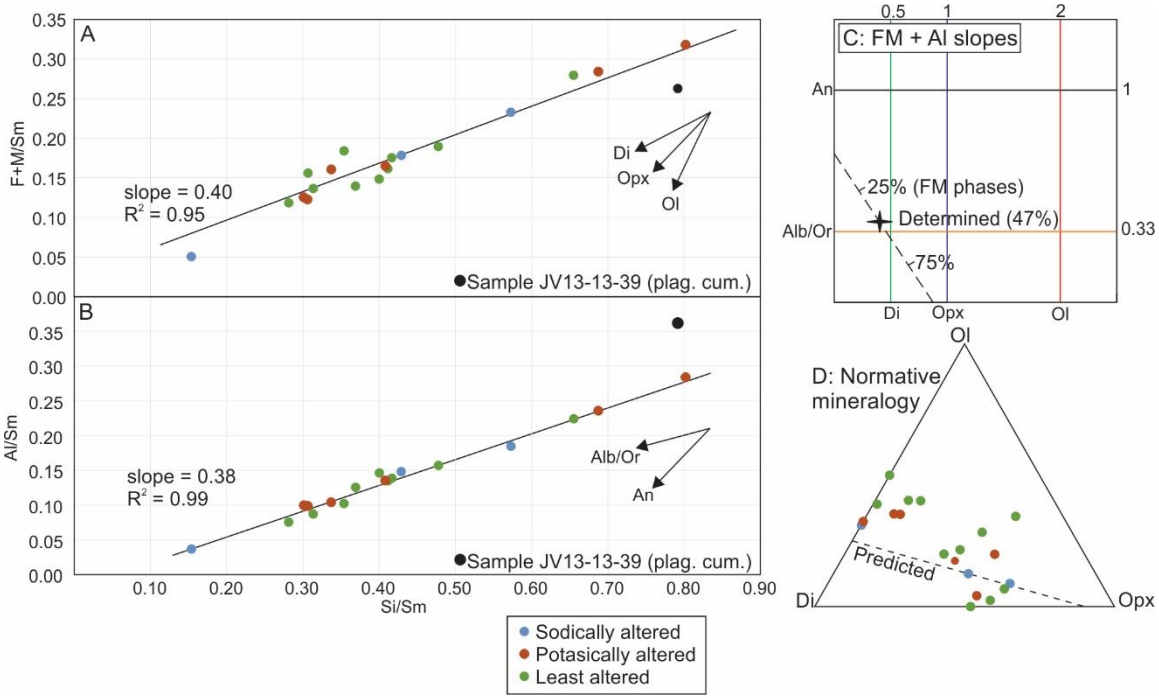

Figure 5.18. A. Sm-normalized Fe and Mg versus Si plot. The resulting slope is 0.40. B. Sm-normalized Al plot. The resulting slope is 0.38. C. Plot of the slope of Al-bearing minerals (Al) and ferromagnesian (FM) phases, olivine and pyroxene (for further discussion see text). D. Normative mineralogy of ferromagnesian silicates and the predicted abundances from PER analysis.

In a Sm-normalized PER diagram of Fe + Mg versus Si, the samples fall on a well-defined trend with slope = 0.40 and R^2 = 0.95 (Figure 5.18A). On the PER diagram of Al versus Si, the data define a slope of 0.38 with R^2 = 0.99 (Figure 5.18B). Sample JV13-13-39 was not used for the calculation of the slope because it falls off the main trend and was likely affected by different magmatic processes (as described in section 5.7.3, this sample is a plagioclase cumulate). As shown by the labelled vectors on these diagrams, rocks that are related to one another by mineral fractionation should display distinctive trends. For example, fractionation of 100% olivine would result in a slope of 1 on Figure 5.18A, but a slope of 0 on Figure 5.18B. Fractionation of 50% diopside and 50% anorthite would result in a slope of 0.5 on both Figure 5.18A and Figure 5.18B.

The PER data trends can be further analyzed on a PER slope diagram featuring ferromagnesian silicates (FM) versus Al-bearing minerals (Al) (Figure 5.18C; modified from Fecova, 2009). The data plot close to the intersection of albite/orthoclase, and

diopside. Normative mineralogy of the least altered samples predicts feldspar in the Hart River sills to consist of 85% An_{48} and 15% orthoclase, and is consistent with PER data. The relative percentage of ferromagnesian phases is less certain because the normative mineralogy cannot be correlated to optical microscopy (olivine and/or orthopyroxene are altered to hornblende and chlorite).

The fractionating ferromagnesian minerals can be determined by using results from normative mineralogy and PER diagrams, on the FM – Al slope diagram (Figure 5.18C). The slopes of the AL PER (0.38) and FM PER (0.40) diagrams are plotted on the FM-AL slope diagram. If a sample would consist of only 85% An_{48} and 15% orthoclase it would have a slope of 0.70 on an Al PER diagram. This slope of 0.70 of the Al PER diagram (Figure 5.18B) is plotted on the Al axis of the FM - Al slope diagram (Figure 5.18C). A straight line is drawn between the two points ((0, 0.70) and (0.40; 0.38)) and extrapolated to the FM axis (Figure 5.18C). This line intersects the FM-axis at a value of 0.87. A slope of 0.87 can result from 75% clinopyroxene and 25% olivine (as shown in section 5.7.3 there is no evidence for fractionation of orthopyroxene). The location of the determined slopes (0.40, 0.38) on the line connecting the FM axis and Al axis indicates a ratio of FM/Al minerals of 47%. The resulting total average fractionating assemblage is estimated at 49% plagioclase (An_{48}), 38% clinopyroxene and 13% olivine.

5.7.3. Stonergram modeling

Brief introduction to the Stonergram

The Stonergram is a numerical and graphical method developed by D.J. Thorkelson to model igneous fractionation, assimilation, accumulation, restite formation, metasomatism and magma mixing. The Stonergram method relies on conserved element logic, mineral stoichiometry and whole rock compositions to detect addition and/or subtraction of phases in the form of oxides, minerals, trace elements, or magmas. The Stonergram approach is similar to PER analysis but utilizes independent multi-oxide calculations instead of algebraic-numerator oxide ratios. Stonergrams also differ in that any immobile and well-determined trace element can be used as a model-constraining element as long as its bulk partition coefficient can be reasonably estimated. For that reason, the model-constraining element may be a truly conserved incompatible element

(e.g., Ba, La), but may alternatively be a less incompatible element (e.g., Lu, Y) or even a compatible element (e.g., Cr, Co). In simple cases, such as those involving closed-system magmatic systems, Stonergrams allow the user to model how samples are related to each other by mineral fractionation or accumulation. For reasons outlined in the previous section, Sm is used as the model-constraining denominator in Stonergram modeling of the Hart River sills.

Successful use of the Stonergram requires compositional input parameters that are consistent with other data such as optical petrography and EMP-determined mineral compositions. If such data is not available, the mineralogical compositions used must be geologically justifiable (based, for example, on acceptable exchange distribution coefficients). For the Hart River sills, Sm is used as a conserved element as it displays an apparent magmatic trend when plotted against a range of other elements, as described in section 5.6.1. The mineral phases used are 1) plagioclase (An_{48} as a nominal starting composition), 2) olivine (with Fe/Mg in equilibrium with melt with exchange distribution coefficient of 0.3 (Roeder and Emslie, 1970), 3) clinopyroxene (Fe/Mg ratio from EMP data), 4) titaniferous magnetite (Fe/Ti ratio adjusted to fit TiO_2 abundance), and 5) apatite. This mineral assemblage is broadly consistent with optical mineralogy and EMP data, and the PER analysis.

The partition coefficient for Sm was determined using the program FraCryst, developed by D.J. Thorkelson. With this program, the partition coefficient of two elements can be determined by fitting a Rayleigh crystallization curve to measured data. Ideally two elements are chosen that have different partition coefficients. For example, an element such as Ni which is compatible in mafic melts, versus Zr, an incompatible element. In order to identify a bulk partition coefficient for the Hart River sills the elements Ni versus Sm and Cr versus Sm were used. Both Ni and Cr are compatible elements in mafic melts, whereas Sm is commonly incompatible (Rollinson, 1993). The trace element behavior was modeled using a partition coefficient of 0.01 for Sm (Figure 5.19), and accordingly this value was used in Stonergram modeling. Using a different conserved element such as Zr or Er yields similar Stonergram modeling results. Samples from Abbott (1997) are included in the modeling because the values for Sm and trends between Sm and other elements appear indistinguishable from the new data collected for this thesis.

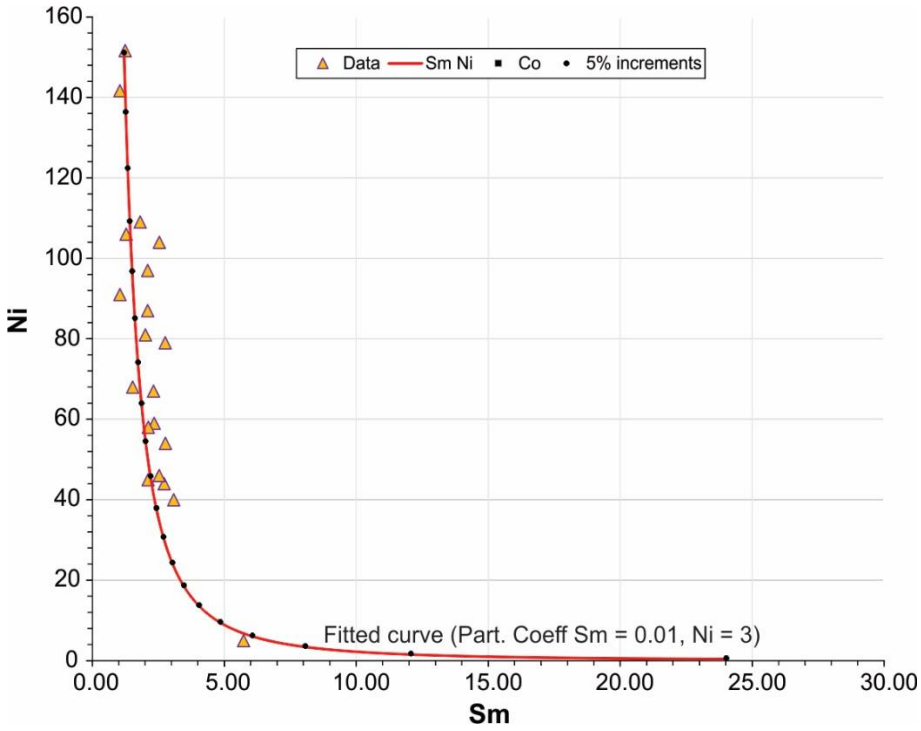

Figure 5.19. Ni – Sm plot. The best-fit modeled curve (red) is used to assess the bulk partition coefficients of Sm and Ni.

Stonergram modeling begins with the selection of a provisional parental composition from which the other (evolved) samples are modeled. The oxides of the parental and evolved samples are normalized to those of the parental melt and the results may be plotted in two ways. In the first way, the parent-normalized values are plotted without further treatment, yielding model curves that are unconstrained by “conserved” element abundances (Figure 5.19). The curves are effectively balanced about the parental line (value of 1), with the value of some oxides plotting above the line, and others below. In the second approach, the procedure of parent-normalization is preceded by normalization to a “conserved” model-constraining element. For each sample, the concentration of each oxide is divided by the abundance of the “conserved” element (Sm). After subsequent parent-normalization, the resulting double-normalized values are plotted. The oxides with doubly normalized values >1 are considered to have been gained by the magmatic system (for example, by crystal accumulation), and those with values <1 are considered to have been lost from the system (for example, by crystal fractionation). Both ways of managing and displaying the data allow the model curves to be adjusted to match the data curves by effectively adding or subtracting minerals from the parental

magma composition. The main difference between the approaches is that the doubly normalized or “constrained” method demonstrates with more certainty whether the evolved samples have gained or lost oxides from the system, and, by extension, whether the evolved samples may represent cumulates or differentiates from crystal fractionation.

Figure 5.20 displays how a specific magma (here sample JV13-2-5Q) would be affected by the removal of 20% An_{48} plagioclase, 20% Di_{70} clinopyroxene or 20% Fo_{78} olivine. The removal of 20% An_{48} plagioclase results in losses of Al_2O_3 and Na_2O and gains of CaO, FeO, MgO, K_2O, TiO_2 and P_2O_5. During fractionation of An_{48} plagioclase the concentration of SiO_2 increases only slightly, because the SiO_2 content within An_{48} plagioclase is the same as that within the parental sample. The removal of 20% Fo_{78} olivine results in losses of FeO and MgO and gains of SiO_2, Al_2O_3, CaO, K_2O, Na_2O, TiO_2 and P_2O_5. The removal of 20% Di_{70} clinopyroxene results in losses of MgO and CaO and gains of SiO_2, Al_2O_3, FeO, Na_2O, K_2O, TiO_2, and P_2O_5.

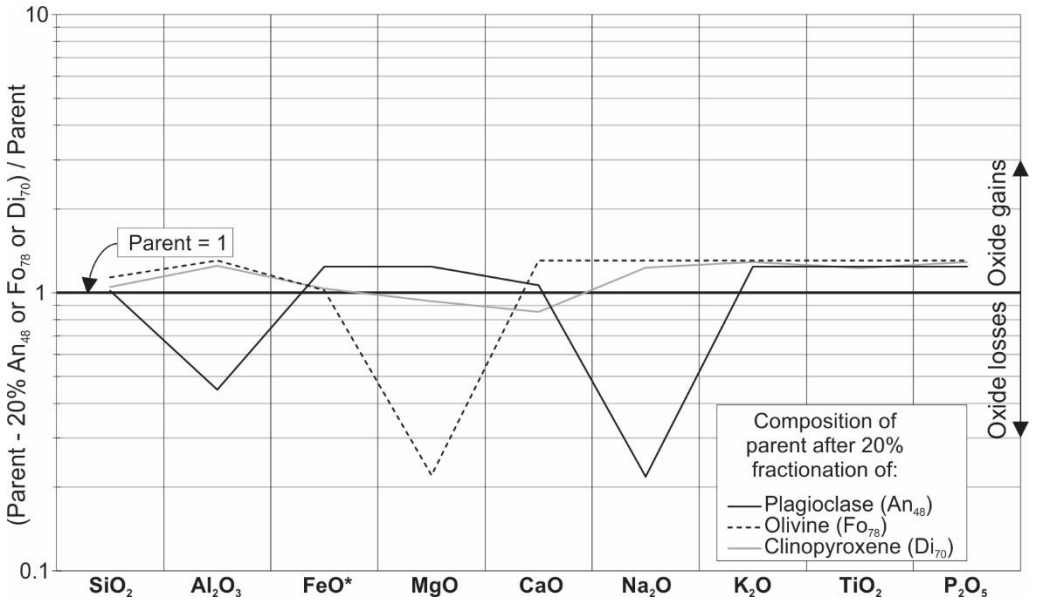

Figure 5.20. Visualization of a modeled composition of a parental melt minus 20% of An_{48} plagioclase, Fo_{78} olivine, and Di_{70} clinopyroxene, with the Stonergram (unconstrained by conserved element logic).

The certainty of Stonergram results is evident from the closeness of fit between the model and data curves of the various oxides. The program quantifies the fit in terms of residuals, i.e., differences between data values and model values. However, not all oxides should be regarded equally, particularly in rock suites which have been chemically

altered through weathering or metamorphism. In such cases, the more mobile oxides such as K_2O and Na_2O are likely to have risen or fallen from their original magmatic concentrations, and the data curves will thereby represent both primary (igneous) and secondary (alteration) processes. As such, achieving a match between the more abundant and less mobile oxides such as SiO_2, Al_2O_3, FeO and MgO will lead to models that are more indicative of primary processes than achieving a match between on the alkali oxides.

Figure 5.21. Modeling of the fractionation of sample JV13-6-25 from parental sample JV13-13-35. The constrained model curve is fitted to the constrained measured curve through the removal of 24.9% An_{48} plagioclase, 5.8% Fo_{85} olivine, 68.5% Di_{73} clinopyroxene, 0.7% magnetite and 0.02% apatite. The oxides Na_2O and K_2O could not be successfully modeled due to secondary alteration. The sum of residual oxides is 0.72 based on the constrained curve.

Figure 5.21 displays a Stonergram of parental sample JV13-13-35 and evolved sample JV13-6-25. The evolved sample is normalized to the parent and plotted as an unconstrained curve and as a constrained curve (double normalized). The constrained model curve is fitted to the constrained measured curve through the removal of 24.9% An_{48} plagioclase, 5.8% Fo_{85} olivine, 68.5% Di_{73} clinopyroxene, 0.7% magnetite and 0.02% apatite. The CaO, Na_2O and K_2O could not be successfully modeled in some samples because their original igneous concentrations have likely been affected by alteration from metamorphism.

Stonergram results

Emphasis is placed on the correct modeling of SiO_2, Al_2O_3, FeO*, TiO_2 and MgO and especially the SiO_2/Al_2O_3 and FeO*/MgO ratios. In contrast to K_2O, Na_2O and CaO, the abundance and ratios of these oxides are considered to better represent the primary magmatic signal. The most primitive samples from each area are used as parental samples, and are then used in the Stonergram to highlight the relation between samples of different areas. The sill transect in area 1 was treated separately. The results are presented in Table 5.4. The Stonergram results echo those of PER diagrams and indicate that the parental samples of areas 1 and 3 underwent significant fractionation of mainly An_{48-65} anorthite and Di_{65-82} clinopyroxene from a melt resembling sample GA4-3 (of area 1). The most primitive samples of different areas can be related through the fractionation of up to 83% clinopyroxene, 16 – 38% An_{48-55} anorthite, up to 63% Fo_{83-84} olivine and minor refractory phases, using sample GA4-3 as a parental melt. The large variation in these numbers highlights a similarity between some of the used samples. For example, a sample with 2% ol, 58% An_{48} and 40% Di_{70} can be related to a sample with 60% An_{48} and 40% Di_{70} through the fractionation of 100% ol. Because these numbers can lead to confusion the data presented in Table 5.4 is recalculated to the percentage of fractionation from a common parent (GA4-3) and visualized in Figure 5.22. Using a graphing method in which plagioclase is plotted against clinopyroxene + forsterite the fractionating assemblage is estimated to be 38% An_{50} plagioclase, 60% Di_{73} clinopyroxene and 8% Fo_{84} forsterite. All of the major element geochemical variation in the Hart River sill samples can be explained by concurrent fractionation of plagioclase, olivine and clinopyroxene from a single parental magma with a composition similar to sample GA4-3.

Table 5.4. Stonergram results.

Area[1]	Parent	Sample	%Change	Plag	An%	Ol	Fo%	Cpx	Di%	Mt	%TiO_2	Ap	C/U	Error
1	jv13-13-35	jv13-4-13	-29.0%	28	48	13	85	58	72	0.9	50	0.1	C	0.50
1	jv13-4-13	JV13-2-5q	-15.0%	23	48	0	85	76	69	0.6	50	0.2	C	0.28
1	JV13-2-5q	JV13-2-5k	-26.0%	39	48	17	85	44	73	0.0	10	0.0	C	0.79
			2.8%	0	0	0		0		98.1	10	1.9		
1	JV13-2-5q	JV13-2-5i	-36.0%	34	48	6	77	60	73	0.0	22	0.0	C	0.69
			1.8%	0	50	0		0		97.6	10	2.4		
1	JV13-2-5q	JV13-2-5m	-14.0%	51	48	2	78	48	70	0.0	22	0.0	C	0.57
			5.5%	0	50	0		0		99.1	12	0.9		
1	jv13-13-35	jv13-6-25	-36.0%	25	48	6	85	69	73	0.7	29	0.0	C	0.72
1	jv13-13-35	Jv13-3-9a	-49.0%	30	48	0	86	68	69	2.1	14	0.1	C	0.48
1	jv13-13-35	GA6-5	-37.0%	29	48	12	84	58	82	1.9	25	0.1	C	0.35
1	jv13-13-35	GA6-3	-43.0%	26	60	15	85	58	73	1.0	45	0.0	C	0.64
1	GA4-3	GA4-2	-15.0%	33	48	0	85	67	73	0.0	22	0.0	C	0.70
			0.7%	0	50	0		0		99.2	7	0.8		
2	GA4-2	jv13-13-35	-4.5%	38	48	63	85	0	73	0.0	22	0.0	C	0.82
			1.5%	0	50	0		0		99.0	15	1.0		
2	jv13-13-35	jv13-12-39	-2.0%	0	50	63	85	0	73	34.7	25	2.2	U	0.84
			19.0%	100	48	0		0		0.0		0.0		
2	jv13-13-35	jv13-12-37	-16.0%	27	65	11	85	59	70	2.0	70	0.2	C	0.78
3	jv13-13-35	jv13-16-50	-38.0%	25	48	4	84	70	75	0.2	100	0.1	C	0.65
3	jv13-16-50	jv13-16-52A	-16.0%	45	48	55	85	0	73	0.0	22	0.0	U	1.86
			7.0%	0	50	0		0		99.6	19	0.4		
3	jv13-16-50	jv13-15-49	-7.0%	0	48	97	79	0	73	3.4	50	0.0	U	1.03
			0.6%	95	48	0		0		0.0		4.8		
4	jv13-13-35	jv13-18-57A	-49.5%	29	55	14	85	56	73	0.7	30	0.0	C	0.22
4	jv13-18-57A	jv13-19-62	-2.0%	8	48	80	85	0	73	11.2	100	1.0	C	0.52
4	jv13-18-57A	jv13-20-64	-55.0%	32	48	15	60	53	65	0.7	15	0.0	C	2.09
			1.0%	61	50	0		0		30.7	50	8.0		

[1]Area number pertains to the sample, not necessarily the parent. Abbreviations used: Plag = plagioclase, An% = % anorthite in plagioclase, Ol = Olivine, Fo% = % forsterite in olivine, Cpx = clinopyroxene, Di% = $ diopside in clinopyroxene. Mt = magnetite, %TiO2 = % TiO2 in magnetite (note that no distinction is made between magnetite and ilmenite, 50% TiO2 in magnetite implies pure ilmenite, whereas 15% - 50% TiO2 implies titaniferous magnetite and ilmenite (at low T, <15% TiO2 can be accomodated in magnetite). Ap = apatite. C =constrained, U = unconstrained by the chosen conserved element (Sm).

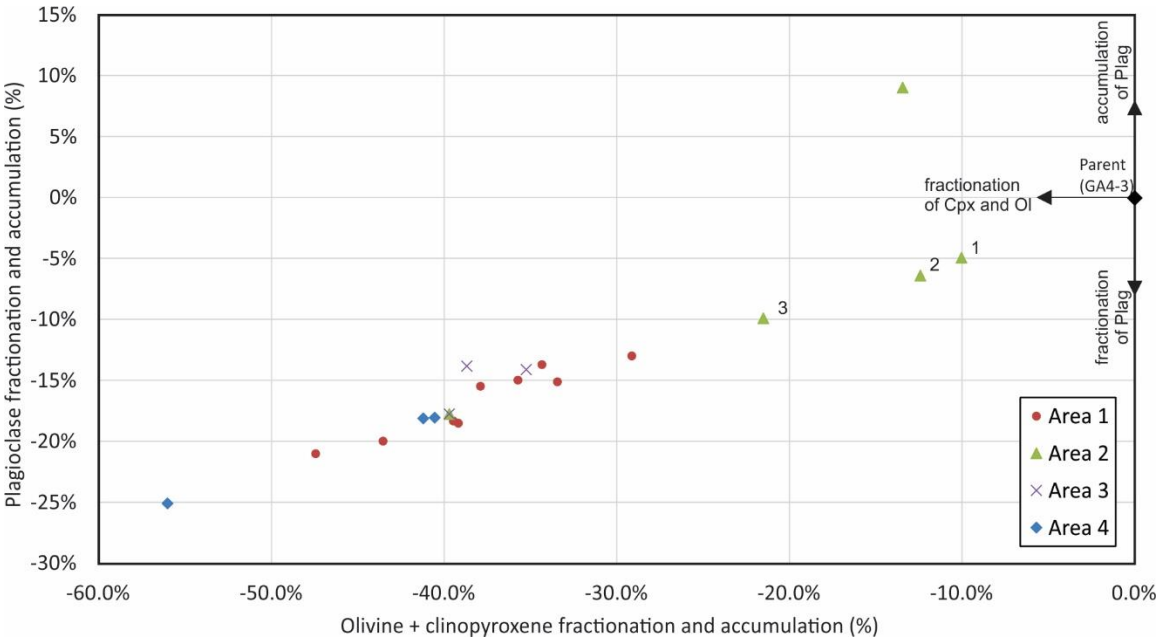

Figure 5.22. Stonergram results indicate that all samples reflect fractional crystallization of An_{48-65} plagioclase (Plag), Di_{65-82} clinopyroxene (Cpx) ± Fo_{60-86} olivine (Ol). The consistent trend indicates all samples were formed by crystallization from a common parent (sample GA4-3). The most primitive samples analyzed for this study are labeled 1,2 & 3 and are used in figure 5.23.

5.7.4. Melting of mantle in the spinel stability field

The Hart River sills formed from partial melting of mantle in the spinel stability field. The minimal Er anomalies in the Hart River sills strongly suggest that there was no residual plagioclase in the source rocks (Walter, 2014). The low Sm/Yb ratio of the Hart River sills is consistent with an absence of residual garnet. During the melting of garnet peridotite, the HREE are preferentially retained in the restite (Johnson, 1998) resulting in high ratios of LREE to HREE in the related magmas. The fractionation of melts from the mantle is modeled using equations for non-modal melting (Shaw, 1970) and estimates for the composition of depleted mantle (Workman and Hart, 2005) and primitive mantle (McDonough and Sun, 1995). The resulting curves are plotted together with the most primitive samples of the Hart River Sills in Figure 5.23. The Dy/Zr ratio of the Hart River sills is consistent with >8% melting of depleted mantle or the melting of >17% primitive mantle in the presence of spinel. The most primitive samples of the Hart River sills were likely already somewhat fractionated and hence the percentage of partial melting may be

overestimated. The previously discussed trace element abundances are consistent with a source rock composition between fertile and depleted mantle.

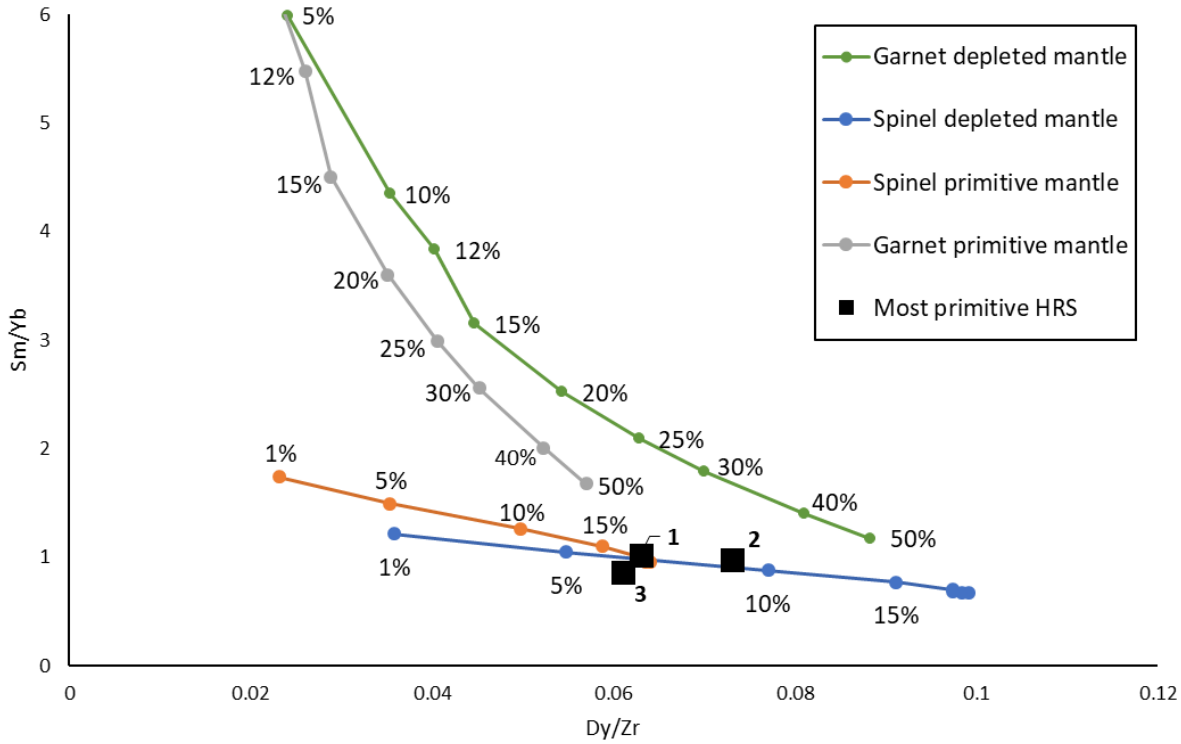

Figure 5.23. Non-modal melting curves of depleted garnet-bearing mantle (G-DM), depleted spinel-bearing mantle (Sp-DM), primitive spinel-bearing mantle (Sp-PM) and primitive garnet-bearing mantle (G-PM). The curves are based on equations in Shaw (1970), the depleted mantle composition of Workman and Hart (2005), the primitive mantle composition of McDonough and Sun (1995), modal mineralogy and partitioning coefficients of garnet and clinopyroxene of Johnson (1998), and partition coefficients of spinel, olivine and orthopyroxene of Kelemen et al. (1993) and references therein. Mantle modal mineralogy and the first mantle melting mode (up to ~25% of partial melting of spinel-bearing mantle and up to ~12% of partial melting of garnet-bearing mantle) after Johnson (1998). The second melting mode of spinel peridotite is 30% olivine, 63% opx and 7% spinel. The second melting mode of garnet peridotite is 36% olivine, 58% opx and 6% garnet. The three most primitive samples (labeled 1,2 & 3 in figure 5.22 of the Hart River sills analyzed for this study are plotted as black squares.

Spinel is stable in fertile peridotite mantle at pressures of approximately 1 to 2 GPa (Walter, 2014), equivalent to depths of ca. 35 - 75 km. The lack of plagioclase in the residuum precludes extraction from shallow (< ~35 km) mantle. The lack of garnet in the

residuum indicates that it is unlikely that the Hart River sills are the result of the upwelling of a mantle plume. In addition, there are no Hart River sills with high MgO wt. % that would indicate the melting of anomalously hot mantle. Instead, the Hart River sills are interpreted to have formed from an episode of rifting along the margin of Laurentia.

The Ta/Nb ratio of the Hart River sills ranges from 0.5 to 17.9, and may indicate either mantle refertilization by carbonatitic (CO_2-rich) melts or melt/fluid interaction with Ti-rich minerals (Green and Wallace, 1988; Green, 1995).

5.7.5. Forward modeling with AlphaMELTS

Liquid lines of descent and mineral chemistries were modeled using the software AlphaMELTS (Ghiorso and Sack, 1995; Smith and Asimow, 2005). Modeling was done at variable oxygen fugacities (Figure 5.24), water contents and pressures, assuming perfect (Rayleigh) fractional crystallization. The parental melt for AlphaMELTS modeling was JV13-12-35, because it is the most primitive sample with known uncertainties. Alphamelts was unable to perfectly model the liquid lines of descent. In particular, the onset of plagioclase crystallization is underestimated. With increasing pressure this effect is further amplified. Models run with varying H_2O content indicate that FeO* enrichment can only have occurred in a dry magma, consistent with the tholeiitic character of the sills. The closest fit of models to the data occurs with a dry magma at a pressure of 100 bars buffered by fayalite-magnetite-quartz.

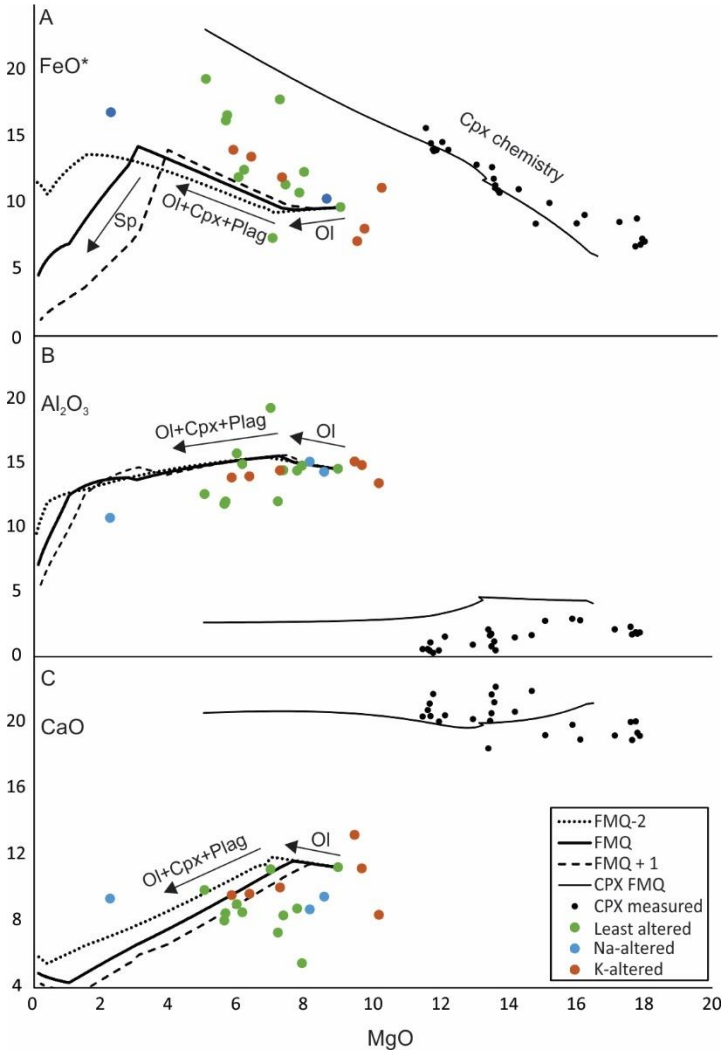

Figure 5.24. **A. FeO versus MgO data and modeling results. The modeling results display the initial fractionation of olivine, followed by fractionation of olivine, clinopyroxene and plagioclase, followed by fractionation of olivine, clinopyroxene, plagioclase and spinel (titaniferous magnetite). B-C. Modeling curves of Al_2O_3 and CaO versus MgO display the fractionation of olivine followed by olivine, clinopyroxene and plagioclase. The modeling results are roughly consistent with the data, with the exception of CaO whose deviation is attributed to alteration and/or weathering. The modeling results are inconsistent with Stonergram results which indicate coeval fractionation of clinopyroxene, plagioclase and olivine. Clinopyroxene compositions could only be successfully modeled using a fayalite-magnetite-quartz buffer (0 delta). All model runs assumed a pressure of 100 bars and a dry magma (higher pressures and water content yielded poor fits).**

5.8. Discussion

5.8.1. Integrated petrogenesis

The Hart River sills are subalkalic gabbro to gabbroic diorite (Figure 5.7). The trace element abundances of the Hart River sills are similar to E-MORB, with the exception of variable LILE enrichment (Figure 5.9). Secondary alteration affected predominantly the alkali metals and to a minor extent CaO (Figure 5.10).

Positive εNd_i values between +1.5 to +4.0 indicate the magmas were derived from a depleted mantle source (Figure 5.11) with only minor crustal enrichment. All of the chemical variation of the Hart River sills can be explained by fractionation from a primitive melt with the composition of sample GA4-3 (Figure 5.22). The fractionating assemblage contained plagioclase, clinopyroxene and olivine. The isotopic ages from this study indicate that this melt was emplaced in a single pulse of magmatism that was < 1 m.y. (Figure 5.15).

The mantle source of the Hart River sills was in the spinel facies. This finding is consistent with melting of approximately 35 - 75 km deep mantle. The continental lithospheric thickness of current plate margins ranges from 30 – 40 km; for plate interiors, the thickness is typically >40 km, and for current mountain belts it ranges up to 70 km (Mooney et al., 1998). It is unlikely that the lithospheric root that underlay the Wernecke Supergroup after Racklan Orogeny at ~1.6 Ga still existed, considering that the lower lithosphere may be removed within 30 – 50 m.y. after orogeny (Houseman et al., 1981; Wang et al., 2014), and that there is no evidence for residual garnet within the mantle source.

The upwelling of mantle plumes commonly results in pulses of magmatism with differing chemical signatures. Older pulses reflect melting of more fertile, deeper mantle, and younger pulses reflect the melting of more depleted and shallower mantle. These signatures have been clearly demonstrated for the Zig Zag Dal basalts in Greenland (Upton et al., 2005) and the Coppermine River basalts in northern Canada (Griselin et al., 1997). There are however also LIPs that are probably plume-derived but do not show geochemical evidence of the upwelling of a mantle plume such as the CAMP event

(Chabou et al., 2010). The Hart River sills represent one pulse of melting of one specific type of mantle, and hence are unlikely to be directly related to the ascent of a mantle plume. It is however possible that other pulses of magmatism close in age to the Hart River sills exist but are not exposed.

The lack of hydrous minerals, the absence of a Nb-Ta trough on multi-element diagrams, the interstitial titaniferous magnetite, and Alphamelts modeling are all consistent with the Hart River sills originating from the melting of dry mantle (Kelemen et al., 2014). Hence, subduction and arc magmatism are unlikely to have been related to mantle melting.

5.8.2. Melt generation

Magmas are principally generated in the continental lithospheric mantle in two ways, 1) addition of heat, and 2) through compositional changes, especially the addition of volatiles (Farmer, 2014, Harry and Leeman, 1995; Turner et al., 1996). The sub-continental lithospheric mantle can also melt through decompression (King and Anderson, 1998). The Hart River sills resulted from the melting of dry mantle. Hence, the addition of volatiles as a cause of magmatism is rejected. The addition of heat can occur conductively either by the ascent of a mantle plume (in this case it is not the plume that melts, but the adjacent or overlying mantle), or by lithospheric delamination (Bird, 1979; Farmer, 2014). The addition of heat through lithospheric delamination is unlikely, considering that the Racklan Orogeny and Hart River magma emplacement are separated in time by >200 m.y., and that lithospheric delamination commonly occurs within 50 m.y. of orogenesis (Houseman et al., 1981; Wang et al., 2014). Additionally, lithospheric delamination is commonly preceded by subduction and leads to mafic volcanism that is more calc-alkaline than the Hart River sills (Kay and Mahlburg Kay, 1993). Decompression melting occurs in two ways, 1) mantle upwelling, and 2) continental thinning (Farmer, 2014). As mentioned earlier there is no direct evidence for the upwelling of a plume. Continental thinning can lead to melting in the asthenosphere depending on the temperature of the melt column and the magnitude of continental thinning (McKenzie and Bickle, 1988). Continental thinning occurs in rift environments, such as the Baikal rift zone in Southern Russia and the great African rift, and can eventually lead to rupture of the continental lithosphere

and/or to the deposition of sedimentary basins. The lack of evidence for an upwelling magmatic plume or addition of volatiles implies that the data is more permissible with magmatism related to a period of rifting.

5.8.3. Comparison to other igneous rocks in western Laurentia and selected 1.38 Ga igneous rocks worldwide

Several magmatic episodes occurred in northwestern Laurentia during the Mesoproterozoic (Figure 5.25). First, the Western Channel diabase was emplaced at 1.59 Ga in the Hornby Bay Group (Hamilton and Buchan, 2010). The Moyie sills were emplaced in the Belt-Purcell Supergroup at 1.47 Ga (Anderson and Davis, 1995; Rogers et al., 2016). The Hart River sills were emplaced in the Wernecke Supergroup at 1.38 Ga, coeval with dykes within the Belt-Purcell Supergroup in the Salmon River arch (Doughty and Chamberlain, 1996). The Mackenzie Dyke swarm, present throughout much of Laurentia was emplaced at 1.27 Ga (LeCheminant and Heaman, 1989). The continuation of the McKenzie Dyke swarm in the Yukon (known locally as the Bear River dykes) was described by Schwab et al. (2004).

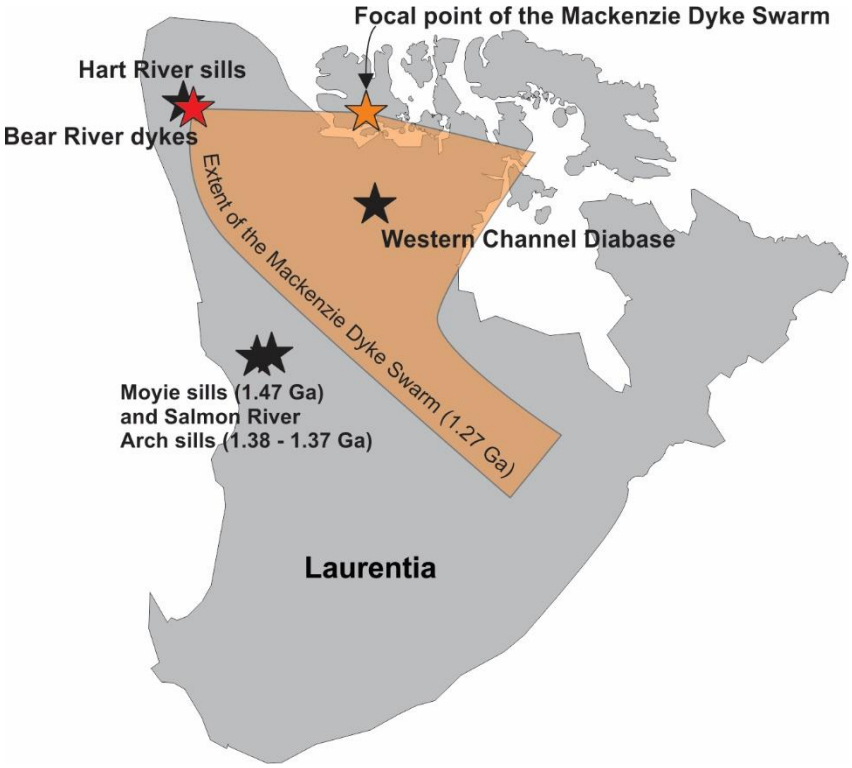

Figure 5.25. Location of Hart River sills in context of selected Mesoproterozoic intrusive rocks in northern Laurentia.

The Hart River sills are compared to the Bear River dykes and the Moyie sills in Figure 5.26. Geochemical data sets for other aforementioned magmatic rocks are not available. Overall, the Hart River sills, Bear River dykes and the Moyie sills appear to display similar features, with relatively high LILE and MORB like REE patterns. The similarities among these magmatic rocks may indicate melting of similar mantle sources at similar depths. Because the Nd and Pb initial isotopic ratios are juvenile, but the abundances of LILE are enriched, the mantle that underwent melting beneath western Laurentia is regarded as somewhat geochemically enriched relative to normal MORB-source mantle. This enrichment is likely to have occurred shortly before Hart River magmatism because the isotopic signatures of Nd and Pb are juvenile; if the enrichment was significantly older, the isotopic ratios would likely be more evolved. The cause of the enrichment is unknown.

The Hart River sills are also compared to other coeval magmatic rocks worldwide in Figure 5.26. Apart from comparatively low TiO_2 content, iron-rich tholeiites within the

Vestfold Hills of Antarctica bear geochemical similarity to the Hart River sills with relatively high LILE and REE similar to N-MORB. No geochemical data is available for coeval sills in the Salmon River arch. The iron-rich tholeiites in Vestfold Hills yielded an age of 1380 ± 7 Ma (Lanyon et al., 1993). A large sill in the Salmon River arch mafic complex was dated at 1379 ± 1 Ma (Doughty and Chamberlain, 1996).

The Hart River sills are also comparable to the coeval Midsommorsø intrusions in Greenland (1382 ± 2 Ma, Upton et al., 2005), dolerites in the Bas Drâa Inlier of Morocco (1381 ± 8 Ma and 1384 ± 6 Ma, Abdelhakim el Bahat et al., 2013), and the Kunene Intrusions in northwestern Namibia (1376 ± 2 Ma, Drüppel, 2007). The Midsommorsø intrusions have similar trace element patterns to the Hart River sills with high LILE and REE similar to N-MORB. However, the Midsommersø intrusions and volcanics have more evolved εNd than the Hart River sills. Dolerites in the Bas Drâa Inlier of Morocco follow the same general trace element pattern, but are more enriched in LILE. The Kunene Intrusions in northwestern Namibia are enriched in LILE, but depleted in REE compared to N-MORB.

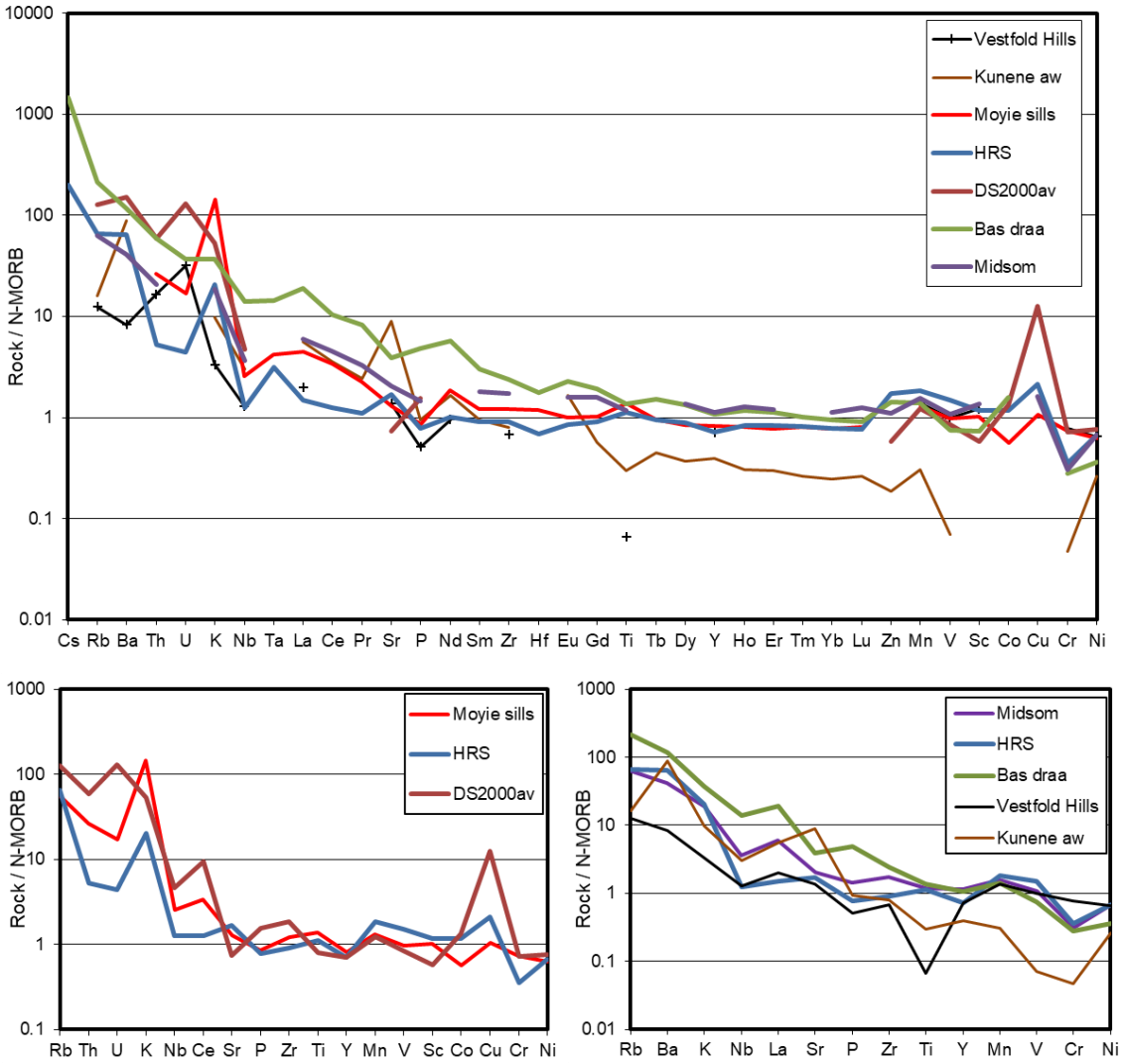

Figure 5.26. A. Comparison of trace elements of the Hart River sills and selected magmatic rocks. B comparison of the Hart River sills, 1.27 Ga Bear River dykes (Schwab et al., 2004) and 1.47 Ga Moyie Sills (Rogers et al., 2016). C. Comparison of Hart River sills and coeval magmatic rocks: the Midsommersø dolerites (Upton et al., 2005), the Kunene Intrusions (Drüppel, 2007), dykes in the Vestfold Hills (Lanyon et al., 1993) and dykes in the Bas Draa Inlier (El Bahat et al., 2013).

5.8.4. Rifting of Columbia

During 1.6 Ga – 1.45 Ga, western Laurentia was connected to Australia and Antarctica, which together is here referred to as the Mawson Continent (Gibson et al., 2008, 2012; Payne et al., 2009; Medig et al., 2014; Thorkelson and Laughton, 2016; Furlanetto et al., 2016). This connection ended at ca. 1.45 Ga and is marked by rift basins

that are currently preserved on Laurentia (Ross et al., 1992; Doe et al., 2012; Daniel et al., 2013; Medig et al., 2014). During this time, the Moyie sills intruded the Belt Purcell basin, a sedimentary succession that contains zircon with Australian provenance (Höy, 1989; Rogers et al., 2016; Ross et al., 1992).

Consistent with the presence of the Hart River sills, and coeval sills farther south on Laurentia, ca. 1.38 Ga rifting occurred along the margin of Western Laurentia (Figure 5.27). This episode of rifting may have led to drifting and the final separation between the Mawson continent and Laurentia. Siberia did not rift from Laurentia until the late Proterozoic (Ernst et al., 2016; Evans et al., 2016). However, Puchkov et al. (2013) concluded that rifting did occur between Siberia, northeastern Laurentia and Baltica at ca. 1.38 Ga. Together with a rift on the western side of Laurentia, this implies that voluminous mafic magmatism occurred concurrently on northeastern Laurentia and along its western margin. Australia and Laurentia were later reattached in a different configuration during the formation of supercontinent Rodinia (Li et al., 2008).

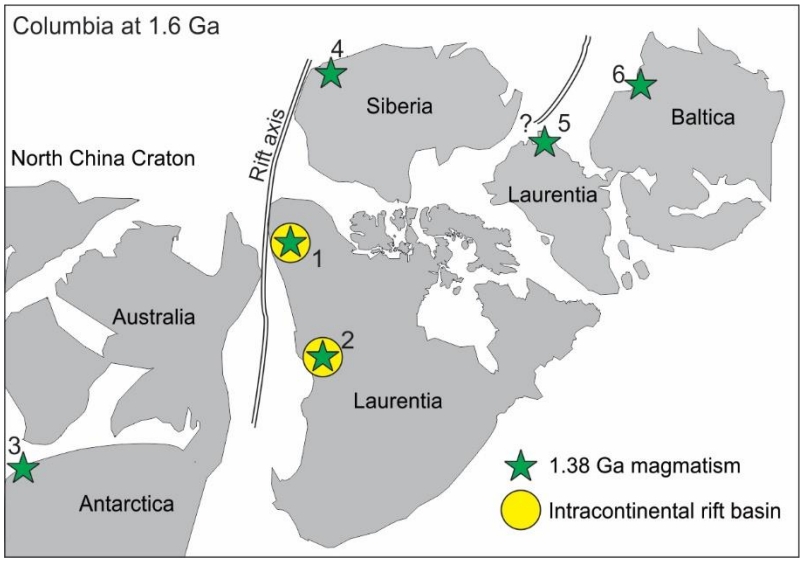

Figure 5.27. Reconstruction of Columbia at 1.6 Ga modified from Furlanetto et al. (2016). A rift is placed along the margin of Laurentia, Australia, Antarctica, and Siberia. The ca. 1.38 Ga magmatism along this rift resulted in the intrusion of the Salmon River arch mafic complex (2, Doughty and Chamberlain, 1996), the Hart River sills (1, this study) and the Chieress dyke swarm (4, Ernst et al., 2000). Also shown is the rift placed along the margin of Siberia, Baltica and northeast Laurentia by Puchkov et al. (2013) based on the Mashak event (6, Puchkov et al., 2013) and the Midsommersø dyke swarm (5, Upton et al., 2005). Also shown are rift basins that developed proximal and roughly coeval with the magmatic events: the Belt-Purcell Supergroup (2, Ross et al., 1992) and the PR1 basin (1, Medig et al., 2014). The Vestfold Hills Dykes (3, Lanyon et al., 1993) are also shown.

5.8.5. Are the Hart River sills a Large Igneous Province?

The Hart River sills have an areal extent of 312 km2, which is smaller than the proposed minimum aerial extent of true LIPs (100,000 km2, Bryan and Ernst, 2008; Ernst, 2014). However, part of the Hart River sills is eroded, and part is present in the subsurface, so the aerial extent underestimates their true size. The proposed minimum volume of true LIPs is 100,000 km^3 (Bryan and Ernst, 2008). The sills commonly occur as one >500 m thick sill with abundant smaller associated dykes, sills and apophyses. In a simplified calculation of intrusive volume, 600 m of thickness is a conservative estimate. In discontinuous outcrop, the sills cover a distance along strike of about 200 km, and 40 km perpendicular to strike. In this case the Hart River sills intrusive volume is 200 x 40 x 0.6

km = 4,800 km^3. If the exposure in the northern Wernecke Mountains included, the sills area be 200 x 100 km and the intrusive volume 200 x 100 x 0.6 km = 12,000 km^3. If the sills continue in the subsurface to the south, the width and intrusive volume would be doubled to 200 x 200 x 0.6 km = 24,000^3. It is possible that the extent of the Hart River sills was even larger, and if the sills are continuous with the sills in the Salmon River Arch (Doughty and Chamberlain, 1996), the intrusive volume would be >100,000 km^3, the proposed minimum volume of LIPs (Bryan and Ernst, 2008).

The Hart River sills were emplaced in a short-lived pulse of magmatism, < 5 m.y., and possibly <1 m.y., similar to many continental flood basalts and other plume-related LIPs (Bryan and Ernst, 2008, Ernst and Bleeker, 2010; Ernst, 2014). However, the geochemical character of the Hart River sills does not indicate a plume origin. As such, a plume origin could be invoked only if the sills were generated by melting of subcontinental lithospheric mantle or asthenospheric mantle in the spinel stability field, along the periphery of a mantle plume head. In order for conduction to be an effective trigger for voluminous melting, this mantle would have to be elevated in temperature prior to conductive heating (Sleep, 1987; 1992; Farmer, 2013). In this scenario, the coeval Salmon River arch dykes and Chieress Dyke swarm (Figure 5.27) would represent magmatism that was distal to the plume head. The plume head would be represented by the Midsommersø dyke swarm in Greenland (Upton et al., 2005), which has an evolved isotopic signature. This interpretation is not preferred, however, because these igneous fields are separated by large distances, and because the Hart River sills have a juvenile isotopic signature. It would instead be expected that the distal dykes and sills become more evolved as they assimilate more country rock. As noted, a rift-related flux of magmatism is a more suitable alternative on the basis of both geochemistry and spatial distribution.

5.9. Conclusions

The Hart River sills are a set of tholeiitic gabbros that occur on northwestern Laurentia. The sills extend from the Ogilvie Mountains to the Wernecke Mountains in northern Yukon (Green, 1972; Abbott, 1997; Thorkelson, 2000). Evidence from crustal reheating at ca. 1.38 Ga suggests that the volume of magma may have been much greater

than currently apparent and possibly greater than 100,000 km^3. The sills were emplaced after the Racklan Orogeny (Thorkelson, 2000), roughly coeval with the development of rift basins along the margin of Laurentia (Ross et al., 1992; Doe et al., 2012; Daniel et al., 2013; Medig et al., 2014), and prior to the deposition of the Pinguicula basin (Medig et al., 2016).

Two new CA-TIMS U-Pb zircon dates of 1382.15 ± 0.39 Ma and 1382.14 ± 0.36 Ma confirm and refine previous dates of ca. 1.38 Ga. The Hart River sills are subalkaline, metaluminous tholeiitic gabbros with SiO_2 content of 46.6– 52.5 wt % and variable Mg# of 20.5 to 72.0. The Hart River sills are enriched in LILE but have REE and HFSE abundances that are similar to N-MORB. PER analysis indicates that all samples are cogenetic and formed by fractionation from a common parent. Stonergram modeling results constrain this fractionating assemblage to 38% An_{50} plagioclase, 60% Di_{73} clinopyroxene and 8% Fo_{84} forsterite. The sills are juvenile and have $\varepsilon Nd \approx 3.5$ except at locations where they have been contaminated by assimilated wall rock. Consistent with these chemical characteristics, the sills were derived from a source similar to, but more fertile than, MORB-source mantle. Trace and rare earth elements indicate that neither plagioclase nor garnet were present in the residuum. The Sm/Yb and Dy/Zr ratios indicate that the Hart River sills formed from >8% partial melting spinel-bearing mantle at 40 – 80 km depth. Supra-subduction zone processes such as aqueous metasomatism of the mantle source is not evident from optical mineralogy, geochemistry, nor Alphamelts modeling results.

The Hart River sills are interpreted as a manifestation of rifting of Australia from Laurentia, signalling the breakup of the Columbia supercontinent. This hypothesis is consistent with the formation of rift basins along the margin of western Laurentia prior to 1.38 Ga (Ross et al., 1992; Doe et al., 2012; Daniel et al., 2013; Medig et al., 2014). The rifting may have continued into a phase of “drifting” and sea-floor spreading, although the size of the potential ocean basin remains unknown. Drifting ended toward the end of the Mesoproterozoic when the continents were re-attached to form the Rodinia supercontinent (Moores, 1981; Li et al., 2008; Milidragovic, 2011).

5.10. Acknowledgements

Funding was provided by NSERC grants to DJT. This is a contribution to IGCP 648.

5.11. References

Abbott, G. (1997). Geology of the Upper Hart River Area, Eastern Ogilvie Mountains, Yukon Territory (116A/10, 116A/11).

Anderson, H. E., & Davis, D. W. (1995). U-Pb geochronology of the Moyie Sills, Purcell Supergroup, southeastern British Columbia: implications for the Mesoproterozoic geological history of the Purcell (Belt Basin). Canadian Journal of Earth Sciences, 32, 1180–1193.

Bell, R. T., & Jefferson, C. W. (1987). An hypothesis for an Australian-Canadian connection in the Late Proterozoic and the birth of the Pacific Ocean. Pacific Rim Congress 87, 39 – 50.

Bird, P. (1979). Continental delamination and the Colorado Plateau. Journal of Geophysical Research, 84(B13), 7561–7571.

Bleeker, W., & Ernst, R. (2006). Short-lived mantle generated magmatic events and their dyke swarms: The key unlocking Earth's paleogeographic record back to 2.6 Ga. In E. Hanksi, S. Mertanen, T. Ramo, & A. A. Vuollo (Eds.), Dyke Swarms - Time Markers of Crustal Evolution (pp. 1–24). Rotterdam: Balkema Publishers. http://doi.org/doi:10.1201/NOE0415398992.ch1\r10.1201/NOE0415398992.ch1

Bleeker, W. (2003). The late Archean record: A puzzle in ca. 35 pieces. Lithos, 71(2–4), 99–134. http://doi.org/10.1016/j.lithos.2003.07.003

Bowen, N. L. (1956). The evolution of igneous rocks. Dover Publications, Inc., New York.

Bryan, S. E., & Ernst, R. E. (2008). Revised definition of Large Igneous Provinces (LIPs). Earth-Science Reviews, 86(1–4), 175–202. http://doi.org/10.1016/j.earscirev.2007.08.008

Campbell, I. H., & Kerr, A. C. (2007). Editorial: The great plume debate: testing the plume theory. Chemical Geology, 241, 149–152.

Chabou, M.C., Bertrand, H., and Sebaï, A. (2010) Geochemistry of the Central Atlantic Magmatic Province (CAMP) in south-western Algeria: Journal of African Earth Sciences, v. 58, p. 211–219, doi: 10.1016/j.jafrearsci.2010.02.009.

Crowley, J. L., Schoene, B., & Bowring, S. A. (2007). U-Pb dating of zircon in the Bishop Tuff at the millennial scale. Geology, 35(12), 1123–1126. http://doi.org/10.1130/G24017A.1

Daniel, C. G., Pfeifer, L. S., Jones, J. V., & McFarlane, C. M. (2013). Detrital zircon evidence for non-Laurentian provenance, Mesoproterozoic (ca. 1490-1450 ma) deposition and orogenesis in a reconstructed orogenic belt, northern New Mexico, USA: Defining the Picuris orogeny. Bulletin of the Geological Society of America, 125(9–10), 1423–1441. http://doi.org/10.1130/B30804.1

Davis, W. J. (1997). U-Pb zircon and rutile ages from granulite xenoliths in the Slave province: Evidence for mafic magmatism in the lower crust coincident with Proterozoic dike swarms. Geology, 25(4), 343–346. http://doi.org/10.1130/0091-7613(1997)025<0343:UPZARA>2.3.CO;2

Deer, W. A., Howie, R. A., & Zussman, J. (1966). An introduction to the rock-forming minerals. L. Richard Clay (The Saucer Press) Ltd, Bungay, Suffolk, London

DePaolo, D. J. (1981). Neodymium isotopes in the Colorado Front Range and crust–mantle evolution in the Proterozoic. Nature, 291(5812), 193–196. http://doi.org/10.1038/291193a0

Doe, M. F., Jones, J. V., Karlstrom, K. E., Thrane, K., Frei, D., Gehrels, G., & Pecha, M. (2012). Basin formation near the end of the 1.60-1.45 Ga tectonic gap in southern Laurentia: Mesoproterozoic Hess Canyon Group of Arizona and implications for ca. 1.5 Ga supercontinent configurations. Lithosphere, 4(1), 77–88. http://doi.org/10.1130/L160.1

Doughty, P. T., & Chamberlain, K. R. (1996). Salmon River Arch revisited: new evidence for 1370 Ma rifting near the end of deposition in the Middle Proterozoic Belt basin. Canadian Journal of Earth Sciences, 33(7), 1037–1052. http://doi.org/10.1139/e96-079

Drüppel, K., Littmann, S., Romer, R. L., & Okrusch, M. (2007). Petrology and isotope geochemistry of the Mesoproterozoic anorthosite and related rocks of the Kunene Intrusive Complex, NW Namibia. Precambrian Research, 156(1–2), 1–31. http://doi.org/10.1016/j.precamres.2007.02.005

Eisbacher, G. H. (1978). Two major Proterozoic unconformities, northern Cordillera. Current Research, Part A. Geological Survey of Canada, Paper 78-1A, 53–58.

El Bahat, A., Ikenne, M., Söderlund, U., Cousens, B., Ernst, R. E., Soulaimani, A., El Janati, M. Hafid, A. (2013). U–Pb baddeleyite ages and geochemistry of dolerite dykes in the Bas Drâa Inlier of the Anti-Atlas of Morocco: Newly identified 1380 Ma event in the West African Craton. Lithos, 174, 101–108. http://doi.org/10.1016/j.lithos.2013.04.003

Ernst, R. E. (2014) Large igneous provinces. Cambridge University Press, 666 p.

Ernst, R. E., & Buchan, K. L. (2004). Igneous Rock Association in Canada 3. Large Igneous Provinces (LIPs) in Canada and adjacent regions: 3 Ga to present. Geoscience Canada, 31(3), 103–126.

Ernst, R. E., Buchan, K. L., Hamilton, M. A., Okrugin, A. V., & Tomshin, M. D. (2000). Integrated Paleomagnetism and U-Pb Geochronology of Mafic Dikes of the Eastern Anabar Shield Region, Siberia: Implications for Mesoproterozoic Paleolatitude of Siberia and Comparison with Laurentia. The Journal of Geology, 108(4), 381–401. http://doi.org/10.1086/314413

Ernst, R. E., Hamilton, M. A., Söderlund, U., Hanes, J. A., Gladkochub, D. P., Okrugin, A. V., Kolotilina, T., Mekhonoshin, A.S., Bleeker, W., LeCheminant, A.N., Buchan, K.L., Chamberlain, K.R., Didenko, A. N. (2016). Long-lived connection between southern Siberia and northern Laurentia in the Proterozoic. Nature Geoscience, 9(April). http://doi.org/10.1038/ngeo2700

Ernst, R. E., Wingate, M. T. D., Buchan, K. L., & Li, Z. X. (2008). Global record of 1600-700 Ma Large Igneous Provinces (LIPs): Implications for the reconstruction of the proposed Nuna (Columbia) and Rodinia supercontinents. Precambrian Research, 160(1–2), 159–178. http://doi.org/10.1016/j.precamres.2007.04.019

Ernst, R. E., Bleeker, W., Söderlund, U., & Kerr, A. C. (2013). Large Igneous Provinces and supercontinents: Toward completing the plate tectonic revolution. Lithos, 174, 1–14. http://doi.org/10.1016/j.lithos.2013.02.017

Ernst, R. E., Fowler, A. D., & Pearce, T. H. (1988). Modelling of igneous fractionation and other processes using Pearce diagrams. Contributions to Mineralogy and Petrology, 100(1), 12–18. http://doi.org/10.1007/BF00399436

Ernst, R.E., and Youbi, N., 2017, How Large Igneous Provinces affect global climate, sometimes cause mass extinctions, and represent natural markers in the geological record: Palaeogeography, Palaeoclimatology, Palaeoecology, v. 478, p. 30–52, doi: https://doi.org/10.1016/j.palaeo.2017.03.014.

Evans, D. A. D., & Mitchell, R. N. (2011). Assembly and breakup of the core of Paleoproterozoic-Mesoproterozoic supercontinent Nuna. Geology, 39(5), 443–446. http://doi.org/10.1130/G31654.1

Evans, D. A. D., Veselovsky, R. V., Petrov, P. Y., Shatsillo, A. V., & Pavlov, V. E. (2016). Paleomagnetism of Mesoproterozoic margins of the Anabar Shield: A hypothesized billion-year partnership of Siberia and northern Laurentia. Precambrian Research, 281, 639–655. http://doi.org/10.1016/j.precamres.2016.06.017

Farmer, G. L. (2013). Continental Basaltic Rocks. Treatise on Geochemistry: Second Edition (2nd ed., Vol. 4). Elsevier Ltd. http://doi.org/10.1016/B978-0-08-095975-7.00303-X

Fecova, K. (2009). Conuma River and Leagh Creek Intrusive Complexes: Windows Into Mid-Crustal Levels of the Jurassic Bonanza Arc, Vancouver Island, British Columbia, MSc thesis, Simon Fraser University, Burnaby. 245 p.

Furlanetto, F., Thorkelson, D. J., Rainbird, R. H., Davis, W. J., Gibson, H. D., & Marshall, D. D. (2016). The Paleoproterozoic Wernecke Supergroup of Yukon, Canada: Relationships to orogeny in northwestern Laurentia and basins in North America, East Australia, and China. Gondwana Research, 39, 14–40. http://doi.org/10.1016/j.gr.2016.06.007

Furlanetto, F., Thorkelson, D. J., Daniel Gibson, H., Marshall, D. D., Rainbird, R. H., Davis, W. J., … Vervoort, J. D. (2013). Late Paleoproterozoic terrane accretion in northwestern Canada and the case for circum-Columbian orogenesis. Precambrian Research, 224, 512–528. http://doi.org/10.1016/j.precamres.2012.10.010

Ghiorso, M. S., & Sack, R. O. (1995). Chemical mass transfer in magmatic processes IV. A revised and internally consistent thermodynamic model for the interpolation and extrapolation of liquid-solid equilibria in magmatic systems at elevated temperatures and pressures. Contributions to Mineralogy and Petrology, 119(2–3), 197–212. http://doi.org/10.1007/BF00307281

Gibson, G. M., Rubenach, M. J., Neumann, N. L., Southgate, P. N., & Hutton, L. J. (2008). Syn- and post-extensional tectonic activity in the Palaeoproterozoic sequences of Broken Hill and Mount Isa and its bearing on reconstructions of Rodinia. Precambrian Research, 166(1–4), 350–369. http://doi.org/10.1016/j.precamres.2007.05.005

Gibson, G. M., Rubenach, M. J., Neumann, N. L., Southgate, P. N., & Hutton, L. J. (2008). Syn- and post-extensional tectonic activity in the Palaeoproterozoic sequences of Broken Hill and Mount Isa and its bearing on reconstructions of Rodinia. Precambrian Research, 166(1–4), 350–369. http://doi.org/10.1016/j.precamres.2007.05.005

Gibson, G., Henson, P., Neumann, N. L., Southgate, P. N., & Hutton, L. J. (2012). Paleoproterozoic-earliest Mesoproterozoic basin evolution in the Mount Isa region, northern Australia and implications for reconstructions of the Nuna and. Episodes, 35(1), 131–141. Retrieved from http://www.kshitija.org/episodes/contents/2012/march/p131-141.pdf

Goodge, J. W., Vervoort, J. D., Fanning, C. M., Brecke, D. M., Farmer, G. L., Williams, I. S., Myrow, P.M., DePaolo, D. J. (2008). A positive test of East Antarctica-Laurentia juxtaposition within the Rodinia supercontinent. Science (New York, N.Y.), 321(2008), 235–240. http://doi.org/10.1126/science.1159189

Goodge, J. W., & Fanning, C. M. (2016). Mesoarchean and Paleoproterozoic history of the Nimrod Complex, central Transantarctic Mountains, Antarctica: Stratigraphic revisions and relation to the Mawson Continent in East Gondwana. Precambrian Research, 285, 242–271. http://doi.org/10.1016/j.precamres.2016.09.001

Green, L. H. (1972). Geology of Nash Creek, Larsen Creek, and Dawson map areas, Yukon Territory. Geological Survey of Canada (Vol. Memoir 364). http://doi.org/10.4095/100697

Green, T. H. (1995). Significance of Nb/Ta as an indicator of geochemical processes in the crust-mantle system. Chemical Geology, 120(3–4), 347–359. http://doi.org/10.1016/0009-2541(94)00145-X

Griselin, M., Arndt, N. T., & Baragar, W. R. A. (1997). Plume-lithosphere interaction and crustal contamination during formation of Coppermine River basalts, Northwest Territories, Canada. Canadian Journal of Earth Science, 34, 958–975.

Halls, H. C. (1982). The importance and potential of mafic dyke swarms in studies of geodynamic processes. Geoscience Canada. http://doi.org/10.12789/gs.v9i3.3309

Hanghøy, B. K. P., & R, G. A. (2013). One View of the Geochemistry of Subduction-Related Magmatic Arcs, with an Emphasis on Primitive Andesite and Lower Crust. Treatise on Geochemistry: Second Edition (4th ed., Vol. 3). Elsevier Ltd. http://doi.org/10.1016/B978-0-08-095975-7.00516-7

Hamilton, M. A., & Buchan, K. L. (2010). U-Pb geochronology of the Western Channel Diabase, northwestern Laurentia: Implications for a large 1.59Ga magmatic province, Laurentia's APWP and paleocontinental reconstructions of Laurentia, Baltica and Gawler craton of southern Australia. Precambrian Research, 183(3), 463–473. http://doi.org/10.1016/j.precamres.2010.06.009

Harry, D. L., & Leeman, W. P. (1995). Partial melting of melt metasomatized subcontinental mantle and the magma source potential of the lower lithosphere. Journal of Geophysical Research Solid Earth, 100(B6), 10255–10269.

Heatherington, A. L., & Mueller, P. A. (1991). Geochemical evidence for Triassic rifting in southwest Florida. Tectonophysics, 188, 291–302.

Houseman, G. A., McKenzie, D. P., & Molnar, P. (1981). Convective instability of a thickened boundary layer and its relevance for the thermal evolution of continental convergent belts. Journal of Geophysical Research Solid Earth, 86(B7), 6115–6132.

Höy, T. (1989). The age, chemistry, and tectonic setting of the Middle Proterozoic Moyie sills, Purcell Supergroup, southeastern British Columbia. Canadian Journal of Earth Sciences, 26, 2305–2317.

Ingle, S., Mueller, P. A., Heatherington, A. L., & Kozuch, M. (2003). Isotopic evidence for the magmatic and tectonic histories of the Carolina terrane: Implications for stratigraphy and terrane affiliation. Tectonophysics, 371(1–4), 187–211. http://doi.org/10.1016/S0040-1951(03)00228-2

Irvine, T. N., & Baragar, W. R. a. (1971). A Guide to the Chemical Classification of the Common Volcanic Rocks. Canadian Journal of Earth Sciences, 8, 523–548. http://doi.org/10.1139/e71-055

Jaffey, A. H., Flynn, K. F., Glendenin, L. E., Bentley, W. C., & Essling, A. M. (1971). Precision measurement of half-lives and specific activities of U235 and U238. Physical Review C, 4(5), 1889–1906. http://doi.org/10.1103/PhysRevC.4.1889

John, T., Schenk, V., Haase, K., Scherer, E., & Tembo, F. (2003). Evidence for a Neoproterozoic ocean in south-central Africa from mid-ocean-ridge-type geochemical signatures and pressure-temperature estimates of Zambian eclogites. Geology, 31(3), 243–246. http://doi.org/10.1130/0091-7613(2003)031<0243:EFANOI>2.0.CO;2

Johnson, K. T. M. (1998). Experimental determination of partition coefficients for rare earth and high-field-strength elements between clinopyroxene, garnet, and basaltic melt at high pressures. Contributions to Mineralogy and Petrology, 133(1–2), 60–68. http://doi.org/10.1007/s004100050437

Jones, J. V., Daniel, C. G., & Doe, M. F. (2015). Tectonic and sedimentary linkages between the Belt-Purcell basin and southwestern Laurentia during the Mesoproterozoic, ca. 1.60–1.40 Ga. Lithosphere, 7(4), 465–472. http://doi.org/10.1130/L438.1

Kamenov, G. D., Perfit, M. R., Jonasson, I. R., & Mueller, P. A. (2005). High-precision Pb isotope measurements reveal magma recharge as a mechanism for ore deposit formation: Examples from Lihir Island and Conical seamount, Papua New Guinea. Chemical Geology, 219(1–4), 131–148. http://doi.org/10.1016/j.chemgeo.2005.02.013

Kay, R. W., & Mahlburg Kay, S. (1993). Delamination and delamination magmatism. Tectonophysics, 219(1–3), 177–189. http://doi.org/10.1016/0040-1951(93)90295-U

King, S. D., & Anderson, D. L. (1998). Edge-driven convection. Earth and Planetary Science Letters, 160(3–4), 289–296. http://doi.org/10.1016/S0012-821X(98)00089-2

Lanyon, R., Black, L. P., & Seitz, H. M. (1993). U-Pb zircon dating of mafic dykes and its application to the Proterozoic geological history of the Vestfold Hills, East Antarctica. Contributions to Mineralogy and Petrology, 115(2), 184–203. http://doi.org/10.1007/BF00321219

Le Bas, M. J., Le Maitre, R. W., Streckeisen, A., & Zanettin, B. (1986). A chemical classification of volcanic rocks based on the total alkali silica diagram. Journal of Petrology, 27(3), 745–750. http://doi.org/10.1093/petrology/27.3.745

LeCheminant, A. N., & Heaman, L. M. (1989). Mackenzie igneous events, Canada: Middle Proterozoic hotspot magmatism associated with ocean opening. Earth and Planetary Science Letters, 96(1–2), 38–48. http://doi.org/10.1016/0012-821X(89)90122-2

Li, Z. X., Bogdanova, S. V., Collins, A. S., Davidson, A., De Waele, B., Ernst, R. E., Fitzsimons, I. C. W., Fuck, R. A., Gladkochub, D. P., Jacobs, J., Karlstrom, K. E., Lu, S., Natapov, L. M., Pease, V., Pisarevsky, S. A., Thrane, K., Vernikovsky, V. (2008). Assembly, configuration, and break-up history of Rodinia: A synthesis. Precambrian Research, 160(1–2), 179–210. http://doi.org/10.1016/j.precamres.2007.04.021

McDonough, W. F., & Sun, S. s. (1995). The composition of the Earth. Chemical Geology, 120(3–4), 223–253. http://doi.org/10.1016/0009-2541(94)00140-4

Medig, K. P. R., Thorkelson, D. J., Davis, W. J., Rainbird, R. H., Gibson, H. D., Turner, E. C., & Marshall, D. D. (2014). Pinning northeastern Australia to northwestern Laurentia in the Mesoproterozoic. Precambrian Research, 249, 88–99. http://doi.org/10.1016/j.precamres.2014.04.018

Medig, K. P. R., Thorkelson, D. J., Davis, W. J., Rainbird, R. H., Gibson, H. D., Turner, E. C., & Marshall, D. D. (2014). Pinning northeastern Australia to northwestern Laurentia in the Mesoproterozoic. Precambrian Research, 249, 88–99. http://doi.org/10.1016/j.precamres.2014.04.018

Mercier, E. (1989). Évènements tectoniques d’origine compressive dans le Protérozoique du nord de la Cordillère Canadienne (montagnes Ogilvie, Yukon). Canadian Journal of Earth Science, 26, 199–205.

Miyashiro, 1974. (1974). Volcanic rock series in island arcs and active continental margins. American Journal of Science, 274, 321–355.

Mooney, W. D., Laske, G., & Masters, T. G. (1998). CRUST 5.1: A global crustal model at 5° × 5°. Journal of Geophysical Research: Solid Earth, 103(B1), 727–747. http://doi.org/10.1029/97JB02122

Moores, E. M. (1991). Southwest U.S.-East Antarctic (SWEAT) connection: A Hypothesis. Geology, 19, 425–428.

Moroskat, M. J. A. (2009). On the genesis of the Blende Zn-Pb-Ag deposit, Wernecke Mountains, Yukon: Structural and geochemical evidence. MSc thesis, University of Alberta, Edmonton, 116 p.

Nichols, J. & Russel, J. K. (2016). Igneous rock associations 20. Pearce element ratio diagrams: linking geochemical data to magmatic processes. Geoscience Canada 43(2),

Nielsen, A. B., Thorkelson, D. J., Gibson, H. D., & Marshall, D. D. (2013). The Wernecke igneous clasts in Yukon, Canada: Fragments of the Paleoproterozoic volcanic arc terrane Bonnetia. Precambrian Research, 238, 78–92. http://doi.org/10.1016/j.precamres.2013.09.017

Payne, J. L., Hand, M., Barovich, K. M., Reid, a., & Evans, D. a. D. (2009). Correlations and reconstruction models for the 2500-1500 Ma evolution of the Mawson Continent. Geological Society, London, Special Publications, 323(1), 319–355. http://doi.org/10.1144/SP323.16

Pearce, J. A. (2008). Geochemical fingerprinting of oceanic basalts with applications to ophiolite classification and the search for Archean oceanic crust. Lithos, 100(1–4), 14–48. http://doi.org/10.1016/j.lithos.2007.06.016

Pearce, J. A., & Parkinson, I. J. (1993). Trace element models for mantle melting: application to volcanic arc petrogenesis. Geological Society, London, Special Publications, 76(1), 373–403. http://doi.org/10.1144/GSL.SP.1993.076.01.19

Puchkov, V. N., Bogdanova, S. V., Ernst, R. E., Kozlov, V. I., Krasnobaev, A. A., Söderlund, U., … Sergeeva, N. D. (2013). The ca. 1380Ma Mashak igneous event of the Southern Urals. Lithos, 174, 109–124. http://doi.org/10.1016/j.lithos.2012.08.021

Rainbird, R. H., & Davis, W. J. (2007). U-Pb detrital zircon geochronology and provenance of the late Paleoproterozoic Dubawnt Supergroup: Linking sedimentation with tectonic reworking of the western Churchill Province, Canada. Bulletin of the Geological Society of America, 119(3–4), 314–328. http://doi.org/10.1130/B25989.1

Roeder P L, & Emslie R F. (1970). Olivine-Liquid Equilibrium. Contributions to Mineralogy and Petrology, 29, 275–289.

Rogers, C., Mackinder, A., Ernst, R.E., Cousens, B. (2016). Mafic magmatism in the Belt-Purcell Basin and Wyoming Province of Western Laurentia. Geological Society of America Special Paper 522, 243-282

Rollinson, H. (1993). Using geochemical data: evaluation, presentation, interpretation. Longman Scientific and Technical, US.

Ross, G. M., Parrish, R. R., & Winston, D. (1992). Provenance and UPb geochronology of the Mesoproterozoic Belt Supergroup (northwestern United States): implications for age of deposition and pre-Panthalassa plate reconstructions. Earth and Planetary Science Letters, 113(1–2), 57–76. http://doi.org/10.1016/0012-821X(92)90211-D

Ross, G. M., & Villeneuve, M. (2003). Provenance of the Mesoproterozoic (1.45 Ga) Belt basin (western North America): Another piece in the pre-Rodinia paleogeographic puzzle. Bulletin of the Geological Society of America, 115(10), 1191–1217. http://doi.org/10.1130/B25209.1

Russell, J.K., and Nichols, J., 1988, Analysis of petrologic hypotheses with Pearce element ratios: Contributions to Mineralogy and Petrology, v. 99, p. 25–35.

Russel, J.K., and Stanley, R., 1990, Origins of the 1954-1960 Lavas, Kilauea Volcano, Hawaii: Major Element Constraints on Shallow Reservoir Magmatic Processes of Crater (Figure: Journal of Geophysical Research, v. 95, p. 5021–5047.

Saccani, E. (2015). A new method of discriminating different types of post-Archean ophiolitic basalts and their tectonic significance using Th-Nb and Ce-Dy-Yb systematics. Geoscience Frontiers, 6(4), 481–501. http://doi.org/10.1016/j.gsf.2014.03.006

Schmitz, M. D., & Schoene, B. (2007). Derivation of isotope ratios, errors, and error correlations for U-Pb geochronology using 205Pb-235U-(233U)-spiked isotope dilution thermal ionization mass spectrometric data. Geochemistry, Geophysics, Geosystems, 8(8), 1–20. http://doi.org/10.1029/2006GC001492

Schwab, D. L., Thorkelson, D. J., Mortensen, J. K., Creaser, R. A., & Abbott, J. G. (2004). The Bear River dykes (1265-1269 Ma): Westward continuation of the Mackenzie dyke swarm into Yukon, Canada. Precambrian Research, 133(3–4), 175–186. http://doi.org/10.1016/j.precamres.2004.04.004

Sears, J. W., & Price, R. A. (2002). The Hypothetical Mesoproterozoic Supercontinent Columbia: Implications of the Siberian-West Laurentian Connection. Gondwana Research, 5(1), 35–39. http://doi.org/10.1016/S1342-937X(05)70885-6

Sears, J. W., & Price, R. A. (1978). The Siberian Connection: A case for Precambrian separation of the North American and Siberian cratons. Geology, 6, 267–270.

Shaw, D. M. (1970). Trace element fractionation during anatexis. Geochimica et Cosmochimica Acta, 34(2), 237–243. http://doi.org/10.1016/0016-7037(70)90009-8

Sleep, N. H. (1987). Lithospheric heating by mantle plumes. Geophysical Journal of the Royal Astronomical Society, 91(1), 1–11. http://doi.org/10.1111/j.1365-246X.1987.tb05209.x

Sleep, N. H. (1992). Hotspot Volcanism and Mantle Plumes. Annual Review of Earth and Planetary Sciences, 20(1), 19–43. http://doi.org/10.1146/annurev.ea.20.050192.000315

Smith, P. M., & Asimow, P. D. (2005). Adiabat-1ph: A new public front-end to the MELTS, pMELTS, and pHMELTS models. Geochemistry, Geophysics, Geosystems, 6(2), 1–8. http://doi.org/10.1029/2004GC000816

Spikings, R. A., Foster, D. A., Kohn, B. P., & Lister, G. S. (2001). Post-orogenic (< 1500 Ma) thermal history of the Proterozoic Eastern Fold Belt, Mount Isa Inlier, Australia. Precambrian Research, 109(1–2), 103–144. http://doi.org/10.1016/S0301-9268(01)00143-7

Sun, S. & McDonough, W. F. (1989). Chemical and isotopic systematics of oceanic basalts: implications for mantle composition and processes. Geological Society, London, Special Publications, 42(1), 313–345. http://doi.org/10.1144/GSL.SP.1989.042.01.19

Thompson, R. I., Roots, C. F., & Mustard, P. S. (1992). Geology of Dawson map area (116B, C) (northeast of Tintina Trench). Geological Survey of Canada, Open File 2849.

Thorkelson, D. J. (2000). Geology and mineral occurrences of the Slats Creek, Fairchild Lake and ``Dolores Creek'' areas, Wernecke Mountains (106D/16, 106C/13, 106C/14), Yukon Territory. Exploration and Geological Services Division, Yukon Region, Bulletin (Vol. 10).

Thorkelson, D. J., Abbott, J. G., Mortensen, J. K., Creaser, R. A., Villeneuve, M. E., Mcnicoll, V. J., & Layer, P. W. (2005). Early and Middle Proterozoic evolution of Yukon, Canada. Canadian Journal of Earth Sciences, 42, 1045–1071. http://doi.org/10.1139/E04-075

Thorkelson, D. J., Furlanetto, F., Medig, K. P. R., & Verbaas, J. (2016). Australia-Laurentia relations in the late Paleoproterozoic: a Wilson cycle followed by sinistral translation. In GSA annual meeting in Denver, Colorado, USA - 2016.

Thorkelson, D. J., & Laughton, J. R. (2016). Paleoproterozoic closure of an Australia-Laurentia seaway revealed by megaclasts of an obducted volcanic arc in Yukon, Canada. Gondwana Research, 33(May 2016), 115–133. http://doi.org/10.1016/j.gr.2015.01.004

Thorkelson, D. J., Mortensen, J. K., Davidson, G. J., Creaser, R. A., Perez, W. A., & Abbott, J. G. (2001). Early Mesoproterozoic intrusive breccias in Yukon, Canada: The role of hydrothermal systems in reconstructions of North America and Australia. Precambrian Research, 111(1–4), 31–55. http://doi.org/10.1016/S0301-9268(01)00155-3

Turner, S., Arnaud, N., Liu, J., Rogers, N., Hawkesworth, C., Harris, N., Kelley, S., van Calsteren, P., Deng, W. (1996). Post-collision, Shoshonitic Volcanism on the Tibetan Plateau: Implications for Convective Thinning of the Lithosphere and the Source of Ocean Island Basalts. Journal of Petrology, 37(1), 45–71. http://doi.org/10.1093/petrology/37.1.45

Upton, B. G. J., Rämö, O. T., Heaman, L. M., Blichert-Toft, J., Kalsbeek, F., Barry, T. L., & Jepsen, H. F. (2005). The Mesoproterozoic Zig-Zag Dal basalts and associated intrusions of eastern North Greenland: Mantle plume-lithosphere interaction. Contributions to Mineralogy and Petrology, 149(1), 40–56. http://doi.org/10.1007/s00410-004-0634-7

Wallace, E., & Green, D. H. (1988). An experimental determination of primary carbonatite magma composition. Nature, 335(22), 343–346.

Walter, M. J. (2013). Melt Extraction and Compositional Variability in Mantle Lithosphere. Treatise on Geochemistry: Second Edition (2nd ed., Vol. 3). Elsevier Ltd. http://doi.org/10.1016/B978-0-08-095975-7.00208-4

Wang, Q., Zhu, D. C., Zhao, Z. D., Liu, S. A., Chung, S. L., Li, S. M., … Mo, X. X. (2014). Origin of the ca. 90Ma magnesia-rich volcanic rocks in SE Nyima, central Tibet: Products of lithospheric delamination beneath the Lhasa-Qiangtang collision zone. Lithos, 198–199(1), 24–37. http://doi.org/10.1016/j.lithos.2014.03.019

Winchester, J. A., & Floyd, P. A. (1977). Geochemical discrimination of different magma series and their differentiation products using immobile elements. Chemical Geology, 20, 325–343. http://doi.org/10.1016/0009-2541(77)90057-2

Wilson JT. 1968. Static or mobile earth: the current scientific revolution. Proc. Am. Philos. Soc.112(5):309–20

Workman, R. K., & Hart, S. R. (2005). Major and trace element composition of the depleted MORB mantle (DMM). Earth and Planetary Science Letters, 231(1–2), 53–72. http://doi.org/10.1016/j.epsl.2004.12.005

Zhang, S., Li, Z. X., Evans, D. A. D., Wu, H., Li, H., & Dong, J. (2012). Pre-Rodinia supercontinent Nuna shaping up: A global synthesis with new paleomagnetic results from North China. Earth and Planetary Science Letters, 353–354, 145–155. http://doi.org/10.1016/j.epsl.2012.07.034

Chapter 6.

Conclusions

6.1. The Wernecke Breccia

The Wernecke Breccia is a 1.599 Ga set of non-magmatic hydrothermal breccias that occurs in northern Yukon, Canada (Bell, 1986a, b; Archer and Schmidt, 1978; Laznicka and Edwards, 1979; Thorkelson, 2000; Thorkelson et al., 2001a; Hunt et al., 2007; Furlanetto et al., 2013). They span an area of 300 x 150 km and host numerous IOCG occurrences that have attracted mineral exploration for several decades (Thorkelson, 2000; Thorkelson et al., 2001a; Thorkelson et al., 2005). Large blocks of wallrock, up to hundreds of metres in size, foundered kilometres deep into the breccia zones (Thorkelson et al., 2001a; Nielsen et al., 2013; Thorkelson and Laughton, 2016). The majority of clasts within the Wernecke Breccia are derived from its direct country rock, the sedimentary Wernecke Supergroup. However, locally abundant clasts were sourced from previously overlying units. These clasts are igneous and have been used in order to reconstruct a volcano-plutonic oceanic arc terrane, called Bonnetia, that was obducted onto northwestern Laurentia during collision with Australia (Furlanetto et al., 2013; Nielsen et al., 2013; Medig et al., 2014; Thorkelson and Laughton, 2016). The recognition of an obducted oceanic arc terrane on northwestern Laurentia has significantly influenced paleogeographic reconstructions (Furlanetto et al., 2013; Nielsen et al., 2013; Thorkelson and Laughton, 2016).

The breccias display mainly potassic and locally sodic and calcic alteration that was caused largely by hydrothermal activity. Locally, the breccia zones host iron oxide copper and gold (IOCG) mineralization (Hitzman et al., 1992). The Wernecke Breccia province may be part of a larger hydrothermal field that extended onto the Gawler Craton of Australia (Thorkelson et al., 2001a; Chapter 3). Researchers have suggested several different mechanisms for the formation of the breccias. These mechanisms include mud diapirism (Lane, 1990), evaporite diapirism (Bell, 1986b; Hunt et al., 2005), fault brecciation (Delaney et al., 1985), diatreme emplacement (Bell and Delaney, 1977; Archer

et al., 1977; Bell, 1978 Tempelman-Kluit, 1981) and hydrothermal fluid surges (Hitzman et al., 1992.; Thorkelson et al., 2001a; Furlanetto et al., 2013; Nielsen et al., 2013; Thorkelson and Laughton, 2016).

6.1.1. Sedimentary clasts that display soft sediment textures in Wernecke Breccia

Before this study, all clasts within Wernecke Breccia were sedimentary clasts correlated to the Wernecke Supergroup, or igneous rocks correlated to Bonnetia. The main research question that led to the writing of chapters 2 and 3 was: 'Does Wernecke Breccia host sedimentary clasts that were not sourced from the Wernecke Supergroup, and if so, can these rocks provide additional constraints for paleogeographic reconstructions?'

During the field season of 2012 Wernecke Breccia zones were examined in the Ogilvie Mountains and Wernecke Mountains. The examined Wernecke Breccia zones contain sedimentary clasts that are unlike the Wernecke Supergroup. These sedimentary clasts within Wernecke Breccia display soft sediment deformation textures. The sedimentary clasts were used in order to reconstruct a Paleo- Mesoproterozoic sedimentary succession on northwestern Laurentia. Whole-rock geochemical data was obtained and detrital zircons were separated from the sedimentary clasts and subjected to U-Pb and Lu-Hf isotopic analyses. The lithology and detrital zircon provenance of the sedimentary clasts further strengthen previously proposed paleogeographic reconstructions.

6.1.2. The source of soft sediment material in Wernecke Breccia: the Wernecke-Ogilvie unlithified succession

The Wernecke Breccia contains sedimentary clasts and ribbons that display soft sediment deformation features. The soft-sediment material includes well bedded red to pink mudstone and sandstone, soft-sediment conglomerate, and green mudstone. Soft sediment deformation occurred during Wernecke Breccia formation. The inferred source of these fragments is herein named the Wernecke-Ogilvie unlithified succession (WOUS). The WOUS was an extensive well bedded succession of sandstone and mudstone that

was deposited over at least 250 x 50 km based on the distribution of clasts within Wernecke Breccia zones. The succession was deposited after the Racklan Orogeny at ca. 1.6 Ga and before the formation of the Wernecke Breccia at 1.599 Ga. The WOUS was deposited on Bonnetia, an oceanic arc terrane that was obducted onto the Laurentian margin between ca. 1.65 and 1.60 Ga.

6.1.3. Detrital zircon from the WOUS indicate derivation from the Gawler Craton

Zircon from the WOUS are predominated by a population with ages 1.78 – 1.68 Ga with evolved εHf of 0 to -12. Other significant age populations range from 1.78 – 2.1 Ga and 2.45 – 2.55 Ga. A small proportion of the grains fall outside of these ranges and have Paleoproterozoic to Archean ages. Most of the grains, including those in the 1.78 – 1.68 Ga age-range, display original crystal faces and rounded edges and corners, and are consistent with derivation from a proximal source. However, there are no known local Laurentian sources for this zircon profile and instead the majority of the grains were sourced from the Gawler Craton, which has yielded similar detrital zircon ages and Hf and Nd isotopic ratios, and which accreted to the Laurentian margin in the late stages of the Racklan orogeny. In addition, the Bonnetian arc may have provided zircon to the WOUS. In this model, the obducted terrane Bonnetia is interpreted as an arc built on the leading edge of the Gawler Craton, or a fringing arc terrane (Thorkelson and Laughton, 2016), which was thrust onto the margin of Laurentia during late Paleoproterozoic collision of Australia with Laurentia.

6.1.4. Clasts within Olympic Dam correlated to soft sediment material within Wernecke Breccia

On the basis of lithological similarity, depositional timing and provenance, we correlate the WOUS remnants preserved within the Wernecke Breccia to bedded facies within the Olympic Dam Breccia Complex of the Gawler Craton in South Australia (McPhie et al., 2011; 2016). The sedimentary overlap assemblage may also correlate to the (possibly) coeval Corunna Conglomerate, Pandurra Formation and the Radium Creek Group in South Australia. The bedded facies within the Olympic Dam Breccia Complex and the WOUS are interpreted as remnants of an intercontinental sedimentary overlap

assemblage that was deposited after the collision of Australia and Laurentia and obduction of Bonnetia. The Pandurra Formation and the Radium Creek Group are tentatively included in this overlap assemblage.

The proposed correlation between the WOUS and inferred source of the bedded facies within the Olympic Dam Breccia Complex strengthen the previously hypothesized link between northwestern Laurentia and the Gawler Craton at 1.6 Ga (Thorkelson et al., 2001). During the interval 1.6 – 1.5 Ga, Australia was sinistrally translated along the margin of Laurentia to allow for a more southerly fit at 1.5 Ga (Medig et al., 2014) and the juxtaposition of northwestern Laurentia with the Mt Isa inlier. During this time, the WOUS was eroded, and the only known remnants of this succession are now present as fragments within the Wernecke Breccia.

6.1.5. The formation of Wernecke Breccia

The process of formation of Wernecke Breccia requires deep excavation of zones in the crust and development of transient open space. The excavations were likely caused by the ascent of volatile-rich fluids and violent venting of rock and gas (Laughton et al., 2005). CO_2 may have been a major component of the fluid and could have been derived from a carbonatitic magma within the mantle or deep crust in a manner similar to that proposed for Verneshots (Nicolayson and Ferguson, 1990; Phipps Morgan et al., 2004). Voluminous hydrothermal activity following brecciation led to the metasomatism of clasts and wallrock and hydrothermal cementation. Terrane obduction and contractional deformation may have contributed to the environment of breccia formation through fluid entrapment and overpressurization. Other previously proposed and new hypotheses such as mud diapirism, evaporite diapirism, rock dissolution, kimberlite volcanism and fault activity are rejected as main causes of breccia formation. Chapter 4 contains a full evaluation of processes and boundary conditions for breccia formation.

6.2. 1.38 Ga magmatism in northwestern Laurentia

The Hart River sills are a set of intermediate to mafic Mesoproterozoic 1.38 Ga sills that occur in Yukon, northern Canada (Abbott, 1997; Thorkelson, 2000; Thorkelson

et al., 2005). The sills are locally voluminous (Abbott et al., 1997), and extend for more than 200 km from east to west. During the emplacement of the Hart River sills, northwestern Laurentia was proximal with other tectonic blocks such as Siberia (Sears and Price, 1978, 2002; David et al., 2016; Ernst et al., 2016), Australia (Bell and Jefferson, 1987; Moores, 1991; Thorkelson et al., 2001; Medig et al., 2014, Chapter 3), and Antarctica (Goodge et al., 2008). Antarctica and Siberia also contain ~1.38 Ga intrusives (Ernst et al., 2008). The following conclusions were drawn based on the geochemical analyses presented in Chapter 5.

6.2.1. New and improved U-Pb ages

Two new cathode luminescence thermal ionization mass spectrometry (CA-TIMS) dates are reported from U-Pb analyses on zircon. These dates are 1382.15 ± 0.39 Ma and 1382.14 ± 0.36 Ma. This new data confirms the continuation of the sills from the Hart River inlier (Abbott, 1997) to 200 km east as originally mapped by Green (1972).

6.2.2. Melting of spinel bearing mantle

The Hart River sills are a set of subalkaline, metaluminous, tholeiitic gabbros that occur on northwestern Laurentia. The sills are juvenile and have εNd ≈ +3.5, apart from one sill sample that assimilated local wall rock. The Hart River sills have trace elements that are relatively enriched in LILE and REE and HFSE that are similar to N-MORB. Consistent with these chemical characteristics, the sills were derived from a source similar to MORB mantle. The Sm/Yb and Dy/Zr ratios indicate that the Hart River sills formed from >8% of partial melting of spinel bearing mantle. Such mantle would have occurred from ~40 to 80 km depth. There is no geochemical evidence for melting of garnet bearing mantle which would indicate upwelling and coeval melting of a mantle plume.

6.2.3. Rifting of Australia from Laurentia

Consistent with the presence of the Hart River sills, and coeval sills farther south on Laurentia and Antarctica, 1.38 Ga rifting occurred along the margin of Western Laurentia. This episode of rifting may have led to drifting and the end of the contiguous

Mawson continent and Laurentia. Together with a rift on the northeastern side of Laurentia (Puchkov et al., 2013) this implies that voluminous mafic magmatism occurred on two sides of Laurentia at 1.38 Ga. Australia and Laurentia were later reattached during the formation of supercontinent Rodinia (Li et al., 2008, Milidragovic et al., 2011), although their relative orientation is unclear.

6.3. The evolution of Yukon Territory from ~1.71 to ~1.38 Ga

The Yukon Territory underwent several periods of extension and sedimentation, punctuated by collision, hydrothermal brecciation and magmatism during the interval 1.71 – 1.38 Ga (Thorkelson et al., 2001; Thorkelson et al., 2005; Furlanetto et al., 2013, 2016; Nielsen et al., 2013; Medig et al., 2014, 2016). During the first period of sedimentation the Wernecke Supergroup was deposited, a >13 km thick sequence of fine grained sedimentary strata (Furlanetto et al., 2016). These sedimentary strata overlie several kilometres of unexposed strata that, in turn, overlie unexposed crystalline basement (Furlanetto et al., 2016; Cook et al., 2004). Furlanetto et al. (2016) interpret basins on Western Australia to be coeval and related to this period of drifting. The Wernecke Supergroup was deposited from 1.66 – 1.60 Ga (Furlanetto et al., 2013; 2016).

During the sedimentation of the Wernecke Supergroup, Bonnetia existed as an outboard terrane (Furlanetto et al., 2013) on the margin of the Gawler Craton (Chapter 3). The Gawler-Bonnetia terrane encroached upon Laurentia and Bonnetia was obducted during the Racklan Orogeny at 1.60 Ga (Furlanetto et al., 2013). From this time onwards, the Gawler Craton of Australia and northwestern Laurentia were connected (Thorkelson et al., 2001; Chapter 3). A sedimentary overlap assemblage, the Wernecke Ogilvie Unlithified Succession (WOUS) was deposited on northwestern Laurentia and is correlated to sedimentary strata present on the Gawler Craton and potentially on the Curnamona Province (Chapter 3).

Shortly after the collision between Australia and Laurentia an IOCG hydrothermal province developed on the Gawler Craton and on Northwestern Laurentia (Thorkelson et al., 2001; Chapter 3). This hydrothermal province led to widespread brecciation and resulted in the Wernecke Breccia on northwestern Laurentia and numerous IOCG

occurrences on the Gawler Craton including the Olympic Dam deposit. The IOCG occurrences on northwestern Laurentia formed via the escape of highly pressurized gas (Chapter 4). Exsolving CO_2 from carbonatites may have provided a source of gas. However, there is no evidence for surficial magmatism. Carbonatitic magmatism may have resulted from distal melting related to voluminous magmatism that occurred on the Gawler Craton and correlated magmatism further east on Laurentia (Chapter 4; Hamilton and Buchan, 2010). The connection between the Gawler Craton and northwestern Laurentia is firmly established by the presence of a sedimentary overlap assemblage that now occurs within Wernecke Breccia (WOUS, Verbaas et al., 2014; Chapter 3) and the Olympic Dam deposit (McPhie et al., 2016; Chapter 3).

The collision between Laurentia and Australia was followed by sinistral translation sometime during the interval 1.6 – 1.45 Ga (Thorkelson et al., 2016). This sinistral translation juxtaposed the Mt. Isa Inlier of Australia with northwestern Laurentia and allowed for immature sediments sourced from the Mt Isa Inlier to be deposited on northwestern Laurentia in the PR1 basin (Medig et al., 2014). Other roughly coeval rift basins occur along the western margin of Laurentia (Ross et al., 1992; Doe et al., 2012; Daniel et al., 2013).

The Hart River sills intruded at 1.38 Ga and are the result of melting of spinel-bearing mantle. The Hart River sills are coeval with sills in northern Washington (1379 ± 1 Ma; Höy, 1989; Rogers, 2016) and sills and dykes in the Vestfold Hills in Antarctica (1380 ± 7 Ma, Lanyon et al., 1993). These magmatic episodes are here interpreted to lie on a rift axis that flanked western Laurentia and signifies the onset of rifting of Australia from Laurentia. Rifting and drifting occurred until the reconfiguration of the continents into supercontinent Rodinia (Li et al., 2008).

6.4. Future work

Several questions about the Paleoproterozoic to Mesoproterozoic evolution of Yukon Territory remain:

- How can the formational process of Wernecke Breccia be identified and confirmed?

- Do greenschist grade rocks of the Racklan Orogeny contain a metamorphic gradient and if so, what is its direction?

- Are the various magmatic episodes during the existence of supercontinent Columbia related to supercontinent evolution?

The formational process of the Wernecke Breccia is yet unclear. The currently available data is consistent with, but not diagnostic of, carbonatite degassing at depth (Chapter 4). Future studies should aim to identify the earliest fluid phases and subject those to detailed isotopic studies. Fluid inclusions containing CO_2 and N_2 were identified in the Igor mineral occurrence. More detailed investigations of the gaseous phases should start at this mineral occurrence.

The Racklan Orogeny is not developed with the same characteristics within the entire Wernecke Supergroup, and it is likely that a metamorphic gradient is preserved within the Wernecke Supergroup. This metamorphic gradient may be preserved as a range in peak metamorphic temperatures, pressures, and mineral assemblages. If present, a metamorphic gradient may be used to further constrain the directionality of collision between Australia and Laurentia at 1.6 Ga.

The first analyses on Proterozoic magmatic rocks commonly include U-Pb zircon or baddeleyite age determinations and paleomagnetic measurements (Ernst et al., 2000) or isotopic analyses (Doughty and Chamberlain, 1996). However, many magmatic episodes have not been assessed geochemically. Geochemistry can be used in order to place importance constraints on paleogeographic reconstructions. The rough similarity of trace element signatures of 1.38 Ga magmatic events around the world (Chapter 5) may be related to the evolution of the supercontinent Columbia. This similarity is currently based on a limited data set that should be expanded.

6.5. References

Abbott, G. (1997). Geology of the Upper Hart River Area, Eastern Ogilvie Mountains, Yukon Territory (116A/10, 116A/11).

Archer, A., Bell, R. T., Delaney, G. D., & Godwin, C. I. (1977). Mineralized breccias of Wernecke Mountains Yukon. Geological Association of Canada, Program with Abstracts 2:5.

Archer, A., & Schmidt, U. (1978). Mineralized breccias of early Proterozoic age, Bonnet Plume River district, Yukon Territory. Canadian Mining and Metallurgical Bulletin, 71, 53–58.

Armit, R. J., Betts, P. G., Schaefer, B. F., Pankhurst, M. J., & Giles, D. (2014). Provenance of the Early Mesoproterozoic Radium Creek Group in the northern Mount Painter Inlier: Correlating isotopic signatures to inform tectonic reconstructions. Precambrian Research, 243, 63–87. http://doi.org/10.1016/j.precamres.2013.12.022

Bell, R. T. (1986). Geological map of northeastern Wernecke Mountains, Yukon Territory. Geological Survey of Canada, Open File (1207).

Bell, R. T. (1978). Breccias and uranium mineralization in the Wernecke Mountains, Yukon Territory - a progress report. Current Research, Part A. Geological Survey of Canada, Paper 78-1, 317–322.

Bell, R. T. (1986). Megabreccias in northeastern Wernecke Mountains, Yukon Territory. Current Research, Part A. Geological Survey of Canada, Paper 1986, 375–384.

Bell, R. T., & Delaney, G. D. (n.d.). Geology of some uranium occurrences in Yukon Territory. Report of Activities, Part A, Geological Survey of Canada, Paper 1-77, 33–37.

Bell, R. T., & Jefferson, C. W. (1987). An hypothesis for an Australian-Canadian connection in the Late Proterozoic and the birth of the Pacific Ocean. Pacific Rim Congress 87, 39 - 50

Daniel, C. G., Pfeifer, L. S., Jones, J. V., & McFarlane, C. M. (2013). Detrital zircon evidence for non-Laurentian provenance, Mesoproterozoic (ca. 1490-1450 ma) deposition and orogenesis in a reconstructed orogenic belt, northern New Mexico, USA: Defining the Picuris orogeny. Bulletin of the Geological Society of America, 125(9–10), 1423–1441. http://doi.org/10.1130/B30804.1

Delaney, G. D. (1985). The Middle Proterozoic Wernecke Supergroup, Wernecke Mountains, Yukon Territory. University of Western Ontario. University of Western Ontario, London, Ontario, PhD thesis

Doe, M. F., Jones, J. V., Karlstrom, K. E., Thrane, K., Frei, D., Gehrels, G., & Pecha, M. (2012). Basin formation near the end of the 1.60-1.45 Ga tectonic gap in southern Laurentia: Mesoproterozoic Hess Canyon Group of Arizona and implications for ca. 1.5 Ga supercontinent configurations. Lithosphere, 4(1), 77–88. http://doi.org/10.1130/L160.1

Ernst, R. E. (2014) Large igneous provinces. Cambridge University Press, 666 p.

Ernst, R. E., Hamilton, M. A., Söderlund, U., Hanes, J. A., Gladkochub, D. P., Okrugin, A. V., Kolotilina, T., Mekhonoshin, A.S., Bleeker, W., LeCheminant, A.N., Buchan, K.L., Chamberlain, K.R., Didenko, A. N. (2016). Long-lived connection between southern Siberia and northern Laurentia in the Proterozoic. Nature Geoscience, 9 (April), 464-469. http://doi.org/10.1038/ngeo2700

Ernst, R. E., Wingate, M. T. D., Buchan, K. L., & Li, Z. X. (2008). Global record of 1600-700 Ma Large Igneous Provinces (LIPs): Implications for the reconstruction of the proposed Nuna (Columbia) and Rodinia supercontinents. Precambrian Research, 160(1–2), 159–178. http://doi.org/10.1016/j.precamres.2007.04.019

Ernst, R.E., and Youbi, N., (2017), How Large Igneous Provinces affect global climate, sometimes cause mass extinctions, and represent natural markers in the geological record: Palaeogeography, Palaeoclimatology, Palaeoecology, v. 478, p. 30–52, doi: https://doi.org/10.1016/j.palaeo.2017.03.014.

Evans, D. A. D., Veselovsky, R. V., Petrov, P. Y., Shatsillo, A. V., & Pavlov, V. E. (2016). Paleomagnetism of Mesoproterozoic margins of the Anabar Shield: A hypothesized billion-year partnership of Siberia and northern Laurentia. Precambrian Research, 281, 639–655. http://doi.org/10.1016/j.precamres.2016.06.017

Furlanetto, F., Thorkelson, D. J., Daniel Gibson, H., Marshall, D. D., Rainbird, R. H., Davis, W. J., Crowley, J., Vervoort, J. D. (2013). Late Paleoproterozoic terrane accretion in northwestern Canada and the case for circum-Columbian orogenesis. Precambrian Research, 224, 512–528. http://doi.org/10.1016/j.precamres.2012.10.010

Furlanetto, F., Thorkelson, D.J., Rainbird, R.H., Davis, W.J., Gibson, H.D., and Marshall, D.D., (2016), The Paleoproterozoic Wernecke Supergroup of Yukon, Canada: Relationships to orogeny in northwestern Laurentia and basins in North America, East Australia, and China: Gondwana Research, v. 39, p. 14–40, doi: 10.1016/j.gr.2016.06.007.

Gillen, D. (2010). A study of IOCG-related hydrothermal fluids in the Wernecke Mountains, Yukon Territory, Canada. PhD Thesis, James Cook University.

Goodge, J. W., Vervoort, J. D., Fanning, C. M., Brecke, D. M., Farmer, G. L., Williams, I. S., Myrow, P.M., DePaolo, D. J. (2008). A positive test of East Antarctica-Laurentia juxtaposition within the Rodinia supercontinent. Science (New York, N.Y.), 321(2008), 235–240. http://doi.org/10.1126/science.1159189

Green. (1972). Geology of Nash Creek, Larsen Creek, and Dawson Creek map-areas, Yukon Territory. Geological Survey of Canada, Memoir 364, p. 157.

Hitzman, M. W., Oreskes, N., & Einaudi, M. T. (1992). Geological characteristics and tectonic setting of Proterozoic iron oxide (CuUAuREE) deposits. Precambrian Research, 58(1–4), 241–287. http://doi.org/10.1016/0301-9268(92)90121-4

Hunt, J. A., Baker, T., & Thorkelson, D. J. (2007). A review of iron oxide copper-gold deposits, with focus on the Wernecke Breccias, Yukon Canada, as an example of a non-magmatic end member and implications for IOCG genesis and classification. Exploration and Mining Geology, 16(3–4), 209–232. http://doi.org/10.2113/gsemg.16.3-4.209

Hunt, J. A., Baker, T., Cleverley, J., Davidson, G. J., Fallick, A. E., & Thorkelson, D. J. (2011). Fluid inclusion and stable isotope constraints on the origin of Wernecke Breccia and associated iron oxide – copper – gold mineralization, Yukon. Canadian Journal of Earth Sciences, 48(10), 1425–1445. http://doi.org/10.1139/e11-044

Hunt, J., Baker, T., & Thorkelson, D. J. (2005). Regional-scale Proterozoic IOCG-mineralized breccia systems: Examples from the Wernecke Mountains, Yukon, Canada. Mineralium Deposita, 40(5), 492–514. http://doi.org/10.1007/s00126-005-0019-5

Kendrick, M. A., Honda, M., Gillen, D., Baker, T., & Phillips, D. (2008). New constraints on regional brecciation in the Wernecke Mountains, Canada, from He, Ne, Ar, Kr, Xe, Cl, Br and I in fluid inclusions. Chemical Geology, 255(1–2), 33–46. http://doi.org/10.1016/j.chemgeo.2008.05.021

Lane, R. A. (1990). Geologic setting and petrology of the Proterozoic Ogilvie Mountain breccias of the Coal Creek Inlier, Southern Ogilvie Mountains, Yukon Territory. M.Sc. thesis. The University of British Columbia.

Laznicka, P., & Edwards, R. J. (1979). Dolores Creek, Yukon – A disseminated copper mineralization in sodic metasomatites. Economic Geology, 74, 1352–1370.

McPhie, J., Kamenetsky, V. S., Chambefort, I., Ehrig, K., & Green, N. (2011). Origin of the supergiant Olympic Dam Cu-U-Au-Ag deposit, South Australia: Was a sedimentary basin involved. Geology, 39(8), 795–798. http://doi.org/10.1130/G31952.1

McPhie, J., Orth, K., Kamenetsky, V., Kamenetsky, M., & Ehrig, K. (2016). Characteristics, origin and significance of Mesoproterozoic bedded clastic facies at the Olympic Dam Cu-U-Au-Ag deposit, South Australia. Precambrian Research, 276, 85–100. http://doi.org/10.1016/j.precamres.2016.01.029

Medig, K. P. R., Thorkelson, D. J., Davis, W. J., Rainbird, R. H., Gibson, H. D., Turner, E. C., & Marshall, D. D. (2014). Pinning northeastern Australia to northwestern Laurentia in the Mesoproterozoic. Precambrian Research, 249, 88–99. http://doi.org/10.1016/j.precamres.2014.04.018

Moores, E. M. (1991). Southwest U.S.-East Antarctic (SWEAT) connection: A Hypothesis. Geology, 19, 425–428.

Nielsen, A. B., Thorkelson, D. J., Gibson, H. D., & Marshall, D. D. (2013). The Wernecke igneous clasts in Yukon, Canada: Fragments of the Paleoproterozoic volcanic arc terrane Bonnetia. Precambrian Research, 238, 78–92. http://doi.org/10.1016/j.precamres.2013.09.017

Rogers, R. L., Mackinder, A., Ernst, R. E., Cousens, B. (2016). Mafic magmatism in the Belt-Purcell Basin and Wyoming Province of western Laurentia. Geological Society of America Special Paper 522, 243 – 260

Ross, G. M., Parrish, R. R., & Winston, D. (1992). Provenance and UPb geochronology of the Mesoproterozoic Belt Supergroup (northwestern United States): implications for age of deposition and pre-Panthalassa plate reconstructions. Earth and Planetary Science Letters, 113(1–2), 57–76. http://doi.org/10.1016/0012-821X(92)90211-D

Sears, J. W., & Price, R. a. (2002). The Hypothetical Mesoproterozoic Supercontinent Columbia: Implications of the Siberian-West Laurentian Connection. Gondwana Research, 5(1), 35–39. http://doi.org/10.1016/S1342-937X(05)70885-6

Sears, J. W., & Price, R. A. (1978). The Siberian Connection: A case for Precambrian separation of the North American and Siberian cratons. Geology, 6, 267–270.

Tempelman-Kluit, D. J. (1981). Nor, summary of assessment work and description of mineral properties. In Yukon Geology and Exploration, 1979-1980, Exploration and Geological Services Division, Yukon Indian and Northern Affairs Canada (pp. 300–301).

Thorkelson, D. J. (2000). Geology and mineral occurrences of the Slats Creek, Fairchild Lake and ``Dolores Creek'' areas, Wernecke Mountains (106D/16, 106C/13, 106C/14), Yukon Territory. Exploration and Geological Services Division, Yukon Region, Bulletin (Vol. 10).

Thorkelson, D. J., Abbott, J. G., Mortensen, J. K., Creaser, R. A., Villeneuve, M. E., Mcnicoll, V. J., & Layer, P. W. (2005). Early and Middle Proterozoic evolution of Yukon, Canada. Canadian Journal of Earth Sciences, 42, 1045–1071. http://doi.org/10.1139/E04-075

Thorkelson, D. J., & Laughton, J. R. (2016). Paleoproterozoic closure of an Australia-Laurentia seaway revealed by megaclasts of an obducted volcanic arc in Yukon, Canada. Gondwana Research, 33(May 2016), 115–133. http://doi.org/10.1016/j.gr.2015.01.004

Thorkelson, D. J., Mortensen, J. K., Davidson, G. J., Creaser, R. A., Perez, W. A., & Abbott, J. G. (2001). Early Mesoproterozoic intrusive breccias in Yukon, Canada: The role of hydrothermal systems in reconstructions of North America and Australia. Precambrian Research, 111(1–4), 31–55. http://doi.org/10.1016/S0301-9268(01)00155-3

Appendix A.

Chapter 3. Detrital zircon of fallback sediments within Wernecke Breccia link the Gawler Craton to Laurentia: supplementary data

Laser ablation inductively coupled mass spectrometry: methods

Zircon grains were separated from rocks using standard techniques and annealed at 900 C° for 60 hours in a muffle furnace. They were mounted in epoxy and polished until the centers of the grains were exposed. Cathodoluminescence (CL) images were obtained with a JEOL JSM-1300 scanning electron microscope and Gatan MiniCL. Zircon was analyzed by laser ablation inductively coupled plasma mass spectrometry (LA-ICPMS) using a Thermo Electron X-Series II quadrupole ICPMS and New Wave Research UP-213 Nd:YAG UV (213 nm) laser ablation system. In-house analytical protocols, standard materials, and data reduction software were used for acquisition and calibration of U-Pb dates and a suite of high field strength elements (HFSE) and rare earth elements (REE). Zircon was ablated with a laser spot of 25 µm wide using fluence and pulse rates of 5 J/cm^2 and 10 Hz, respectively, during a 45 second analysis (15 sec gas blank, 30 sec ablation) that excavated a pit ~25 µm deep. Ablated material was carried by a 1.2 L/min He gas stream to the nebulizer flow of the plasma. Dwell times were 5 ms for Si and Zr, 200 ms for ^{49}Ti and 207Pb, 80 ms for ^{206}Pb and ^{238}U, 40 ms for ^{202}Hg, ^{204}Pb, ^{208}Pb, ^{232}Th and 10 ms for all other HFSE and REE. Background count rates for each analyte were obtained prior to each spot analysis and subtracted from the raw count rate for each analyte. Ablations pits that appear to have intersected glass or mineral inclusions were identified by time-resolved data that show large fluctuations in Ti or P. U-Pb dates from these analyses are considered valid if the time-resolved U-Pb ratios appear to have been unaffected by the inclusions. Analyses that appear contaminated by common Pb were rejected based on an intensity of mass 204 above baseline. For concentration calculations, background-subtracted count rates for each analyte were internally normalized to ^{29}Si and calibrated with respect to NIST SRM-610 and -612 glasses as the primary standards. Temperature was calculated from the titanium in zircon thermometer

(Watson et al., 2006). Because there are no constraints on the activity of TiO_2 in the source rocks, an average value in crustal rocks of 0.6 was used.

For U-Pb and $^{207}Pb/^{206}Pb$ dates, instrumental fractionation of the background-subtracted ratios was corrected and dates were calibrated with respect to interspersed measurements of the Plešovice zircon standard (Sláma et al., 2008). Two analyses of Plešovice were done for every 10 analyses of unknown zircon; a polynomial fit to the standard analyses yields each sample-specific fractionation factor. Signals at mass 204 were indistinguishable from zero following subtraction of mercury backgrounds measured during the gas blank (<1000 cps ^{202}Hg), and thus dates are reported without common Pb correction. Radiogenic isotope ratio and age error propagation for all analyses includes uncertainty contributions from counting statistics and background subtraction. For spot analyses that are individually interpreted (e.g., detrital zircon analyses), the uncertainty from the standard calibration is propagated into the error on each date. This uncertainty is the standard deviation of the time-varying U/Pb fractionation factor and the standard error of the mean of the time-invariant, smaller $^{207}Pb/^{206}Pb$ fractionation factor. Data were collected in one experiment in August 2013. Standard calibration uncertainty for $^{207}Pb/^{206}Pb$ dates is 0.6% (2σ) and for $^{206}Pb/^{238}U$ dates is 5.4% (2σ). Age interpretations are based on $^{207}Pb/^{206}Pb$ dates for >1000 Ma zircon. Analyses with >25% discordance are not considered. Errors on the $^{207}Pb/^{206}Pb$ and $^{206}Pb/^{238}U$ dates from individual analyses are given at 2σ, as are the errors on the weighted mean dates.

A zircon secondary reference material was treated as an unknown to assess accuracy, interspersed as groups of two analyses for every 20 unknown analyses. Weighted mean dates are calculated using Isoplot 3.0 (Ludwig, 2003) from errors on individual dates that do not include the standard calibration uncertainties. However, errors on weighted mean dates include the standard calibration uncertainties within each experiment and are given at 2σ. FC-1 zircon (1098 Ma from unpublished chemical abrasion thermal ionization mass spectrometry (CA-TIMS) data, Boise State University) yielded a weighted mean $^{207}Pb/^{206}Pb$ date of 1079 ± 17 Ma (MSWD=1.5, n=10) and $^{206}Pb/^{238}U$ date of 1077 ± 54 Ma (MSWD=0.9, n=13).

References

Ludwig, K.R., 2003, User's Manual for Isoplot 3.00. *Berkeley Geochronology Center: Berkeley, CA*, 70 p.

Sláma, J., Košler, J, Condon, D.J., Crowley, J.L., Gerdes, A., Hanchar, J.M., Horstwood, M.S.A., Morris, G.A., Nasdala, L., Norberg, N., Schaltegger, U., Schoene, B. Tubrett, M.N, Whitehouse, M.J. 2008. Plešovice zircon — A new natural reference material for U–Pb and Hf isotopic microanalysis. Chemical *Geology*, 249: pp. 1-35.

Watson, E.B., Wark, D.A., Thomas, J.B. 2006. Crystallization thermometers for zircon and rutile. Contributions to Mineralogy and Petrology, 151: 413-433.

Appendix B.

Crustal features possibly related to Wernecke Breccia

Cryptoexplosion structures are essentially debated cross cutting breccia bodies that have been described in a variety of locations and are the result of impact cratering, evaporite diapirism, volatile rich eruptions, or deep lithospheric gas blasts (Verneshots) associated with alkaline and alkaline ultramafic magmatism (Dietz, 1963; Bucher, 1963; Armstutz, 1964; Nicolayson and Ferguson, 1990; Luczaj, 1998; Phipps Morgan et al., 2004). The cryptoexplosion theory was developed at the same time as the impact crater theory and signifies a debate between supporters of an endogenic versus an exogenic origin for semi-circular breccia bodies. Although the original cryptoexplosion structures described by Bucher (1963) have since been incorporated in the Earth Impact Database as proven impact structures, the theory has continued to receive support in its application to other structures (Nicolaysen and Fergusen, 1990; Phipps Morgan et al., 2004). The theory was expanded and elaborated upon by Phipps Morgan et al., (2004) who termed the process of localized lithospheric degassing 'Verneshots' and argues that these lithospheric blasts of gas occur concurrently with continental flood basalts. Phipps Morgan et al., (2004) also explain endogenic shock metamorphism by Verneshots. However, shock metamorphism as an effect of Verneshots is not supported by researchers of impact craters (Horz, 1968; Stoffler and Langenhorst, 1994; French, 1998; Glikson, 2005; Reimold, 2007; French and Koeberl, 2010). The possible presence of shock metamorphic features at endogenic craters has been a topic of debate for example regarding the Tunguska event in Russia (Kvasnytsya, 2013; Vannuchi, 2015), and at potential cryptoexplosion structures on the 38th parallel in the US (Snyder and Gerdemann, 1965; Snyder, 1970; Nicolayson and Ferguson, 1990; Rampino and Volk; 1996; Luczaj, 1998). A review of the credibility of shock metamorphic features at cryptoexplosion structures is outside of the scope of this study. However, if the Wernecke Breccia are the result of mantle degassing shock metamorphism is not necessarily present.

Eight cryptoexplosion structures on the 38th parallel in the US define an array of more than 500 km from eastern Kansas to southern Illinois (Snyder and Gerdemann, 1965; Snyder, 1970; Nicolayson and Ferguson, 1990; Rampino and Volk; 1996; Luczaj,

1998). Researchers have been unable to identify whether these structures are formed by an endogenic process, associated with Permian to Cretaceous highly volatile ultramafic volcanism (Kiilsgaard et al., 1962; Amstutz, 1964; McCall, 1964; Snyder and Gerdemann, 1965; Bucher, 1965; Nicolaysen and Ferguson, 1990) or by impact cratering (Dietz, 1963; French, 1990; Sharpton and Grieve, 1990; Rampino and Volk, 1996). The linearity of these 8 structures makes it unlikely that they formed by several impact events, hence according to researchers supporting an origin as impact craters the structures are interpreted as the result of a string of bolides, also known as a cantena (Rampino and Volk, 1996). This theory implies that all eight structures have the same age. The relative ages of the structures were examined by Luczaj (1998), who concluded on the basis of crosscutting relationships that the age of the structures differ and hence, that they formed by an endogenic process. Interestingly, in the middle of the lineament of the cryptoexplosion strucures, a cluster of IOCG occurrences is present (Nold et al., 2014). There are also several kimberlites along the lineament (Faure, 2010), a form of lithospherically modified carbonatitic melt (Russel et al., 2012).

The Gilf Kebir region in Egypt is host to 1300 small crater like structures that were initially described by Paillou et al., (2004). There is no magmatism associated with the structures. Paillou et al., (2004) infer an impact crater origin for this crater field, but this hypothesis was later retracted by Paillou et al., (2006), and has never found traction with impact crater researchers (French and Koeberl, 2010; Reimold and Koeberl, 2014). Paillou et al., (2006) infer a hydrothermal origin for the crater field, but also note that this model is not consistent with all characteristics.

The Bajada del Diablo field is a crater field in Patagonia that was described by Acevedo et al., (2009), and further explored by Prezzi et al. (2012) and Acevedo et al. (2012) that was interpreted as an impact crater field. An interesting debate ensued between impact researchers dismissing an interpretation as impact craters and Acevedo and co-workers (Reimold and Koeberl et al., 2014; Acevedo et al., 2014; Reimold and Koeberl, 2014; Acevedo et al., 2016). Ultimately more detailed field work and data from both these crater fields is needed, but in the absence of concurrent magmatism (or only minor alkali magmatism) the possibility remains that these craters formed via hydrothermal fluid surges.

References

Acevedo, R.D., Rabassa, J., Corbella, H., Orgeira, M.J., Prezzi, C., Ponce, J.F., Martínez, O., González-Guillot, M., Rocca, M., and Subías, I. (2014). Comment on “Impact structures in Africa: A review” by Reimold and Koeberl [J. Afr. Earth Sci. 93 (2014) 57-175]: Journal of African Earth Sciences, v. 100, p. 755–756, doi: 10.1016/j.jafrearsci.2014.07.020.

Acevedo, R.D., Rabassa, J., Ponce, J.F., Martínez, O., Orgeira, M.J., Prezzi, C., Corbella, H., González-Guillot, M., Rocca, M., Subías, I., and Vásquez, C. (2012). The Bajada del Diablo astrobleme-strewn field, central Patagonia Argentina: Extending the exploration to surrounding areas: Geomorphology, v. 169–170, p. 151–164, doi: 10.1016/j.geomorph.2012.04.020.

Acevedo, R.D., Rabassa, J., Corbella, H., Orgeira, M.J., Prezzi, C., Ponce, J.F., Martínez, O., González-Guillot, M., Rocca, M., and Subías, I. (2014). Comment on “Impact structures in Africa: A review” by Reimold and Koeberl [J. Afr. Earth Sci. 93 (2014) 57–175]: Journal of African Earth Sciences, v. 100, p. 755–756, doi: 10.1016/j.jafrearsci.2014.07.020.

Acevedo, R.D., Rabassa, J., Rocca, M., González-Guillot, M., Martínez, O., Subías, I., Corbella, H., Prezzi, C., Orgeira, M.J., and Ponce, J.F. (2016). Further comment to “Reply to Comment on impact structures in Africa: A review (Short Note)” by Reimold and Koeberl [J. Afr. Earth Sci. 100 (2014) 757–758]: Journal of African Earth Sciences, v. 118, p. 315–316, doi: 10.1016/j.jafrearsci.2015.02.004.

Acevedo, R.D., Rabassa, J., Rocca, M., González-Guillot, M., Martínez, O., Subías, I., Corbella, H., Prezzi, C., Orgeira, M.J., and Ponce, J.F., (2016). Further comment to “Reply to Comment on impact structures in Africa: A review (Short Note)” by Reimold and Koeberl [J. Afr. Earth Sci. 100 (2014) 757–758]: Journal of African Earth Sciences, v. 118, p. 315–316, doi: 10.1016/j.jafrearsci.2015.02.004.

Amstutz, G.C. (1964). Impact, cryptoexplosion, or diapiric movements? Kansas Academy of Science Transactions, v. 67, p. 343–356.

Bucher, W.H. (1963). Cryptoexplosion structures caused from without or from within the earth? (“astroblemes” or “geoblemes?”): American Journal of Science, v. 261, p. 597–649.

Bucher, W.H. (1965). The largest so-called meteorite scars in three continents as demonstrably tied to major terrestrial structures: New York Academy of Sciences Annals, v. 123, p. 897–903.

Dietz, R.S. (1963). Cryptoexplosion structures: A discussion: American Journal of Science, v. 262, p. 650–654.

Hörz, F., H. (1968). Statistical measurements of deformation structures and refractive indices in experimentally shock loaded quartz, in French, B.M. and Short, N.M. eds., Shock Metamorphism of Natural Materials, Mono Book Corp, Baltimore, MD, p. 243–253.

French, B.M. (1998). Traces of Catastrophe: A handbook of shock metamorfic effects in terrestial meteorite impact structure: Lunar and Planetary Institute, NASA, p. 120.

French, B.M., and Koeberl, C. (2010) The convincing identification of terrestrial meteorite impact structures: What works, what doesn't, and why: Earth-Science Reviews, v. 98, p. 123–170, doi: 10.1016/j.earscirev.2009.10.009.

Glikson, A. (2005). Asteroid/comet impact clusters, flood basalts and mass extinctions: Significance of isotopic age overlaps: Earth and Planetary Science Letters, v. 236, p. 933–937, doi: 10.1016/j.epsl.2005.05.007.

Kiilsgaard, T.H., Heyl, A.V., and Brock, M.R. (1962). The Crooked Creek disturbance, southeast Missouri: U.S. Geological Survey Professional Paper, v. 450 E, p. 75–89.

L.O., N., and Ferguson, J. (1990). Cryptoexplosion structures, shock deformation and siderophile concentration related to explosive venting of fluids associated with alkaline ultramafic magmas: Tectonophysics, v. 171, p. 303–335.

Luczaj, J. (1998). Argument supporting explosive igneous activity for the origin of "cryptoexplosion" structures in the midcontinent, United States: Geology, v. 26, p. 295–298, doi: 10.1130/0091-7613(1999)027<0279:ASEIAF>2.3.CO;2.

McCall, G.J.H. (1964). Are cryptovolcanic structures due to meteoric impact? Nature, v. 201, p. 251–254.

Paillou, P., Elbarkooky, a, Barakat, a, Malezieux, J., Reynard, B., Dejax, J., and Heggy, E. (2004). Discovery of the largest impact crater field on Earth in the Gilf Kebir region, Egypt: Comptes Rendus Geosciences, v. 336, p. 1491–1500, doi: 10.1016/j.crte.2004.09.010.

Paillou, P., Reynard, B., Malézieux, J.M., Dejax, J., Heggy, E., Rochette, P., Reimold, W.U., Michel, P., Baratoux, D., Razin, P., and Colin, J.P. (2006), An extended field of crater-shaped structures in the Gilf Kebir region, Egypt: Observations and hypotheses about their origin: Journal of African Earth Sciences, v. 46, p. 281–299, doi: 10.1016/j.jafrearsci.2006.05.006.

Phipps Morgan, J., Reston, T.J., and Ranero, C.R. (2004). Contemporanious mass extinctions flood basalts and "impact signals": are mantle plume-induced lithospheric gas explosions the causal link? Earth and Planetary Science Letters, v. 217, p. 263–284.

Prezzi, C.B., Orgeira, M.J., Acevedo, R.D., Ponce, J.F., Martinez, O., Rabassa, J.O., Corbella, H., Vásquez, C., González-Guillot, M., and Subías, I. (2012). Geophysical characterization of two circular structures at Bajada del Diablo (Patagonia, Argentina): Indication of impact origin: Physics of the Earth and Planetary Interiors, v. 192–193, p. 21–34, doi: 10.1016/j.pepi.2011.12.004.

Rampino, M.R., and Volk, T. (1996). Multiple impact event in the Paleozoic; collision with a string of comets or asteroids? Geophysical Research Letters, v. 23, p. 49–52.

Reimold, W.U., and Koeberl, C. (2014). Reply to “Comment on impact structures in Africa: A review (Short Note)” by Acevedo, R.D. et al.: Journal of African Earth Sciences, v. 100, p. 757–758, doi: 10.1016/j.jafrearsci.2014.08.012.

Reimold, W.U. (2007). The Impact Crater Bandwagon (Some problems with the terrestrial impact cratering record): Meteoritics & Planetary Science, v. 42, p. 1467–1472, doi: 10.1111/j.1945-5100.2007.tb00585.x.

Reimold, W.U., and Koeberl, C. (2014). Impact structures in Africa: A review: Journal of African Earth Sciences, v. 93, p. 57–175, doi: 10.1016/j.jafrearsci.2014.01.008.

Russell, J.K., Porritt, L. a., Lavallée, Y., and Dingwell, D.B. (2012). Kimberlite ascent by assimilation-fuelled buoyancy: Nature, v. 481, p. 352–356, doi: 10.1038/nature10740.

Sharpton, V.L., and Grieve, R.A.F. (1990). Meteorite impact, cryptoexplosion, and shock metamorphism; A perspective on the evidence at the K/T boundary, in Sharpton, V. and Ward, P. eds., Global Catastrophes in Earth history; an interdisciplineray conference on impacts ,vocanism and mass mortality: Geological Society of America Special Paper 247, p. 301–318.

Shavers, E.J., Ghulam, A., Encarnacion, J., Bridges, D.L., and Luetkemeyer, P.B. (2016). Carbonatite associated with ultramafic diatremes in the Avon Volcanic District, Missouri, USA: Field, petrographic, and geochemical constraints: Lithos, v. 248–251, p. 506–516, doi: 10.1016/j.lithos.2016.02.005.

Snyder, F.G., and Gerdemann, P.E. (1965). Explosive igneous activity along an Illinois-Missouri-Kansas axis: American Journal of Science, v. 263, p. 465–493.

Stöffler, D., (1972). Deformation and transformation of rock-forming minerals by natural and experimental shock processes: I. Behavior of minerals under shock compression: Fortschritte Mineralogie, v. 49, p. 50–113.

Appendix C.

Chapter 5. 1.38 Ga magmatism on northwestern Laurentia: supplementary data

Whole rock major, minor and trace element geochemistry

Whole rock major, minor, and trace element geochemistry is reported in Table C-1. Analytical uncertainties were assessed graphically following Nielsen (2011) and are reported in Table C2.

Table C.1. Whole rock major and trace elements of the Hart River sills. Locations as in Table 5.1.

		Sample (all sample codes preceded by 'JV13-')																			
Analyte	Unit	2-5i	2-5k	2-5q	2-5m	3-9a	6-25	4-13	13-35	12-37	12-39	15-49	19-62	16-50	16-52A	20-64	18-57A	GA4-2[5]	GA4-3[5]	GA6-3[5]	GA6-5[5]
SiO_2[1]	%	49.7	48.7	49.9	46.6	49.9	50.2	50.5	49.1	50.6	47.5	49.1	49.5	50	44.4	51	48.36	48.4	48.9	50.48	48.96
$Al2O_3$[1]	%	11.4	11.5	13.9	11.4	13.1	14.7	14.1	14.3	13.8	18.4	15.3	13.5	14.2	12.06	10	13.62	14.1	14.7	14.6	13.8
Fe_2O_3[1]	%	17.3	17.6	12.14	18.7	12	12.2	11.7	10.5	11	7.81	12.8	15.1	13.1	20.52	18	14.56	8.49	7.67	13.56	12.65
MnO[1]	%	0.26	0.24	0.211	0.24	0.19	0.18	0.21	0.26	0.22	0.15	0.25	0.21	0.28	0.347	0.3	0.215	0.17	0.15	0.22	0.19
MgO[1]	%	5.36	5.37	7.04	6.8	9.86	7.88	7.55	8.73	8.22	6.64	5.76	5.66	7.52	4.79	2.2	6.16	9.14	9.14	5.98	6.9
CaO[1]	%	7.7	8.09	8.01	6.94	8.15	8.46	8.55	11	9.13	10.6	8.72	9.32	5.22	9.44	9.1	9.38	10.6	12.8	8.34	9.57
Na_2O[1]	%	2.1	2.45	2.82	2.49	1.81	2.47	3.11	2.4	2.73	2.69	2.92	2.01	3.19	1.8	3.4	1.78	1.81	1.51	2.93	1.71
K2O[1]	%	1.65	1.08	1.82	1.1	1.81	0.86	1.68	1.29	0.69	1.5	1.6	2.01	1.8	0.87	0.6	2.79	2.05	2.07	1.46	1.56
TiO_2[1]	%	1.69	1.65	1.002	1.93	1.23	1.1	0.94	0.86	0.66	0.53	1.09	1.12	1.15	2.997	3	1.4	0.541	0.432	1.01	0.93
P_2O_5[1]	%	0.12	0.11	0.06	0.09	0.06	0.08	0.07	0.06	0.05	0.03	0.08	0.09	0.06	0.08	0.3	0.1	0.05	0.04	0.09	0.07
LOI[1]	%	2.27	2.05	2.32	2.3	2.67	2.73	2.32	2.41	2.3	3.39	2.06	1.51	2.49	1.57	0.4	1.7	3.25	2.8	2.13	1.9
Total[1]	%	99.5	98.8	99.24	98.7	101	101	101	101	99.4	99.3	99.6	100	99	98.88	99	100.1	99.8	100.3	100.77	98.63
Au[2]	ppb	6	<1	<1	<1	<1	<1	<1	<1	<1	<1	<1	<1	<1	<1	<1	<1				
Ag[2/3]	ppm	<0.5	<0.5	<0.5	<0.5	<0.5	<0.5	<0.5	<0.5	<0.5	<0.5	<0.5	<0.5	0.8	<0.5	<0.5	<0.5	0.55	0.27	0	0.7
As[2]	ppm	5	6	5	<1	13	7	4	7	10	6	5	4	6	<1	13	10				
Ba[1]	ppm	377	240	1566	281	711	157	316	161	77	249	597	166	975	413	82	390	483.09	483.7	253.73	135.17
Be[1]	ppm	<1	<1	<1	<1	<1	<1	<1	<1	<1	<1	<1	<1	1	<1	1	<1				
Bi[4]	ppm	<0.1	<0.1	<0.1	<0.1	<0.1	<0.1	<0.1	<0.1	<0.1	<0.1	<0.1	<0.1	<0.1	<0.1	<0.1	<0.1	0.02	0.02	0.02	
Br[2]	ppm	<0.5	<0.5	<0.5	<0.5	<0.5	<0.5	<0.5	<0.5	<0.5	<0.5	<0.5	<0.5	<0.5	<0.5	<0.5	<0.5				
Cd[3]	ppm	<0.5	<0.5	<0.5	<0.5	0.7	<0.5	<0.5	<0.5	<0.5	2.3	1.2	<0.5	5.3	<0.5	<0.5	<0.5				
Co[2]	ppm	54	54.4	45.4	63.6	48.3	47.5	45.9	42.6	44.9	35.3	42.3	49.1	42.7	61.6	29	50.5	41.53	40.23	49	48.6
Cr[2]	ppm	<0.5	<0.5	18.7	14.9	255	162	222	228	27.2	176	95	74.9	185	<0.5	<0.5	110	1411	1131	20	200
Cs[4]	ppm	2	2.5	0.7	1.9	0.5	0.8	3.4	1.1	1.1	2.3	0.8	1	0.5	1.5	0.3	2.2	3.67	1.29	2.44	2.61
Cu[3]	ppm	400	433	144	143	224	168	138	123	75	107	147	169	59	392	18	195	79.15	55.38	157	124

		Sample (all sample codes preceded by 'JV13-')																			
Analyte	**Unit**	**2-5i**	**2-5k**	**2-5q**	**2-5m**	**3-9a**	**6-25**	**4-13**	**13-35**	**12-37**	**12-39**	**15-49**	**19-62**	**16-50**	**16-52A**	**20-64**	**18-57A**	**GA4-2[5]**	**GA4-3[5]**	**GA6-3[5]**	**GA6-5[5]**
Ga[4]	ppm	18	18	16	18	14	16	13	13	14	15	18	17	16	20	21	18				
Ge[4]	ppm	1.9	1.8	1.7	1.9	1.8	1.6	1.5	1.8	1.6	1.2	1.8	1.6	1.8	2.2	2.1	1.7				
Hf[4]	ppm	1.7	1.6	1.2	1.4	1.9	1.3	1	0.7	0.8	0.5	1.2	1.5	1.2	1.4	3.5	1.6	0.67	0.61	1.48	1.66
Hg[2]	ppm	<1	<1	<1	<1	<1	<1	<1	<1	<1	<1	<1	<1	<1	<1	<1	<1				
In[4]	ppm	<0.1	<0.1	<0.1	<0.1	<0.1	<0.1	<0.1	<0.1	<0.1	<0.1	<0.1	<0.1	<0.1	<0.1	<0.1	<0.1				
Ir[2]	ppb	<1	<1	<1	<1	<1	<1	<1	<1	<1	<1	<1	<1	<1	<1	<1	<1				
Mo[4]	ppm	<2	<2	<2	<2	<2	<2	<2	<2	<2	<2	<2	<2	<2	<2	<2	<2	0.03	0.07	3.41	1.02
Nb[4]	ppm	4.1	3.7	2.5	2.6	5.6	2.3	1.7	1.3	1.1	0.6	2.2	2.2	1.7	2.9	9.7	2.8	1.42	1.38	2.97	3.22
Ni[3]	ppm	40	44	45	67	104	81	109	106	68	91	58	54	87	46	5	79	151.6	141.66	59	97
Pb[3]	ppm	<5	<5	<5	<5	8	<5	<5	16	<5	25	247	<5	962	9	7	<5	0.66	3.83	0	0
Rb[4]	ppm	36	33	37	36	34	19	43	31	21	38	54	44	44	32	8	82	68.08	53.05	41.38	45.77
S[3]	%	0.16	0.09	0.036	0.11	0.36	0.04	0.08	0.05	0.04	0.05	0.04	0.05	0.08	0.057	0	0.068				
Sb[2]	ppm	8.6	11	5	3.9	11.7	15.4	5.6	17.7	10.8	11.7	11.1	9.7	5.7	6.5	8.9	10.2	0.2	0.56	2.51	0.25
Sc[2]	ppm	48.6	48.7	43	50.2	43.6	51.1	44.8	50	50.9	37.2	38.3	47	46.8	56.1	45	44.3	45.25	44.83	42.9	
Se[2]	ppm	<0.5	<0.5	<0.5	<0.5	<0.5	<0.5	<0.5	<0.5	<0.5	<0.5	<0.5	<0.5	<0.5	<0.5	<0.5	<0.5				
Sn[4]	ppm	<1	<1	<1	<1	<1	<1	<1	<1	<1	<1	<1	1	<1	1	<1	<1	0.25	0.62	1.5	1.9
Sr[1]	ppm	159	123	165	125	112	98	198	133	131	183	203	223	134	215	102	134	152.98	142.59	138.34	127.17
Ta[4]	ppm	0.34	0.3	0.29	0.2	0.34	0.19	0.13	2.54	0.12	0.21	0.2	0.26	0.17	0.27	0.8	0.27	0.14	0.15	0.192	0.18
Th[4]	ppm	0.93	0.76	0.61	0.64	0.43	0.52	0.41	0.33	0.36	0.21	0.46	0.61	0.32	1.1	2	0.48	0.24	0.29	2,143	0.5
U[4]	ppm	0.29	0.25	0.19	0.22	0.29	0.17	0.12	0.1	0.11	0.07	0.17	0.22	0.13	0.28	0.6	0.16	0.07	1.16	0.147	0.14
V[1]	ppm	592	637	318	1012	406	391	341	312	284	227	331	384	373	1118	82	407	2328	201	368	284
W[2]	ppm	<1	<1	<1	<1	<1	<1	<1	<1	<1	<1	<1	<1	<1	<1	<1	<1				
Y[1]	ppm	25	22	16	18	21	21	17	13	13	9	16	23	16	19	50	20	10.17	8.58	21.3	19.4
Zn[2/3]	ppm	123	88	63	104	169	75	58	80	82	195	261	100	728	89	71	82	60.72	51.32	78	95
Zr[1]	ppm	81	71	59	64	91	62	49	38	40	26	58	72	54	64	162	78	20.92	20.69	55.92	58.8

		Sample (all sample codes preceded by 'JV13-')																			
Analyte	Unit	2-5i	2-5k	2-5q	2-5m	3-9a	6-25	4-13	13-35	12-37	12-39	15-49	19-62	16-50	16-52A	20-64	18-57A	GA4-2[5]	GA4-3[5]	GA6-3[5]	GA6-5[5]
La[4]	ppm	5.36	4.58	3.44	3.44	5.7	2.4	2.15	1.58	2.27	1.54	3.31	4.12	3.46	5.41	6.5	3.93	1.59	1.59	3.79	3.49
Ce[4]	ppm	13.6	11.7	8.64	9.1	10	6.94	5.53	4.5	5.78	4.09	8.82	10.9	8.56	12.6	20	10.9	4.37	4.02	9.92	9.14
Pr[4]	ppm	2.02	1.77	1.34	1.4	1.43	1.12	0.99	0.7	0.91	0.63	1.38	1.63	1.29	1.75	3.4	1.67	0.7	0.6	1,358	1.19
Nd[4]	ppm	10.2	8.95	6.62	7.11	6.94	5.87	5.19	3.67	4.63	3.35	6.64	8.37	6.45	8.4	18	8.83	3.67	3.02	6.98	6.81
Sm[4]	ppm	3.08	2.72	2.11	2.32	2.54	2.01	1.81	1.28	1.53	1.05	2.12	2.77	2.1	2.53	5.7	2.76	1.24	1.05	2.34	2.1
Eu[4]	ppm	1.2	1.07	0.754	0.77	0.67	0.68	0.67	0.5	0.58	0.5	0.88	1.01	0.87	1.04	1.6	1.05	0.4	0.45	0.893	0.75
Gd[4]	ppm	4.22	3.85	2.86	3.14	3.34	3.18	2.66	1.9	2.16	1.52	2.89	3.74	2.81	3.35	7.9	3.71	1.66	1.54	3.33	3.19
Tb[4]	ppm	0.77	0.72	0.56	0.59	0.65	0.61	0.52	0.36	0.39	0.3	0.57	0.74	0.56	0.64	1.5	0.72	0.28	0.22	0.62	0.57
Dy[4]	ppm	4.89	4.54	3.59	3.79	4.33	3.84	3.27	2.31	2.51	1.91	3.56	4.57	3.54	3.98	9.5	4.4	1.98	1.73	3.39	3.46
Ho[4]	ppm	1.01	0.94	0.71	0.8	0.91	0.81	0.68	0.51	0.54	0.38	0.72	0.96	0.72	0.87	2	0.9	0.42	0.35	0.76	0.76
Er[4]	ppm	2.99	2.73	2.09	2.38	2.66	2.46	2.05	1.47	1.52	1.05	2.08	2.88	2.07	2.48	5.8	2.65	1.2	1.03	2.33	2.28
Tl[4]	ppm	0.27	0.24	0.29	0.28	0.23	0.32	0.6	0.27	0.19	0.39	0.33	0.22	0.26	0.21	0.1	0.38				
Tm[4]	ppm	0.43	0.41	0.322	0.36	0.39	0.37	0.32	0.22	0.23	0.16	0.32	0.44	0.35	0.37	0.9	0.385	0.18	0.14	0.373	0.34
Yb[4]	ppm	2.77	2.59	2.13	2.24	2.54	2.46	2.07	1.49	1.5	1.08	2.06	2.71	2.09	2.35	5.9	2.37	1.16	0.99	2.25	2.29
Lu[4]	ppm	0.41	0.39	0.317	0.33	0.39	0.35	0.3	0.21	0.22	0.16	0.31	0.4	0.29	0.338	0.9	0.343	0.18	0.14	0.339	0.31
Mass[2]	g	1.43	1.42	1.315	1.37	1.29	1.48	1.56	1.39	1.37	1.27	1.47	1.35	1.37	1.51	1.6	1.293				

Analysed via [1]: Inductively coupled plasma mass spectrometry on diluted fused lithium meta-/tetraborate sample (using a Varian Vista ICP), [2]: Instrumental neutron activation analysis, [3]: Inductively coupled plasma mass spectrometry on (near) total digested sample, [4]: Inductively coupled plasma mass spectrometry on diluted fused lithium meta-/tetraborate sample (using a Permer Elkin Sciex ICP/MS). [5]See table 5-1 for original sample numbers and Abbott (1997) for methods.

Table C.2. Analytical uncertainties of whole rock major and trace element geochemistry

Analyte (%)	SiO_2[1]	$Al2O_3$[1]	Fe_2O_3[1]	MnO[1]	MgO[1]	CaO[1]	Na_2O[1]	K2O[1]	TiO_2[1]	P_2O_5[1]	LOI[1]	S[3]	Total
Detection Limit	0.01	0.01	0.01	0.001	0.01	0.01	0.01	0.01	0.001	0.01		0.001	0.01
Absolute error	0.3	0.2	0.25	0.04	0.1	0.5	0.15	0.3	0.4	0		0.1	
Relative error (%)	1.5	1	1	6	1	1	2	11	12	1		1	

Analyte (ppm)	Au[2]	Ag[2/3]	As[2]	Ba[1]	Be[1]	Bi[4]	Br[2]	Cd[3]	Co[2]	Cr[2]	Cs[4]	Cu[3]	Ga[4]
Detection Limit	0.001	0.5	1	1	1	0.1	0.5	0.5	0.1	0.5	0.1	1	1
Absolute error	n/a	n/a	2	2	1	1.5	n/a	0.5	1	3	0.3	2	1
Relative error (%)	n/a	n/a	5	4	2	1	n/a	1	4	10	3	4	1

Analyte (ppm)	Ge[4]	Hf[4]	Hg[2]	In[4]	Ir[2]	Mo[4]	Nb[4]	Ni[3]	Pb[3]	Rb[4]	Sb[2]	Sc[2]	Se[2]
Detection Limit	0.5	0.1	1	0.1	0.001	2	0.2	1	5	1	0.1	0.01	0.5
Absolute error	0.7	0.7	n/a	n/a	n/a	0.3	0.8	2	7	2	0.3	0.3	n/a
Relative error (%)	1	5	n/a	n/a	n/a	2.5	11	10	2	3	2	2	n/a

Analyte (ppm)	Sn[4]	Sr[1]	Ta[4]	Th[4]	U[4]	V[1]	W[2]	Y[1]	Zn[2/3]	Zr[1]	La[4]	Ce[4]	Pr[4]
Detection Limit	1	2	0.01	0.05	0.01	5	1	1	1	1	0.05	0.05	0.01
Absolute error	1	2	0.3	1	0.5	1	n/a	3	5	2	2	3	0.2
Relative error (%)	0.5	2.5	2	7.5	3	5	n/a	7	9	7	11	11	8

Analyte (ppm)	Nd[4]	Sm[4]	Eu[4]	Gd[4]	Tb[4]	Dy[4]	Ho[4]	Er[4]	Tl[4]	Tm[4]	Yb[4]	Lu[4]
Detection Limit	0.05	0.01	0.005	0.01	0.01	0.01	0.01	0.01	0.05	0.005	0.01	0.002
Absolute error	1.5	0.4	0.5	0.5	0.3	0.8	0.2	0.5	0.5	0.5	0.2	0.3
Relative error (%)	4	6	1	16	7	4	5	5	8	1	4	1

Analysed via [1]: Inductively coupled plasma mass spectrometry on diluted fused lithium meta-/tetraborate sample (using a Varian Vista ICP), [2]: Instrumental neutron activation analysis, [3]: Inductively coupled plasma mass spectrometry on (near) total digested sample, [4]: Inductively coupled plasma mass spectrometry on diluted fused lithium meta-/tetraborate sample (using a Permer Elkin Sciex ICP/MS). Absolute and relative errors were assessed graphically using measurements of duplicates and standards error envelopes. N/a indicates a lack of data points to envelop.

Laser ablation inductively coupled mass spectrometry: methods

Zircon grains were separated from rocks using standard techniques and annealed at 900 °C for 60 hours in a muffle furnace. They were mounted in epoxy and polished until their centers were exposed. Cathodoluminescence (CL) images were obtained with a

JEOL JSM-1300 scanning electron microscope and Gatan MiniCL. Zircon was analyzed by laser ablation inductively coupled plasma mass spectrometry (LA-ICPMS) using a ThermoElectron X-Series II quadrupole ICPMS and New Wave Research UP-213 Nd:YAG UV (213 nm) laser ablation system. In-house analytical protocols, standard materials, and data reduction software were used for acquisition and calibration of U-Pb dates and a suite of high field strength elements (HFSE) and rare earth elements (REE). Zircon was ablated with a laser spot of 25 µm wide using fluence and pulse rates of 5 J/cm^2 and 10 Hz, respectively, during a 45 second analysis (15 sec gas blank, 30 sec ablation) that excavated a pit ~25 µm deep. Ablated material was carried by a 1.2 L/min He gas stream to the nebulizer flow of the plasma. Dwell times were 5 ms for Si and Zr, 200 ms for ^{49}Ti and ^{207}Pb, 80 ms for ^{206}Pb, 40 ms for ^{202}Hg, ^{204}Pb, ^{208}Pb, ^{232}Th, and ^{238}U and 10 ms for all other HFSE and REE. Background count rates for each analyte were obtained prior to each spot analysis and subtracted from the raw count rate for each analyte. Ablation pits that appear to have intersected glass or mineral inclusions were identified based on titanium and phosphorus. U-Pb dates from these analyses are considered valid if the U-Pb ratios appear to have been unaffected by the inclusions. Analyses that appear contaminated by common lead were rejected. For concentration calculations, background-subtracted count rates for each analyte were internally normalized to ^{29}Si and calibrated with respect to NIST SRM-610 and -612 glasses as the primary standards. Temperature was calculated from the Titanium in zircon thermometer (Watson et al., 2006). Because there are no constraints on the activity of TiO_2, an average value in crustal rocks of 0.8 was used.

Data were collected in December 2014. For U-Pb and ^{207}Pb/^{206}Pb dates, instrumental fractionation of the background-subtracted ratios was corrected and dates were calibrated with respect to interspersed measurements of zircon standards and reference materials. The primary standard Plešovice zircon (Sláma et al., 2008) was used to monitor time-dependent instrumental fractionation based on two analyses for every 10 analyses of unknown zircon.

Radiogenic isotope ratio and age error propagation for all analyses includes uncertainty contributions from counting statistics and background subtraction. For groups of analyses that are collectively interpreted from a weighted mean date (i.e., igneous

zircon analyses), a weighted mean date is first calculated using Isoplot 3.0 (Ludwig, 2003) using errors on individual dates that do not include a standard calibration uncertainty, and then a standard calibration uncertainty is propagated into the error on the weighted mean date. This uncertainty is the local standard deviation of the polynomial fit to the interspersed primary standard measurements versus time for the time-dependent, relatively larger U/Pb fractionation factor, and the standard error of the mean of the consistently time-invariant and smaller $^{207}Pb/^{206}Pb$ fractionation factor. These uncertainties are 1.4% (2σ) for $^{206}Pb/^{238}U$ and 0.8% (2σ) for $^{207}Pb/^{206}Pb$. Age interpretations are based on $^{207}Pb/^{206}Pb$ dates. Errors on the weighted mean dates are given at 2σ for samples with probability of fit >0.05. For samples with probability of fit <0.05, errors on the weighted mean dates are given at 95% confidence, which is the internal error multiplied by the square root of the MSWD.

A zircon secondary reference material was treated as an unknown to assess accuracy, interspersed as groups of two analyses for every 20 unknown analyses. Weighted mean dates are calculated using Isoplot 3.0 (Ludwig, 2003) from errors on individual dates that do not include the standard calibration uncertainties. However, errors on weighted mean dates include the standard calibration uncertainties within each experiment and are given at 2σ. FC1 zircon (1098 Ma from unpublished chemical abrasion thermal ionization mass spectrometry (CA-TIMS) data, Boise State University) yielded a weighted mean $^{207}Pb/^{206}Pb$ date of 1087 ± 18 Ma (MSWD=1.5, probability of fit=0.13, n=12) and a $^{206}Pb/^{238}U$ date of 1093 ± 17 Ma (MSWD=1.1, probability of fit=0. 37, n=13). These results indicate that accurate dates were obtained.

LA-ICPMS geochronology and zircon geochemistry results

LA-ICPMS geochronology are reported in Table C-3 and in Figure C1. Twenty-one analyses from JV13-39c yielded a weighted mean date of 1368 ± 16 Ma (MSWD = 1.5, probability of fit = 0.13). Forty-eight analyses from JV13-53 yielded a weighted mean date of 1386 ± 15 Ma (MSWD=1.7, probability of fit = 0.003). Thirty-two analyses from JV13-61 yielded a weighted mean date of 1384 ± 16 Ma (MSWD = 1.5, probability of fit=0.03).

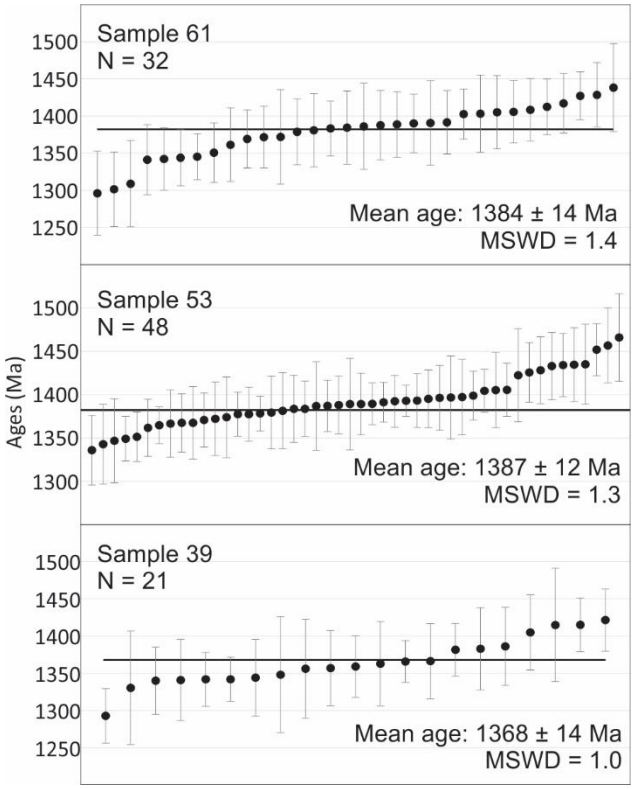

Figure C.1. LA-ICPMS U-Pb age determinations of three Hart River sill samples.

Table C.3. Laser ablation inductively coupled plasma mass spectrometry U-Pb age determinations on zircon of three Hart River sill sample (locations as in Table 5.1)

analysis	U ppm	Th ppm	Pb* ppm	Th / U	^{206}Pb / ^{204}Pb	$^{206}Pb^*$ / $^{207}Pb^*$	±2σ %	$^{207}Pb^*$ / ^{235}U	±2σ %	$^{206}Pb^*$ / ^{238}U	±2σ %	error corr.	Age $^{206}Pb^*$ / $^{207}Pb^*$	± Ma	Disc. %
Sample JV13-39C															
L141	100	73	31	0.73	1099.5	11.134	2.2	2.91	4.8	0.235	4.2	0.89	1422	42	4
L134	136	88	41	0.65	3690.5	11.171	1.9	2.87	4.5	0.233	4.1	0.91	1415	36	5
S198	259	204	82	0.79	5921.3	11.173	4.0	2.94	8.4	0.239	7.4	0.88	1415	76	3
L135	214	89	62	0.42	3871.3	11.231	2.6	2.92	4.3	0.238	3.3	0.78	1405	51	2
S211	186	175	57	0.94	1808.0	11.342	2.7	2.77	5.2	0.228	4.4	0.85	1386	53	5
L133	169	60	49	0.36	5293.8	11.361	2.9	2.90	5.4	0.239	4.5	0.84	1383	55	0
L140	318	167	95	0.53	10271.6	11.370	1.9	2.91	5.4	0.240	5.0	0.94	1381	36	0
L137	159	105	48	0.66	2889.3	11.460	2.6	2.79	4.5	0.232	3.6	0.81	1366	51	2
S202	491	653	160	1.33	3625.8	11.463	1.5	2.76	4.5	0.229	4.3	0.95	1366	28	3
L136	158	111	48	0.70	5389.3	11.481	3.0	2.79	5.5	0.233	4.7	0.85	1363	57	1
S213	273	246	88	0.90	3935.7	11.504	2.2	2.85	5.6	0.238	5.2	0.92	1359	42	-1
S210	232	403	82	1.74	8000.7	11.516	2.6	2.76	3.2	0.231	1.8	0.57	1357	51	1
S214	162	84	47	0.52	12886.1	11.520	3.5	2.82	6.1	0.236	5.0	0.82	1356	67	-1
S217	149	124	46	0.83	11089.4	11.569	4.0	2.77	7.2	0.232	6.0	0.83	1348	78	0
S195	196	180	61	0.92	8224.9	11.594	2.7	2.72	5.0	0.228	4.2	0.84	1344	52	1
S215	303	229	95	0.75	4270.8	11.606	1.5	2.83	3.3	0.238	2.9	0.89	1342	30	-3
S209	287	277	90	0.97	1217.8	11.607	1.9	2.81	3.2	0.236	2.5	0.80	1342	36	-2
S196	194	181	63	0.93	1369.3	11.612	2.8	2.81	7.3	0.237	6.8	0.92	1341	55	-2
S201	135	126	42	0.93	1430.0	11.617	2.4	2.84	4.4	0.239	3.7	0.85	1340	45	-3
S199	131	84	37	0.64	3809.6	11.675	4.0	2.61	6.5	0.221	5.2	0.80	1330	77	3
S219	367	416	126	1.13	3959.0	11.905	1.9	2.77	5.6	0.239	5.3	0.94	1293	37	-7
Sample JV13-53															
L109	178	101	53	0.57	4342.9	10.878	2.7	2.94	6.4	0.232	5.8	0.91	1466	51	8
L97	488	376	154	0.77	10567.4	10.931	2.3	2.96	6.4	0.235	6.0	0.94	1457	43	7
L95	969	999	336	1.03	1625163.3	10.959	1.6	3.05	7.3	0.242	7.1	0.98	1452	30	4
L113	449	365	142	0.81	4805.6	11.055	2.4	2.90	5.2	0.232	4.6	0.88	1435	46	6
L99	225	137	68	0.61	3496.6	11.059	2.2	2.94	4.4	0.236	3.8	0.86	1435	43	5
L108	455	367	146	0.81	5569.7	11.061	1.9	2.96	4.6	0.238	4.2	0.91	1434	37	4
L111	378	216	116	0.57	2214.0	11.068	2.0	2.97	5.7	0.239	5.4	0.94	1433	39	4
S171	191	150	55	0.79	13943.3	11.096	2.0	2.84	4.0	0.228	3.4	0.86	1428	39	7
L100	542	440	177	0.81	323595.3	11.111	1.8	3.01	4.2	0.242	3.7	0.90	1426	34	2
L96	236	130	72	0.55	3218.2	11.129	2.8	2.97	5.1	0.240	4.2	0.83	1422	54	3
S154	333	338	103	1.02	3216.0	11.228	1.6	2.86	3.6	0.233	3.2	0.89	1406	31	4
L106	564	423	180	0.75	27592.9	11.230	2.3	2.94	5.0	0.239	4.5	0.89	1405	43	2
S174	730	713	219	0.98	5745.1	11.235	1.3	2.74	4.1	0.223	3.9	0.95	1404	25	7

analysis	U ppm	Th ppm	Pb* ppm	Th/U	$^{206}Pb/^{204}Pb$	$^{206}Pb^*/^{207}Pb^*$	±2σ %	$^{207}Pb^*/^{235}U$	±2σ %	$^{206}Pb^*/^{238}U$	±2σ %	error corr.	Age $^{206}Pb^*/^{207}Pb^*$	± Ma	Disc. %
Sample JV13-53 (continued															
L107	523	423	174	0.81	14613.1	11.267	1.5	3.02	4.4	0.247	4.2	0.94	1399	28	-2
L103	303	207	92	0.68	2633.4	11.277	2.3	2.87	3.7	0.235	2.9	0.79	1397	44	3
L101	533	441	162	0.83	5646.4	11.279	2.5	2.78	5.5	0.228	4.9	0.89	1397	48	5
S173	601	626	187	1.04	2728.7	11.282	2.0	2.81	3.2	0.230	2.6	0.80	1396	37	4
S169	522	630	169	1.21	4021.4	11.289	1.7	2.88	4.5	0.236	4.1	0.92	1395	33	2
S145	533	579	167	1.09	42636.6	11.301	1.6	2.79	3.4	0.229	3.0	0.88	1393	31	5
S149	538	615	168	1.14	1730.7	11.302	0.9	2.83	2.7	0.232	2.6	0.94	1393	18	3
L110	664	565	209	0.85	6544.7	11.306	1.6	2.80	6.0	0.229	5.8	0.97	1392	30	4
S157	587	674	186	1.15	8862.6	11.311	1.2	2.84	3.4	0.233	3.2	0.94	1391	23	3
S158	542	653	169	1.21	2569.8	11.322	1.3	2.79	3.6	0.229	3.4	0.94	1390	24	4
S150	343	346	109	1.01	2244.7	11.324	1.8	2.95	3.8	0.242	3.4	0.88	1389	35	-1
L104	402	242	122	0.60	11413.4	11.325	2.8	2.90	4.3	0.238	3.3	0.77	1389	53	1
S165	91	40	25	0.45	678.6	11.329	3.9	2.85	5.9	0.234	4.5	0.76	1388	74	2
S155	799	1217	270	1.52	7839.8	11.331	1.7	2.86	3.7	0.235	3.2	0.88	1388	33	2
S162	390	333	114	0.85	13210.1	11.337	1.5	2.71	5.1	0.223	4.9	0.95	1387	30	6
S142	278	198	82	0.71	1190.7	11.337	2.7	2.77	4.7	0.228	3.9	0.83	1387	51	5
S15`	231	186	69	0.80	1362.5	11.356	1.7	2.83	3.5	0.233	3.0	0.88	1384	32	2
S164	308	263	91	0.85	4710.1	11.357	2.0	2.77	4.3	0.229	3.8	0.89	1384	39	4
L105	353	270	109	0.76	15645.9	11.370	2.3	2.81	4.3	0.232	3.6	0.85	1381	44	3
L102	300	213	92	0.71	3100.3	11.383	2.2	2.84	4.9	0.235	4.4	0.89	1379	42	2
S148	1058	1292	342	1.22	32861.0	11.389	1.0	2.86	3.1	0.237	2.9	0.94	1378	20	1
S175	750	806	232	1.07	9053.2	11.393	1.6	2.69	5.7	0.222	5.5	0.96	1377	31	6
S144	1684	2655	561	1.58	15520.5	11.393	1.3	2.70	5.0	0.223	4.8	0.96	1377	25	6
S160	202	155	60	0.76	3063.5	11.415	2.4	2.80	4.7	0.232	4.0	0.86	1374	47	2
S143	1229	1473	409	1.20	9836.9	11.425	2.2	2.85	4.3	0.236	3.7	0.86	1372	43	0
S163	484	489	148	1.01	7811.1	11.434	1.6	2.76	5.4	0.228	5.1	0.95	1371	31	3
S152	391	409	124	1.05	5443.8	11.452	2.2	2.89	4.7	0.240	4.2	0.89	1368	42	-2
S172	595	1407	231	2.36	11146.6	11.453	1.7	2.84	3.8	0.236	3.3	0.89	1367	34	0
L98	343	255	111	0.74	11533.9	11.457	2.0	2.95	5.1	0.245	4.7	0.92	1367	39	-3
S156	375	363	119	0.97	14616.0	11.469	1.1	2.91	3.5	0.242	3.4	0.95	1365	21	-2
S153	765	808	241	1.06	20714.5	11.487	1.7	2.86	5.3	0.238	5.0	0.95	1362	33	-1
S170	731	1385	261	1.89	6584.1	11.549	1.5	2.79	4.6	0.234	4.4	0.95	1351	29	0
S159	750	797	233	1.06	284033.1	11.563	1.3	2.78	3.1	0.233	2.8	0.90	1349	26	0
L112	211	99	63	0.47	3571.6	11.576	2.5	2.87	5.1	0.241	4.5	0.87	1347	49	-3
L114	409	293	127	0.72	6448.7	11.601	2.4	2.77	4.4	0.233	3.7	0.84	1343	46	-1
S168	321	304	98	0.95	1815.4	11.642	2.1	2.78	4.1	0.235	3.5	0.86	1336	40	-2
Sample JV13-61															
L121	217	140	67	0.64	28538.6	11.037	3.1	2.95	5.0	0.236	3.9	0.78	1438	59	5
L117	544	625	183	1.15	8320.3	11.093	2.3	2.84	5.1	0.228	4.5	0.89	1429	43	7
L120	655	479	202	0.73	18822.2	11.101	1.7	2.91	4.6	0.234	4.3	0.93	1427	32	5
L124	540	524	172	0.97	25031.9	11.160	2.1	2.84	3.7	0.230	3.0	0.82	1417	40	6
L123	414	536	142	1.30	2617.7	11.188	2.0	2.83	4.5	0.229	4.1	0.90	1412	37	6
S182	265	311	87	1.18	10334.4	11.211	2.2	2.90	4.1	0.236	3.4	0.84	1408	42	3

analysis	U ppm	Th ppm	Pb* ppm	Th/U	$^{206}Pb/^{204}Pb$	$^{206}Pb^*/^{207}Pb^*$	±2σ %	$^{207}Pb^*/^{235}U$	±2σ %	$^{206}Pb^*/^{238}U$	±2σ %	error corr.	Age $^{206}Pb^*/^{207}Pb^*$	± Ma	Disc. %
Sample JV13-61 (continued															
S183	426	386	130	0.91	7116.6	11.227	2.2	2.86	4.2	0.233	3.5	0.85	1406	42	4
L119	478	367	151	0.77	7719.3	11.230	2.6	2.91	5.5	0.237	4.9	0.89	1405	49	2
L130	318	149	94	0.47	5251.8	11.241	2.7	2.91	4.9	0.237	4.1	0.84	1403	52	2
S187	199	179	59	0.90	8800.4	11.245	1.8	2.77	4.1	0.226	3.7	0.90	1403	34	6
L115	287	186	87	0.65	7292.8	11.310	2.2	2.83	4.2	0.232	3.5	0.85	1392	43	3
L132	122	68	35	0.55	805.6	11.316	3.0	2.78	4.4	0.228	3.3	0.75	1391	57	5
L131	395	303	124	0.77	6596.2	11.319	2.1	2.87	5.7	0.236	5.3	0.93	1390	39	2
S178	1203	1726	420	1.44	13900.2	11.326	2.3	2.82	4.6	0.231	4.0	0.87	1389	44	3
L126	320	169	94	0.53	7957.6	11.333	2.4	2.86	3.9	0.235	3.1	0.78	1388	47	2
S189	264	196	77	0.74	6084.8	11.342	3.0	2.76	5.5	0.227	4.6	0.84	1386	58	5
L116	71	21	20	0.30	813.5	11.349	3.0	2.96	5.9	0.244	5.1	0.86	1385	58	-2
S177	449	456	140	1.01	19510.4	11.352	2.6	2.73	4.2	0.225	3.3	0.79	1384	49	6
S191	673	567	212	0.84	988709.6	11.359	1.9	2.86	6.0	0.236	5.7	0.95	1383	37	1
S188	263	203	77	0.77	6205.6	11.373	2.6	2.79	3.5	0.230	2.4	0.69	1381	49	3
L118	450	340	135	0.76	6658.7	11.385	2.3	2.71	4.1	0.223	3.4	0.82	1379	44	6
L125	108	48	31	0.44	1755.5	11.426	3.3	2.87	4.0	0.238	2.2	0.55	1372	64	0
S184	215	159	62	0.74	17502.8	11.428	2.2	2.73	3.7	0.226	3.1	0.82	1372	41	4
S180	491	815	177	1.66	9854.6	11.442	2.0	2.75	3.9	0.228	3.3	0.85	1369	39	3
L129	343	243	108	0.71	4888.4	11.489	2.6	2.88	5.6	0.240	5.0	0.89	1361	50	-2
L128	472	724	173	1.54	5984.3	11.553	2.1	2.81	4.0	0.236	3.5	0.86	1351	40	-1
S194	1023	1523	367	1.49	18921.1	11.585	1.6	2.78	3.9	0.233	3.6	0.91	1345	31	-1
S185	422	579	137	1.37	1683.8	11.593	2.0	2.72	3.5	0.228	2.9	0.83	1344	38	1
L122	40	12	11	0.30	703.7	11.599	5.2	2.79	6.7	0.234	4.2	0.62	1343	101	-1
S181	76	32	22	0.42	1793.2	11.603	4.6	2.88	5.7	0.242	3.5	0.61	1342	88	-4
S192	758	1961	325	2.59	17481.6	11.604	2.2	2.72	3.7	0.229	3.0	0.81	1342	42	1
L127	245	248	82	1.01	3543.6	11.609	2.4	2.84	5.1	0.239	4.5	0.88	1341	47	-3
S190	249	166	74	0.67	5522.3	11.804	3.0	2.73	4.9	0.234	3.9	0.79	1309	58	-3
S193	457	371	144	0.81	31108.4	11.850	2.6	2.79	4.9	0.239	4.2	0.85	1301	50	-6
S179	273	126	78	0.46	2115.1	11.884	2.9	2.73	5.4	0.235	4.5	0.84	1296	57	-5

Isotope ratio and date errors do not include systematic calibration errors of 0.76% ($^{207}Pb/^{206}Pb$), 1.42% ($^{206}Pb/^{238}U$) (2 sigma). Trace element concentrations were deleted from analyses known to have intersected inclusions of other minerals based on P and Ti. Ablation used a laser spot size of 25 microns, and a laser firing repetition rate of 10 Hz.

Table C.4. Zircon chemistry obtained via laser ablation inductively coupled mass spectrometry on three Hart River sill samples

	Concentrations (ppm)																					
	P	Ti	Y	Nb	La	Ce	Pr	Nd	Sm	Eu	Gd	Tb	Dy	Ho	Er	Tm	Yb	Lu	Hf	Ta	Th	U	T(°C)[1]
Sample JV13-39C																							
L141	234.5	18.00	1506	1.27		4.13	0.17	3.19	7.65	1.20	41.94	14.08	159.7	56.36	220.0	53.0	571	59.9	6259	0.54	72.8	100	828
L134	206.2	15.82	1389	0.90		2.94	0.10	2.77	4.46	0.99	32.54	11.56	138.5	50.63	204.7	48.9	543	56.6	6013	0.70	88.1	136	814
S198	280.4	9.88	2302	2.39		4.29	0.19	2.57	6.94	1.15	51.83	18.40	230.8	82.95	334.2	76.2	773	93.2	6601	1.12	203.7	259	766
L135	328.7	17.55	1139	2.95		4.19	0.01	0.51	2.00	0.41	17.47	6.60	94.4	39.97	181.9	47.6	537	59.3	6234	1.57	88.9	214	825
S211	326.4	14.17	2620	1.75	0.05	6.20	0.18	2.70	12.63	1.62	67.75	22.35	272.4	94.16	376.3	82.6	837	101.2	8489	0.91	175.1	186	803
L133	285.2	16.81	1052	2.00		2.72	0.08	1.09	2.43	0.57	17.40	6.66	91.2	36.21	164.3	42.5	490	56.0	6281	0.93	60.2	169	821
L140	361.7	11.20	1817	3.97		7.71	0.07	1.78	5.10	0.56	34.77	13.61	171.7	62.91	269.7	70.9	768	82.7	7384	1.78	167.4	318	779
L137	195.5	11.00	1346	0.93		2.62	0.11	2.49	3.53	0.86	32.37	11.01	141.4	51.62	199.0	51.5	562	58.2	6160	1.02	104.8	159	777
S202	501.6	18.09	5045	5.27		3.94	0.11	2.09	7.18	1.83	89.97	37.55	497.9	186.67	756.3	165.9	1595	195.3	7173	1.60	652.8	491	829
L136	262.7	14.65	1872	1.14		3.66	0.14	2.52	6.96	1.28	46.88	16.49	200.3	65.48	270.4	65.1	689	70.0	6882	0.84	111.1	158	806
S213	411.0	14.80	2991	2.44	0.08	8.16	0.23	3.99	15.46	1.64	78.05	26.75	339.3	111.99	437.0	101.9	1068	117.6	7398	1.60	246.0	273	807
S210	600.6	20.22	5105	4.26		12.26	0.41	12.30	36.23	5.25	188.94	55.92	611.5	193.90	715.0	150.6	1404	167.9	8060	1.44	402.9	232	841
S214	230.1	10.82	1022	1.83		3.04	0.03	1.78	2.95	0.36	18.49	7.75	99.9	36.57	162.1	41.8	457	52.6	6180	1.32	84.5	162	775
S217	278.9	17.62	2005	1.48		3.27	0.06	1.70	6.50	0.95	51.19	18.38	203.6	76.15	301.2	71.4	766	82.8	6883	1.05	123.6	149	826
S195	377.6	17.47	2512	2.32		8.81	0.30	3.97	12.60	1.86	68.17	22.98	280.6	91.35	372.4	84.0	875	97.0	6956	1.11	180.3	196	825
S215	220.7	10.21	1534	0.95		3.39	0.09	2.01	6.06	0.80	37.18	12.86	156.9	57.24	227.5	54.2	579	63.6	6202	0.87	228.9	303	769
S209	344.3	13.58	2688	2.08	0.01	5.46	0.12	2.67	9.79	1.27	64.51	21.45	277.9	97.17	388.8	87.3	860	107.4	9521	1.33	277.5	287	798
S196	352.1	16.71	2632	2.29	0.05	6.82	0.28	4.96	13.04	2.01	77.69	24.41	308.9	100.14	382.7	88.9	937	101.0	6934	1.16	181.2	194	820
S201	278.3	17.06	2317	1.41		4.70	0.11	3.68	10.20	1.43	61.21	20.51	237.6	81.97	332.6	76.9	758	95.3	8472	1.11	126.0	135	822
S199	219.1	8.02	1217	0.93		3.27	0.10	1.92	5.71	0.86	34.27	11.28	134.9	46.00	181.1	45.0	479	50.5	6056	0.84	83.7	131	746
S219	597.0	15.57	4627	5.68		12.63	0.29	8.39	25.60	3.74	140.85	46.42	516.8	170.94	658.5	147.2	1491	156.0	6397	1.59	415.7	367	813

	Concentrations (ppm)																						
	P	Ti	Y	Nb	La	Ce	Pr	Nd	Sm	Eu	Gd	Tb	Dy	Ho	Er	Tm	Yb	Lu	Hf	Ta	Th	U	T(°C)[1]
Sample JV13-53																							
L109	295.3	5.40	1874	0.91		6.25	0.08	2.13	7.10	0.55	46.34	15.61	197.7	69.54	288.5	70.6	761	76.3	5474	0.84	100.8	178	710
L97	643.6	6.40	4964	1.88		13.71	0.40	7.19	23.64	1.60	129.89	45.79	541.6	195.12	735.7	168.5	1724	175.4	4928	1.09	376.1	488	725
L95	885.6	10.66	4393	11.22	0.03	37.26	0.28	5.25	19.94	0.99	111.45	41.81	511.1	177.32	678.1	157.8	1640	161.4	5345	7.05	999.5	969	774
L113	551.7	6.70	4813	1.62	0.05	11.84	0.35	7.38	23.77	2.30	132.28	44.67	534.6	187.34	720.7	164.0	1676	165.6	5771	0.99	364.9	449	730
L99	348.3	4.49	2186	1.01		7.88	0.13	4.21	9.92	0.71	55.89	19.40	237.3	80.80	338.6	80.6	825	82.6	5645	0.63	136.7	225	694
L108	609.0	6.26	4892	1.78		12.50	0.32	7.88	24.14	1.88	132.33	44.93	552.6	185.70	714.8	168.4	1711	172.2	5306	0.79	367.1	455	723
L111	467.7	7.90	2357	1.66		15.18	0.06	2.26	8.29	0.54	51.01	18.55	251.6	89.23	355.6	83.9	904	93.2	5408	1.29	215.5	378	745
S171	313.2	5.21	2541	1.25		7.12	0.12	2.75	9.20	0.59	57.12	19.90	256.5	92.49	391.2	87.1	815	112.3	8120	1.07	149.6	191	707
L100	675.3	6.83	4670	2.03		12.64	0.37	6.77	18.09	1.39	123.84	42.75	514.9	177.33	700.5	163.7	1627	164.8	6243	1.87	439.7	542	731
L96	310.0	4.83	1840	1.16		10.07	0.10	2.08	6.77	0.31	35.55	15.09	188.1	70.03	281.8	66.8	695	69.7	5904	0.85	129.5	236	701
S154	467.7	6.37	5321	1.28		7.46	0.24	5.52	17.03	1.30	129.08	43.72	543.4	205.63	803.6	175.4	1601	212.2	7581	0.88	337.9	333	725
L106	566.1	5.40	4011	1.38		15.53	0.25	6.61	18.15	1.03	105.38	35.29	437.3	151.59	618.3	135.9	1392	143.3	5529	1.10	422.7	564	710
S174	822.9	8.32	6935	4.12		21.67	0.43	9.03	27.11	1.38	169.96	59.22	727.3	261.59	1035.4	226.5	2143	259.8	7164	2.49	712.7	730	750
L107	562.4	5.73	4359	2.79		10.32	0.21	7.12	19.18	1.60	107.33	38.86	478.0	165.77	647.6	149.4	1585	158.3	5696	2.46	422.6	523	716
L103	432.9	6.01	2976	0.82		7.91	0.15	3.47	12.97	0.93	76.11	26.52	323.0	112.34	444.7	105.4	1071	113.4	5712	0.81	207.1	303	720
L101	476.3	5.22	4211	1.32		12.86	0.43	6.98	20.19	1.28	113.73	36.86	448.6	151.46	597.0	137.2	1337	142.0	5694	1.01	441.4	533	707
S173	742.8	5.85	6694	2.85	0.05	16.71	0.41	8.11	25.90	1.60	162.04	58.46	703.2	245.22	984.3	215.8	2018	243.6	7408	1.43	626.5	601	717
S169	668.7	12.71	4582	4.39		24.72	0.20	4.60	13.53	1.01	109.70	39.84	485.8	174.47	694.9	158.0	1415	183.9	7419	3.30	629.8	522	791
S145	767.8	7.75	7503	2.73	0.04	18.24	0.45	10.08	34.55	2.48	196.52	69.92	840.7	288.21	1116.9	246.5	2287	271.0	7390	1.43	578.9	533	743
S149	616.0	5.97	6542	2.15		16.00	0.29	8.03	23.46	1.47	161.79	57.58	690.3	244.04	980.1	206.5	1846	240.5	8506	1.45	615.4	538	719
L110	659.4	6.41	5258	2.28	0.02	19.30	0.35	9.23	27.54	2.02	145.48	48.68	589.8	197.64	765.5	175.8	1830	171.3	5321	1.30	565.3	664	725
S157	565.3	7.11	3627	3.38	0.06	22.51	0.12	4.22	11.87	0.93	80.41	27.96	351.7	129.98	530.4	116.6	1070	139.3	8407	2.26	673.6	587	735
S158	680.6	7.18	7234	3.13		22.23	0.44	12.13	31.86	2.41	192.51	66.89	799.0	269.15	1054.8	227.5	2045	266.4	7266	1.44	653.2	542	736
S150	425.2	5.19	4159	0.78		10.64	0.19	4.57	12.31	0.94	97.80	33.85	396.2	151.33	630.5	136.6	1137	163.8	9124	0.87	345.5	343	707
L104	541.9	5.80	2727	4.28		16.56	0.14	2.21	8.15	0.45	60.86	21.59	280.5	103.80	440.9	105.4	1069	114.7	6369	2.93	242.0	402	717

	Concentrations (ppm)																						
	P	Ti	Y	Nb	La	Ce	Pr	Nd	Sm	Eu	Gd	Tb	Dy	Ho	Er	Tm	Yb	Lu	Hf	Ta	Th	U	T(°C)[1]
Sample JV13-53 (continued)																							
S155	965.7	7.65	10262	3.99	1.99	37.48	0.92	17.11	41.67	2.64	279.21	91.34	1087.2	375.09	1531.4	306.7	2644	334.1	7695	1.44	1217.4	799	742
S162	518.0	5.69	4352	1.84		11.70	0.28	5.46	18.81	1.35	112.35	38.80	475.1	168.83	679.4	149.1	1433	166.6	6874	1.19	332.9	390	715
S142	400.1	5.03	3091	1.16		7.18	0.11	4.39	11.54	0.92	77.01	26.92	332.6	111.29	477.2	110.5	1113	121.1	5996	0.95	197.7	278	704
S15`	267.8	3.88	2193	0.96		9.53	0.08	1.84	7.15	0.37	40.63	15.78	211.0	77.01	323.8	71.8	653	90.9	7913	0.58	186.0	231	682
S164	434.4	4.61	3917	1.41		8.80	0.14	3.63	13.58	0.97	94.54	32.40	402.4	144.54	589.6	132.0	1204	158.9	7314	1.33	262.5	308	697
L105	495.0	6.86	3908	1.27		7.33	0.33	5.23	16.12	1.19	103.58	36.46	421.6	150.64	600.6	132.6	1335	139.5	5714	0.59	269.5	353	732
L102	389.3	4.60	2847	0.86		8.26	0.12	3.17	12.26	0.50	74.72	25.82	300.9	105.72	429.4	100.4	1021	107.4	5851	0.77	213.1	300	696
S148	939.7	5.73	9706	4.72		36.89	0.61	12.87	33.82	1.93	237.27	83.80	1013.4	367.50	1424.2	303.0	2676	335.8	7578	2.84	1292.0	1058	716
S175	757.7	7.93	6542	2.07		20.28	0.53	10.33	27.80	1.95	172.04	60.48	703.3	246.78	933.4	201.3	1922	214.3	7157	1.20	806.1	750	745
S144	957.5	7.63	9329	1.71	0.20	54.08	0.94	17.44	41.00	1.66	260.47	83.81	992.0	338.45	1307.6	271.8	2414	269.5	7312	1.36	2655.0	1684	741
S160	290.3	5.38	2406	0.78		6.47	0.11	4.23	9.70	0.75	57.94	21.32	256.6	93.97	374.3	85.2	827	103.6	6946	0.67	154.7	202	710
S143	535.2	3.62	4664	0.71	0.05	36.74	0.50	8.96	22.39	0.55	121.04	41.17	488.8	161.52	619.1	138.1	1225	120.9	6858	0.63	1473.1	1229	677
S163	560.9	7.12	5920	1.76	0.05	11.99	0.41	6.64	21.85	1.66	144.94	52.08	614.3	215.44	866.8	192.3	1822	218.6	7232	1.23	488.6	484	735
S152	504.6	7.70	6060	1.49		9.04	0.36	6.04	20.24	1.71	146.22	54.13	641.7	227.21	904.8	196.2	1775	240.2	7235	1.07	408.8	391	742
S172	241.3	3.93	4008	0.39		8.39	0.21	5.24	14.77	2.33	98.50	32.87	404.1	144.11	576.6	122.4	1063	126.8	7813	0.21	1406.7	595	683
L98	492.0	5.96	3872	1.12		6.97	0.21	5.50	18.37	1.52	103.39	34.96	448.3	154.90	576.2	141.4	1474	143.3	5667	1.02	254.6	343	719
S156	477.7	5.62	4335	1.53		10.07	0.21	4.87	12.91	1.11	103.48	35.94	452.6	160.67	663.0	140.5	1262	166.0	8967	1.56	363.2	375	714
S153	784.4	8.07	6410	5.46		36.73	0.24	7.49	21.96	1.24	146.28	54.55	693.2	233.41	974.9	211.9	1934	257.2	8878	3.93	807.7	765	747
S170	717.1	8.44	8055	2.73		18.88	0.44	10.42	30.34	2.22	210.63	72.26	846.2	288.43	1156.9	247.2	2100	275.9	8157	1.56	1384.6	731	751
S159	536.4	4.28	5389	1.44	0.04	21.43	0.40	8.03	21.27	1.08	134.75	47.19	551.4	192.89	775.0	163.8	1465	171.5	8186	1.08	796.8	750	690
L112	338.0	5.97	1386	2.26		7.43	0.04	1.50	3.82	0.40	26.58	11.08	137.4	53.64	221.3	54.5	625	62.6	5487	1.86	98.7	211	719
L114	613.2	6.72	4425	1.66	0.06	10.70	0.26	5.83	18.82	1.52	112.16	41.05	494.3	170.61	672.9	155.5	1590	158.6	5575	1.41	293.0	409	730
S168	459.9	6.12	4202	1.04		7.95	0.17	5.87	12.13	0.91	96.98	36.07	422.8	154.69	630.6	137.2	1239	156.9	8025	0.78	303.8	321	721

	Concentrations (ppm)																						
	P	Ti	Y	Nb	La	Ce	Pr	Nd	Sm	Eu	Gd	Tb	Dy	Ho	Er	Tm	Yb	Lu	Hf	Ta	Th	U	T(°C)[1]
Sample JV13-61																							
L121	266.2	4.75	1638	0.99		3.30	0.10	1.54	6.09	0.46	35.52	12.62	173.6	62.49	262.8	66.1	690	71.1	6570	1.13	139.9	217	699
L117	399.5	4.06	3852	0.87		15.36	0.31	7.11	19.76	2.01	115.87	37.91	437.7	144.74	519.6	117.2	1148	105.6	4765	0.39	625.2	544	686
L120	527.5	4.13	4206	2.08		11.76	0.19	4.55	14.47	1.30	89.11	32.69	418.3	149.65	605.7	141.0	1426	145.4	5630	1.25	479.1	655	687
L124	1019.0	5.00	8122	12.04	0.06	34.81	0.45	13.92	36.88	4.11	215.25	73.96	916.7	305.01	1168.2	265.0	2550	252.6	7372	4.67	524.0	540	704
L123	826.9	3.74	5794	7.86		31.25	0.42	8.88	25.38	1.59	133.98	47.51	584.4	195.37	789.6	185.3	1856	181.8	7880	3.63	536.5	414	679
S182	308.3	4.90	2567	3.89	0.01	9.51	0.10	3.61	10.30	1.32	63.84	21.76	273.0	95.73	367.4	78.9	714	83.7	8858	4.53	311.4	265	702
S183	600.2	3.89	5701	3.07	0.04	15.37	0.34	6.96	19.44	1.40	125.74	47.53	585.9	204.30	834.2	187.4	1726	197.5	9046	2.24	386.4	426	682
L119	653.9	3.42	4602	5.46		15.61	0.18	5.17	15.19	1.79	95.92	35.19	457.0	167.95	678.7	165.2	1675	161.9	6665	3.44	367.5	478	672
L130	297.7	1.32	2277	1.12		10.08	0.10	2.94	8.26	1.18	57.45	20.59	250.5	86.37	312.1	69.8	676	57.0	5175	0.44	148.8	318	601
S187	188.8	1.63	1703	0.22		5.19	0.05	1.19	4.40	0.46	33.07	12.91	161.5	57.58	241.1	52.3	478	55.1	7887	0.17	178.8	199	616
L115	580.5	3.70	4227	4.87	0.01	11.66	0.18	4.23	15.37	1.94	99.33	36.14	451.3	160.37	635.3	153.9	1579	154.5	5793	2.59	185.6	287	678
L132	428.8	2.32	4358	1.26		10.11	0.19	3.68	14.46	2.74	95.49	35.93	466.8	160.52	628.3	138.8	1382	125.3	6671	1.49	67.6	122	642
L131	623.3	6.22	4833	7.11	0.01	16.29	0.30	8.08	22.42	2.25	136.42	45.58	547.9	188.82	712.9	166.7	1662	153.6	6758	3.85	302.6	395	723
S178	1209.2	8.04	7504	34.25		77.46	0.37	8.77	27.21	2.64	177.47	63.92	784.0	270.75	1058.6	237.9	2286	228.1	7891	14.36	1726.5	1203	746
L126	536.5	5.69	2791	7.89		17.68	0.11	4.59	11.01	1.02	79.50	28.62	354.6	115.17	450.1	105.4	1078	102.7	5822	5.39	169.1	320	715
S189	465.8	7.79	2753	7.08		11.43	0.03	2.76	7.87	0.36	53.45	20.75	270.9	99.56	416.7	94.6	940	111.6	8474	4.12	196.0	264	743
S177	736.6	7.32	6144	5.40		16.12	0.34	9.11	30.23	2.66	165.80	58.76	731.1	241.45	937.4	212.1	2036	228.0	6097	2.73	455.7	449	738
S191	595.5	4.54	4852	4.16		19.14	0.41	6.34	22.58	1.77	114.94	42.22	538.0	178.79	703.2	156.9	1574	155.3	6409	2.89	566.6	673	695
S188	430.9	4.08	3838	2.11		8.87	0.19	5.30	12.41	0.98	83.40	30.53	373.3	133.64	550.1	122.2	1125	130.7	8775	2.05	202.7	263	686
L118	573.6	3.35	4664	3.55		15.11	0.31	6.51	15.32	1.98	102.60	39.06	503.0	169.88	682.5	160.4	1577	148.6	6532	2.48	340.1	450	670
L125	285.4	3.57	1482	3.40		7.23	0.01	0.66	3.74	0.46	27.76	10.82	146.4	53.38	230.6	57.5	576	63.2	6261	2.15	47.8	108	675
S184	446.6	3.73	3712	2.39		10.25	0.10	3.64	11.61	1.49	79.80	28.58	376.2	131.52	544.4	120.8	1138	133.3	9174	2.36	158.7	215	679
S180	379.4	4.26	4212	1.66	0.03	8.90	0.28	5.40	15.50	2.18	110.22	37.33	462.2	152.67	601.6	135.6	1260	119.2	4654	0.39	814.6	491	690
L129	573.1	3.56	4137	2.24		16.60	0.17	5.42	16.86	1.89	96.26	35.64	438.5	153.54	617.5	144.0	1460	136.3	5473	1.38	242.8	343	675
L128	452.2	5.52	2987	3.44		28.44	0.15	4.28	11.01	0.77	72.83	27.80	328.8	107.88	392.5	83.3	770	69.4	8793	2.79	724.3	472	712

	Concentrations (ppm)																					
	P	Ti	Y	Nb	La	Ce	Pr	Nd	Sm	Eu	Gd	Tb	Dy	Ho	Er	Tm	Yb	Lu	Hf	Ta	Th	U	T(°C)[1]
Sample JV13-61 (continued)																							
S194	1036.4	7.21	6055	19.79		73.16	0.18	6.48	19.41	1.93	136.62	52.98	626.7	213.10	874.6	196.2	1877	174.6	7484	10.14	1523.4	1023	736
S185	593.4	4.39	5749	4.54		24.00	0.38	8.54	21.71	2.27	120.34	47.28	551.3	195.07	790.1	167.6	1505	169.0	8371	4.03	578.8	422	693
S192	697.0	5.53	4688	6.59		83.03	0.29	7.60	24.36	1.11	154.16	49.66	587.8	171.55	588.7	121.9	1132	98.4	6547	3.46	1960.6	758	712
L127	276.5	3.98	2896	0.90		4.56	0.13	3.90	9.77	1.14	63.44	22.81	308.6	105.41	439.3	100.3	1027	101.3	5739	0.53	248.2	245	684
S190	554.1	5.28	3113	13.43		18.83	0.03	1.79	6.93	0.76	55.34	22.12	302.7	115.07	473.0	113.4	1168	124.9	7871	5.69	165.9	249	708
S193	704.5	4.69	5446	7.66		16.99	0.31	6.15	20.71	1.61	128.62	46.19	587.6	209.80	800.1	176.8	1811	178.2	8089	3.97	370.9	457	698
S179	389.2	5.04	2085	7.11		11.28	0.05	1.03	5.20	0.37	37.67	13.82	198.1	73.66	318.2	75.6	855	90.8	7719	4.99	126.3	273	704

All trace element data was collected with the mean count method. Analyses that intersected inclusions of other minerals were rejected based on time resolved P and Ti analyses and not included in this table. Backgrounds were monitored between sweeps 10 - 20. Sample counts integrated from sweeps 28 - 54. [1]Ti in zircon thermometry following Watson et al. 2006.

Chemical abrasion thermal ionization mass spectrometry: methods

U-Pb dates were obtained by the chemical abrasion isotope dilution thermal ionization mass spectrometry (CA-TIMS) method from analyses composed of single zircon grains. Zircon was separated from rocks using standard techniques and mounted in epoxy and polished until the centers of the grains were exposed. Cathodoluminescence (CL) images were obtained with a JEOL JSM-1300 scanning electron microscope and Gatan MiniCL. Zircon was removed from the epoxy mounts and subjected to a modified version of the chemical abrasion method of Mattinson (2005), reflecting analysis of single grains or fragments of grains. Grains were selected for dating based on CL images.

Zircon was placed in a muffle furnace at 900°C for 60 hours in quartz beakers. Single grains were then transferred to 3 ml Teflon PFA beakers and loaded into 300 µl Teflon PFA microcapsules. Fifteen microcapsules were placed in a large-capacity Parr vessel and the grains partially dissolved in 120 µl of 29 M HF for 12 hours at 180°C. The contents of the microcapsules were returned to 3 ml Teflon PFA beakers, HF removed, and the residual grains immersed in 3.5 M HNO_3, ultrasonically cleaned for an hour, and fluxed on a hotplate at 80°C for an hour. The HNO_3 was removed and grains were rinsed twice in ultrapure H2O before being reloaded into the 300 µl Teflon PFA microcapsules (rinsed and fluxed in 6 M HCl during sonication and washing of the grains) and spiked with the Boise State University mixed ^{233}U-^{235}U-^{205}Pb tracer solution. Zircon was dissolved in Parr vessels in 120 µl of 29 M HF with a trace of 3.5 M HNO_3 at 220°C for 48 hours, dried to fluorides, and re-dissolved in 6 M HCl at 180°C overnight. U and Pb were separated from the zircon matrix using an HCl-based anion-exchange chromatographic procedure (Krogh, 1973), eluted together and dried with 2 µl of 0.05 N H_3PO_4.

Pb and U were loaded on a single outgassed Re filament in 5 µl of a silica-gel/phosphoric acid mixture (Gerstenberger and Haase, 1997), and U and Pb isotopic measurements made on a GV Isoprobe-T multicollector thermal ionization mass spectrometer equipped with an ion-counting Daly detector. Pb isotopes for analyses with smaller amounts of radiogenic Pb were measured by peak-jumping all isotopes on the Daly detector for 160 cycles, and corrected for 0.16 ± 0.03% / a.m.u. (1 sigma error) mass fractionation. Pb isotopes for analyses with larger amounts of radiogenic Pb were measured by a Faraday-Daly routine that cycles 200 times between placing mass 204 in

the axial Daly collector and masses 205-208 on the H1-H4 Faraday detectors to placing mass 205 in the axial Daly and masses 206-208 in the H1-H3 Faradays, providing real-time Daly gain correction. These results were corrected for 0.10 ± 0.03%/a.m.u. (1 sigma error) mass fractionation. Transitory isobaric interferences due to high-molecular weight organics, particularly on 204Pb and 207Pb, disappeared within approximately 30 cycles, while ionization efficiency averaged 104 cps/pg of each Pb isotope. Linearity (to ≥1.4 x 106 cps) and the associated deadtime correction of the Daly detector were monitored by repeated analyses of NBS982, and have been constant since installation. Uranium was analyzed as UO^{2+} ions in static Faraday mode on 1011 ohm resistors for 200-300 cycles, and corrected for isobaric interference of $^{233}U^{18}O^{16}O$ on $^{235}U^{16}O^{16}O$ with an $^{18}O/^{16}O$ of 0.00206. Ionization efficiency averaged 20 mV/ng of each U isotope. U mass fractionation was corrected using the known $^{233}U/^{235}U$ ratio of the Boise State University tracer solution.

U-Pb dates and uncertainties were calculated using the algorithms of Schmitz and Schoene (2007), $^{235}U/^{205}Pb$ of 77.93 and $^{233}U/^{235}U$ of 1.007066 for the Boise State University tracer solution, and U decay constants recommended by Jaffey et al. (1971). $^{206}Pb/^{238}U$ ratios and dates were corrected for initial ^{230}Th disequilibrium using a Th/U[magma] = 3.0 ± 0.3 using the algorithms of Crowley et al. (2007), resulting in an increase in the $^{206}Pb/^{238}U$ dates of ~0.09 Ma. All common Pb in analyses was attributed to laboratory blank and subtracted based on the measured laboratory Pb isotopic composition and associated uncertainty. U blanks are difficult to precisely measure, but are estimated at 0.07 pg.

Weighted mean $^{207}Pb/^{206}Pb$ dates were calculated from equivalent dates using Isoplot 3.0 (Ludwig, 2003). Errors on the weighted mean dates are given as ± x / y, where x is the internal error based on analytical uncertainties only, including counting statistics, subtraction of tracer solution, and blank and initial common Pb subtraction, and y includes the U decay constant uncertainties propagated in quadrature. Internal errors should be considered when comparing our dates with $^{206}Pb/^{238}U$ dates from other laboratories that used the same Boise State University tracer solution or a tracer solution that was cross-calibrated using EARTHTIME gravimetric standards. Errors including uncertainties in the tracer calibration and 238U decay constant (Jaffey et al., 1971) should be considered

when comparing our dates with those derived from other decay schemes (e.g., $^{40}Ar/^{39}Ar$, ^{187}Re-^{187}Os). Errors for weighted mean dates are given at 2σ.

Normative mineralogy

The understanding of intrusive rocks with obscured primary mineralogy, such as the Hart River sills, is greatly aided by normative mineralogy. Normative mineralogy is the 'ideal' mineralogy of a rock based solely on whole rock major element analyses. Normative mineralogy combined with optical microscopy, REE diagrams, and other interpretative tools can be extremely powerful. CIPW normative mineralogy is presented in Table C5 (the cation norm yields similar results).

Table C.5. CIPW normative mineralogy of the Hart River sills (locations as in Table 5.1).

Mineral	Ap	Il	Or	Ab	An	Mt	Di	Hy	Ol	Q	Ne
Sodically altered											
jv13-20-64	0.69	5.85	3.53	29.83	11.83	2.25	28.31	13.51	0.00	4.20	0.00
jv13-12-37	0.12	1.31	4.24	24.02	24.38	1.38	18.41	20.58	5.57	0.00	0.00
jv13-6-25	0.19	2.16	5.24	21.55	27.36	1.50	12.68	25.79	3.54	0.00	0.00
Least altered											
JV13-2-5k	0.27	3.30	6.70	21.78	18.03	2.22	19.76	26.44	1.51	0.00	0.00
JV13-2-5m	0.22	3.88	6.86	22.24	17.72	2.37	15.12	18.54	13.04	0.00	0.00
jv13-16-52A	0.19	5.98	5.38	15.95	23.30	2.58	21.42	16.03	9.16	0.00	0.00
GA6-3	0.21	1.97	8.85	25.43	22.95	1.67	15.79	14.13	9.00	0.00	0.00
jv13-13-35	0.14	1.68	7.81	20.82	24.91	1.29	25.04	0.88	17.43	0.00	0.00
jv13-4-13	0.17	1.83	10.19	27.00	20.06	1.44	18.98	4.18	16.15	0.00	0.00
jv13-15-49	0.19	2.15	9.80	25.61	24.64	1.60	16.41	5.38	14.22	0.00	0.00
jv13-12-39	0.07	1.05	9.30	19.48	35.48	0.98	16.06	0.00	15.19	0.00	2.39
jv13-16-50	0.15	2.30	11.16	28.32	19.91	1.65	5.69	18.39	12.44	0.00	0.00
JV13-2-5q	0.15	2.01	5.11	25.16	24.09	1.54	14.41	24.61	2.92	0.00	0.00
JV13-2-5i	0.31	2.97	9.67	18.52	23.34	1.71	18.12	20.75	0.00	4.61	0.00
Potassically altered											
GA6-5	0.17	1.86	9.68	15.19	26.64	1.59	18.87	23.99	2.00	0.00	0.00
Jv13-3-9a	0.14	2.42	11.02	15.78	22.95	1.49	14.99	23.07	8.14	0.00	0.00
jv13-19-62	0.21	2.19	12.21	17.49	22.60	1.87	20.45	16.17	6.80	0.00	0.00
GA4-2	0.12	1.09	12.79	16.18	25.66	1.08	24.02	3.79	15.27	0.00	0.00
GA4-3	0.10	0.85	12.63	12.11	28.11	0.95	30.17	0.00	14.50	0.00	0.59
jv13-18-57A	0.24	2.75	16.97	15.51	21.55	1.80	21.48	4.94	14.77	0.00	0.00

See section 5.6.1. for justification of sample grouping by alteration. Ap = apatite, Il = ilmenite, Or = orthoclase, Ab = albite, An = anorthite, Mt = magnetite, Di = diopside, Hy = hypersthene, Ol = olivine, Q = quartz, Ne = nepheline

Pyroxene compositions by electron microprobe

Mineral compositions were obtained via a Cameca SX50 electron microprobe at the University of British Columbia. Clinopyroxene occurs small as islands in hornblende. Both minerals have nearly identical electron backscatter coefficients and hence it is nearly impossible to correctly identify pyroxene prior to the analyses. All pyroxene was analyzed on settings that allow for both the correct analyses of amphibole and pyroxene and the distinction was made later. Data were rejected if the analyses did not sum to 98 – 102 %,

if calculated total cations varied by more than 1 % after adjustment of the proportions of Fe^{3+} and Fe^{2+}, and if the charge balance varied by more than 1%. Averages per thin section were subsequently used as input for the mineral chemistry of fractionating pyroxene in the stonergram (Table C.6).

Table C.6. Clinopyroxene compositions obtained via electron microprobe

Sample	FeO	Fe_2O_3	Na_2O	MgO	Al_2O_3	SiO_2	K_2O	CaO	TiO_2	Cr_2O_3	MnO	NiO	% Fe^{3+}
JV13-2-5Q-1	0.28	0.07	0.01	0.80	0.07	1.93	0.00	0.84	0.01	0.00	0.01	0.00	0.20
JV13-2-5Q-2	0.36	0.09	0.01	0.67	0.01	1.95	0.00	0.89	0.00	0.00	0.01	0.00	0.20
Average 5Q cpx	**0.32**	**0.08**	**0.01**	**0.73**	**0.04**	**1.94**	**0.00**	**0.86**	**0.00**	**0.00**	**0.01**	**0.00**	
JV13-12-37-1	0.27	0.11	0.03	0.77	0.07	1.91	0.00	0.83	0.01	0.00	0.01	0.00	0.30
JV13-12-37-2	0.36	0.04	0.03	0.76	0.09	1.93	0.00	0.75	0.01	0.00	0.02	0.00	0.10
JV13-12-37-3	0.29	0.07	0.02	0.76	0.04	1.94	0.00	0.87	0.00	0.00	0.01	0.00	0.20
JV13-12-37-4	0.26	0.09	0.02	0.77	0.02	1.95	0.00	0.90	0.00	0.00	0.01	0.00	0.25
JV13-12-37-5	0.28	0.07	0.02	0.76	0.05	1.95	0.00	0.85	0.00	0.00	0.01	0.00	0.20
Average 37 cpx	**0.29**	**0.08**	**0.02**	**0.76**	**0.06**	**1.94**	**0.00**	**0.84**	**0.01**	**0.00**	**0.01**	**0.00**	
JV13-3-9a-1	0.19	0.08	0.02	0.94	0.09	1.91	0.00	0.76	0.01	0.00	0.01	0.00	0.30
JV13-3-9a-2	0.14	0.08	0.01	0.99	0.08	1.91	0.00	0.76	0.00	0.01	0.00	0.00	0.35
JV13-3-9a-3	0.11	0.09	0.02	0.97	0.10	1.89	0.00	0.79	0.01	0.02	0.00	0.00	0.45
JV13-3-9a-4	0.16	0.07	0.01	0.98	0.08	1.92	0.00	0.77	0.01	0.01	0.01	0.00	0.30
JV13-3-9a-5	0.14	0.07	0.01	0.97	0.08	1.91	0.00	0.79	0.01	0.01	0.01	0.00	0.35
JV13-3-9a-6	0.18	0.10	0.01	0.97	0.07	1.91	0.00	0.75	0.01	0.00	0.01	0.00	0.35
Average 9a cpx	**0.15**	**0.08**	**0.01**	**0.97**	**0.09**	**1.91**	**0.00**	**0.77**	**0.01**	**0.01**	**0.01**	**0.00**	
JV13-2-5m-1	0.38	0.07	0.02	0.67	0.05	1.94	0.00	0.85	0.01	0.00	0.01	0.00	0.15
JV13-2-5m-2	0.40	0.10	0.01	0.66	0.03	1.94	0.00	0.84	0.00	0.00	0.01	0.00	0.20
JV13-2-5m-3	0.40	0.07	0.01	0.69	0.02	1.95	0.00	0.83	0.00	0.00	0.01	0.00	0.15
JV13-2-5m-4	0.42	0.05	0.02	0.66	0.03	1.97	0.00	0.85	0.00	0.00	0.01	0.00	0.10
JV13-2-5m-5	0.35	0.06	0.01	0.74	0.04	1.95	0.00	0.83	0.01	0.00	0.01	0.00	0.15
JV13-2-5m-6	0.38	0.07	0.01	0.67	0.02	1.96	0.00	0.87	0.00	0.00	0.01	0.00	0.15
Average 5m cpx	**0.39**	**0.07**	**0.01**	**0.68**	**0.03**	**1.95**	**0.00**	**0.85**	**0.00**	**0.00**	**0.01**	**0.00**	
JV13-18-57a-1	0.21	0.05	0.01	0.88	0.13	1.89	0.00	0.79	0.01	0.01	0.01	0.00	0.20
JV13-18-57a-2	0.20	0.07	0.02	0.82	0.07	1.92	0.00	0.88	0.01	0.01	0.01	0.00	0.25
JV13-18-57a-3	0.34	0.11	0.02	0.69	0.07	1.91	0.00	0.84	0.01	0.00	0.01	0.00	0.25
JV13-18-57a-4	0.25	0.06	0.01	0.84	0.12	1.90	0.00	0.77	0.01	0.01	0.01	0.00	0.20
JV13-18-57a-5	0.23	0.06	0.01	0.89	0.12	1.90	0.00	0.76	0.01	0.01	0.01	0.00	0.20
Average 57a cpx	**0.25**	**0.07**	**0.02**	**0.83**	**0.10**	**1.90**	**0.00**	**0.81**	**0.01**	**0.01**	**0.01**	**0.00**	

References

Crowley, J.L., Schoene, B., Bowring, S.A., 2007, U-Pb dating of zircon in the Bishop Tuff at the millennial scale: Geology 35:1123-1126.

Gerstenberger, H., Haase, G., 1997, A highly effective emitter substance for mass spectrometric Pb isotope ratio determinations: Chemical Geology 136:309-312.

Jaffey, A.H., Flynn, K.F., Glendenin, L.E., Bentley, W.C., and Essling, A.M., 1971, Precision measurements of half-lives and specific activities of 235U and 238U, Physical Review C, 4:1889-1906.

Krogh, T.E., 1973, A low contamination method for hydrothermal decomposition of zircon and extraction of U and Pb for isotopic age determination: Geochimica et Cosmochimica Acta 37:485-494.

Ludwig, K.R., 2003, User's Manual for Isoplot 3.00. Berkeley Geochronology Center: Berkeley, CA, 70 p.

Mattinson, J.M., 2005, Zircon U-Pb chemical abrasion ("CA-TIMS") method: combined annealing and multi-step partial dissolution analysis for improved precision and accuracy of zircon ages: Chemical Geology 220:47-66.

Schmitz, M.D., Schoene, B., 2007, Derivation of isotope ratios, errors and error correlations for U-Pb geochronology using 205Pb-235U-(233U)-spiked isotope dilution thermal ionization mass spectrometric data: Geochemistry, Geophysics, Geosystems (G3) 8, Q08006, doi:10.1029/2006GC001492.

Sláma, J., Košler, J, Condon, D.J., Crowley, J.L., Gerdes, A., Hanchar, J.M., Horstwood, M.S.A., Morris, G.A., Nasdala, L., Norberg, N., Schaltegger, U., Schoene, B. Tubrett, M.N, Whitehouse, M.J. 2008. Plešovice zircon — A new natural reference material for U–Pb and Hf isotopic microanalysis. Chemical Geology, 249: 1-35.

Watson, E.B., Wark, D.A., Thomas, J.B. 2006. Crystallization thermometers for zircon and rutile. Contributions to Mineralogy and Petrology, 151: 413-433.

Appendix D.

Field relations and whole rock geochemistry of the Hart River volcanics

The Hart River volcanics are volcanic rocks that occur in Yukon Territory (Chapter 5, map sheet NTS 116A/10). The Hart River volcanics is a volcano-sedimentary succession that consists of pillowed basalt and black slates. Poor exposure in the area has impeded the observation of stratigraphic relations between the over- and underlying units. The underlying unit was originally interpreted as black slate of the Paleoproterozoic upper Gillespie Lake Group (Abbott, 1997); however, black slate is uncommon in the Gillespie Lake Group and this was a tentative interpretation (Thorkelson, 2000; J.G. Abbott, pers. comm., 2013).

Several samples of Hart River volcanics and massive aphanitic greenstone that was interpreted to belong to the Hart River volcanics by Abbott (1997) were analyzed for whole rock geochemistry. Whole rock geochemistry indicates that the Hart River volcanics are not as extensive as previously thought and are limited to several pillow basalts (Figure C-1A). The aphanitic greenstone that was grouped with the Hart River volcanics is in fact a hydrothermally altered Hart River sill that occurs close to the Hart River deposit. The Hart River volcanics are more siliceous than the Hart River sills (Table D-1, Figure D-1B, 53 – 58 % wt. SiO_2). They fall in the andesite, basaltic andesite and basaltic trachy-andesite fields on an SiO_2 – total alkali elements classification diagram. The Hart River sills, despite being variously fractionated, have a narrow range of SiO_2 content of maximum < 51 wt. %. The Hart River volcanics also display different Sm-Nd isotope ratio evolution (Table D-2, Figure D-1C). The distinct geochemical signature of the Hart River volcanics precludes a scenario in which the Hart River sills fed the Hart River volcanics. Instead, the Hart River volcanics are interpreted to belong to a younger volcano-sedimentary succession that was structurally emplaced alongside the Hart River sills. Possible correlatives are the Neoproterozoic Mount Harper Group or the Cambro-Ordovician Dempster Volcanics. The Mount Harper Group and the Dempster volcanics both contain mafic volcanic rocks, and are contained in thin thrust nappes near the Hart River volcanics (Abbott, 1997).

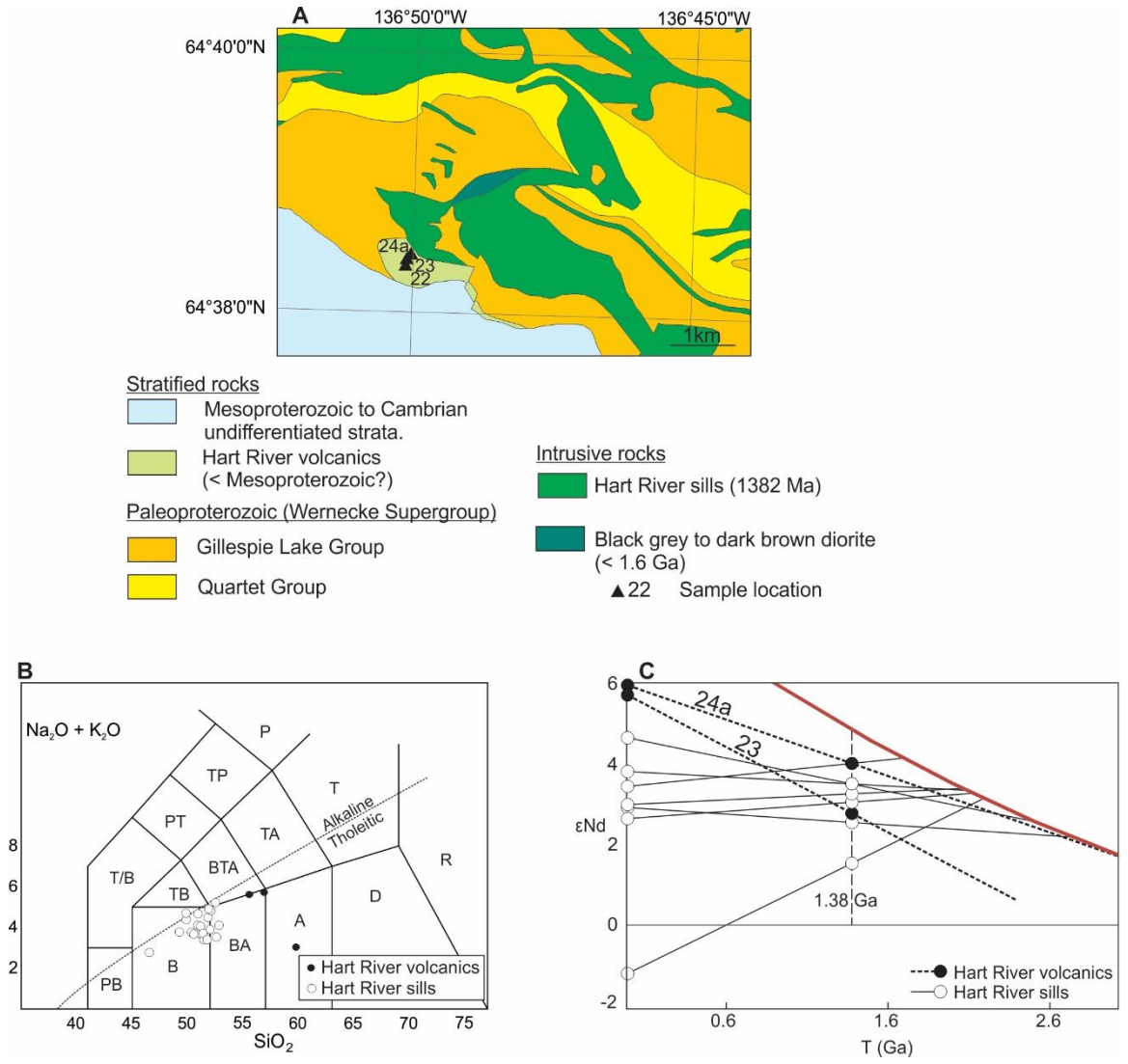

Figure D.1. **A. Simplified geological map of the Hart River inlier (modified after Abbot, 1997). B. Total alkali – SiO_2 diagram indicating the high SiO_2 content of the Hart River volcanics relative to the Hart River sills (LeBas et al., 1986; Irvine and Barager, 1979). C. εNd evolution, assuming the Hart River volcanics are 1.38 Ga. The depleted mantle curve of DePaolo (1981) is shown in red.**

Table D.1. Whole rock geochemistry of the Hart River volcanics

Analyte (%)	SiO_2[1]	$Al2O_3$[1]	Fe_2O_3[1]	MnO[1]	MgO[1]	CaO[1]	Na_2O[1]	K2O[1]	TiO_2[1]	P_2O_5[1]	LOI[1]	S[3]	Total
Detection Limit	0.01	0.01	0.01	0.001	0.01	0.01	0.01	0.01	0.001	0.01		0.001	0.01
Absolute error	0.3	0.2	0.25	0.04	0.1	0.5	0.15	0.3	0.4	0		0.1	
Relative error (%)	1.5	1	1	6	1	1	2	11	12	1		1	
JV13-6-22	58.24	12.28	17.14	0.05	3.15	0.37	0.12	2.85	2.924	0.23	3.39	0.005	100.7
JV13-6-23	53.86	14.54	10.41	0.178	7.29	4.76	4.9	0.51	1.106	0.09	2.66	0.021	100.3
jv13-6-24A	55.29	14.54	9.32	0.157	5.52	6.85	4.48	1.05	1.087	0.07	2.15	0.03	100.5

Analyte (ppm)	Au[2]	Ag[2/3]	As[2]	Ba[1]	Be[1]	Bi[4]	Br[2]	Cd[3]	Co[2]	Cr[2]	Cs[4]	Cu[3]	Ga[4]
Detection Limit	0.001	0.5	1	1	1	0.1	0.5	0.5	0.1	0.5	0.1	1	1
Absolute error	n/a	n/a	2	2	1	1.5	n/a	0.5	1	3	0.3	2	1
Relative error (%)	n/a	n/a	5	4	2	1	n/a	1	4	10	3	4	1
JV13-6-22	< 1	< 0.5	7	370	2	0.6	< 0.5	< 0.5	26.8	147	6.6	2	17
JV13-6-23	< 1	< 0.5	7	115	< 1	< 0.1	< 0.5	< 0.5	43.5	141	1.1	70	14
jv13-6-24A	< 1	< 0.5	9	423	< 1	< 0.1	< 0.5	< 0.5	43.2	144	1.3	119	14

Analyte (ppm)	Ge[4]	Hf[4]	Hg[2]	In[4]	Ir[2]	Mo[4]	Nb[4]	Ni[3]	Pb[3]	Rb[4]	Sb[2]	Sc[2]	Se[2]
Detection Limit	0.5	0.1	1	0.1	0.001	2	0.2	1	5	1	0.1	0.01	0.5
Absolute error	0.7	0.7	n/a	n/a	n/a	0.3	0.8	2	7	2	0.3	0.3	n/a
Relative error (%)	1	5	n/a	n/a	n/a	2.5	11	10	2	3	2	2	n/a
JV13-6-22	4.3	4.3	< 1	< 0.1	< 1	< 2	14	64	15	102	11.1	21.4	< 0.5
JV13-6-23	1.5	1.3	< 1	< 0.1	< 1	< 2	1.8	75	< 5	9	11.4	51.5	< 0.5
jv13-6-24A	1.6	1.2	< 1	< 0.1	< 1	< 2	1.7	74	< 5	17	16.3	50	< 0.5

Analyte (ppm)	Sn[4]	Sr[1]	Ta[4]	Th[4]	U[4]	V[1]	W[2]	Y[1]	Zn[2/3]	Zr[1]	La[4]	Ce[4]	Pr[4]
Detection Limit	1	2	0.01	0.05	0.01	5	1	1	1	1	0.05	0.05	0.01
Absolute error	1	2	0.3	1	0.5	1	n/a	3	5	2	2	3	0.2
Relative error (%)	0.5	2.5	2	7.5	3	5	n/a	7	9	7	11	11	8
JV13-6-22	2	17	1.19	7.74	3.67	428	< 1	22	98	195	31.4	72.7	8.15
JV13-6-23	< 1	48	0.16	0.46	0.15	338	< 1	20	85	59	2.21	6.99	1.17
jv13-6-24A	< 1	86	0.28	0.41	0.13	353	< 1	20	63	58	2.23	6.59	1.14

Analyte (ppm)	Nd[4]	Sm[4]	Eu[4]	Gd[4]	Tb[4]	Dy[4]	Ho[4]	Er[4]	Tl[4]	Tm[4]	Yb[4]	Lu[4]	
Detection Limit	0.05	0.01	0.005	0.01	0.01	0.01	0.01	0.01	0.05	0.005	0.01	0.002	
Absolute error	1.5	0.4	0.5	0.5	0.3	0.8	0.2	0.5	0.5	0.5	0.2	0.3	Mass[2]
Relative error (%)	4	6	1	16	7	4	5	5	8	1	4	1	(g)
JV13-6-22	32.6	6.68	1.5	5.77	0.95	5.4	1.06	3.1	0.5	0.487	3.21	0.482	1.197
JV13-6-23	6.38	2.24	0.775	3.32	0.65	4.11	0.85	2.59	0.15	0.394	2.62	0.372	1.168
jv13-6-24A	5.83	2	0.757	3.09	0.62	3.81	0.8	2.45	0.17	0.36	2.36	0.376	1.257

Analysed via [1]: Inductively coupled plasma mass spectrometry on diluted fused lithium meta-/tetraborate sample (using a Varian Vista ICP), [2]: Instrumental neutron activation analysis, [3]: Inductively coupled plasma mass spectrometry on (near) total digested sample, [4]: Inductively coupled plasma mass spectrometry on diluted fused lithium meta-/tetraborate sample (using a Perkin Elmer Sciex ICP/MS). Error analysis follows chapter 3. UTM locations in NAD 1983 : JV13-6-22: 413011E 7169405N. JV13-6-23: 412974E, 7169426N, JV13-6-24A: 412960E, 7169426N.

Table D.2. Isotope analyses on 2 samples of the Hart River volcanics (UTM locations in table C-1)

	Nd (ppm)	Sm (ppm)	$\frac{^{143}Nd}{^{144}Nd}$	$\frac{^{147}Sm}{^{144}Nd}$	εNd_0	$\varepsilon Nd_{1.38}$	T_{DM}^{1}
JV13-6-23	6.62	2.34	0.51293	0.213778	5.61	2.61	-
JV13-6-24A	6.69	2.29	0.51294	0.207021	5.92	4.12	2.3

	Pb ppm	$\frac{^{206}Pb}{^{204}Pb}$	$\frac{^{207}Pb}{^{204}Pb}$	$\frac{^{208}Pb}{^{204}Pb}$
JV13-6-23	< 5	18.184	14.441	37.726
JV13-6-24A	< 5	18.302	15.606	38.037

	Rb (ppm)	Sr (ppm)	$\frac{^{87}Sr}{^{86}Sr}$	error	$\frac{^{87}Sr}{^{86}Sr_i}$
JV13-6-23	9	48	0.71808	4.4E-04	0.708
JV13-6-24A	17	86	0.71758	3.0E-05	0.707

[1]**Following methods outlined in DePaolo (1981)**

References

Abbott, G. (1997). Geology of the Upper Hart River Area, Eastern Ogilvie Mountains, Yukon Territory (116A/10, 116A/11). Exploration and Geological Services Division, Yukon Region, Bulletin (Vol. 9).

DePaolo, D. J. (1981). Neodymium isotopes in the Colorado Front Range and crust–mantle evolution in the Proterozoic. Nature, 291(5812), 193–196. http://doi.org/10.1038/291193a0

Irvine, T. N., & Baragar, W. R. a. (1971). A Guide to the Chemical Classification of the Common Volcanic Rocks. Canadian Journal of Earth Sciences, 8, 523–548. http://doi.org/10.1139/e71-055

Le Bas, M. J., Le Maitre, R. W., Streckeisen, A., & Zanettin, B. (1986). A chemical classification of volcanic rocks based on the total alkali silica diagram. Journal of Petrology, 27(3), 745–750. http://doi.org/10.1093/petrology/27.3.745

Thorkelson, D. J. (2000). Geology and mineral occurrences of the Slats Creek, Fairchild Lake and ``Dolores Creek'' areas, Wernecke Mountains (106D/16, 106C/13, 106C/14), Yukon Territory. Exploration and Geological Services Division, Yukon Region, Bulletin (Vol. 10).

Appendix E.

Preliminary detrital zircon geochronology of a newly recognized volcanic succession in the Coal Creek Inlier

A volcano-sedimentary succession containing lithic wacke and lapilli tuff occurs in the Coal Creek Proterozoic Inlier in the Ogilvie Mountains (Fig, Peters and Thorkelson, 2011). Peters and Thorkelson (2011) interpreted this succession as a clast within Wernecke Breccia. However, during subsequent investigation in the field season of 2012, it was noted that the volcano-sedimentary succession lies unconformably on the Quartet Group of the Wernecke Supergroup.

The volcano-sedimentary sequence occurs close to the Yukon Olympic Mineral Occurrence and will be referred to here as the Olympic volcanics. The maximum age of the Olympic volcanics is constrained by the ~1.6 Ga Racklan Orogeny that deformed the Wernecke Supergroup, but not the Olympic volcanics. The minimum age is constrained by Cambrian sediments, which appear to lie stratigraphically above the Olympic volcanics. The Olympic volcanics may be equivalent to the Dempster volcanics which crop out approximately 40 km south of the Olympic volcanics.

Detrital zircon was separated from the Olympic volcanics and sent to Boise State University, Idaho, for laser ablation inductively coupled mass spectrometry U-Pb age determinations. Detrital zircon ages fall in the range 2.1 – 1.6 Ga and 3.0 – 2.4 Ga (Figure D-2, Table D-1). Although this is a modest data set both in terms of the number of zircon analysed and the error on individual analyses, the data are consistent with a Laurentian detrital zircon signature similar to that of the Wernecke Supergroup (Furlanetto et al., 2016).

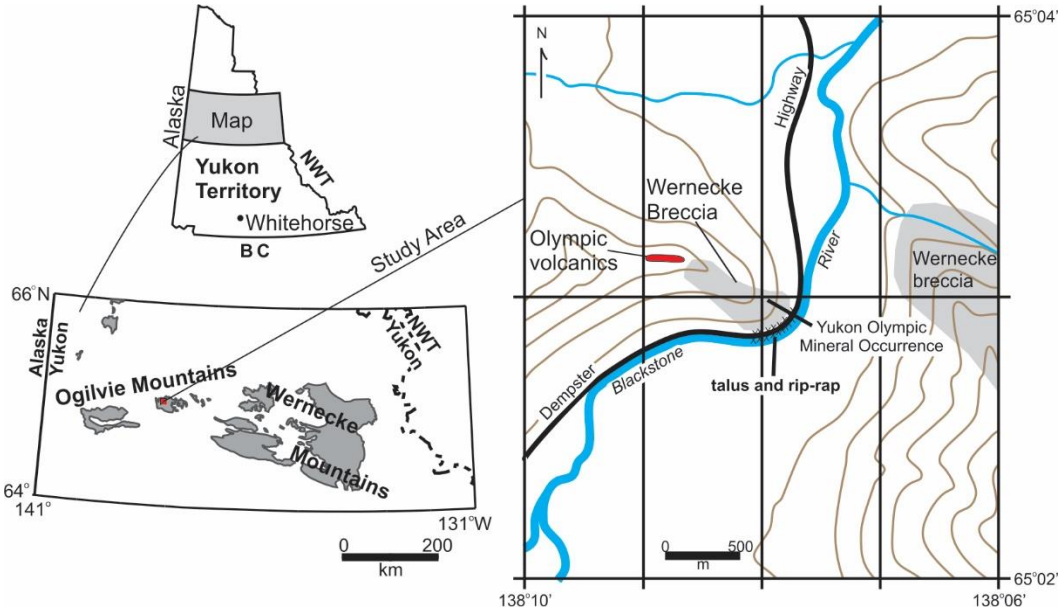

Figure E.1. Location of the Olympic volcanics, UTM NAD 1983: 634213E, 721761N. (modified after Peters and Thorkelson, 2011).

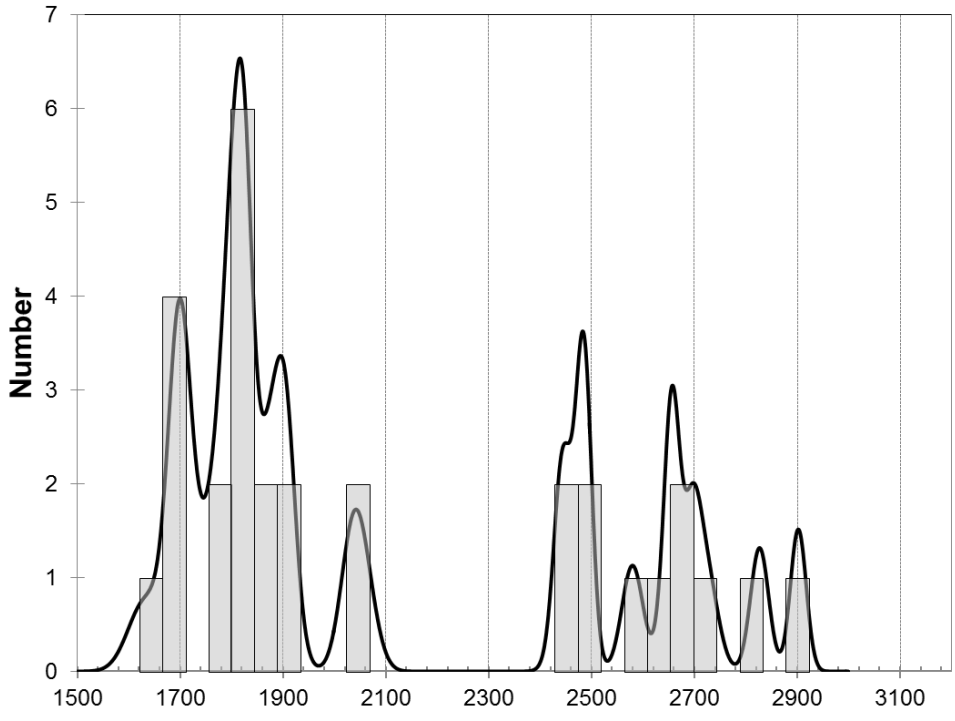

Figure E-2. Preliminary detrital zircon data, n = 30, < 20% discordance.

Table E.1. Preliminary detrital zircon data obtained by LA-ICPMS

analysis	U ppm	Th ppm	Pb* ppm	Th/U	$^{206}Pb/^{204}pb$	$^{206}Pb^*/^{207}pb^*$	±2σ %	$^{207}pb^*/^{235}U$	±2σ %	$^{206}pb^*/^{238}U$	±2σ %	error corr.	$^{206}Pb^*/^{207}pb^*$	± Ma	Disc. %
Sample JV13-39C															
JV-12 94	262	75	194	0.29	1557668	0.583	6.149	1.716	6.149	0.210	1.898	3.04475E-16	2902	31	-2
JV-12 75	159	305	126	1.92	2955	0.481	8.449	2.078	8.449	0.200	2.167	7.76112E-16	2827	35	10
JV-12 77	252	347	197	1.38	2176	0.521	8.696	1.918	8.696	0.188	2.726	2.99715E-16	2723	45	1
JV-12 98	237	185	171	0.78	4259	0.535	6.518	1.870	6.518	0.185	2.036	5.35498E-16	2695	34	-2
JV-12 100	69	41	43	0.59	9541	0.476	5.879	2.101	5.879	0.181	1.721	-3.5119E-16	2658	29	6
JV-12 85	176	121	111	0.69	25073	0.476	5.230	2.103	5.230	0.180	2.116	-1.60476E-16	2653	35	5
JV-12 93	172	134	108	0.78	2310	0.464	5.883	2.155	5.883	0.172	2.471	7.33276E-16	2580	41	5
JV-12 73	**231**	**180**	**131**	**0.78**	**4046**	**0.420**	**5.736**	**2.380**	**5.736**	**0.163**	**1.789**	**-3.46196E-16**	**2488**	**30**	**9**
JV-12 89	172	88	108	0.51	320026	0.488	6.007	2.048	6.007	0.163	1.757	-3.36654E-16	2483	30	-3
JV-12 79	**453**	**296**	**213**	**0.65**	**4565**	**0.368**	**15.432**	**2.714**	**15.432**	**0.160**	**2.763**	**0**	**2457**	**47**	**18**
JV-12 80	**182**	**143**	**114**	**0.79**	**3551**	**0.468**	**5.622**	**2.139**	**5.622**	**0.159**	**1.860**	**0**	**2442**	**31**	**-1**
JV-12 78	154	112	74	0.73	7007	0.380	7.506	2.633	7.506	0.127	2.896	3.26871E-16	2054	51	-1
JV-12 102	249	301	114	1.21	2421	0.317	7.319	3.154	7.319	0.125	2.655	-1.82802E-16	2033	47	13
JV-12 86	210	47	83	0.23	4258	0.338	6.049	2.961	6.049	0.117	2.004	2.93053E-16	1907	36	2
JV-12 96	84	61	38	0.73	3892	0.352	6.860	2.843	6.860	0.116	2.819	0	1898	51	-2
JV-12 76	130	113	59	0.87	3470	0.345	8.042	2.901	8.042	0.115	3.346	-5.28078E-16	1880	60	-2
JV-12 95	161	108	68	0.67	2053	0.329	5.917	3.037	5.917	0.115	2.604	0	1874	47	2
JV-12 84	**347**	**239**	**136**	**0.69**	**6776**	**0.300**	**6.930**	**3.329**	**6.930**	**0.112**	**1.616**	**-6.34619E-16**	**1826**	**29**	**7**
JV-12 92	223	212	90	0.95	73743	0.299	5.073	3.345	5.073	0.111	2.757	0	1823	50	8
JV-12 74	136	92	56	0.68	6899	0.321	7.740	3.111	7.740	0.111	2.899	0	1819	53	1
JV-12 72	213	137	78	0.64	12295	0.289	5.217	3.457	5.217	0.111	2.265	0	1809	41	9
JV-12 103	394	324	133	0.82	12999	0.253	7.555	3.950	7.555	0.110	2.173	-2.16399E-16	1804	40	19
JV-12 104	450	104	154	0.23	57849	0.294	6.707	3.404	6.707	0.110	2.918	5.44502E-16	1801	53	8
JV-12 83	33	54	17	1.63	291	0.331	6.643	3.024	6.643	0.109	4.437	0	1790	81	-3
JV-12 71	81	95	35	1.17	909	0.300	6.128	3.329	6.128	0.108	2.617	2.21564E-16	1768	48	4
JV-12 70	215	63	76	0.29	14949	0.300	7.585	3.339	7.585	0.105	3.485	0	1708	64	1
JV-12 99	376	694	134	1.85	4838	0.237	7.513	4.227	7.513	0.104	2.527	0	1701	47	20
JV-12 87	241	280	100	1.16	9519	0.291	7.772	3.434	7.772	0.104	2.733	0	1701	50	3
JV-12 91	**250**	**198**	**89**	**0.79**	**2043**	**0.269**	**6.096**	**3.724**	**6.096**	**0.104**	**2.075**	**5.61634E-16**	**1697**	**38**	**10**
JV-12 81	**140**	**212**	**64**	**1.51**	**1209**	**0.316**	**9.939**	**3.165**	**9.939**	**0.100**	**3.488**	**-4.09937E-16**	**1630**	**65**	**-9**

Isotope ratios and ages are NOT corrected for initial common Pb. Isotope ratio and apparent age errors include systematic calibration errors of 4.35936180005707% (208Pb/232Th), 0.384940709988595% (207Pb/206Pb), 2.27342364952939% (206Pb/238U) (all 1-sigma). Sweep-by-sweep downhole fractionation of U/Pb ratios NOT corrected via Si/Zr fractionation factor. Ablation used a laser spot size of 25 microns, and a laser firing repetition rate of 10 Hz. Sample analyses in bold intersected inclusions

References

Peters, T. J., & Thorkelson, D. J. (2010). Volcano-sedimentary megaclast in Wernecke breccia, Yukon, and its bearing on the Proterozoic evolution of northwestern Laurentia. *Yukon Exploration and Geology*, 197–206.

Furlanetto, F., Thorkelson, D. J., Rainbird, R. H., Davis, W. J., Gibson, H. D., & Marshall, D. D. (2016). The Paleoproterozoic Wernecke Supergroup of Yukon, Canada: Relationships to orogeny in northwestern Laurentia and basins in North America, East Australia, and China. *Gondwana Research*, *39*, 14–40. http://doi.org/10.1016/j.gr.2016.06.007